Quantum illumination for practical jamming-resilient LIDAR

A thesis presented in candidature for the degree Doctor of Philosophy.

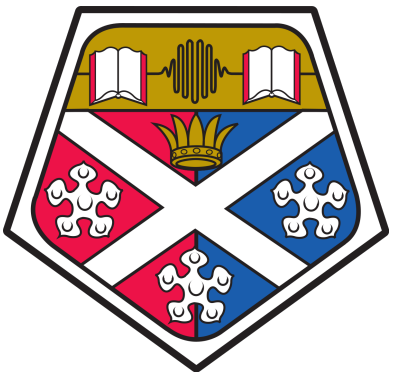

Written By

Richard James Murchie

The University of Strathclyde
Department of Physics
Glasgow, Scotland

2024

Declaration of Authors Rights

This thesis is the result of the author's original research. It has been composed by the author and has not been previously submitted for examination which has led to the award of a degree.

The copyright of this thesis belongs to the author under the terms of the United Kingdom Copyright Acts as qualified by University of Strathclyde Regulation 3.50. Due acknowledgement must always be made of the use of any material contained in, or derived from, this thesis.

Signed: 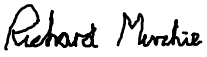

Dated: August 15, 2024

Abstract

Quantum-enhanced sensing technologies aim to use novel effects stemming from quantum physics to benefit sensing applications. Such technologies can allow for sensing in regimes for which conventional devices cannot, or they can demonstrate improved performance compared to these conventional devices. We present a quantum-enhanced LIDAR protocol that is practical for real-life use and has an operator-friendly approach to detector data processing and inference of target object presence or absence. The overarching objective of this thesis is to describe such a protocol. Our protocol is based on a quantum illumination system with click detectors (Geiger-mode single-photon avalanche photo-diodes), which uses time-correlated coincidence click-counting. We developed a theoretical framework that processes detector data into a metric intrinsically linked to the likelihood of the absence or presence of a target. This approach allows for complicated multi-channel detector data to condense into an intuitive single value. Furthermore, the theoretical framework also has a level of self-calibration inbuilt. We also characterise the functionality of our protocol in operator-friendly terms such as time-required for confident detection. Our results reinforce the advantage of quantum states, when compared to classical light in certain environmental and technological conditions, particularly when we desire covertness. These advantages persist even when operating at room temperature with off-the-shelf components, a crucial requirement for the practical roll-out of quantum-enhanced technologies. Additionally, we have demonstrated robustness to jamming, for both fast and slow dynamic jamming. Lastly, the theory provides the formalism to include any of the other non-classical correlations of our source; this feature improves the jamming-resilience of the protocol due to noise exclusion and a relative increase of heralding gain. Due to its user-operability and experimental-demonstration with off-the-shelf components, our protocol could hasten the adoption of quantum-enhanced sensing technology.

Acknowledgements

I begin my acknowledgements to my two supervisors: Prof. John Jeffers and Dr. Jonathan Pritchard. Both of whom gave me a bounty of wisdom, patience and enthusiasm towards this project. I feel fortunate to have such involved and supportive supervisors. One lasting bit of wisdom though is to always get the ribs, just in case. Another person who deserves much acknowledgement is Mateusz Mrozowski, the master of alignment. I am indebted to him for the effort he gave towards turning the LLV into reality. I have enjoyed the past four years sharing music and other esoteric things; hopefully, you finally have time for Diablo. I would also like to acknowledge Dr Gareth Brown at the DSTL for his interest, useful discussions and suggestions during this project. Also, thanks to my family for their support over the years, ma coastal characters for aw the beach tinnies and to Becca, ma chérie.

List of publications

The following journal papers and conference contributions were written during the period of study:

- R.J. Murchie, J.D. Pritchard, and J. Jeffers. "Object detection and rangefinding with quantum states using simple detection", Phys. Rev. Appl., Vol. 21, p. 064008, (2024).
- M.P. Mrozowski, R.J. Murchie, J. Jeffers, and J.D. Pritchard, "Demonstration of quantum-enhanced rangefinding robust against classical jamming", Opt. Express, Vol. 32, p. 2916, (2024).
- R.J. Murchie, M.P. Mrozowski, J.D. Pritchard, and J.Jeffers, "Towards Simple-detection Quantum Illumination LIDAR", NATO 10th Military Sensing Symposium (STO-SET-311/RSY), (2023).
- R.J. Murchie, J.D. Pritchard, and J. Jeffers, "Theoretical comparison of quantum and classical illumination for simple detection-based LIDAR", Proc. SPIE 1556, Vol. 11835, p. 118350G, (2021).

List of acronyms

This a list of the acronyms used in this thesis alongside its definition:

- **CDF**: Cumulative density function
- **CI**: Classical illumination
- **CRLB**: Cramér-Rao lower bound
- **CW**: Continuous wave
- **EM**: Electromagnetic
- **FOM**: Figure of merit
- **h.c**: Hermitian conjugate
- **H1/0**: Object present/absent
- **HE**: Heralding efficiency
- **HG**: Heralding gain
- **HP**: High pass
- **JSA**: Joint spectral amplitude
- **LIDAR**: Light detection and ranging
- **LLV**: Log-likelihood value
- **M:TBSS**: Multi mode distributed twin-beam squeezed state
- **ND**: Neutral density
- **NRF**: Noise reduction factor
- **PBS**: Polarising beamsplitter
- **POVM**: Positive operator-valued measure
- **ppKTP**: Periodically poled potassium titanyl phosphate
- **Q.A.**: Quantum advantage
- **QFI**: Quantum Fisher information
- **QI**: Quantum illumination

- **QKD**: Quantum key distribution
- **RADAR**: Radio detection and ranging
- **SNR**: Signal-to-noise ratio
- **SPAD**: Single-photon avalanche diode
- **SPDC**: Spontaneous parametric down-conversion
- **TCSPC**: Time correlated single-photon counting
- **TMSV**: Two-mode squeezed vacuum

Contents

Chapter 1: Introduction

This thesis aims to give a thorough exposition of the quantum-enhanced LIDAR protocol developed at the University of Strathclyde. We developed this protocol with the feasibility of real-life experimental implementation and ease of use at mind. When we mention 'quantum-enhanced' this refers to the use of features which require the theory of quantum mechanics and therefore have no analogue in classical physics.

1.1 Remote sensing background

Remote sensing technologies which involve the electromagnetic spectrum to probe the presence and range of a possible target object are prevalent in the modern world. Conventional RADAR functions by sending out classical electromagnetic radiation and then measuring what reflects back towards the detectors [1]. In particular, RADAR is more suited to long-range target detection than LIDAR because LIDAR wavelengths are more susceptible to scattering and absorption in the atmosphere (particularly through rain and fog) than RADAR wavelengths [2]. Enhanced conventional RADAR performance is afforded in certain situations with protocols such as noise radar, which uses the correlations between the random emitted signal and the return statistics [3]. Optical LIDAR is more suited for precise target detection over shorter ranges in comparison to RADAR systems, due to the wavelengths used [4], [5]. LIDAR has application in ground surveys [6], monitoring sea-levels [7] and aiding navigation in autonomous vehicles [8], to name but a few. Developments in detector technology have enabled LIDAR protocols to operate at the single-photon level [9]. Moreover, developments in computational analysis have facilitated 3D imaging with single-pixel detectors [10]. Both of these developments paved the way for single-photon cameras [11], [12]. Further developments demonstrated that both single-photon LIDAR and imaging can function in adverse conditions expected for real-life application [13], [14].

In this thesis we refer to classical illumination (CI) as a simplified conventional LIDAR protocol where an unmodulated pulse of light sent towards a point-source possible target object

back-reflects towards our detector for measurement as shown in Fig. 1.2 a). CI can still be regarded as in some sense a quantum protocol due to the detectors being quantum devices and that it can register a single-photon event; however we derive its name from the fact the measurement statistics on average for CI are not non-classical, unlike QI (which we now define).

1.2 Review of quantum illumination

Quantum mechanics describes features which are not intuitive to our classical understanding of the world, such as entanglement [15]. In recent times, much work has focused on harnessing these peculiar features of quantum mechanics into novel scientific and engineering applications [16]. Such developments continue even though entanglement, for example, is notorious for being very difficult to detect in real-life situations. In the context of both remote sensing and quantum mechanics, the two possibilities of object present or absent each correspond to its own quantum channel. The use of entanglement for object detection is apparent as studies from Sacchi in 2005 show entanglement can improve our ability to discern different quantum channels correctly, crucially even in entanglement-breaking situations encountered outside of laboratory environments [17], [18].

In 2008, Lloyd introduced the term 'quantum illumination' (QI) in his seminal paper [19]. QI involves the use of an initially entangled light source to perform object detection. In essence, object detection via QI entails sending a probe state of the light field (conventionally the signal) towards a possible target object and recording the light that reaches the detection system, which may include some signal reflected off the target as shown in Fig. 1.2 c). The target, if it is present, sits in a noise bath of classical light, which is detected by the signal detector whether or not the target is there. A joint entanglement-based measurement is made upon the signal and the other mode (the idler). An object's presence, for both QI and CI, is revealed by returned signal, otherwise that light is lost to the environment and the object's absence results in a return of solely noise as shown in Fig. 1.2 b) and d), respectively. QI allows us to pick out returned signal photons from this noise more easily and so provides more information per photon sent to the target. Often in literature for QI, spontaneous parametric down-conversion (SPDC) generates the entangled light source as shown in Fig. 2.3. Figure 1.1 is a simple diagram which shows how SPDC light is used for object detection via our QI protocol. In particular for the Lloyd paper, the QI light source is treated more simply as a d-mode maximally entangled two-beam state, with each mode in the signal and idler beams containing a single-photon. This early work describes an intrinsic advantage over single-photon CI in the regime with a weak

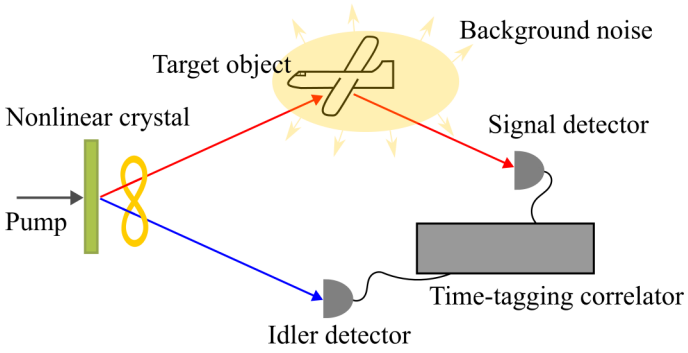

Figure 1.1 – Schematic of our QI scheme for object detection with our light source generated from a non-degenerate SPDC process.

emitted signal and strong environmental background noise. Lloyd demonstrates that there is a factor of d improvement of the SNR for QI compared to single-photon CI. This work clearly shows how entanglement can improve system performance for object detection. QI is remarkable as an entanglement-utilising protocol, as its benefit persists even in entanglement-breaking situations. This further validates the claims made by Sacchi years prior. Moreover, we quantify this persistence of quantum advantage by a measure of non-classicality of the information content of a state, known as quantum discord [20]. However, the protocol developed by Lloyd does have some issues if we wish to map it onto a realistic quantum-enhanced LIDAR system. For example, Lloyd describes that measurement is an optimal joint measurement on the idler and signal photons, which is either unknown or difficult to implement experimentally. In particular, retainment of the idler photon such that we can measure it jointly with the signal photon greatly adds to the complexity of the experimental setup. Even a simple experimental implementation to retain the idler by means of a delay line for the idler beam is inappropriate for LIDAR due to the often unknown signal photon delay. Furthermore, QI is not compared with the optimal scheme for classical object detection and the background noise model is unrealistic as it does not consider thermal light with a Bose-Einstein photon-number distribution. Lastly, the theoretical treatment does not derive the entangled twin beam state from a physical process such as SPDC (which would include multi-photons and not just single photons). A more thorough theoretical treatment by Shapiro and Lloyd extended QI to allow multi-photons and compared QI to object detection with coherent-state transmission. This work demonstrated that QI does not outperform classical methods with coherent detection when in low noise regimes [21]. Tan et al. extended the theory of QI to use Gaussian states as the QI light source. This work demonstrated that QI outperforms all CI methods in lossy, high noise and

low signal strength scenarios [22]. Moreover, in ideal conditions with an entangled source, up to a 6 dB enhancement in the error-probability exponent is obtained over the optimal classical system [23], [24]. Here, we define the optimality of these measurements by the minimum probability of error given by the Helstrom bound [25]. Unfortunately, the optimal measurement scheme required to achieve this bound experimentally is unknown. Nevertheless, early work by Guha and Erkmen presented phase-sensitive measurement schemes which realise up to 3 dB enhancement in the error-probability exponent [26]; however, these schemes are difficult to implement experimentally. Therefore, the first experimental demonstration (by Lopaeva et al.) of optical wavelength QI involved a more experimentally-simple approach using photo-counting and second order correlation measurements [27]. Following this, much theoretical analysis has accumulated for optical- or microwave-based joint-measurement QI protocol variants [28]–[47]. There are also experimental demonstrations of optical- or microwave-based QI protocols which require joint-measurement and phase-sensitivity [48]–[51]. However, the protocols which require joint-measurement and/or phase-sensitivity are impractical for use outside of the laboratory due to their experimental demands. Lastly, recent research by Nair and Gu provides universal performance bounds for idler-assisted sensing [52]. These performance bounds are universal because it is independent of the type of probe and measurement used.

It is possible to exploit not the entanglement but the strong correlations of the photon pairs generated in the weak limit of the SPDC process to obtain a quantum advantage with a simpler detection protocol. These photon pairs have several possible correlations, including photon-number, temporal and spectral. Instead of a joint entanglement-based measurement on the signal and idler modes, we make individual measurements upon each mode. Even with individual measurements, the non-classical correlations with the signal mode and idler mode enhances the sensitivity of the signal mode measurement via heralding. The signal mode is the mode which contains information about the presence or absence of the possible target object. We frame target detection via QI as a quantum state discrimination problem, due to the binary situation of the object present (H1) or absent (H0) hypotheses [53]. More generally, we recognise that QI as a state discrimination problem is similar to QI as a quantum parameter estimation problem [54]–[57].

To continue in the vein of considering QI protocols without using a joint measurement scheme, systems with independent quadrature measurements on the signal and idler show that QI retains an advantage over CI, while not necessarily being better than the best possible classical source [58]–[60]. More recently, a new approach from work by Reichert et al. for QI with independent quadrature measurements, which uses heterodyne measurement on the

signal channel to condition the idler channel with a phase shift for the idler channel homodyne measurement, demonstrates a 3 dB enhancement in the error-probability exponent compared to the optimal classical system [61]. A similar approach from Shi et al. demonstrates the optimal advantage of this technique [62], [63]. Unrelated to quadrature measurements, studies show that QI with photon-counting and second-order correlation measurements retains advantage over CI [64]–[70]. Recently, work from Blakey et al. demonstrates a QI-based target detection method using non-local cancellation of dispersion [71], [72]. More pertinently however, studies show a quantum enhancement from QI with simple photo-counting by click detectors [73]–[79]. Research by Yang et al. shows a QI protocol with simple photo-counting with multiplexed click detectors, which can (in the limit of many detectors) reproduce the photon-number distribution of the incident state and provide resilience to sensor dead-time [80]. QI with photon-counting using click detectors is the easiest to implement experimentally, which suggests that it is suitable as an approach for developing a practical quantum-enhanced LIDAR.

Object detection and range-finding in a realistic noise and loss environment is challenging. In an unrealistic scenario without noise or loss a heralded QI scheme can provide signal states to interrogate the object that are very different, depending on the result of the heralding measurement, which provides a quantum advantage. However, with noise and loss this quantum advantage disappears almost completely by the time the light gets to the detectors. We show that the detectors themselves provide sub-optimal measurements, all of which means that we need a framework that can work with the tiny remaining advantage over multiple experimental shots. This thesis presents a model for object detection and range-finding with quantum states using simple detection with Geiger-mode click photo-detectors. Literature already exists for quantum-enhanced range-finding, for example, pioneering early work by Rarity et al. which predates the terminology of QI demonstrated range-finding using non-classical correlations from a photon pair source [81]. Furthermore, performance analysis of a QI-based LIDAR which uses the Doppler effect for velocity estimation is in separate work by Zhuang et al. and Reichert et al. [82], [83], with the ultimate limit on this estimation for range (and velocity) described in work by Huang et al. [84]. Additionally, later developments in QI-based detection schemes have also demonstrated range-finding [85]–[90]. However, the method that we present treats detector data differently in that multiple detector data channels are condensed into a single metric. This approach means we can also include the often-overlooked information from non-coincidence events to enhance state discrimination. Our framework has a degree of self-calibration due to the statistical approach and the parameter regimes typically encountered in QI. The method facilitates easy comparison between different detection schemes, for example

CI and QI, for inference of an object's presence and range via a metric whose interpretation depends on the likelihood of an object's presence. Our results quantify the advantage of QI over CI when performing target discrimination in a noisy thermal environment. We provide an operator-friendly approach to quantifying system performance via estimation of the time required to detect a target with a given confidence level. Moreover, we have extended our theory to include any of the correlations available, which further enhances state discrimination. Finally, we have applied our theoretical framework to experimentally demonstrate the jamming-resilience of quantum-enhanced range-finding [91].

For regimes where QI does not out-perform optimal classical protocols, such as high signal mean photon number regimes $\bar{n} \gg 1$, there exist advantageous protocols inspired by QI. For example, Liu et al. uses coherent detection and the random and chaotic time-frequency characteristics between a classically-correlated reference and probe beam [92]. Moreover, Brougham et al. uses random coherent states with different amplitudes to mimic a thermal distribution (on average) upon each individual mode [93]. This approach mimics QI, as each individual mode in QI has a thermal distribution. This protocol uses photo-counting rather than coherent detection. Other protocols such as the work by Torromé extends QI to consider three modes instead, with an increase of SNR compared to a two-mode QI equivalent; however, there is no practical experimental implementation to realise this three-mode QI yet [94], [95]. Furthermore, quantum-enhanced object detection need not use QI as the underlying protocol or inspiration. For example, a quantum LIDAR based off thresholded detection with photon-number resolving detectors [96], a quantum interferometer RADAR [97] and the Maccone-Ren proposal [98]. However, for example, an impracticality of the Maccone-Ren proposal is its extreme sensitivity to noise. Therefore, we do not consider these alternative protocols further, as we consider the object detection and range-finding problem in the context of experimentally-practical protocols that function in weak signal strength and high noise regimes.

1.3 System overview

An overview of our system for performing optical detection of a target object immersed in a thermal background using simple detection is shown schematically in Fig. 1.2 for both CI and QI regimes. For the CI system, we use a single-mode beam to interrogate the target and data provided by recording click-counts on the signal detector. We consider a QI source produced by a pulsed pump laser with repetition rate f_{rep}. Each pump pulse produces, via parametric down-conversion [99], [100], a QI source state located centrally within a single pulse temporal

window of duration $1/f_{\text{rep}}$. The mechanism for state production is a quasi-simultaneous photon pair production from one pump photon. The quasi-simultaneous nature of the pair production provides effective short term temporal correlations that are exploited to enable target detection and range-finding via coincident detection. Outside this very short timescale the two beams are effectively uncorrelated. QI has a level of background noise jamming-resilience due to the coincidence detection method, as background noise is mostly filtered out unless in accidental coincidence with an idler detection. Each state is described mathematically by Eq. 2.46 which is the output of the SPDC process: the twin-beam state. We assume that the pump is of a strength that it produces a twin-beam state with a mean photon number much smaller than one. This state is distributed over two spatially separated modes: the signal beam and the idler beam. Within the short correlation timescale the twin-beam state has non-classical photon-number, frequency and polarisation inter-beam correlations; outside it the two beams are uncorrelated. Note that for QI, we do not necessarily require a pulsed pump. The intrinsic correlations of the SPDC source enable application of a continuous wave (CW) pump to this same framework, with the corresponding time window of a single shot equal to a coincidence detection window duration τ_c. For CI, we assume that the signal is a pulsed source with repetition rate f_{rep} with the same frequency and mean photon number as the QI signal. Our form of CI is not the best implementation possible for CI as we are not using coherent detection methods, for example. We use its statistics to derive the single-shot click probabilities associated with a single pulse window duration $1/f_{\text{rep}}$.

The detectors in our protocol are Geiger-mode avalanche photo-diodes, insensitive to phase and which register a click or a no-click event for each experimental shot of the system, hence the term 'simple detection' [101]. As production of our signal is near the single-photon level, the detectors are thresholded (in sensitivity) such that single-photon events can trigger them. This makes them appropriate for use in realistic low signal strength sensing environments. All loss of light in our system unrelated to interaction with the target object, such as detector quantum efficiency and coupling loss, are accounted for by the system loss parameter. We define the idler detector system loss η_{I} and the signal detector system loss η_{S}, where $\eta_{\text{I/S}} = 1$ represents no loss. Whereas all forms of loss due to the probing process with the target object, such as absorption and scattering, are accounted for by the signal attenuation factor ξ, where $\xi = 1$ represents no loss from the probing of a target.

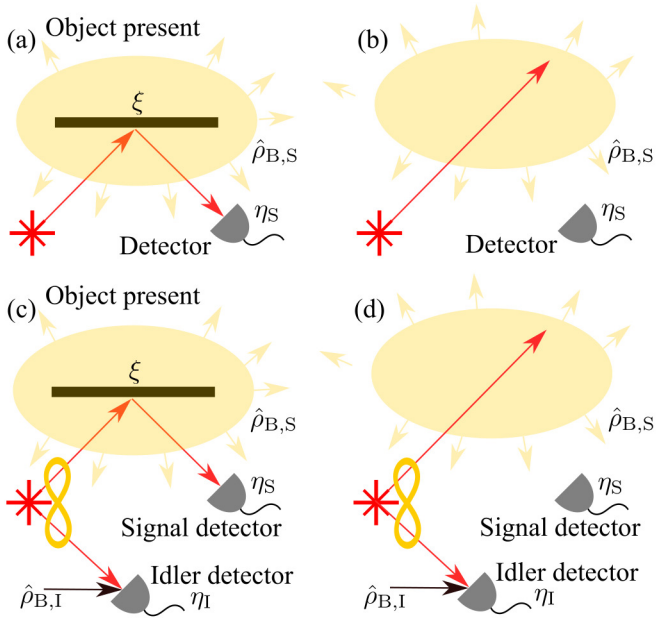

Figure 1.2 – Schematic of optical LIDAR for a target of finite reflectivity ξ in a thermal background $\hat{\rho}_{B,S}$. In the CI regime with target (a) present or (b) absent, a single-mode signal beam is used to interrogate the target with a single signal detector used to measure the return field mode. In the QI regime with target (c) present or (d) absent, a photon pair-source is used to illuminate the target, with an additional detector used to directly measure the idler mode (accounting for idler background noise $\hat{\rho}_{B,I}$) providing a coincident detection channel.

1.4 Overview of thesis

This thesis aims to provide a user-friendly exposition of a quantum-enhanced practical LIDAR protocol. From this, an aim is to quantify the system performance for both quantum-enhanced LIDAR and an unentangled (CI) benchmark. Our discussion about system performance leads to the advantage of considering multi-mode correlations between the correlated beams of the quantum-enhanced system. Lastly, we aim to demonstrate the suitability of our detector data processing framework for our system in the presence of jamming (dynamically varying background noise). Concerning the scope of this thesis, we avoid over-generalising our description of the LIDAR protocol for the user-friendliness of our exposition. Hence, we limit the scope to a quantum illumination-based system with click detectors. Conversely, to avoid restricting this protocol to a particular experimental setup, we ensure that we can apply this protocol to a variety of experimental conditions. For example, our protocol is appropriate irrespective of the wavelengths involved or whether our pump is CW or pulsed.

The thesis is organised as follows. In Ch.2 the relevant background theory of quantum optics is presented for our characterisation of non-classicality and the states of light used. Chapter 3

gives the necessary theory for observables and measurements. Chapter 3 also presents the derivation and expression of the click probabilities which characterise our object detection model. Chapter 4 demonstrates how we analyse system performance for QI and CI with the defined figures of merit. Chapter 5 extends the theory of our QI protocol to include any form of two-beam correlation that the SPDC output could possess. Chapter 6 describes our protocol for range-finding and provides counter-measures for dynamic jamming attacks. Chapter 7 provides the methodology for the numerical simulations used throughout this thesis. Chapter 8 presents the experimental data from our QI laboratory experiment. Chapter 9 concludes the thesis with a discussion of current capabilities, issues with the system and future applications.

Chapter 2: Background theory

LIDAR requires the generation, transmission and detection of an electromagnetic field (EM-field). Hence, this chapter provides background theory and the mathematical framework for the characterisation of light. This thesis considers electromagnetic radiation through the framework of a 'mode' [102]. An EM-field satisfies Maxwell's equations. Within the field is a mode, which is uniquely described by the set of values within the degrees of freedom a field possesses: such as frequency and polarisation.

Maxwell's equations for the EM-field in a vacuum are

$$\nabla \times \mathbf{E} = -\frac{\partial \mathbf{B}}{\partial t}, \tag{2.1a}$$

$$\frac{1}{\mu_0}\nabla \times \mathbf{B} = \epsilon_0 \frac{\partial \mathbf{E}}{\partial t} + \mathbf{J}, \tag{2.1b}$$

$$\nabla \cdot \mathbf{E} = \frac{\sigma}{\epsilon_0}, \tag{2.1c}$$

$$\nabla \cdot \mathbf{B} = 0, \tag{2.1d}$$

where $\mathbf{E}$ is the classical electric field vector, $\mathbf{B}$ is the classical magnetic field vector, μ_0 is the vacuum permeability, ϵ_0 is the vacuum permittivity, σ is the charge density and $\mathbf{J}$ is the current density [103]. We will mostly be concerned with the electric field as a plane-wave in 3-D Cartesian space. This is a monochromatic electric field vector with only one polarisation

$$\mathbf{E}_\omega \equiv E_\omega(\mathbf{r}, t) = \alpha(\omega) e^{i(\mathbf{k}(\omega)\cdot\mathbf{r} - \omega t)} + \alpha^*(\omega) e^{-i(\mathbf{k}(\omega)\cdot\mathbf{r} - \omega t)}, \tag{2.2a}$$

$$= E^+_\omega(\mathbf{r}, t) + E^-_\omega(\mathbf{r}, t), \tag{2.2b}$$

where ω is the angular frequency of the source, $\mathbf{r} = (r_x, r_y, r_z)$ are the spatial Cartesian coordinates, $\mathbf{k}(\omega) = (k_x(\omega), k_y(\omega), k_z(\omega))$ is the wave-vector and $E^+_\omega(\mathbf{r}, t)$ is the positive-frequency component of the electric field vector which contains $\alpha(\omega)$ the amplitude of the field. This plane-wave solution satisfies Maxwell's equations.

The work presented in this thesis requires quantisation of the electromagnetic (EM)-field,

due to the use of light which cannot be described via the classical theory of electromagnetism. Quantum-mechanical operators that operate on a Hilbert space are used to describe a mode of the quantised EM field. The modes of the classical EM-field satisfy the harmonic oscillator partial differential equation. Therefore we quantise using quantum harmonic oscillators in the next section. Analysis of quantum systems is benefited by use of the quantum harmonic oscillator as it is a rare system in quantum mechanics with an analytic solution.

2.1 Quantisation of the electromagnetic field

Quantisation of the EM-field is a procedure first written down by Dirac [104]. This procedure begins by defining a vector $\mathbf{A}$ and scalar potential ϕ such that

$$\mathbf{B} = \nabla \times \mathbf{A}, \tag{2.3a}$$

$$\mathbf{E} = -\nabla\phi - \frac{\partial \mathbf{A}}{\partial t}. \tag{2.3b}$$

We substitute Eq. 2.3a and Eq. 2.3b into the Maxwell equations Eq. 2.1b and Eq. 2.1c. This substitute yields

$$\nabla(\nabla \cdot \mathbf{A}) - \nabla^2 \mathbf{A} + \frac{1}{c^2}\frac{\partial}{\partial t}\nabla\phi + \frac{1}{c^2}\frac{\partial^2}{\partial t^2}\mathbf{A} = \mu_0 \mathbf{J}, \tag{2.4a}$$

$$-\epsilon_0 \nabla^2 \phi - \epsilon_0 \nabla \cdot \left(\frac{\partial}{\partial t}\mathbf{A}\right) = \sigma. \tag{2.4b}$$

Both Eq. 2.4a and Eq. 2.4b are referred to as the field equations. These equations determine the EM-field, based off a given distribution of current $\mathbf{J}$ and charge σ. However, the above forms for the field equations are complicated, therefore it is convenient to introduce the Coulomb gauge, which requires $\nabla \cdot \mathbf{A} = 0$. The Coulomb gauge allows for simplification of our analysis as the potentials can vary, all while leaving the physically measurable field unaffected. By invoking the Coulomb gauge condition we reduce the redundancies of the vector potential; this is useful as we wish to minimise the number of dynamic variables which describe the field dynamics. A further simplification is facilitated by application of Helmholtz' theorem, which states that we can write a vector field as a sum of two components (one component with zero divergence and the other component with zero curl). We can write the current density as $\mathbf{J} = \mathbf{J}_\mathrm{T} + \mathbf{J}_\mathrm{L}$, where $\mathbf{J}_\mathrm{T}$ is the transverse component (which has no divergence) and $\mathbf{J}_\mathrm{L}$ is the longitudinal component (which has no curl). Further analysis means that $\mathbf{J}_\mathrm{L} = \epsilon_0 \frac{\partial}{\partial t}\nabla\phi$. This further analysis eliminates the scalar potential from Helmholtz' theorem decomposed field equation with the transverse

current density. Therefore, the field equation Eq. 2.4a simplifies to

$$-\nabla^2\mathbf{A} + \frac{1}{c^2}\frac{\partial^2}{\partial t^2}\mathbf{A} = \mu_0\mathbf{J}_\mathrm{T}, \tag{2.5}$$

this is equivalent to the transverse field equation if we were to use the Lorentz gauge instead ($\nabla\cdot\mathbf{A} + \frac{1}{c^2}\frac{\partial}{\partial t}\phi = 0$). The Lorentz gauge is useful as it has relativistic invariance, unlike the Coulomb gauge. However, for the scope of this thesis we shall focus on the quantisation in the Coulomb gauge only. We can also use Helmholtz' theorem to decompose Eq. 2.3b, which means we can state the transverse electric field $\mathbf{E}_\mathrm{T}$ in terms of the vector potential as

$$\mathbf{E}_\mathrm{T} = -\frac{\partial\mathbf{A}}{\partial t}. \tag{2.6}$$

The quantisation procedure is set for the free-space classical field, which is a region of space where $\mathbf{J}_\mathrm{T} = 0$ and there are no free charges. In free-space the electric field is entirely transverse and so we set $\mathbf{E} = \mathbf{E}_\mathrm{T}$. By setting the transverse current density to zero this further simplifies the field equation Eq. 2.5 into the form

$$-\nabla^2\mathbf{A} + \frac{1}{c^2}\frac{\partial^2\mathbf{A}}{\partial t^2} = 0. \tag{2.7}$$

Imagining the field is within a cubic cavity of side length L allows the decomposition of $\mathbf{A}$ into a Fourier series

$$\mathbf{A}(\mathbf{r},t) = \sum_{\mathbf{k}}\sum_{s=1}^{2} e_{\mathbf{k},s}\left(\mathbf{A}_{\mathbf{k},s}(t)e^{i\mathbf{k}\cdot\mathbf{r}} + \mathbf{A}^*_{\mathbf{k},s}(t)e^{-i\mathbf{k}\cdot\mathbf{r}}\right), \tag{2.8}$$

where s is the index for the polarisation and $e_{\mathbf{k},s}$ is the unit polarisation vector. This unit polarisation vector has the condition $e_{\mathbf{k},s}\cdot\mathbf{k} = 0$ to ensure that the vector potential is transverse, as required by the Coulomb gauge. It also has the condition $e_{\mathbf{k},s}\cdot e_{\mathbf{k},s'} = \delta_{s,s'}$, which ensures that two different polarisations are perpendicular to each other and that two identical polarisations are parallel to each other. The Fourier coefficients $\left(\mathbf{A}_{\mathbf{k},s}(t) = \mathbf{A}_{\mathbf{k},s}e^{-i\omega_\mathbf{k}t}, \mathbf{A}^*_{\mathbf{k},s}(t) = \mathbf{A}^*_{\mathbf{k},s}e^{i\omega_\mathbf{k}t}\right)$ satisfy the simple classical harmonic equation. For example, $\mathbf{A}_{\mathbf{k},s}(t)$ satisfies

$$\frac{\partial^2\mathbf{A}_{\mathbf{k},s}(t)}{\partial t^2} + \omega_\mathbf{k}^2\mathbf{A}_{\mathbf{k},s}(t) = 0. \tag{2.9}$$

In terms of the time-independent components $\left(\mathbf{A}_{\mathbf{k},s}, \mathbf{A}^*_{\mathbf{k},s}\right)$ the energy of a mode of the EM-field in this cavity is

$$\mathcal{E}_{\mathbf{k},s} = \epsilon_0 V\omega^2\left(\mathbf{A}_{\mathbf{k},s}\mathbf{A}^*_{\mathbf{k},s} + \mathbf{A}^*_{\mathbf{k},s}\mathbf{A}_{\mathbf{k},s}\right), \tag{2.10}$$

where $V = L^3$ is the volume of the quantisation cavity. Furthermore, as our system is a simple harmonic oscillator we can introduce the conjugate variables corresponding to generalised position $\mathbf{Q}_{\mathbf{k},s}$ and momentum $\mathbf{P}_{\mathbf{k},s}$ and express the energy of the field in terms of these variables as

$$\mathcal{E}_{\mathbf{k},s} = \frac{1}{2}\left(\mathbf{P}^2_{\mathbf{k},s} + \omega^2_{\mathbf{k}}\mathbf{Q}^2_{\mathbf{k},s}\right). \tag{2.11}$$

Hence, we can express the time-independent component $\mathbf{A}_{\mathbf{k},s}$ in terms of the position and momentum variables as

$$\mathbf{A}_{\mathbf{k},s} = \frac{1}{\sqrt{4\epsilon_0 V \omega^2_{\mathbf{k}}}}\left(i\mathbf{P}_{\mathbf{k},s} + \omega_{\mathbf{k}}\mathbf{Q}_{\mathbf{k},s}\right). \tag{2.12}$$

Equation 2.8 and Eq. 2.9 show that the vector potential is described by a set of harmonic oscillators and so quantisation of the EM-field is achieved by converting the position and momentum variables into quantum-mechanical operators. Thus, $\mathbf{Q}_{\mathbf{k},s} \to \hat{q}_{\mathbf{k},s}$, $\mathbf{P}_{\mathbf{k},s} \to \hat{p}_{\mathbf{k},s}$ and $\mathbf{A}_{\mathbf{k},s} \to \hat{A}_{\mathbf{k},s}$. This quantised field is dynamically described by a quantum harmonic oscillator. Our quantum operators that were our classical variables must satisfy the canonical commutation relations

$$[\hat{q}_{\mathbf{k},s}, \hat{p}_{\mathbf{k}',s'}] = \hat{q}_{\mathbf{k},s}\hat{p}_{\mathbf{k}',s'} - \hat{p}_{\mathbf{k}',s'}\hat{q}_{\mathbf{k},s} = i\hbar\delta_{\mathbf{k}\mathbf{k}'}\delta_{s,s'}, \tag{2.13a}$$

$$[\hat{q}_{\mathbf{k},s}, \hat{q}_{\mathbf{k}',s'}] = 0, \tag{2.13b}$$

$$[\hat{p}_{\mathbf{k},s}, \hat{p}_{\mathbf{k}',s'}] = 0, \tag{2.13c}$$

where $\delta_{\mathbf{k}\mathbf{k}'}$ is the Kronecker delta which has $\delta_{\mathbf{k}\mathbf{k}'} = 0$ for $\mathbf{k} \neq \mathbf{k}'$ and $\delta_{\mathbf{k}\mathbf{k}'} = 1$ for $\mathbf{k} = \mathbf{k}'$. The commutator relation Eq. 2.13a is non-zero when $\mathbf{k} = \mathbf{k}'$ and $s = s'$, hence the two observables position and momentum cannot be measured infinitely accurately in a quantised field: the details behind this are discussed in Ch. 2.3. Furthermore, for any canonically conjugate operators $\hat{X}$ and $\hat{Y}$ (i.e $[\hat{X}, \hat{Y}] = z$, where z is a complex number), if there is a time-dependence for these operators then the equal-time commutator

$$[\hat{X}(t), \hat{Y}(t)] = z, \tag{2.14}$$

is the same as its commutator when there is no time-dependency upon those operators.

With the equal-time commutator result in mind we now demonstrate the similarity between the abstract canonical position and momentum operators to the canonical position and momentum for the field in position-space. In the Coulomb gauge, $-\epsilon_0\hat{E}(\mathbf{r}, t)$ is the canonical momentum of the field, where $\hat{A}(\mathbf{r}, t)$ is the canonical position for the field. The equal-time

commutator between Cartesian components of these operators is

$$[\hat{A}_i(\mathbf{r},t), -\epsilon_0\hat{E}_j(\mathbf{r}^{'},t)] = i\hbar\delta_{\mathrm{T}ij}(\mathbf{r}-\mathbf{r}^{'}), \tag{2.15}$$

where $\delta_{\mathrm{T}ij} = \frac{1}{(2\pi)^3}\int d\mathbf{k}(\delta_{ij} - \frac{k_i k_j}{k^2})e^{i\mathbf{k}\cdot(\mathbf{r}-\mathbf{r}^{'})}$ is the transverse delta-function. Equation 2.15 results from a rigorous derivation of the quantisation of the EM field beginning with a Lagrangian with appropriate conjugate variables which lead onto expressing the field variables already defined. Furthermore, the reason why we express this commutator between the Cartesian components is that the Cartesian components are not independent of each other (due to the transverse nature of the vector potential and field). The similarity of Eq. 2.15 to the canonical position and momentum commutator in Eq. 2.13a is obvious.

Further analysis with a quantised field is benefited by introducing the (dimensionless) canonical creation operator

$$\hat{a}^{\dagger}_{\mathbf{k},s} = \frac{1}{\sqrt{2\hbar\omega}}(\omega\hat{q}_{\mathbf{k},s} - i\hat{p}_{\mathbf{k},s}), \tag{2.16}$$

this relates to the time-independent vector potential amplitude as $\hat{A}^{\dagger}_{\mathbf{k},s} = \sqrt{\frac{\hbar}{2V\epsilon_0\omega_{\mathbf{k}}}}\hat{a}^{\dagger}_{\mathbf{k},s}$. The creation operator $\hat{a}^{\dagger}_{\mathbf{k},s}$ in effect 'creates' a quantum of energy $\hbar\omega$ in a mode, also referred to as a photon in the context of optics. The creation operator and its hermitian conjugate (h.c.), the destruction operator has a commutator relation derived from Eq. 2.13a. This commutator relation is $[\hat{a}_{\mathbf{k},s}, \hat{a}^{\dagger}_{\mathbf{k},s}] = \delta_{\mathbf{k}\mathbf{k}'}\delta_{s,s'}$. This commutation shows that each quantised mode influences itself only.

From Eq. 2.6 and Eq. 2.8 the multi-mode classical electric field vector in a free-space cubic cavity (when spatial freedom constrained to the z-axis, is collinear on the z-axis and considering only one polarisation) is

$$E(z,t) = i\sum_{k_z}\omega_k\left(A_k e^{-i(\omega_k t - k_z z)} - A_k^* e^{i(\omega_k t - k_z z)}\right), \tag{2.17}$$

where ω_k represents the frequency for a given wavenumber k, which for the constrained field on one axis the wavenumber is thus $k = |\mathbf{k}| = k_z$. For the remainder of this thesis we omit the unit polarisation vector $e_{\mathbf{k},s}$ and only consider one polarisation, for brevity. We also consider that the cavity walls have periodic boundary conditions, therefore the wave-vector z-component takes the discrete values $k_z = \frac{2\pi\nu}{L}$, where ν is any integer. It is simple to recast the above as a

multi-mode quantum-mechanical electric field operator, as

$$\hat{E}(z,t) = i\sum_{k_z}\sqrt{\frac{\hbar\omega_k}{2\epsilon_0 V}}\big(\hat{a}_k e^{-i(\omega_k t - k_z z)} - \hat{a}_k^\dagger e^{i(\omega_k t - k_z z)}\big). \tag{2.18}$$

However, later in this thesis there is a conscious effort to ensure that the number of modes within each quantum system is limited, for the sake of simplicity. It is wise to define the classical electric field vector over entire frequency domain, this requires a change from discrete modes to continuous modes. We can imagine our cavity z-axis having infinite extent but with a finite cross-sectional $A_{\text{c.s}}$ area perpendicular to the z-axis. As we are restricted to one axis, the wavenumber $k = \frac{\omega}{c}$ is equivalent to the mode variable k_z. From our relation of wavenumber to angular frequency, the mode spacing is $\Delta\omega = \frac{2\pi c}{L}$. The mode spacing must tend to zero $\Delta\omega \to 0$ if we wish to consider the set of modes as a continuum, which justifies the condition that our cavity z-axis length L has an infinite extent. Therefore, we convert from a discrete sum of modes to a continuous integral via the relation $\sum_{k_z} \to \frac{1}{\Delta\omega}\int d\omega$. We also convert from the discrete mode destruction operator to its continuous counterpart as $\hat{a} \to (\Delta\omega)^{\frac{1}{2}}\hat{a}(\omega)$ [105]. The creation operator is similarly converted. The quantum-mechanical electric field operator for a multi-mode state over the entire frequency domain is

$$\hat{E}(z,t) = i\int d\omega\sqrt{\frac{\hbar\omega}{4\pi c\epsilon_0 A_{\text{c.s}}}}\left(\hat{a}(\omega)e^{i(k_z(\omega)z-\omega t)} - \hat{a}^\dagger(\omega)e^{-i(k_z(\omega)z-\omega t)}\right), \tag{2.19a}$$

$$= \hat{E}^+(\mathbf{r},t) + \hat{E}^-(\mathbf{r},t), \tag{2.19b}$$

where $\hat{a}^\dagger(\omega)$ is the creation operator for frequency ω, $k_z(\omega)$ is the z-axis wave-vector for frequency ω and $\hat{E}^-(\mathbf{r},t)$ contains the creation operator term in the decomposition of the electric field into positive and negative frequency terms.

An important concept to now introduce is Hilbert space $\mathfrak{H}$ as each mode of the quantised EM-field has its own. This is a vector space with an inner product $\langle\cdot,\cdot\rangle$ which has a norm $||\cdot||$ defined as

$$||v_1|| = \sqrt{\langle v_1, v_1\rangle}, \tag{2.20}$$

for a vector $v_1 \in \mathfrak{H}$. The space $\mathfrak{H}$ must be complete with respect to the norm $||v_1 - v_2||$, where $v_2 \in \mathfrak{H}$. In other words every Cauchy sequence converges to an element in $\mathfrak{H}$. A Cauchy sequence is a sequence in which the elements become arbitrarily close to each other as the sequence progresses. The properties required for a Hilbert space are all useful in the analysis of light. For example, the existence of the inner product allows for the similarity between two states to be

investigated. No similarity means they are orthogonal, which is easily defined in inner product terms as $\langle \cdot, \cdot \rangle = 0$.

Another useful concept to introduce is Dirac notation. This notation succinctly describes quantum states and their actions with inner-products and outer-products. For example, a system with a wave-function $\psi(x)$ with spatial coordinates has a state vector $|\psi\rangle$ which fully describes the system in Hilbert space. The state vector $|\psi\rangle$ can be expanded into a basis of energy eigenstates $|E_n\rangle$. To demonstrate this we begin with the Hamiltonian eigenvalue equation,

$$\hat{H}|E_n\rangle = E_n|E_n\rangle, \tag{2.21}$$

for energy E_n at energy level n. For the scope of this thesis, in quantum-mechanics the Hamiltonian is an operator which specifies the energy of a quantum system. The Hamiltonian is also useful for expressing the evolution of a quantum state $|\psi(t)\rangle$ in the interaction picture. The time-dependent Schrodinger equation is

$$i\hbar\frac{\partial|\psi(t)\rangle}{\partial t} = \hat{H}(t)|\psi(t)\rangle, \tag{2.22}$$

this describes the time-evolution of a quantum state $|\psi(t)\rangle$. If we take an initial time $t = 0$, any quantum state at time t is solved to be

$$|\psi(t)\rangle = e^{-\frac{i}{\hbar}\int_0^t d\tilde{t}\hat{H}(\tilde{t})}|\psi(0)\rangle. \tag{2.23}$$

The initial quantum state is $|\psi(0)\rangle = |\psi\rangle$. We now frame the state vector $|\psi\rangle$ in the energy eigenstate basis

$$|\psi\rangle = \sum_{n=0}^{\infty} E_n|E_n\rangle, \tag{2.24}$$

where $E_n = \langle E_n|\psi\rangle$.

In summary, this section quantised the EM-field, introduced the concept of the Hamiltonian and its purposes, Hilbert space and Dirac notation. The following section elaborates upon the creation operator for a single mode and how a basis based off of photon number (the Fock basis) in Hilbert space allows for straight-forward analysis of light.

2.2 The Fock state

The creation of a photon from the initial state of a single-mode vacuum in Dirac notation is

$$\hat{a}^\dagger|0\rangle = |1\rangle. \tag{2.25}$$

Here $|1\rangle$ represents a single-photon Fock state as

$$|1\rangle = (0, 1, 0, \dots)^{\mathrm{T}}, \tag{2.26}$$

with the vector an element of (infinite-dimensional) Hilbert space. The Fock state is a quantum state and these states can be used as a basis for the quantum state vector of a mode, as the Fock basis spans its Hilbert space. In less mathematical terms, this means that any possible photon-number a mode can have can be described by a Fock state.

An arbitrary single-mode pure quantum state $|\psi\rangle$ expressed in the Fock basis is

$$|\psi\rangle = \sum_{n=0}^{\infty} c_n|n\rangle, \tag{2.27}$$

for a set of complex numbers c_n and the n-photon Fock states $|n\rangle$. The Fock states form an orthonormal basis, as $\langle n|m\rangle = \delta_{nm}$. Using this the inner product of $|\psi\rangle$ with itself is therefore very simple

$$\langle\psi|\psi\rangle = \sum_{n=0}^{\infty} c_n c_n^*, \tag{2.28}$$

where for a normalised state Eq. 2.28 equals to one. Otherwise, an unnormalised state $|\psi\rangle_{\text{unnorm}}$ can become normalised by

$$|\psi\rangle = \frac{|\psi\rangle_{\text{unnorm}}}{\langle\psi|\psi\rangle_{\text{unnorm}}} \tag{2.29}$$

As useful as analysis with state vectors are, it is often more convenient to analyse quantum states in the density matrix formalism. The state vector $|\psi\rangle$ in terms of a density matrix is

$$\hat{\rho} = |\psi\rangle\langle\psi| = \sum_{n,m=0}^{\infty} c_{n,m}|n\rangle\langle m|, \tag{2.30}$$

where $c_{n,m} = c_n c_m^*$ is a complex coefficient and $|n\rangle$ and $|m\rangle$ are Fock states. The terms $c_{n,n}$ are known as the populations and they give the probability of a quantum state inhabiting the eigenstate $|n\rangle$. The terms $c_{n,m}$ when $c \neq m$ are called the coherences and these contain the phase information about the state. Therefore, a state is fully characterised by its density matrix;

however, only pure states $\mathcal{P} = 1$ can be expressed in terms of a state vector. Purity $\mathcal{P}$ is defined as $\mathcal{P} = \mathrm{Tr}(\hat{\rho}^2)$. A state with purity $\mathcal{P} < 1$ is referred to as a mixed state and cannot be described by a state vector: this fact illustrates the benefit of density matrix formalism. One frequently encountered mixed state is a state with only diagonal elements in the photon-number basis. The lack of coherences in such a density matrix represents the lack of knowledge available for this state; this means we only have probabilistic information about the state in that basis. Most states encountered are mixed states with only diagonal elements, often due to interactions and the resulting decoherence with the environment.

The operators $(\hat{a}^\dagger, \hat{a})$ are not observable, as they are not Hermitian. However, the number operator $\hat{n} = \hat{a}^\dagger \hat{a}$ is Hermitian, i.e. observable. The expectation value of this operator is the mean photon number $\bar{n}$. For example, for the state $|\psi\rangle = \frac{1}{\sqrt{2}}\big(|0\rangle + |1\rangle\big)$ its mean photon number is

$$\bar{n} = \langle\psi|\hat{n}|\psi\rangle = \frac{1}{2}. \tag{2.31}$$

The Hamiltonian of a single-mode of the quantised EM-field is reexpressed with the number operator $\hat{n}$ as

$$\hat{H} = (\hat{n} + \frac{1}{2})\hbar\omega. \tag{2.32}$$

Analysis and characterisation of quantum states with the Fock basis is relied upon heavily in this thesis, however the consideration of quantum states through the framework of phase-space in the next section is a worthwhile discussion.

2.3 Phase-space and the coherent state

The knowledge that an observer has of a state's measurable quantities is at odds with classical theory due to the Heisenberg uncertainty principle, which sanctions that two conjugate observables (such as position $\hat{q}$ and momentum $\hat{p}$) cannot be fully known simultaneously. The Heisenberg uncertainty relation sets a lower bound on the uncertainty of measuring these two observables defined as [106], [107]

$$\Delta\hat{q}\Delta\hat{p} \geq \frac{\hbar}{2}, \tag{2.33}$$

where for any operator $\hat{A}$ we have $\Delta\hat{A} = \sqrt{\langle\hat{A}^2\rangle - \langle\hat{A}\rangle^2}$ and the notation $\langle\hat{A}\rangle = \mathrm{Tr}(\hat{\rho}\hat{A})$ represents the expectation value of an operator $\hat{A}$ for any specified quantum state $\hat{\rho}$. The operators $\hat{q}$ and

$\hat{p}$ are rescaled to be the dimensionless quadrature operators for a single-mode field, thus

$$\hat{X}_1 = \frac{1}{2}(\hat{a} + \hat{a}^\dagger), \tag{2.34a}$$

$$\hat{X}_2 = \frac{1}{2i}(\hat{a} - \hat{a}^\dagger) \tag{2.34b}$$

represent the dimensionless quadrature operators associated with the position and momentum operators respectively. The commutator relation for the quadrature operators is $[\hat{X}_1, \hat{X}_2] = \frac{i}{2}$. Furthermore, the Heisenberg uncertainty principle is restated in terms of these quadrature operators as

$$(\Delta\hat{X}_1)^2(\Delta\hat{X}_2)^2 \geq \frac{1}{16}. \tag{2.35}$$

The quadratures are orthogonally out of phase of each other. The quadratures define phase space on a 2D plane. The rationale of this section is that analysis of a system in phase-space rather than via the Fock basis is often easier and the effect that some operators have upon quantum states is visually apparent.

The single-mode vacuum has a state vector $|\psi\rangle = |0\rangle$. The vacuum minimises the uncertainty relation as $\Delta\hat{X}_1 = \Delta\hat{X}_2 = \frac{1}{2}$. The displacement operator is

$$\hat{D}(\alpha) = e^{\alpha\hat{a}^\dagger - \alpha^*\hat{a}}, \tag{2.36}$$

for a complex number α. Application of the displacement operator to the vacuum yields the Glauber-Sudarshan coherent state with state vector [108]

$$\hat{D}(\alpha)|0\rangle = |\alpha\rangle = e^{-\frac{|\alpha|^2}{2}} \sum_{n=0}^{\infty} \frac{\alpha^n}{n!}|n\rangle. \tag{2.37}$$

This state also minimises the Heisenberg uncertainty relation. It is a valuable state to consider, as it is the most 'classical-like' of quantum states and its properties lend itself as a reasonable approximation for mathematically expressing a single-mode output of laser light. Figure 2.1 shows both the (a) vacuum state and (b) coherent state with amplitude $|\alpha| = \frac{1}{2}$ and phase $\theta = \frac{\pi}{4}$ on phase space, with the shaded circle as the area of uncertainty. Figure 2.1(b) also shows that the coherent state has uncertainty of amplitude $\Delta|\alpha|$ as the circle of uncertainty is shaded for different values of $|\alpha|$ from the origin, similarly there is an uncertainty of phase $\Delta\theta$, both the amplitude and phase are more intuitive properties of a state than its quadratures.

The coherent state and its role with phase space are important to note also. For example, $\langle\hat{X}_1\rangle_\alpha = \mathscr{R}(\alpha)$ and $\langle\hat{X}_2\rangle_\alpha = \mathscr{I}(\alpha)$, where the subscript denotes that its the expectation value

of the operator in the state $|\alpha\rangle$. This shows that the complex α-plane can represent phase-space. Any quantum state can be expressed in terms of the coherent state as coherent states form an over-complete basis. The ability of the coherent state to represent any state vector is elucidated by phase space and the complex α-plane being analogous. Any state vector $|\psi\rangle$ is expressed in the coherent state basis as

$$|\psi\rangle = \int \frac{d^2\alpha}{\pi} |\alpha\rangle\langle\alpha|\psi\rangle, \tag{2.38}$$

where the integral is over the entire complex α-plane so $d^2\alpha = d\mathscr{R}(\alpha)d\mathscr{I}(\alpha)$. This is an alternative to using the Fock basis for the expression of a state.

Another approach to framing a quantum state in the coherent basis is via the P-function [109], [110], which under certain conditions can be considered as a phase-space probability distribution. Knowledge of this function can help us characterise and visualise a quantum state. For an arbitrary density matrix $\hat{\rho}$ in the photon-number basis, it is re-expressed in the coherent basis as

$$\hat{\rho} = \int P(\alpha)|\alpha\rangle\langle\alpha| d^2\alpha, \tag{2.39}$$

where $P(\alpha) = \frac{e^{|\alpha|^2}}{\pi^2} \int e^{|u|^2} \langle -u|\hat{\rho}|u\rangle e^{u^*\alpha - u\alpha^*} d^2u$. The P-function is not always well-behaved or properly defined, sometimes it has negative values or is highly singular. In such situations the interpretation of $P(\alpha)$ as a phase-space probability distribution is invalid. If the P-function is not properly defined and well-behaved the state typically has observable properties that are not obtainable in classical physics. We call such states non-classical. For non-classical states other phase-space quasi-probability distributions such as the Husimi function or the Wigner function are used to express the state in question [111], [112]. In this thesis only the P-function is used, due to its benefit when transforming classical-like quantum states into the coherent basis and that it allows an easy check whether a state is non-classical or not.

2.4 Single-mode squeezing

For classical-like states there is a noise floor that determines how precisely a measurement can be made. This floor is dubbed the shot noise, which in our context originates from quantum fluctuations and Heisenberg's uncertainty principle. However, squeezing allows measurements of observables to be more precise than classical physics would allow. From the used (squeezed) non-classical states many applications result; for example, the detection of gravitational waves, which were previously inaccessible as quantum fluctuations drowned out the extremely weak signal of these waves [113], [114].

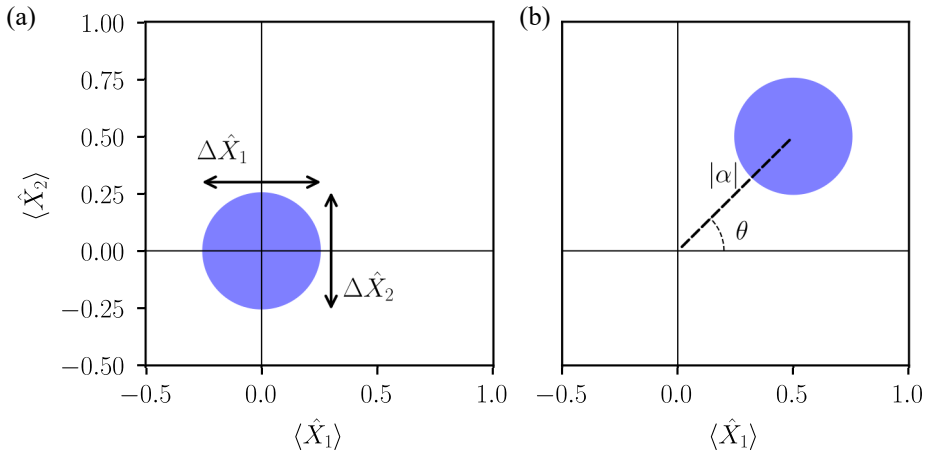

FIGURE 2.1 – Phase-space portraits for (a) the single-mode vacuum state and (b) the single-mode coherent state. The $\hat{X}_1$ quadrature is in the x-axis and the $\hat{X}_2$ quadrature is in the y-axis. The uncertainty of the quadratures are annotated in (a) and the effect displacement has upon the vacuum is shown in (b), for a complex number $\alpha = |\alpha| e^{i\theta}$.

There is squeezing of a quadrature of the field if either $(\Delta \hat{X}_1)^2 < \frac{1}{4}$ or $(\Delta \hat{X}_2)^2 < \frac{1}{4}$. If one quadrature if squeezed, then the other must compensate by being more uncertain than before the squeezing. The nomenclature of 'squeezing' is apparent in the phase-phase portrait of quadrature squeezing in Fig. 2.2. The single-mode squeezing operator is

$$\hat{S}_1(r) = e^{\frac{1}{2}(\zeta^* \hat{a}^2 - \zeta \hat{a}^{\dagger 2})}, \tag{2.40}$$

where the squeezing complex number $\zeta = re^{i\theta}$, with r as the squeeze parameter which dictates the amount of the squeezing acted upon the state and $0 \leq r \leq \infty$, and θ is the phase. When the phase $\theta = 0$, the effect of $\hat{S}_1(r)$ upon the two quadratures of the vacuum state is

$$(\Delta \hat{X}_1)^2 = \frac{1}{4} e^{-2r}, \tag{2.41a}$$

$$(\Delta \hat{X}_2)^2 = \frac{1}{4} e^{2r}. \tag{2.41b}$$

In the degenerate case of no squeezing $r = 0$, the vacuum state is recovered and the quadrature uncertainties are at the values set by the quantum fluctuations of the vacuum. However for $r > 0$ the $\hat{X}_1$ quadrature uncertainty is reduced below what classical physics allows, as shown in the phase-space portrait for the quadrature squeezed vacuum state in Fig. 2.2. In other words, the single-mode squeezing operator when the phase $\theta = 0$ squeezes the $\hat{X}_1$ quadrature. Whereas the $\hat{X}_2$ quadrature is anti-squeezed, i.e. its uncertainty is increased accordingly.

Experimentally, single-mode squeezing can be produced by a degenerate parametric down-

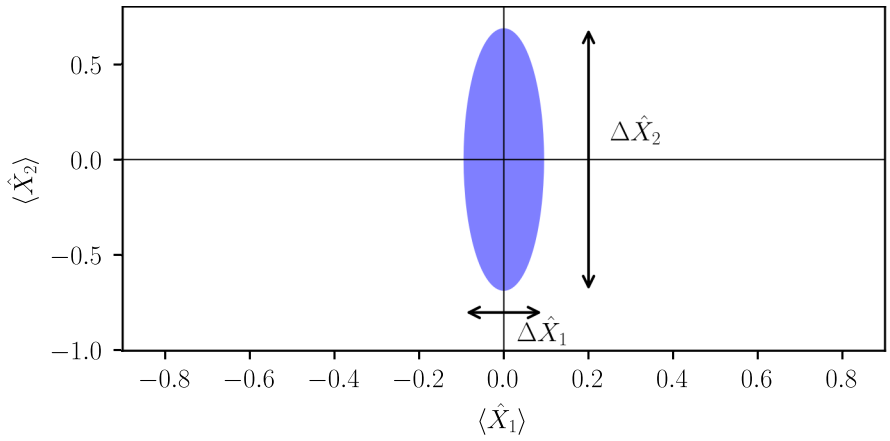

FIGURE 2.2 – Phase-space portrait for the $\hat{X}_1$ quadrature squeezed vacuum state. The squeezing parameter $r = 1$. $(\Delta \hat{X}_1)^2 \approx 0.0338$ and $(\Delta \hat{X}_2)^2 \approx 1.847$.

converter [115]. In this situation, light from a strong coherent pump beam is converted to light of a lower frequency in two modes after interaction (via the $\chi^{(2)}$ nonlinear susceptibility) with a nonlinear non-centrosymmetric crystal. If the frequencies of the two modes are the same, the wave-vectors are the same such that they are collinear and they have the same polarisation then they can be considered as one mode. A nonlinear material is defined as a material with any susceptibility $\chi^{(n)} \neq 0,\ n \geq 2$. Moreover, the parametric approximation is made, which is the approximation that the pump mode operator $\hat{a}_{\mathrm{P}}$ can be transformed into a classical variable α, this simplifies the calculation with this operator greatly. The parametric approximation was applied to Eq. 2.40. The classical amplitude of the pump α and the second-order susceptibility $\chi^{(2)}$ is encoded in the squeezing complex number $\zeta = \alpha\chi^{(2)}$ [116]. The parametric approximation is possible due to the pump field being orders of magnitude stronger than the output modes from the nonlinear process. The degenerate parametric down-conversion interaction is modelled by the operator $\hat{S}(r)$ acting upon the vacuum, as described mathematically earlier. The aforementioned results assume that a monochromatic and intensity stabilised coherent state is used. In the following section, (non-degenerate) parametric down-conversion for broadband light is described. Non-degenerate parametric down-conversion is equivalent to squeezing upon two modes and this is where non-classical effects are far more pronounced and interesting. It is two-mode squeezing which underpins the non-classical light source considered in this thesis.

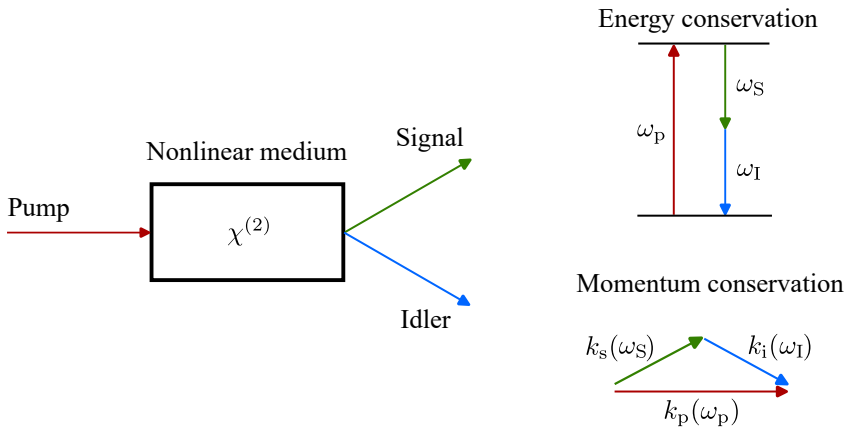

Figure 2.3 – Diagram of the SPDC process involving the pump, signal and idler beam. Energy conservation is shown in the energy diagram and conservation of momentum is shown with the wave-vectors.

2.5 SPDC process

Spontaneous parametric down-conversion (SPDC) is an invaluable tool in quantum optics. It underpins the generation of the quantum-correlated twin-beam state of light used in this research. The output from SPDC results in light with strong temporal, spatial and polarisation correlations. Moreover, this light has many applications, for example in quantum information processing for the heralding of a single-photon source. However, as a single-photon source it has problems due to the probabilistic output of these single-photons and that if the purity of these single-photons is desired, this causes them to be exceedingly rare events.

SPDC is initiated by a strong pump field driven into a noncentrosymmetric crystal: as only noncentrosymmetric materials have a $\chi^{(2)}$ nonlinear susceptibility. This pump field is expressed as a coherent state and it has its own mode denoted by the labeling (p). The interaction of the pump field with the nonlinear material (often a crystal) induces a polarisation in the material and the output of this process is a twin-beam, which is a highly entangled bipartite state $|\psi\rangle_{\text{SPDC}}$ with modes conventionally referred to as the signal (S) and idler (I), as shown in Fig. 2.3. In this section the SPDC output is initially derived from the Hamiltonian interaction; this serves to mathematically express the experimental conditions required for effective generation of these states. Following this derivation, the SPDC process and its relation to multi-mode squeezing is demonstrated.

The classical interaction Hamiltonian of the pump field and the nonlinear medium is [117]

$$H_{\text{int}}(t) \propto \int E_{\text{p}}(\mathbf{r},t)\cdot\tilde{D}(\mathbf{r},t)d\mathbf{r}, \tag{2.42}$$

introducing the electric field displacement vector $\tilde{D}(\mathbf{r},t)$. The introduced vector allows for the nonlinear interaction of the medium and the pump light. Therefore, it is decomposed into linear and nonlinear components $\tilde{D}(\mathbf{r},t) = \tilde{D}^{(1)}(\mathbf{r},t) + \tilde{P}^{\mathrm{NL}}(\mathbf{r},t)$. As three fields of light are being dealt with the nonlinear polarisation term is restricted to just the $\chi^{(2)}$ term, hence $\tilde{P}^{\mathrm{NL}} = \epsilon_0\chi^{(2)}E_{\mathrm{S}}(\mathbf{r},t)E_{\mathrm{I}}(\mathbf{r},t)$ and the linear term in the electric displacement vector is neglected. Therefore, the $\chi^{(2)}$ classical interaction Hamiltonian is now proportional to

$$H_{\chi^{(2)}}(t) \propto \epsilon_0\chi^{(2)} \int E_{\mathrm{p}}(\mathbf{r},t)E_{\mathrm{S}}(\mathbf{r},t)E_{\mathrm{I}}(\mathbf{r},t)d\mathbf{r} \tag{2.43}$$

The following derivation is simplified by assuming that the pump, signal and idler beams are all collinear and that spatial freedom is restricted to the z-axis for a crystal with length L_{c}. Moreover, the signal and idler electric fields are replaced with their quantum-mechanical operators. Thus, the quantum-mechanical interaction Hamiltonian with energy conserving terms only is [118]

$$\hat{H}(t) \propto \epsilon_0\chi^{(2)} \int_{-\frac{L_{\mathrm{c}}}{2}}^{\frac{L_{\mathrm{c}}}{2}} dz E_{\mathrm{P}}^{+}(z,t)\hat{E}_{\mathrm{S}}^{-}(z,t)\hat{E}_{\mathrm{I}}^{-}(z,t) + \mathrm{h.c}, \tag{2.44}$$

where the parametric approximation is applied to ensure that the electric field of the pump $E_{\mathrm{p}}(z,t)$ is treated classically. We define the classical electric field of the pump (over the entire frequency domain) as

$$E_{\mathrm{p}}(z,t) = \int d\omega_{\mathrm{p}} \left(\alpha(\omega_{\mathrm{p}})e^{i(k_z(\omega_{\mathrm{p}})z-\omega_{\mathrm{p}}t)} + \alpha^*(\omega_{\mathrm{p}})e^{-i(k_z(\omega_{\mathrm{p}})z-\omega_{\mathrm{p}}t)}\right). \tag{2.45}$$

Additionally, for $\hat{E}_{\mathrm{S}}^{-}(z,t)$ and $\hat{E}_{\mathrm{I}}^{-}(z,t)$ in Eq. 2.44 we use the electric field operator with negative frequency components as defined in Eq. 2.19b. From this Hamiltonian the output of the SPDC process is received

$$|\psi\rangle_{\mathrm{SPDC}} = e^{-\frac{i}{\hbar}\int_{t_0}^{t}\hat{H}(t')dt'}|0,0\rangle, \tag{2.46}$$

where we use the short-hand $|0,0\rangle = |0\rangle_{\mathrm{S}} \otimes |0\rangle_{\mathrm{I}}$, with $\otimes$ representing the tensor product between two different Hilbert spaces.

Explicit calculation of $|\psi\rangle_{\mathrm{SPDC}}$ in the form given in Eq. 2.46 is difficult, therefore a perturbation expansion is applied [119]. Therefore, the state is approximately

$$|\psi\rangle_{\mathrm{SPDC}} \approx |0,0\rangle - \frac{i}{\hbar}\int_0^t dt'\hat{H}(t')|0,0\rangle + \left(\frac{-i}{\hbar}\right)^2 \int_0^t dt'\hat{H}(t')\int_0^{t'} dt''\hat{H}(t'')|0,0\rangle + \ldots \tag{2.47}$$

We focus on calculation of the first two terms in Eq. 2.47. After substitution of the necessary expressions into Eq. 2.44, the time integrals in Eq. 2.47 has its limits replaced to $(-\infty, \infty)$; this is reasonable as our interest is in the state after it is in the crystal. Solving this time integral yields the term $2\pi\delta(\omega_S + \omega_I - \omega_p)$ which involves the Dirac delta function. Therefore, the energy conservation condition required for effective SPDC dictates that $\omega_p = \omega_S + \omega_I$, as visualised in Fig. 2.3 and encoded in the Hamiltonian Eq. 2.44. The energy conservation condition also removes the time-dependence of Eq. 2.47. Following this, the z-integral is solved, which yields the term $L_c\text{sinc}(\Delta k(\omega_S, \omega_I)\frac{L_c}{2})$, where the phase-mismatch $\Delta k = k_p(\omega_p) - k_S(\omega_S) - k_I(\omega_I)$ encodes the phase-matching conditions for an effective SPDC process, also visualised in Fig. 2.3. The pump frequency integral is neglected as there is no dependency on pump frequency, due to the energy conservation condition.

The SPDC state is approximately

$$|\psi\rangle_{\text{SPDC}} \approx |0,0\rangle + i\int\int d\omega_S d\omega_I \left(\chi^{(2)} \frac{1}{2cA_{c.s}}\, f(\omega_S, \omega_I)\hat{a}_I^\dagger(\omega_I)\hat{a}_S^\dagger(\omega_S)|0,0\rangle\right), \tag{2.48}$$

where we have only used the first two terms of Eq. 2.47 to calculate Eq. 2.48. Additionally the joint spectral amplitude (JSA) is $f(\omega_S, \omega_I) = \alpha(\omega_S + \omega_I)\sqrt{\omega_S\omega_I}L_c\text{sinc}(\Delta k\frac{L_c}{2})$. Equation 2.48 is an entangled state photon-pair and vacuum state. The non-classical character of this state is dependent upon $f(\omega_S, \omega_I)$ being non-factorisable between the terms corresponding to the signal and idler modes.

The crystal length integral is evaluated to be $L_c\text{sinc}(\Delta k\frac{L_c}{2})$ this means that if the phase-mismatch $\Delta k = 0$ then the pump energy is transferred into the signal and idler fields as effectively as possible. However, if $\Delta k = \frac{2m\pi}{L}$, for any integer $m \neq 0$ then there is no SPDC process, as the signal and idler electric field does not build up due to destructive interference. Therefore, the system should be designed such that the phase-mismatch $\Delta k \approx 0$ for effective SPDC to occur — engineering this is not a trivial problem. Due to different frequencies having different refractive indexes and consequently different phase shifts there is a limitation on what is chosen as the pump frequency, polarisation and crystal length for phase-matching. Phase-matching is possible with a birefringent crystal (a material with a refractive index depending on its polarisation and wave-vector). This phase-matching with a birefringent crystal depends on suitable choices for pump frequency and polarisation. An alternative that does not require such stringent conditions as normal phase-matching is quasi-phase matching [120]. This requires specially designed crystals that have what is known as a poling period, which is regions of alternating polarisation, this causes a cancelling any build-up of phase-mismatch. The catch is that its not as efficient as

birefringent phase-matching for SPDC; however, the signal and idler beam collection optics are more simplistic and there is greater freedom of polarisation and frequency choices. These benefits outweighs this relative lack of efficiency and quasi-phase matching is more widespread in use.

Now that the SPDC output state has been derived from Hamiltonian interaction, it is time to relate this state to the abstract case of using a two-mode squeezing operator $\hat{S}(\omega_{\mathrm{S}}, \omega_{\mathrm{I}})$ acting upon the vacuum. This operator for two-mode squeezing is

$$\hat{S}_2(\omega_{\mathrm{S}}, \omega_{\mathrm{I}}) = e^{-\zeta(\omega_{\mathrm{S}}+\omega_{\mathrm{I}})\hat{a}_{\mathrm{S}}^{\dagger}(\omega_{\mathrm{S}})\hat{a}_{\mathrm{I}}^{\dagger}(\omega_{\mathrm{I}})+\zeta^{*}(\omega_{\mathrm{S}}+\omega_{\mathrm{I}})\hat{a}_{\mathrm{S}}(\omega_{\mathrm{S}})\hat{a}_{\mathrm{I}}(\omega_{\mathrm{I}})}, \tag{2.49}$$

where the squeezing complex number $\zeta(\omega_{\mathrm{S}} + \omega_{\mathrm{I}})$ is a function of the signal and idler modes. The operator in Eq. 2.49 describes multi-mode squeezing; which is when squeezing of the quantum fluctuations is in the superposition of the two modes, rather than in the quadrature of a single-mode. We can define the (summation and difference) superposition quadrature operators in terms of the single-mode quadrature operators given in Eq. 2.34, with the relevant mode-labelling, as $\hat{X}_1^s = \frac{1}{\sqrt{2}}\left(\hat{X}_{\mathrm{I}:1} + \hat{X}_{\mathrm{S}:1}\right)$, $\hat{X}_1^d = \frac{1}{\sqrt{2}}\left(\hat{X}_{\mathrm{I}:1} - \hat{X}_{\mathrm{S}:1}\right)$, $\hat{X}_2^s = \frac{1}{\sqrt{2}}\left(\hat{X}_{\mathrm{I}:2} + \hat{X}_{\mathrm{S}:2}\right)$ and $\hat{X}_2^d = \frac{1}{\sqrt{2}}\left(\hat{X}_{\mathrm{I}:2} - \hat{X}_{\mathrm{S}:2}\right)$ [121]. Where $\hat{X}_{\mathrm{I}:1}$ represents the $\hat{X}_1$ quadrature operator for the idler mode, for example. The summation and difference superposition quadrature commutator relations are equivalent to the single-mode relation with $[\hat{X}_1^s, \hat{X}_2^s] = \frac{i}{2}$ and $[\hat{X}_1^d, \hat{X}_2^d] = \frac{i}{2}$, respectively. When we set the phase $\theta = 0$ of the exponential form of $\zeta(\omega_{\mathrm{S}} + \omega_{\mathrm{I}})$, both $\hat{X}_1^s$ and $\hat{X}_2^d$ are squeezed by the operator Eq. 2.49, whereas the other two quadratures are anti-squeezed. If we wish to visualise the squeezing upon this system, the following approach can be useful. For an arbitrary quadrature operator $\hat{X}_\theta$ there is its quadrature eigenstate $|X_\theta\rangle$. Hence, from this eigenstate, we can plot on phase-space the probability distribution for any quadrature operator and state $|\psi\rangle$ as $\mathrm{P}(X_\theta, \theta) = |\langle X_\theta|\psi\rangle|^2$. Following from this, Hong-yi and Klauder derived the eigenstates for the superposition quadrature operators [122].

Non-classical correlations between the two modes are exhibited due to this two-mode squeezing. The resulting photon-number, frequency, temporal and polarisation correlations between the two modes are what we explicitly and implicitly use in this thesis, rather than direct measurement of the squeezed two-mode superposition quadrature. The two-mode squeezing operator applied to the vacuum over the entire frequency domain for signal and idler is

$$|\psi\rangle_{\hat{\mathrm{S}}_2} = \int\int d\omega_{\mathrm{S}} d\omega_{\mathrm{I}} \hat{S}_2(\omega_{\mathrm{S}}, \omega_{\mathrm{I}})|0, 0\rangle. \tag{2.50}$$

Applying the disentangling theorem to the operator results in the operator which is easier to calculate with [123], the details for this derivation is given later in a more general form in Eq. 5.4b. We set $re^{i\theta} = \zeta(\omega_S + \omega_I)$ and thus the state vector from the two-mode squeezing operator $\hat{S}_2$ is

$$|\psi\rangle_{\hat{S}_2} = \text{sech}(r) \int\int d\omega_S d\omega_I \Big(|0,0\rangle - e^{i\theta} \tanh(r) \hat{a}_S^\dagger(\omega_S) \hat{a}_I^\dagger(\omega_I) |0,0\rangle + \dots \Big), \tag{2.51}$$

therefore it is easy to see that $|\psi\rangle_{\hat{S}_2} \propto |\psi\rangle_{\text{SPDC}}$, when the perturbation expansion of Eq. 2.47 is fully calculated. In other words the SPDC state is a superposition of photon-pair creations, another indication that this is a non-classical state of light. The two-mode squeezing operator is used in the quantum state of light in the LIDAR model as it provides an easy route to expressing simplified forms of the output of the SPDC process.

2.6 Quantum coherence function

Another tool for characterising light is via analysis of the correlations and coherence properties exhibited by a state of light [124]. The quantum degree of first order coherence function at the space-time points (z_1, t_1) and (z_2, t_2) is

$$g^{(1)}(z_1, t_1; z_2, t_2) = \frac{\langle \hat{E}^-(z_1, t_1) \hat{E}^+(z_2, t_2) \rangle}{\Big(\langle \hat{E}^-(z_1, t_1) \hat{E}^+(z_1, t_1) \rangle \langle \hat{E}^-(z_2, t_2) \hat{E}^+(z_2, t_2) \rangle \Big)^{\frac{1}{2}}}, \tag{2.52}$$

this function reveals if the two fields, when superposed, will display interference fringes. It is also useful for determining the spectrum of the light via the Wiener-Khintchine theorem [125]. To further simplify Eq. 2.52 the fields are considered to be stationary, that is their properties do not vary with time and so the initial time t_1, t_2 is irrelevant. In reality however, states are not stationary and their properties are only stable for a period of time known as its coherence time τ_{coh}: an assumption is made that for any inspected time delay $\tau \ll \tau_{\text{coh}}$. Following this, a fixed spatial point is set and the time delay $\tau = t_2 - t_1 - \frac{z_2 - z_1}{c}$ is defined, therefore Eq. 2.52 (for stationary light) simplifies to

$$g^{(1)}(\tau) = \frac{\langle \hat{E}^-(t) \hat{E}^+(t+\tau) \rangle}{\langle \hat{E}^-(t) \hat{E}^+(t) \rangle}. \tag{2.53}$$

Clearly the first order quantum coherence function measures the correlations between the electric field of the light. Whereby $|g^{(1)}(\tau)| = 1$ signifies first order coherence, $|g^{(1)}(\tau)| = 0$ signifies first order incoherence and $|g^{(1)}(\tau)| \neq 1, 0$ signifies first order partial coherence. When the coherence

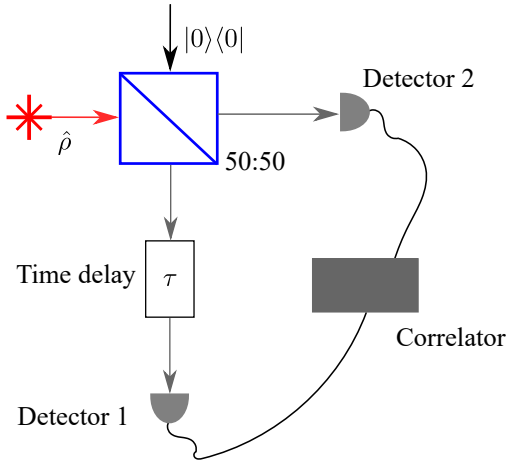

FIGURE 2.4 – The Hanbury Brown and Twiss interferometer. The light to be analysed $\hat{\rho}$ enters a 50:50 beamsplitter. One output arm has a variable time delay τ. There is a detector for each output arm of the beamsplitter and they are connected to a correlator.

time $\tau_{\text{coh}} = \infty$, the single-mode case for the first order quantum coherence function is

$$g^{(1)}(\tau) = e^{-i\tau}. \tag{2.54}$$

Hence, any single-mode field at any delay is first order coherent $|g^{(1)}(\tau)| = 1$. We lead onto the second order quantum coherence function which is a useful tool to identify properties pertaining to non-classical light. The second order quantum coherence function (with the same simplifications applied) is

$$g^{(2)}(\tau) = \frac{\langle \hat{E}^-(t)\hat{E}^-(t+\tau)\hat{E}^+(t+\tau)\hat{E}^+(t)\rangle}{\langle \hat{E}^-(t)\hat{E}^+(t)\rangle^2}. \tag{2.55}$$

This measures the intensity correlations within the field, rather than the electric field correlations, where the intensity of a light field is $I(t) = \langle \hat{E}^-(t)\hat{E}^+(t)\rangle$. The Hanbury-Twiss-Brown interferometer is depicted in Fig. 2.4, this experiment enabled calculation of the $g^{(2)}(\tau)$ properties of the analysed light [126], assuming that the delay is less than the coherence time of the light. The single-mode case of the second order quantum coherence function is

$$g^{(2)}(\tau) = \frac{\langle : (\hat{a}^\dagger\hat{a})^2 : \rangle}{\langle \hat{a}^\dagger\hat{a}\rangle^2} = \frac{\langle \hat{n}(\hat{n}-1)\rangle}{\langle \hat{n}\rangle^2}, \tag{2.56}$$

where : : represents normal ordering of operators, which in this context is where all creation operators are to the left of the destruction operators. The normal ordering is expected as photo-detection is an absorptive process [127]. Moreover, the right-hand-side of Eq. 2.56 is instructive

of how measurement in quantum-mechanics perturbs the system which is being measured, as the same mode is being measured twice. The second order quantum coherence function is interesting because it is capable of yielding results which are forbidden in classical physics. Any value of $g^{(2)}(0) < 1$ is a purely quantum behaviour as such values in classical physics are not permissible as a possible measurement, as shown by the Cauchy-Schwarz inequality defined in Eq. 2.69. Hence such negative values are a good indicator of non-classical light. Light that exhibits the non-classical property that $g^{(2)}(\tau) > g^{(2)}(0)$, for a delay τ, is known as anti-bunched light. When measuring anti-bunched light, we observe that a detection event reduces the chance of another detection event immediately after the first detection event. The single-photon state has $g^{(2)}(0) = 0$, which is obvious as a photon cannot be split in two, hence an instantaneous second detection is impossible. Light that has $g^{(2)}(0) > g^{(2)}(\tau)$ is known as bunched light, which is detection of light raises the chance of an immediate follow-up detection. The photons cluster together. Lastly, Poissonian light has a second order quantum coherence function $g^{(2)}(0) = 1$, this means that subsequent detection of light is a completely random process: each photon arrival time is independent from each other.

2.7 Characterisation of the states of light

The preceding sections provides a tool-kit on how to characterise a state of light. Analysis with the Fock state basis, coherent state basis and phase-space and quantum coherence functions are all used in this section. Each modality of analysis has its own virtues when differentiating between all of the light sources considered in this thesis.

2.7.1 Noise source

We cannot escape noise. The environment and our detectors are flooded by it. For example, photo-detectors suffer from noise intrinsic to their detection system, dubbed dark noise. There are detector counts spontaneously produced or stimulated from within the detector due to the electronics, after-pulsing stimulated from prior incident light, or the blackbody emission due to the non-zero temperature of the detector material. Noise from the background environment is similarly random. However, what is considered as 'noise' need not be random, it can be from a coherent light source aimed at our detectors by a hostile party. Therefore, it is more general to define noise as any light source incident upon our detectors that is not from the intended light generated for the LIDAR system.

Electromagnetic radiation generated from a body with a temperature T is governed by the

theory of blackbody radiation. In particular, light cast from the sun is well approximated by the theory of blackbody radiation: which of course is a major source of environmental noise. Such light will be referred to as thermal light from now on, which is in thermal equilibrium with its environment. This form of light has a density matrix given by the Boltzmann distribution, given in the single-mode case as

$$\hat{\rho}_{\text{th}} = \frac{e^{-\frac{\hat{H}}{\text{k}_\text{B}T}}}{\text{Tr}(e^{-\frac{\hat{H}}{\text{k}_\text{B}T}})}, \tag{2.57}$$

where $\hat{H}$ is the Hamiltonian of a single-mode of the quantised EM-field and k_B is the Boltzmann constant. This section will focus on noise as a thermal state of light. In the following derivation, brevity is achieved by introducing the dimensionless factor $\beta \equiv \frac{\hbar\omega}{\text{k}_\text{B}T}$. Using the Hamiltonian from Eq. 2.32, $\hat{1} = \sum_{n=0}^{\infty} |n\rangle\langle n|$ and that $\text{Tr}f(\hat{n}) = \sum_{n=0}^{\infty}\langle n|f(\hat{n})|n\rangle = \sum_{n=0}^{\infty} f(n)$, the density matrix of single-mode thermal light is now

$$\hat{\rho}_{\text{th}} = \frac{\sum_{n=0}^{\infty} e^{-\beta n}|n\rangle\langle n|}{\sum_{m=0}^{\infty} e^{-\beta m}}. \tag{2.58}$$

Solving the infinite series on the denominator of Eq 2.58 and knowing that $\langle\hat{n}\rangle = \bar{n} = \frac{1}{e^{\beta}-1}$ the density matrix is hence

$$\hat{\rho}_{\text{th}} = \sum_{n=0}^{\infty} \frac{\bar{n}^n}{(\bar{n}+1)^{n+1}}|n\rangle\langle n|. \tag{2.59}$$

This state is a mixed state $\mathcal{P} < 1$ with only diagonal elements in its density matrix and so it is described by a statistical average of energy levels of the quantum harmonic oscillator. This state also has a well-behaved P-function, therefore in the coherent state basis the single-mode thermal state is

$$\hat{\rho}_{\text{th}} = \frac{1}{\pi\bar{n}} \int d^2\tilde{\alpha} e^{-\frac{|\tilde{\alpha}|^2}{\bar{n}}} |\tilde{\alpha}\rangle\langle\tilde{\alpha}| \tag{2.60}$$

The photon-number distribution is given by $P(n) = \langle n|\hat{\rho}_{\text{th}}|n\rangle = \frac{\bar{n}^n}{(\bar{n}+1)^{n+1}}$, for any photon-number n. Single-mode thermal light is referred to as super-poissonian light as the variance of the mean photon number is greater than the mean photon number $\Delta\hat{n}^2_{\text{th}} = \bar{n}(2\bar{n}+1)$. This light has the second order quantum coherence function $g^{(2)}(0) = 2 > g^{(2)}(\tau)$, which is photon-bunched light. The photon number statistics for single-mode thermal light has a Bose-Einstein distribution, shown by Fig. 2.5.

2.7.2 Classical illumination

The involvement of CI in the LIDAR model is required for there to be any qualitative and quantitative reason as to why QI-based protocols are beneficial. The light source for CI is

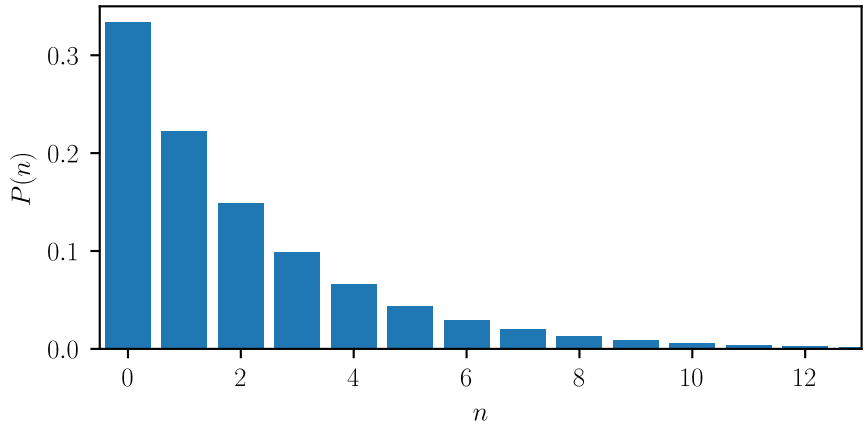

FIGURE 2.5 – Photon-number distribution for a single-mode thermal state of light with mean photon number $\bar{n} = 2$. The probability is on the y-axis and the photon-number is on the x-axis.

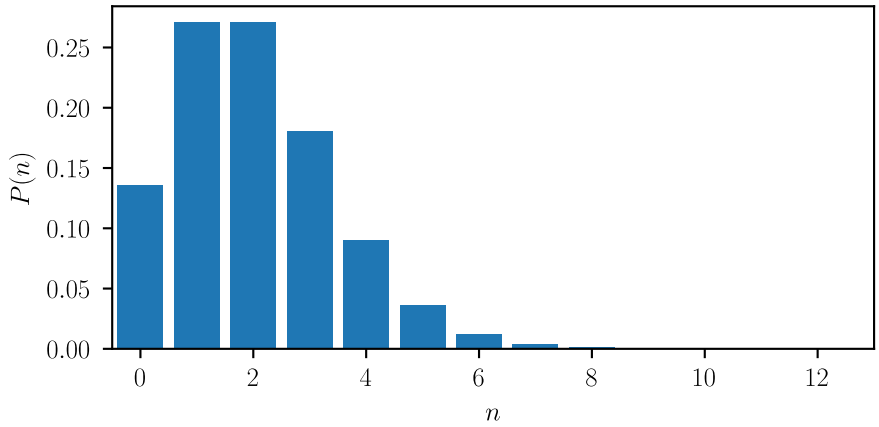

FIGURE 2.6 – Photon-number distribution for a single-mode coherent state of light with mean photon number $\bar{n} = 2$. The probability is on the y-axis and the photon-number is on the x-axis.

modelled with a single-mode thermal state in the remainder of the thesis, however it is also possible to use the single-mode coherent state $|\alpha\rangle$ as the CI light source.

It is trivial for the single-mode coherent state to be represented by the P-function and the coherent state basis as

$$\hat{\rho}_{\text{coh}} = \int d^2\beta \delta(\mathscr{R}(\alpha) - \mathscr{R}(\beta))\delta(\mathscr{I}(\alpha) - \mathscr{I}(\beta))|\beta\rangle\langle\beta| = |\alpha\rangle\langle\alpha|, \tag{2.61}$$

this expression makes intuitive sense. Its photon-number distribution is given by $P(n) = e^{-|\alpha|^2}\frac{|\alpha|^{2n}}{n!}$, where $|\alpha|^2 = \bar{n}$, this distribution is shown in Fig. 2.6. Single-mode coherent state light is a type of Poissonian light as the variance of the mean photon number is equal to the mean photon number $\Delta\hat{n}^2_{\text{coh}} = \bar{n}$. Therefore, as $\Delta\hat{n}^2_{\text{coh}} < \Delta\hat{n}^2_{\text{th}}$, there is less variation in the

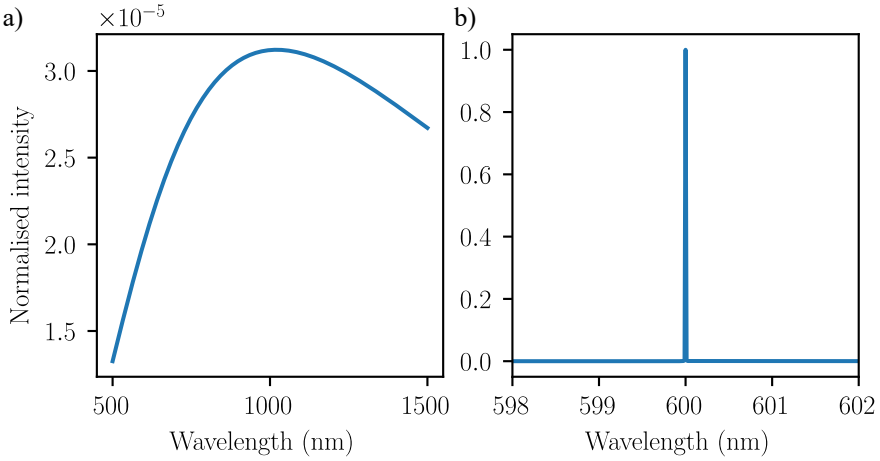

Figure 2.7 – Spectral distributions for a) thermal light with temperature $T = 5000$ K with normalised spectral radiance on the y-axis and b) Laser light with an idealised Lorentzian distribution with central frequency $\omega_c = 500$ THz and a spectral linewidth of 1 GHz.

return statistics and hence it would provide more knowledge about the system for someone probing a possible target object. The single-mode coherent state is thus more advantageous to the single-mode thermal state for object detection performance. However, this advantage comes at the price of reduced covertness, as the single-mode thermal state can be disguised more easily within the background noise due to its coherence properties. Single-mode states only have a single frequency, therefore to discuss the spectral differences between thermal light and coherent light we extend to multi-modes. The spectral distributions of both (multi-mode) thermal and coherent light is shown in Fig. 2.7. Multi-mode coherent light is an approximate model for continuous-wave laser light with an idealised Lorentzian spectral distribution and the spectral distribution of the thermal light is given by Planck's law. It is clear that the multi-mode coherent light has a sharp spectral distribution compared to the multi-mode thermal light. Thus the multi-mode coherent light is easier to detect than the multi-mode thermal light on account of its spectral properties.

2.7.3 Quantum illumination

The following analysis considers the twin-beam output from the SPDC process to be an entangled quantum state known as the two-mode squeezed vacuum (TMSV) [99]. It is a simplification of the form given in Eq. 2.51 as each beam has only one mode. Later in this thesis an extended form of the SPDC output is derived which considers multiple discrete modes for each beam.

The state vector for the TMSV state is

$$|\psi\rangle_{\text{TMSV}} = \text{sech}(r)\sum_{n=0}^{\infty}(-1)^n e^{in\theta}\big(\tanh(r)\big)^n|n\rangle_{\text{S}}\otimes|n\rangle_{\text{I}}, \tag{2.62a}$$

$$= \sum_{n=0}^{\infty}\sqrt{\lambda_n}|\psi\rangle_{\text{S}}\otimes|\psi\rangle_{\text{I}}. \tag{2.62b}$$

Equation 2.62b is known as the Schmidt decomposition [128], with Schmidt eigenvalues λ_n where $\sum_{n=0}^{\infty}\lambda_n = 1$ and $|\psi\rangle_{\text{S/I}}$ are orthonormal states for the signal or idler mode. We can quantify the degree of entanglement by evaluating the Schmidt number $K = \big(\sum_{n=0}^{\infty}\lambda_n^2\big)^{-1}$, if there is only one Schmidt eigenvalue ($K = 1$) then the state is separable and hence is not entangled. Otherwise, if there large Schmidt number there is a large degree of entanglement in that chosen basis. Following this, the density matrix for the TMSV state in terms of the two-mode squeezing operator and the two-mode vacuum is

$$\hat{\rho}_{\text{TMSV}} = \text{Tr}_{\text{P}}\Big(\hat{S}(\chi^{(2)})|\alpha\rangle_{\text{P}}\otimes|0,0\rangle\times\text{h.c}\Big), \tag{2.63}$$

where the pump field is traced out of the composite Hilbert space. This process of partial tracing is illustrated as follows. A generic density matrix with a composite Hilbert space $\mathfrak{H}_{1,2}$ of two Hilbert spaces $\mathfrak{H}_1$ and $\mathfrak{H}_2$ is defined in the Fock basis as

$$\hat{\rho}_{\mathfrak{H}_{1,2}} = \sum_{n,m,p,q=0}^{\infty} c_{n,m,p,q}|n\rangle\langle m|\otimes|p\rangle\langle q|, \tag{2.64}$$

where $c_{n,m,p,q}$ is a complex number. The partial trace over the Hilbert space $\mathfrak{H}_2$ in $\hat{\rho}_{\mathfrak{H}_{1,2}}$ is

$$\text{Tr}_{\mathfrak{H}_2}\left(\hat{\rho}_{\mathfrak{H}_{1,2}}\right) = \sum_{j=0}^{\infty}\sum_{n,m,p,q=0}^{\infty} c_{n,m,p,q}|n\rangle\langle m|\times\langle j|p\rangle\langle q|j\rangle, \tag{2.65}$$

this is clearly an expression only in the Hilbert space $\mathfrak{H}_1$ as each eigenstate of Hilbert space $\mathfrak{H}_2$ has an inner product applied to it. Experimentally this partial tracing can be achieved by a spectral filter. We evaluate Eq. 2.63 and therefore the TMSV density matrix expressed in the Fock basis is

$$\hat{\rho}_{\text{TMSV}} = \text{sech}(r)^2\sum_{n,m=0}^{\infty}(-1)^{n+m}e^{in\theta-im\theta}\big(\tanh(r)\big)^{n+m}|n,n\rangle\langle m,m| \tag{2.66}$$

However, we omit the off-diagonal elements in the TMSV state as we use detectors which are insensitive to the off-diagonal elements, therefore we can simplify Eq. 2.66 by setting $n = m$.

We can omit the off-diagonal elements because our detectors projects only upon the diagonal elements of the state. We refer to this state with only diagonal elements as the QI state $\hat{\rho}_{\mathrm{SI}}$ and not the TMSV. This is because the QI state $\hat{\rho}_{\mathrm{SI}}$ has the measurable properties of a two-mode correlated thermal state and does not need to be generated from a SPDC process. Hence the QI density matrix expressed in the Fock basis is [100]

$$\hat{\rho}_{\mathrm{SI}} = (\cosh(r))^{-2} \sum_{n=0}^{\infty} (\tanh(r))^{2n} |n,n\rangle\langle n,n|, \tag{2.67a}$$

$$= \sum_{n=0}^{\infty} \frac{\bar{n}^n}{(\bar{n}+1)^{n+1}} |n,n\rangle\langle n,n|, \tag{2.67b}$$

where the mean photon number is $\bar{n} = \sinh^2(r)$. The QI state has non-classical inter-mode correlations. We can quantify the degree of correlation with the noise reduction factor (NRF) [129], which is defined as

$$\mathrm{NRF} = \frac{\langle \left(\Delta(\hat{n}_{\mathrm{S}} - \hat{n}_{\mathrm{I}})\right)^2 \rangle}{\langle \hat{n}_{\mathrm{S}} + \hat{n}_{\mathrm{I}} \rangle}, \tag{2.68}$$

where $\langle \left(\Delta(\hat{n}_{\mathrm{S}} - \hat{n}_{\mathrm{I}})\right)^2 \rangle$ is the variance of the expectation value of the photon-number difference operator. Classical states are lower bounded by a NRF $= 1$, whereas our QI state has a NRF $= 0$ as the variance of the expectation value of the photon-number difference operator is zero. Another approach to demonstrate the non-classicality of our inter-mode correlations is by showing that our state does not satisfy the Cauchy-Schwarz inequality [130]. In terms of the number operators for a state with two modes the Cauchy-Schwarz inequality is

$$\langle :\hat{n}_{\mathrm{S}}:^2 \rangle \langle :\hat{n}_{\mathrm{I}}:^2 \rangle \geq \langle \hat{n}_{\mathrm{S}} \hat{n}_{\mathrm{I}} \rangle^2, \tag{2.69}$$

this form of the Cauchy-Schwarz inequality is derived from a more general expression $\langle \hat{I}_{\mathrm{S}} \hat{I}_{\mathrm{I}} \rangle^2 \leq \langle \hat{I}_{\mathrm{S}}^2 \rangle \langle \hat{I}_{\mathrm{I}}^2 \rangle$ in terms of intensity operators and with $\hat{I}^2 \propto \left(\hat{E}^-\right)^2 \left(\hat{E}^+\right)^2$ ensuring the normal-ordering and $\hat{E}$ as the electric field operator [131], [132]. For our QI state this inequality is not satisfied, which demonstrates it has non-classical correlations, as

$$4\bar{n}^4 \not\geq 4\bar{n}^4 + 4\bar{n}^3 + \bar{n}^2. \tag{2.70}$$

If a measurement device only has access to one of the modes, the other mode must be traced out. Doing so will make the QI state appear to be a thermal state [133]. Furthermore, the thermal statistical properties of one mode of the QI state when the other mode is ignored is also implied by the no-signalling theorem [134]. The CI light source (when we wish to use the

thermal state as our probe) is equivalent to the QI light source with the idler mode ignored, under the assumption that the signal mean photon number $\bar{n}$ for both are equal. Ignoring one mode is represented by taking the partial trace of that mode, hence

$$\mathrm{Tr}_{\mathrm{I}}(\hat{\rho}_{\mathrm{SI}}(\bar{n})) \equiv \hat{\rho}_{\mathrm{th}}(\bar{n}). \tag{2.71}$$

This feature means that CI can use the single-mode thermal state as the light source as for a fair and direct comparison of CI and QI. Moreover, an intruder will only see thermal photon statistics, which are identical to the photon statistics exhibited by background noise: ideal for covertness. The accuracy of using our QI state to express the SPDC output can be checked by an experimental setup involving the Hanbury-Brown and Twiss interferometer. For example, imagine the situation where only one beam of our QI state is involved in the interferometer with the vacuum. If we measure $g^{(2)}(0) = 2$ this demonstrates that this beam only has one mode, as required by the photon-bunching statistics of a single-mode thermal state. In effect this indirectly demonstrates the accuracy of describing our light for a QI system as a two-mode state.

In summary, this chapter begins with the quantisation of the EM field. We introduce the canonical creation and destruction operator for a mode of the EM field. After, we introduce the concept of Hilbert space and we then express a general form of the state vector of a quantum state. Following on from this, we introduce the Fock state. The Fock state is useful as our detectors discussed later in the thesis are in the photon-number basis. We also introduce the coherent state and phase-space. We can express quantum states in the coherent state basis — this formulation allows visualisation of our quantum states in phase-space. These concepts help with characterising the light we use. Additionally; the coherent state basis simplifies calculations later in this thesis. We also introduce the non-classical effect known as single-mode squeezing. The introduction of single-mode squeezing primes us for leading onto the discussion about SPDC (a process which generates the non-classical light we consider in this thesis). An overarching theme of this chapter is to introduce the tools and techniques we use later in this thesis to characterise light. With this in mind, we discuss the quantum coherence function. The second-order quantum coherence function helps us recognise when a state of light demonstrates non-classical photon statistics. With the suite of techniques and tools introduced, we proceed to characterise the types of light relevant to our LIDAR protocol: the background noise, CI and QI.

Chapter 3: Measurement theory and observables

This chapter is a primer on the theory of measurement and observables. Also shown are the methods to calculate the observables in our LIDAR protocol. Following this, there is an exposition on optimal state discrimination and how state discrimination using click probabilities is sub-optimal. This chapter concludes with a section about hypothesis testing with click-count distributions and the log-likelihood value.

3.1 Measurement operators

Measurement of a quantum state can change the state in question. This effect is particularly apparent with (ideal) projective measurements. For example, a projector $\hat{P}_n = |\lambda_n\rangle\langle\lambda_n|$ acting upon a state $\hat{\rho} = \sum_{m=0}^{\infty} \lambda_m |\lambda_m\rangle\langle\lambda_m|$, where $|\lambda_m\rangle$ is an eigenstate of $\hat{\rho}$, will result in the (normalised) post-measurement density matrix

$$\hat{\rho}' = \frac{\hat{P}_n \hat{\rho} \hat{P}_n}{\mathrm{Tr}(\hat{P}_n \hat{\rho} \hat{P}_n)}, \tag{3.1a}$$

$$= |\lambda_n\rangle\langle\lambda_n|. \tag{3.1b}$$

The denominator, which normalises the state, is the probability p_n that the measurement n is made by the projector $\hat{P}_n$. We calculate this probability p_n as

$$p_n = \mathrm{Tr}\big(\hat{P}_n \hat{\rho} \hat{P}_n\big) = \lambda_n. \tag{3.2}$$

However, we must extend our theory to generalised measurements. This is because it is not sufficient, for a realistic system, to describe measurement of a quantum state via a measurement apparatus (and the form of the post-measurement state) if we only consider a projective measurement upon a quantum state Q. We consider a scenario that is known as

the measurement model, which entails the interaction of our quantum state and an initially uncorrelated measurement apparatus (ancilla A) state, after this interaction we perform a projective measurement upon our ancilla and then we trace the ancilla sub-system. A unitary operator $\hat{U}$ describes the interaction between our quantum state and the ancilla. Our quantum state and ancilla has the density matrix $\hat{\rho}$ and $\hat{\sigma} = \sum_k \lambda_k |e_k\rangle\langle e_k|$, respectively. Where $|e_k\rangle$ is an eigenstate of the ancilla density matrix $\hat{\sigma}$. We define a projector for the measurement outcome α as

$$\hat{P}_\alpha = \sum_l |f_{\alpha l}\rangle\langle f_{\alpha l}|, \tag{3.3}$$

where $|f_{\alpha l}\rangle$ forms an orthonormal basis over the ancilla system and it satisfies the completeness relation $\hat{1} = \sum_\alpha \hat{P}_\alpha$. The unnormalised post-measurement state of our system is

$$\mathrm{Tr}_A\big(\hat{P}_\alpha \hat{U}\hat{\rho}\otimes\hat{\sigma}\hat{U}^\dagger\hat{P}_\alpha\big) = \mathcal{A}_\alpha(\hat{\rho}), \tag{3.4}$$

where $\mathcal{A}_\alpha$ is a linear map on the system density matrix, which we refer to $\mathcal{A}_\alpha$ as a quantum operation. We can restate the quantum operation $\mathcal{A}_\alpha$ in terms of operators acting only upon the quantum state Q

$$\mathcal{A}_\alpha(\hat{\rho}) = \sum_{l,k} A_{\alpha,l,k}\hat{\rho}A^\dagger_{\alpha,l,k}, \tag{3.5}$$

where $A_{\alpha,l,k} = \sqrt{\lambda_k}\langle f_{\alpha l}|\hat{U}|e_k\rangle$. Equation 3.5 is known as the Kraus decomposition of the quantum operation $\mathcal{A}_\alpha$, where $A_{\alpha,l,k}$ are known as Kraus operators [135]. From the Kraus operators we can see how a projective measurement relates to our measurement model. The probability that we measure an outcome α at our measurement apparatus is

$$p_\alpha = \mathrm{Tr}\big(\mathcal{A}_\alpha(\hat{\rho})\big). \tag{3.6}$$

From the Kraus operators we define a POVM (positive operator-valued measure). The POVM is an operator that when applied to a state describes the measurement statistics for a measurement outcome α [136]

$$\hat{\pi}_\alpha = \sum_{l,k} \hat{A}^\dagger_{\alpha,l,k}\hat{A}_{\alpha,l,k}. \tag{3.7}$$

A POVM comprises a set of POVM elements $S_{\hat{\pi}}$ and within this set for each result m there is a

POVM element $\hat{\pi}_m$. A POVM has the following properties

$$\hat{\pi}_n^\dagger = \hat{\pi}_m, \tag{3.8a}$$

$$\hat{\pi}_m \geq 0, \text{ as for all } m: \langle\psi|\hat{\pi}_m|\psi\rangle \text{ for all } |\psi\rangle, \tag{3.8b}$$

$$\sum_{m=0}^{|S_{\hat{\pi}}|} \hat{\pi}_m = \hat{1}, \tag{3.8c}$$

Eq. 3.8a shows their Hermiticity and therefore they make observable measurements by construction. Eq. 3.8b shows that their expectation values correspond to probabilities of the result of m. Eq. 3.8c shows that all of the probabilities related to the POVM will sum to unity. Equations 3.8 together allow the interpretation of probabilities from the POVM acting upon a state. Moreover, as a POVM pertains to the measurement statistics it corresponds to many different quantum operations, therefore a POVM does not uniquely specify the post-measurement state. From Eq. 3.6, due to the cyclic invariance of the trace, the probability of a measurement outcome α in terms of the POVM element $\hat{\pi}_\alpha$ is

$$p_\alpha = \mathrm{Tr}\big(\hat{\rho}\hat{\pi}_\alpha\big). \tag{3.9}$$

The formalism pertaining to generalised measurement facilitates the development of our QI model. It also allows calculation of the optimal measurements one can make, as shown in Ch. 3.5.

3.2 Click detector theory

We focus on a 'simple detection' LIDAR system, which entails the use of click detectors. These detectors for a set measurement window can only register either a click event or a no-click event. Their use facilitates experimental simplicity, therefore granting the possibility of this protocol functioning in difficult real-life sensing scenarios.

The experimental component that can represent the click detector is the SPAD (single-photon avalanche diode) [137]. They can function in the so-called Geiger-mode, aptly named due its click detector nature. Such detectors only reveal whether light was incident or not, rather than the full information about the amount of incident light. Moreover, SPADs in the Geiger-mode are receptive to incident light that arrives in packets of quanta, such as single-photons. What allows this level of sensitivity is a high reverse bias voltage that places the system precariously close to triggering an avalanche current. This avalanche current initiates when incident light hits an atom in a positively charged area and creates an electron-hole pair. A weak electric field

permeates this area and thus separates the electron-hole pair. The electron then drifts towards the region with a strong electric field, resulting in an increasing velocity for the electron. The electron then collides with other atoms generating new electron-hole pairs in a cascade effect. A large number of electrons now results in a high (and measurable) signal. The detector is reset, in a process called quenching, by applying a forward current to counter the avalanche and return the positive charge to the anode, this whole process to reset is known as sensor dead-time.

In realistic systems there are downsides and inefficiencies to SPADs. Such a high level of sensitivity means that SPADs are vulnerable to dark-counts: which is when the detector is triggered from causes other than the incident photons. For a photo-detector in the same mode as the incident light, there is a probability that it clicks according to the detector quantum efficiency and the state of the incident light itself. For example, any vacuum component of the incident state reduces the click probability. Moreover, the click probability increases with an increase of the contribution of single-photons and multi-photons to the quantum state. However, with these detectors, we are unable to distinguish whether a click event was due to a single-photon or multi-photon. For a state that only consists of a single-photon the click probability is equal to the detector quantum efficiency. Finally, uncertainty in the time taken from incident light to read-out of a measurable photocurrent is known as the detector timing jitter.

The use of click detectors means that the inference of object presence depends upon the probability of a click event. A relevant click POVM acting upon a quantum state gives the probability of a click event for that state. The no-click POVM element $\hat{\pi}_{\times}$ for a detector, in the scenario of no background noise and perfect efficiency, can be found from the photon number distribution moment generating functions [123], [138] and we now proceed to derive this POVM. We begin the derivation of the click detector POVM by introducing the quantum-mechanical formulation of the photo-count distribution given by Kelley and Kleiner. The number of photo-counts m over a period of time t with a detector quantum efficiency η for a generic quantum state with density matrix $\hat{\rho}$ is

$$p_m(t) = \mathrm{Tr}\left(\hat{\rho} : \frac{(\eta \hat{a}^\dagger \hat{a})^m}{m!} e^{-\eta \hat{a}^\dagger \hat{a}} :\right). \tag{3.10}$$

We then extract the POVM for m photo-counts from Eq. 3.10 due to the Born rule

$$\hat{\pi}_m(\eta) =: \frac{(\eta \hat{a}^\dagger \hat{a})^m}{m!} e^{-\eta \hat{a}^\dagger \hat{a}} :, \tag{3.11a}$$

$$= \frac{-\eta^m}{m!} \frac{\partial^m}{\partial \eta^m} : e^{-\eta \hat{a}^\dagger \hat{a}} : . \tag{3.11b}$$

We can restate the exponential term $:e^{-\eta\hat{a}^\dagger\hat{a}}:$ by using operator ordering theorems and that the exponential term commutes with the number operator $\hat{n}$ — therefore is diagonal in the photon-number basis

$$\hat{M}(\eta) =: e^{-\eta\hat{a}^\dagger\hat{a}} :, \tag{3.12a}$$

$$= e^{\ln(1-\eta)\hat{a}^\dagger\hat{a}}, \tag{3.12b}$$

$$= (1-\eta)^{\hat{a}^\dagger\hat{a}}, \tag{3.12c}$$

$$= \sum_{n=0}^{\infty}(1-\eta)^n|n\rangle\langle n|. \tag{3.12d}$$

From Eq. 3.11b and Eq. 3.12d we state the POVM for detecting m photo-counts as

$$\hat{\pi}_m(\eta) = \eta^m \sum_{n=m}^{\infty}\binom{n}{m}(1-\eta)^{n-m}|n\rangle\langle n|. \tag{3.13}$$

Hence, the no-click POVM is when we register $m=0$ photo-counts. Furthermore, when there is perfect quantum efficiency $\eta = 1$ it is obvious that the only non-zero eigenstate of Eq. 3.13 is when the photon-number $n=0$. The no-click POVM is

$$\hat{\pi}_\times =: e^{-\hat{a}^\dagger\hat{a}}: \; = |0\rangle\langle 0|. \tag{3.14}$$

It is clear that the click POVM element must be the complement of this

$$\hat{\pi}_\checkmark = \hat{1} - \hat{\pi}_\times. \tag{3.15}$$

The normal ordering is expected as photo-detection is an absorptive process. In such an idealised scenario, registering a no-click means projection onto the vacuum state. However, a realistic system which entails system loss η and incidence of thermal background noise $\hat{\rho}_{\text{th}}(\bar{n}_{\text{B}})$ is instead projection onto a mixed state [139]. The no-click POVM element in this more realistic scenario

$$\hat{\pi}_\times = \frac{1}{1+\bar{n}_{\text{B}}} :e^{-\frac{\eta}{1+\bar{n}_{\text{B}}}\hat{a}^\dagger\hat{a}}: , \tag{3.16a}$$

$$= \frac{1}{1+\bar{n}_{\text{B}}} e^{\ln(1-\frac{\eta}{1+\bar{n}_{\text{B}}})\hat{a}^\dagger\hat{a}}, \tag{3.16b}$$

$$= \frac{1}{1+\bar{n}_{\text{B}}}\left(1-\frac{\eta}{1+\bar{n}_{\text{B}}}\right)^{\hat{a}^\dagger\hat{a}}, \tag{3.16c}$$

$$= \frac{1}{1+\bar{n}_{\text{B}}}\sum_{n=0}^{\infty}\left(1-\frac{\eta}{1+\bar{n}_{\text{B}}}\right)^{n}|n\rangle\langle n|, \tag{3.16d}$$

which is effectively projection onto a thermal state. Let us consider the two detector system required by quantum LIDAR described previously in Ch. 1.3. The idler detector click POVM element for a detector when there is thermal background noise $\hat{\rho}_{\text{th}}(\bar{n}_{\text{B,I}})$ and idler system loss η_{I}

$$\hat{\pi}_{\text{I}} = \hat{1} - \frac{1}{1+\bar{n}_{\text{B,I}}} \sum_{n=0}^{\infty} \left(1 - \frac{\eta_{\text{I}}}{1+\bar{n}_{\text{B,I}}}\right)^n |n\rangle\langle n|. \tag{3.17}$$

Furthermore, the signal detector click POVM element for a detector subject to thermal background noise, $\hat{\rho}_{\text{th}}(\bar{n}_{\text{B,S}})$, with signal system loss η_{S} and the signal attenuation parameter ξ is

$$\hat{\pi}_{\text{S}} = \hat{1} - \frac{1}{1+\bar{n}_{\text{B,S}}} \sum_{n=0}^{\infty} \left(1 - \frac{\xi\eta_{\text{S}}}{1+\bar{n}_{\text{B,S}}}\right)^n |n\rangle\langle n|. \tag{3.18}$$

For CI, the signal detector is the only detector. We consider on CI a thermal light source, which is equivalent to the QI light source with the same signal mean photon number and the idler detector ignored. Therefore, the CI click probability

$$\begin{aligned} \text{Pr}_{\text{CI:th}} &= \text{Tr}\big(\hat{\rho}_{\text{th}}(\bar{n})\hat{\pi}_{\text{S}}\big), && (3.19a)\\ &= \sum_{n=0}^{\infty} \frac{\bar{n}^n}{(\bar{n}+1)^{n+1}} - \frac{1}{1+\bar{n}_{\text{B,S}}} \frac{\bar{n}^n}{(\bar{n}+1)^{n+1}} \left(1 - \frac{\eta_{\text{S}}}{1+\bar{n}_{\text{B,S}}}\right)^n. && (3.19b) \end{aligned}$$

For QI, measurement at the idler detector conditions the signal beam. Therefore, we consider the idler click probability first. We define the idler system loss η_{I} and the thermal background noise state for the idler detector $\hat{\rho}_{\text{B,I}}$ with mean photon number $\bar{n}_{\text{B,I}}$. Hence, the idler click probability is

$$\begin{aligned} \text{Pr}_{\text{I}} &= \text{Tr}\big(\hat{\rho}_{\text{SI}}\hat{\pi}_{\text{I}}\big), && (3.20a)\\ &= \sum_{n=0}^{\infty} \frac{\bar{n}^n}{(\bar{n}+1)^{n+1}} - \frac{1}{1+\bar{n}_{\text{B,I}}} \frac{\bar{n}^n}{(\bar{n}+1)^{n+1}} \left(1 - \frac{\eta_{\text{I}}}{1+\bar{n}_{\text{B,I}}}\right)^n. && (3.20b) \end{aligned}$$

Now that the idler click probability has been calculated, the coincidence click probability

$$\text{Pr}_{\text{S|I,1}} = \text{Tr}\left(\frac{\text{Tr}_{\text{I}}(\hat{\rho}_{\text{SI}}\hat{\pi}_{\text{I}})\hat{\pi}_{\text{S}}}{\text{Pr}_{\text{I}}}\right). \tag{3.21}$$

This is not expanded due to its lack of brevity; however, it is easy to numerically implement. The non-coincidence click probability is similar,

$$\text{Pr}_{\text{S|I,0}} = \text{Tr}\left(\frac{\text{Tr}_{\text{I}}(\hat{\rho}_{\text{SI}}(\hat{1} - \hat{\pi}_{\text{I}}))\hat{\pi}_{\text{S}}}{1 - \text{Pr}_{\text{I}}}\right). \tag{3.22}$$

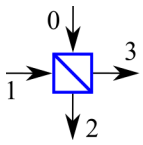

Figure 3.1 – Representation of a lossless beamsplitter often encountered in quantum optics. The input modes with labelling 0 and 1 and output modes with labelling 2 and 3.

We emulate the absence of an object by replacing the signal state with the vacuum and use the notation H0 to refer to the absence of an object (null hypothesis). Consequently, the object absent click probability for CI and QI (coincidence and non-coincidence) is

$$\mathrm{Pr}_{\mathrm{H0}} = \mathrm{Tr}\big(|0\rangle\langle 0|\hat{\pi}_{\mathrm{S}}\big). \tag{3.23}$$

3.3 Modelling with beam-splitters

Beam-splitters play an important role for modelling the effect of the light that falls upon a detector [140]. They mix states of light and facilitate the modelling of imperfect photo-detection. Figure 3.1 depicts the lossless beamsplitter, which has two input modes and two output modes as required by quantum optics. For simplicity the beamsplitter is symmetrical, in other words transmission from mode 0 to mode 2 is the same as transmission from mode 1 to mode 3. Moreover, the transmission $|t|^2$ and reflection $|r|^2$ parameters must adhere to $|t|^2 + |r|^2 = 1$ and $r^*t + rt^* = 0$, for energy conservation in a symmetric beam-splitter — one with the reflection and transmission coefficients that are the same for each input. The input modes have the destruction operators $\hat{a}_0$ and $\hat{a}_1$. These operators relate to the output mode destruction operators $\hat{a}_2$ and $\hat{a}_3$ by

$$\begin{pmatrix} \hat{a}_2 \\ \hat{a}_3 \end{pmatrix} = \begin{pmatrix} t & r \\ r & t \end{pmatrix} \begin{pmatrix} \hat{a}_0 \\ \hat{a}_1 \end{pmatrix}. \tag{3.24}$$

We desire a (unitary) beamsplitter operator $\hat{U}$, one which succinctly describes the action of a beamsplitter upon both modes. Conventionally $\hat{U}$ is known and leads to the derivation of the beamsplitter relations in Eq. 3.24. However, our derivation is framed in the reverse order because it is more intuitive for understanding to begin with the relations in Eq. 3.24 and lead towards $\hat{U}$. The derivation of $\hat{U}$ begins by setting $\hat{a}_2$ ($\hat{a}_3$ has a similar method)

$$\hat{a}_2 = \cos\frac{\theta}{2}\hat{a}_0 + i\sin\frac{\theta}{2}\hat{a}_1, \tag{3.25a}$$

$$= \hat{a}_0 \sum_{n=0}^{\infty} \frac{(-1)^n(\frac{\theta}{2})^{2n}}{(2n)!} + i\hat{a}_1 \sum_{n=0}^{\infty} \frac{(-1)^n(\frac{\theta}{2})^{2n+1}}{(2n+1)!}, \tag{3.25b}$$

where $\theta = 2\cos^{-1}(t)$. Equation 3.25b satisfies the Baker-Hausdorff lemma when $\hat{A} = \frac{1}{2}(\hat{a}_0^\dagger \hat{a}_1 + \hat{a}_0 \hat{a}_1^\dagger)$, $\hat{B} = \hat{a}_0$ and $\lambda = -\theta$. The Baker-Hausdorff lemma is

$$e^{i\lambda\hat{A}}\hat{B}e^{-i\lambda\hat{A}} = \hat{B} + i\lambda[\hat{A},\hat{B}] + \frac{(i\lambda)^2}{2!}[\hat{A},[\hat{A},\hat{B}]] + \dots \tag{3.26}$$

This means that there is an operator $\hat{U}$ which enacts the beamsplitter transformation, defined as

$$\hat{U} = e^{i\lambda\hat{A}} = e^{-i\frac{\theta}{2}(\hat{a}_0^\dagger \hat{a}_1 + \hat{a}_0 \hat{a}_1^\dagger)}, \tag{3.27}$$

such that

$$\begin{pmatrix} \hat{a}_2 \\ \hat{a}_3 \end{pmatrix} = \hat{U} \begin{pmatrix} \hat{a}_0 \\ \hat{a}_1 \end{pmatrix} \hat{U}^\dagger. \tag{3.28}$$

The derivation of $\hat{U}$ means that the calculations that involve beamsplitter transformations are more succinct, particularly when coherent states are involved.

3.3.1 CI CLICK PROBABILITIES

There are multiple methods available to calculate the probability that a detector will click (or not click). One method is from the POVMs described in Ch. 3.2, although this is an easy method it may seem quite abstract and does not allow easy calculation of a photon-number distribution. Therefore, this section provides the method for calculation of the click probability through the beamsplitter approach. The state incident upon our detector $\hat{\rho}_\mathrm{S}$ is of direct interest for calculation of the click probability. Figure 3.2 depicts the CI beamsplitter model. The state incident upon our detector is expressed via the beamsplitter model in terms of the source light $\hat{\rho}_\mathrm{source}$, the background noise state $\hat{\rho}_\mathrm{B}$ and the beamsplitter operator with transmission parameter $|t|^2$ as

$$\hat{\rho}_\mathrm{S} = \mathrm{Tr}_3\left(\hat{U}\hat{\rho}_\mathrm{source} \otimes \hat{\rho}_\mathrm{B}\hat{U}^\dagger\right). \tag{3.29}$$

Derivation of $\hat{\rho}_\mathrm{S}$ is greatly helped by use of the coherent state basis. This basis affords simplicity because the beamsplitter operator easily acts upon the displacement operator. For example, $\hat{U}\hat{D}_0(\alpha)\hat{U}^\dagger = \hat{D}_2(t\alpha)\hat{D}_3(r\alpha)$.

We focus first on the CI protocol with the source light as a coherent state, $\hat{\rho}_\mathrm{source} = |\alpha\rangle\langle\alpha|$, (with mean photon number $\bar{n} = |\alpha|^2$) and the background noise as a thermal state $\hat{\rho}_\mathrm{B} = \hat{\rho}_\mathrm{th}(\bar{n}_\mathrm{B})$. We also make extensive use of the Gaussian integral $\int d^2\alpha e^{-a|\alpha|^2 + b\alpha^* + b^*\alpha} = \frac{\pi}{a}e^{\frac{|b|^2}{a}}$. Calculation of the state incident upon the detector $\hat{\rho}_\mathrm{S}$ begins with the input states expressed in the coherent

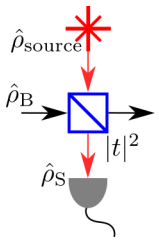

FIGURE 3.2 – Representation of the mixing of source light $\hat{\rho}_{\text{source}}$ and background noise light $\hat{\rho}_{\text{B}}$. A beamsplitter with transmission parameter $|t|^2$ and mode 2 is retained, which contains the state incident upon the detector $\hat{\rho}_{\text{S}}$.

state basis and application of the beamsplitter transformations

$$\hat{\rho}_{\text{S}} = \text{Tr}_3\left(\hat{U}|\alpha\rangle_0\langle\alpha| \otimes \frac{1}{\pi\bar{n}_{\text{B}}}\int d^2\beta e^{\frac{-|\beta|^2}{\bar{n}_{\text{B}}}}|\beta\rangle_1\langle\beta|\hat{U}^\dagger\right), \tag{3.30a}$$

$$= \text{Tr}_3\left(\frac{1}{\pi\bar{n}_{\text{B}}}\int d^2\beta e^{\frac{-|\beta|^2}{\bar{n}_{\text{B}}}}|t\alpha + r\beta\rangle_2\langle t\alpha + r\beta| \right. \tag{3.30b}$$

$$\left. \otimes\, |r\alpha + t\beta\rangle_3\langle r\alpha + t\beta|\right),$$

$$= \frac{1}{\pi\bar{n}_{\text{B}}}\int d^2\beta e^{\frac{-|\beta|^2}{\bar{n}_{\text{B}}}}|t\alpha + r\beta\rangle\langle t\alpha + r\beta|. \tag{3.30c}$$

Now with the state incident upon the detector derived, the CI click probability

$$\text{Pr}_{\text{CI:coh}} = 1 - \text{Tr}\big(\hat{\rho}_{\text{S}}|0\rangle\langle 0|\big), \tag{3.31a}$$

$$= 1 - \frac{1}{\pi\bar{n}_{\text{B}}}\int d^2\beta e^{\frac{-|\beta|^2}{\bar{n}_{\text{B}}}} e^{-|t\alpha + r\beta|^2}, \tag{3.31b}$$

$$= 1 - \frac{e^{\frac{-|t|^2|\alpha|^2}{1+|r|^2\bar{n}_{\text{B}}}}}{1 + |r|^2\bar{n}_{\text{B}}}, \tag{3.31c}$$

$$= 1 - \frac{e^{\frac{-\xi\eta_{\text{S}}\bar{n}}{1+\bar{n}_{\text{B,S}}}}}{1 + \bar{n}_{\text{B,S}}}, \tag{3.31d}$$

where $|t|^2 = \xi\eta_{\text{S}}$ and $\bar{n}_{\text{B}} = \frac{\bar{n}_{\text{B,S}}}{|r|^2}$. We are only interested in the measured background noise $\bar{n}_{\text{B,S}}$. Therefore the denominator of the actual background noise $\bar{n}_{\text{B}}$ acts to negate the effect of the beamsplitter model reflecting a portion of the background light. An alternative calculation of Eq. 3.31d via the Fock basis is given in Appendix A. For the scenario of background noise in the coherent state and thermal source light the click probability is easily found from Eq. 3.31d by swapping $\xi\eta_{\text{S}}\bar{n}$ with $\bar{n}_{\text{B,S}}$ and vice versa.

We now present CI with the source light as a thermal state $\hat{\rho}_{\text{source}} = \hat{\rho}_{\text{th}}(\bar{n})$. The analysis with the beamsplitter transformations differs slightly to CI with the source light as a coherent

state due to a variable change in the integral. The state incident upon the detector

$$\hat{\rho}_{\mathrm{S}} = \mathrm{Tr}_3\Big(\hat{U}\frac{1}{\pi\bar{n}}\int d^2\alpha e^{\frac{-|\alpha|^2}{\bar{n}}}|\alpha\rangle_0\langle\alpha| \otimes \frac{1}{\pi\bar{n}_{\mathrm{B}}}\int d^2\beta e^{\frac{-|\beta|^2}{\bar{n}_{\mathrm{B}}}}|\beta\rangle_1\langle\beta|\hat{U}^\dagger\Big), \tag{3.32a}$$

$$= \frac{1}{\pi^2\bar{n}\bar{n}_{\mathrm{B}}}\int d^2\alpha d^2\beta e^{-\frac{|\alpha|^2}{\bar{n}}-\frac{|\beta|^2}{\bar{n}_{\mathrm{B}}}}|t\alpha + r\beta\rangle\langle t\alpha + r\beta|. \tag{3.32b}$$

We introduce a variable $\gamma = t\alpha + r\beta$ and convert the β variable integral to a γ variable integral, where $d^2\beta = \frac{d^2\gamma}{|r|^2}$. These steps allow for calculation of the α variable integral. Hence, derivation of $\hat{\rho}_{\mathrm{S}}$ continues

$$\hat{\rho}_{\mathrm{S}} = \frac{1}{\pi^2\bar{n}\bar{n}_{\mathrm{B}}|r|^2}\int d^2\alpha d^2\gamma e^{\frac{-|\gamma|^2}{|r|^2\bar{n}_{\mathrm{B}}}} e^{-|\alpha|^2\left(\frac{1}{\bar{n}}+\frac{|t|^2}{|r|^2\bar{n}_{\mathrm{B}}}\right)+\alpha\frac{\gamma^* t}{|r|^2\bar{n}_{\mathrm{B}}}+\alpha^*\frac{\gamma t^*}{|r|^2\bar{n}_{\mathrm{B}}}}, \tag{3.33a}$$

$$= \frac{1}{\pi\big(|r|^2\bar{n}_{\mathrm{B}}+\bar{n}|t|^2\big)}\int d^2\gamma e^{-|\gamma|^2\frac{1}{|r|^2\bar{n}_{\mathrm{B}}+\bar{n}|t|^2}}|\gamma\rangle\langle\gamma|, \tag{3.33b}$$

$$= \hat{\rho}_{\mathrm{th}}(|r|^2\bar{n}_{\mathrm{B}}+\bar{n}|t|^2). \tag{3.33c}$$

Therefore, the object present CI click probability when there is a thermal state for source and noise is

$$\mathrm{Pr}_{\mathrm{CI:th}} = 1 - \mathrm{Tr}\big(\hat{\rho}_{\mathrm{S}}|0\rangle\langle 0|\big), \tag{3.34a}$$

$$= 1 - \frac{1}{\bar{n}_{\mathrm{B}}|r|^2 + |t|^2\bar{n} + 1}, \tag{3.34b}$$

$$= 1 - \frac{1}{\bar{n}_{\mathrm{B,S}} + \eta_{\mathrm{S}}\xi\bar{n} + 1}. \tag{3.34c}$$

When an object is absent the type of light produced is irrelevant, all that matters is the type of noise. The absence of an object is expressed in the beamsplitter diagram method by replacing the signal state with the vacuum. The object absent click probability in a thermal noise system is trivial to find in the beamsplitter approach due to the scaling which causes the noise to be unaffected by the beamsplitter. The object absent CI click probability is

$$\mathrm{Pr}_{\mathrm{H0}} = 1 - \mathrm{Tr}(\hat{\rho}_{\mathrm{B,S}}|0\rangle\langle 0|), \tag{3.35a}$$

$$= 1 - \frac{1}{1+\bar{n}_{\mathrm{B,S}}}. \tag{3.35b}$$

3.3.2 POVM FROM BEAMSPLITTER MODEL

The beamsplitter model also allows derivation of the click POVM element given in Ch. 3.2. We start our derivation with the generic click probability for the scenario of thermal noise

$$\Pr = 1 - \mathrm{Tr}\left(\mathrm{Tr}_3(\hat{U}\hat{\rho}\otimes\hat{\rho}_{\mathrm{th}}\hat{U}^\dagger)|0\rangle_2\langle 0|\right), \tag{3.36}$$

where we have used the mode labelling convention in Fig. 3.1. For an unknown no-click POVM element $\pi_{\times,2}$ the generic click probability defined in Eq. 3.36 is equivalent to

$$\Pr = 1 - \mathrm{Tr}\left(\hat{\rho}\hat{\pi}_{\times,2}\right). \tag{3.37}$$

Equating both Eq. 3.36 and Eq. 3.37 then solving for the unknown no-click POVM element is

$$\hat{\pi}_{\times,2} = \mathrm{Tr}_1\left((\hat{1}\otimes\hat{\rho}_{\mathrm{th}})\hat{U}^\dagger(|0\rangle\langle 0|\otimes\hat{1})\hat{U}\right). \tag{3.38}$$

The following derivation finds a closed-form summation over the Fock basis for Eq. 3.38. Firstly,

$$\hat{U}^\dagger(|0\rangle\langle 0|\otimes\hat{1})\hat{U} = \frac{1}{\pi}\hat{U}^\dagger\int d^2\alpha|0\rangle_2\langle 0|\otimes|\alpha\rangle_3\langle\alpha|\hat{U}, \tag{3.39a}$$

$$= \frac{1}{\pi}\int d^2\alpha|r^*\alpha\rangle_0\langle r^*\alpha|\otimes|t^*\alpha\rangle_1\langle t^*\alpha|, \tag{3.39b}$$

and

$$\hat{1}\otimes\hat{\rho}_{\mathrm{th}} = \hat{1}_0\otimes\frac{1}{\pi\bar{n}_{\mathrm{B}}}\int d^2\beta|\beta\rangle_1\langle\beta|. \tag{3.40}$$

Substitution of Eq. 3.39b and Eq. 3.40 into Eq. 3.38 and mode relabelling (mode 1 to mode 3 and mode 0 to mode 2) yields

$$\hat{\pi}_{\times,2} = \frac{1}{\pi^3\bar{n}_{\mathrm{B}}}\int d^2\beta d^2\alpha d^2\gamma e^{\frac{-|\beta|^2}{\bar{n}_{\mathrm{B}}}}|r^*\alpha\rangle\langle r^*\alpha|\otimes\langle\gamma|\beta\rangle\langle\beta|t^*\alpha\rangle_3\langle t^*\alpha|\gamma\rangle, \tag{3.41a}$$

$$= \frac{1}{\pi^3\bar{n}_{\mathrm{B}}}\int d^2\beta d^2\alpha d^2\gamma\times$$

$$\times\, e^{-|\beta|^2(\frac{\bar{n}_{\mathrm{B}}+1}{\bar{n}_{\mathrm{B}}})-|t^*\alpha|^2-|\gamma|^2+\gamma^*\beta+\beta^*t^*\alpha+t\alpha^*\gamma}|r^*\alpha\rangle\langle r^*\alpha|, \tag{3.41b}$$

$$= \frac{1}{\pi^2\bar{n}_{\mathrm{B}}|r|^2}\int d^2\beta d^2\tilde{\alpha}e^{-|\beta|^2(\frac{\bar{n}_{\mathrm{B}}+1}{\bar{n}_{\mathrm{B}}})-|\frac{t^*}{r^*}\tilde{\alpha}|^2+\beta^*\frac{t^*}{r^*}\tilde{\alpha}+\beta\frac{t}{r}\tilde{\alpha}^*}|\tilde{\alpha}\rangle\langle\tilde{\alpha}| \tag{3.41c}$$

In the above derivation $\gamma = \gamma_r + i\gamma_i$ is decomposed into real and imaginary parts to compute this integral as a well known Gaussian integral. We also employ a change of variable $\tilde{\alpha} = r^*\alpha$,

hence $d^2\alpha = \frac{d^2\tilde{\alpha}}{|r|^2}$. The $d^2\beta$ integral is easily solved with the double Gaussian integral cited earlier. Now, the no-click POVM

$$\hat{\pi}_{\times,2} = \frac{1}{\pi|r|^2(\bar{n}_{\mathrm{B}}+1)} \int d^2\tilde{\alpha} e^{-|\tilde{\alpha}|^2 \frac{|t|^2}{|r|^2} \frac{1}{\bar{n}_{\mathrm{B}}+1}} |\tilde{\alpha}\rangle_2\langle\tilde{\alpha}|. \tag{3.42}$$

Setting $\bar{b} = \frac{|r|^2}{|t|^2}(\bar{n}_{\mathrm{B}}+1)$ displays Eq. 3.42 in the P-representation of a single-mode thermal state with mean photon number $\bar{b}$ and a factor of $|t|^{-2}$ in front

$$\hat{\pi}_{\times,3} = \frac{1}{\pi|t|^2\bar{b}} \int d^2\tilde{\alpha} e^{\frac{-|\tilde{\alpha}|^2}{\bar{b}}} |\tilde{\alpha}\rangle\langle\tilde{\alpha}|. \tag{3.43}$$

The measured background noise thermal state mean photon number $\bar{n}_{\mathrm{B,S}}$ is unaffected by the beamsplitter. Similar to earlier the actual background noise is scaled $\bar{n}_{\mathrm{B}} = \frac{\bar{n}_{\mathrm{B,S}}}{|r|^2}$. A generic factor ζ is introduced, which could represent the system loss or system loss and signal attenuation. This factor ζ relates to the transmission magnitude $|t|^2 = \zeta$ and reflection magnitude $|r|^2 = 1-\zeta$. Equation 3.43 is converted into the Fock-basis. Therefore, the generic no-click POVM element with measured background noise $\bar{n}_{\mathrm{B,S}}$ and generic loss factor ζ for mode A is

$$\hat{\pi}_{\times,\mathrm{A}}(\zeta, \bar{n}_{\mathrm{B,S}}) = \frac{1}{\bar{n}_{\mathrm{B,S}}+1} \sum_{n=0}^{\infty} \left(\frac{\bar{n}_{\mathrm{B,S}}+1-\zeta}{\bar{n}_{\mathrm{B,S}}+1} \right)^n |n\rangle_{\mathrm{A}}\langle n|. \tag{3.44}$$

This leads onto the generic click POVM element for mode A

$$\hat{\pi}_{\checkmark,\mathrm{A}}(\zeta, \bar{n}_{\mathrm{B,S}}) = \hat{1}_{\mathrm{A}} - \hat{\pi}_{\times,\mathrm{A}}(\zeta, \bar{n}_{\mathrm{B,S}}). \tag{3.45}$$

Equation 3.45 is clearly equivalent to the complement of the no-click POVM element in Eq. 3.16d, with the relevant parameter changes.

3.3.3 QI CLICK PROBABILITIES

Figure 3.3 depicts the beamsplitter model for QI, with a separate beamsplitter for both idler and signal beams. The idler beamsplitter accounts for idler system loss η_{I} and the measured background noise of the idler detector $\bar{n}_{\mathrm{B,I}}$. The signal beamsplitter accounts for the signal system loss η_{S}, signal attenuation from probing a target object ξ and the measured background noise of the signal detector $\bar{n}_{\mathrm{B,S}}$. Calculation of the click probabilities for QI via the beamsplitter method differs from the CI approach as there is not a well-behaved P-representation of the source light $\hat{\rho}_{\mathrm{SI}}$. However, this is not a problem due to the theory of thermal-difference states [141]. The (non-classical) idler click conditioned state is a thermal-difference state because the

unconditioned (no idler detector measurement) signal state and the idler no-click conditioned signal state are both thermal. It is important to note is that the signal detector is situated on the reflected arm of the output of the signal beamsplitter, this changes the signal beamsplitter transmission parameter $|t|^2 = 1 - \xi\eta_{\mathrm{S}}$. This change of the output position is not necessary, but it keeps the calculations consistent with the mode positioning shown in Fig. 3.3. For both thermal and coherent noise scenarios for the signal channel, the idler click probability is the same as it is shielded from the environment and thus only has dark counts with thermal state photon statistics. The idler detector click probability in a more succinct form than Eq. 3.20a thanks to the beamsplitter approach is

$$\mathrm{Pr}_{\mathrm{I}} = 1 - \frac{1}{\bar{n}_{\mathrm{B,I}} + \eta_{\mathrm{I}}\bar{n} + 1}. \tag{3.46}$$

We consider thermal noise for the signal channel first. The unconditioned signal state upon the signal detector is identical to CI with thermal source light $\hat{\rho}_{\mathrm{source}} = \hat{\rho}_{\mathrm{th}}(\bar{n})$ and thermal noise. As shown already in Eq. 3.33c this state is

$$\hat{\rho}_{\mathrm{S}} = \hat{\rho}_{\mathrm{th}}(\bar{n}_{\mathrm{B,S}} + \xi\eta_{\mathrm{S}}\bar{n}). \tag{3.47}$$

This means that the unconditioned click probability is

$$\mathrm{Pr}_{\mathrm{S}} = 1 - \frac{1}{\bar{n}_{\mathrm{B,S}} + \xi\eta_{\mathrm{S}}\bar{n} + 1}. \tag{3.48}$$

For calculation of the idler measurement conditioned states we invoke POVM formalism for brevity. The density matrix of the idler no-click conditioned state before it is incident on the signal detector,

$$\hat{\rho}_{\mathrm{I}|\times} = \frac{\mathrm{Tr}_{\mathrm{I}}(\hat{\rho}_{\mathrm{SI}}(\hat{1} - \hat{\pi}_{\mathrm{I}}))}{1 - \mathrm{Pr}_{\mathrm{I}}}, \tag{3.49}$$

$$= \hat{\rho}_{\mathrm{th}}(\bar{n}_{\times}), \tag{3.50}$$

where $\bar{n}_{\times} = \mathrm{Tr}(\hat{\rho}_{\mathrm{I}|\times}\hat{n}) = \bar{n}\frac{(1+\bar{n}_{\mathrm{B,I}}-\eta_{\mathrm{I}})}{(1+\bar{n}_{\mathrm{B,I}}+\bar{n}\eta_{\mathrm{I}})}$. Following a similar process to that described earlier with beamsplitters in Eq. 3.33c, the idler no-click conditioned state incident upon the signal detector is

$$\hat{\rho}_{\mathrm{S|I,0}} = \hat{\rho}_{\mathrm{th}}(\bar{n}_{\mathrm{B,S}} + \xi\eta_{\mathrm{S}}\bar{n}_{\times}). \tag{3.51}$$

This means that the non-coincidence click probability is

$$\mathrm{Pr}_{\mathrm{S|I},0} = 1 - \frac{1}{\bar{n}_{\mathrm{B,S}} + \xi\eta_{\mathrm{S}}\bar{n}_{\times} + 1}. \tag{3.52}$$

With both the unconditioned and idler no-click conditioned states before they are incident on the signal detector defined, the idler click conditioned state before the signal detector is

$$\hat{\rho}_{\mathrm{I}|\checkmark} = \frac{1}{\mathrm{Pr}_{\mathrm{I}}}\Big(\hat{\rho}_{\mathrm{th}}(\bar{n}) - (1-\mathrm{Pr}_{\mathrm{I}})\hat{\rho}_{\mathrm{th}}(\bar{n}_{\times})\Big), \tag{3.53}$$

so using the same process as in Eq. 3.33c, the idler click conditioned state incident upon the signal detector is

$$\hat{\rho}_{\mathrm{S|I},1} = \mathrm{Tr}_3\Big(\hat{U}\hat{\rho}_{\mathrm{th}}(\bar{n}_{\mathrm{B}}) \otimes \hat{\rho}_{\mathrm{I}|\checkmark}\hat{U}^{\dagger}\Big) \tag{3.54a}$$

$$= \frac{1}{\mathrm{Pr}_{\mathrm{I}}}\Big(\hat{\rho}_{\mathrm{th}}(\xi\eta_{\mathrm{S}}\bar{n} + \bar{n}_{\mathrm{B,S}}) - (1-\mathrm{Pr}_{\mathrm{I}})\hat{\rho}_{\mathrm{th}}(\xi\eta_{\mathrm{S}}\bar{n}_{\mathrm{X}} + \bar{n}_{\mathrm{B,S}})\Big), \tag{3.54b}$$

which yields the coincidence click probability

$$\mathrm{Pr}_{\mathrm{S|I},1} = 1 - \frac{1}{\mathrm{Pr}_{\mathrm{I}}}\Big((1-\mathrm{Pr}_{\mathrm{S}}) - (1-\mathrm{Pr}_{\mathrm{I}})(1-\mathrm{Pr}_{\mathrm{S|I},0})\Big), \tag{3.55a}$$

$$= 1 - \frac{1}{\mathrm{Pr}_{\mathrm{I}}}\left(\frac{1}{(\xi\eta_{\mathrm{S}}\bar{n} + \bar{n}_{\mathrm{B,S}} + 1)} - (1-\mathrm{Pr}_{\mathrm{I}})\frac{1}{(\xi\eta_{\mathrm{S}}\bar{n}_{\mathrm{X}} + \bar{n}_{\mathrm{B,S}} + 1)}\right). \tag{3.55b}$$

The QI object absent click probability for thermal noise is given by Eq. 3.35b. These expressions for the click probabilities are more succinct than the summation forms given in Ch. 3.2.

We now consider the scenario when there is coherent noise on the signal detector $\hat{\rho}_{\mathrm{B,S}} = |\beta\rangle\langle\beta|$. This represents a situation where a hostile party may actively jam our LIDAR system with a strong coherent beam. We assume that the idler detector noise is unaffected and therefore is still thermal. This is a reasonable assumption as the idler detector is shielded from the environment. Moreover, the dark count noise on the signal detector is still thermal, but for simplicity it is neglected due to the likely orders of magnitude stronger coherent noise incident on the signal detector. The use of the beam-splitter model to calculate the QI click probabilities in this situation is required, as there does not exist a simplistic click POVM element for the signal detector coherent noise scenario. The states before the signal detector $\hat{\rho}_{\mathrm{source}}$, $\hat{\rho}_{\mathrm{I}|\times}$ and $\hat{\rho}_{\mathrm{I}|\checkmark}$ are the same as defined earlier, due to the idler detector still being affected by thermal noise. However, the states incident upon the signal detector are different. The unconditioned state

incident on the signal detector is similar to Eq. 3.30c, albeit with the noise and source swapped

$$\hat{\rho}_{\mathrm{S}} = \frac{1}{\pi\bar{n}} \int d^2\alpha e^{\frac{-|\alpha|^2}{\bar{n}}} |r\alpha + t\beta\rangle\langle r\alpha + t\beta|, \tag{3.56}$$

where $|\alpha|^2 = \bar{n}$ and $|\beta|^2 = \frac{\bar{n}_{\mathrm{B,S}}}{|t|^2}$. This means that the unconditioned click probability is

$$\mathrm{Pr}_{\mathrm{S}} = 1 - \frac{e^{\frac{-\bar{n}_{\mathrm{B,S}}}{1+\xi\eta_{\mathrm{S}}\bar{n}}}}{1 + \xi\eta_{\mathrm{S}}\bar{n}} \tag{3.57}$$

The idler no-click conditioned state incident upon the signal detector

$$\hat{\rho}_{\mathrm{S|I,0}} = \frac{1}{\pi\bar{n}_{\times}} \int d^2\gamma e^{\frac{-|\gamma|^2}{\bar{n}_{\times}}} |r\gamma + t\beta\rangle\langle r\gamma + t\beta|, \tag{3.58}$$

where $|\gamma|^2 = \bar{n}_{\times}$. Hence, we express the non-coincidence click probability

$$\mathrm{Pr}_{\mathrm{S|I,0}} = 1 - \frac{e^{\frac{-|t|^2|\beta|^2}{1+|r|^2\bar{n}_{\times}}}}{1 + |r|^2\bar{n}_{\times}}, \tag{3.59a}$$

$$= 1 - \frac{e^{\frac{-\bar{n}_{\mathrm{B,S}}}{1+\xi\eta_{\mathrm{S}}\bar{n}_{\times}}}}{1 + \xi\eta_{\mathrm{S}}\bar{n}_{\times}}. \tag{3.59b}$$

Following from this, the idler click conditioned state incident upon the signal detector

$$\begin{aligned}\hat{\rho}_{\mathrm{S|I,1}} = \frac{1}{\mathrm{Pr}_{\mathrm{I}}}\Bigg(&\frac{1}{\pi\bar{n}} \int d^2\alpha e^{\frac{-|\alpha|^2}{\bar{n}}} |r\alpha + t\beta\rangle\langle r\alpha + t\beta| - \\ &- (1 - \mathrm{Pr}_{\mathrm{I}})\frac{1}{\pi\bar{n}_{\times}} \int d^2\gamma e^{\frac{-|\gamma|^2}{\bar{n}_{\times}}} |r\gamma + t\beta\rangle\langle r\gamma + t\beta|\Bigg),\end{aligned} \tag{3.60}$$

which yields the coincidence click probability

$$\mathrm{Pr}_{\mathrm{S|I,1}} = 1 - \frac{1}{\mathrm{Pr}_{\mathrm{I}}}\Big((1 - \mathrm{Pr}_{\mathrm{S}}) - (1 - \mathrm{Pr}_{\mathrm{I}})(1 - \mathrm{Pr}_{\mathrm{S|I,0}})\Big), \tag{3.61a}$$

$$= 1 - \frac{1}{\mathrm{Pr}_{\mathrm{I}}}\left(\frac{e^{\frac{-\bar{n}_{\mathrm{B,S}}}{1+\xi\eta_{\mathrm{S}}\bar{n}}}}{1 + \xi\eta_{\mathrm{S}}\bar{n}} - (1 - \mathrm{Pr}_{\mathrm{I}})\frac{e^{\frac{-\bar{n}_{\mathrm{B,S}}}{1+\xi\eta_{\mathrm{S}}\bar{n}_{\times}}}}{1 + \xi\eta_{\mathrm{S}}\bar{n}_{\times}}\right). \tag{3.61b}$$

The object absent click probability for both CI and QI with Poissonian noise is

$$\mathrm{Pr}_{\mathrm{H0}} = 1 - e^{-\bar{n}_{\mathrm{B,S}}}. \tag{3.62}$$

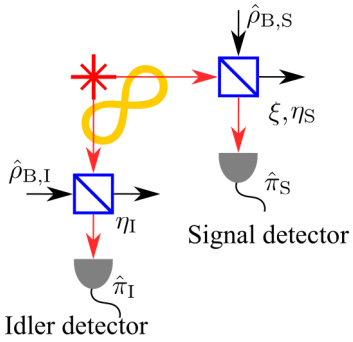

Figure 3.3 – Beamsplitter model for QI. Shows the twin-beam state directed towards both the idler and signal detector beamsplitters where the relevant noise state is mixed and the source is attenuated by the respective factor.

3.4 Photon-number distributions and heralding gain

If we assess the heralding gain for our QI system we are able to quantify explicitly the advantage of the idler detector measurement. We define the heralding gain (HG) as

$$\mathrm{HG} = \frac{\mathrm{Tr}(\hat{\rho}_{\mathrm{S|I},1}\hat{n})}{\mathrm{Tr}(\hat{\rho}_{\mathrm{S}}\hat{n})}. \tag{3.63}$$

The HG is the ratio of the expectation value of the photon number for the idler click conditioned signal state and the unconditioned signal state. For an idealised scenario with perfect efficiency, no loss, or no noise the HG is

$$\mathrm{HG} = 1 + \frac{1}{\bar{n}}. \tag{3.64}$$

Equation 3.64 tends to infinity as the mean photon number tends $\bar{n} \to 0$, therefore this shows that the advantage of idler click conditioning improves as the mean photon number $\bar{n}$ reduces. Of course, this improvement comes at the cost of reduction of the probability of an idler click. For realistic scenarios with non-unity detection efficiency, noise and loss the HG is instead

$$\mathrm{HG} = \frac{\mathrm{Pr}_{\mathrm{I}}^{-1}\Big(\bar{n}\xi\eta_{\mathrm{S}} + \bar{n}_{\mathrm{B,S}} - (1-\mathrm{Pr}_{\mathrm{I}})(\bar{n}_{\times}\xi\eta_{\mathrm{S}} + \bar{n}_{\mathrm{B,S}})\Big)}{\bar{n}\xi\eta_{\mathrm{S}} + \bar{n}_{\mathrm{B,S}}}. \tag{3.65}$$

However, as the HG is based off the photon number expectation values it does not capture the statistical differences from different types of noise (thermal or Poisson), therefore the photon-number distributions are more instructive of the effect of idler click/no-click conditioning than the HG

The photon-number distribution means we can visually demonstrate the advantage of the

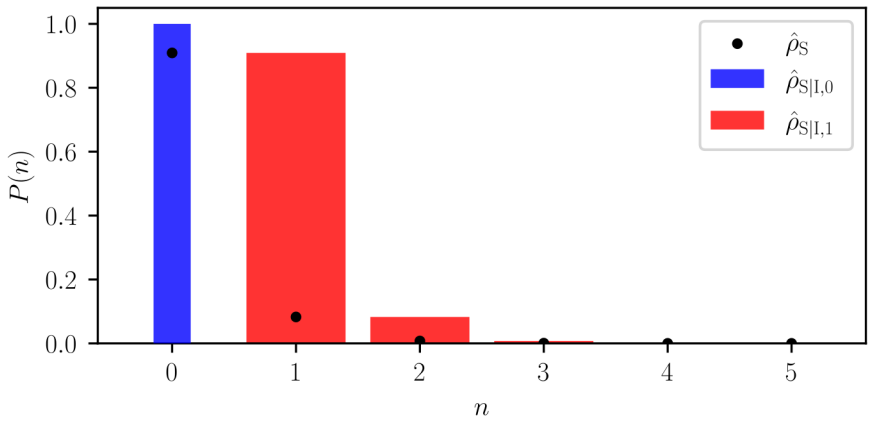

FIGURE 3.4 – Photon number distributions in the scenario of no noise or loss and perfect detection. The y-axis has the photon-number probability $P(n)$ and the x-axis has the photon-number n. Plotted is the unconditioned state (black dots), idler click conditioned state (red bars) and idler no-click conditioned state (thin blue bars). Mean photon number of the signal state $\bar{n} = 0.1$.

idler detector measurement. Moreover, comparison of the photon-number distribution statistics for the unconditioned state and the idler click conditioned state gives an alternative approach for quantifying the idler detector measurement advantage. Of course, this quantified advantage does not translate to the advantage we have for our QI system in practice, due to the lack of photon-number resolving detectors, which can not use the full difference of photon-number distributions. In practice, we can only discriminate between the quantum states via the relevant click probabilities. The photon-number distribution for any state $\hat{\rho}$ is found by the equation

$$P(n) = \mathrm{Tr}\Big(\hat{\rho}|n\rangle\langle n|\Big). \tag{3.66}$$

For an idealised scenario with perfect efficiency, no loss, or no noise the photon-number distribution for the unconditioned $\hat{\rho}_S$, idler no-click conditioned $\hat{\rho}_{S|I,0}$ and idler click conditioned $\hat{\rho}_{S|I,1}$ states is shown in Fig. 3.4. We can see from Fig. 3.4 that an idler no-click results in the conditioned signal state to be the vacuum state. Whereas, an idler click conditions the signal state to have its vacuum component completely suppressed. This complete suppression of the vacuum component guarantees the presence of a photon, in other words it heralds a photon. In a more realistic quantum LIDAR scenario, however, noise, system loss and high signal attenuation cause the conditioned signal photon number distributions to become much less clear-cut in their difference. Figure 3.5 (with thermal noise) and Fig. 3.6 (with Poisson noise) illustrates this. For the parameters shown the unconditioned, no-click conditioned and

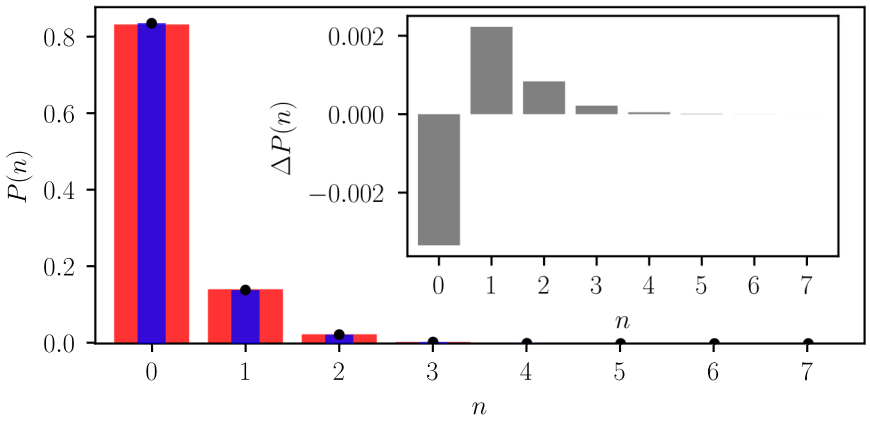

Figure 3.5 – Photon number distributions for a realistic system with thermal noise. The y-axis has the photon-number probability $P(n)$ and the x-axis has the photon-number n. Plotted is the unconditioned state (black dots), idler click conditioned state (red bars) and idler no-click conditioned state (thin blue bars). An inset is plotted with the photon-number distribution difference $\Delta P(n)$ on the y-axis and photon-number n on the x-axis. Mean photon number of the signal state $\bar{n} = 0.1$, signal attenuation factor $\xi = 8.84 \times 10^{-3}$, idler channel system loss $\eta_{\mathrm{I}} = 0.5$, signal channel system loss $\eta_{\mathrm{S}} = 0.5$, idler detector background noise mean photon number $\bar{n}_{\mathrm{B,I}} = 4.49 \times 10^{-4}$ and signal detector background noise mean photon number $\bar{n}_{\mathrm{B,S}} = 0.2$.

click-conditioned signal photon number distributions are hardly different. We can see the size of the conditioning effect if we take the difference in the two conditioned probability distributions, $\Delta P(n) = P(n)_{\mathrm{I},1} - P(n)_{\mathrm{I},0}$ which is plotted as an inset, where $P(n)_{\mathrm{I},1}$ and $P(n)_{\mathrm{I},1}$ is the idler click and idler no-click conditioned photon number distribution, respectively. Appendix B explicitly defines the photon number distributions for a realistic system with either thermal or Poissonian noise. This difference shows the small residual conditioning effect. It seems clear that conditioning in a realistic system with multiple shots of the experiment will only cause a tiny change in the number of counts at the signal detector when the idler fires. Hence a well-developed statistical framework is required to extract the information, which is what the remainder of this chapter presents. It should also be noted that the parameters used in both Fig. 3.5 and Fig. 3.6 understate the difficulty when using realistic parameters encountered experimentally. There is not a large difference of the photon-number distribution for Fig. 3.5 and Fig. 3.6 due to the relatively low level of signal detector background noise.

3.5 Quantum state discrimination

The use of click detectors means that inference of the presence or absence of an object depends upon comparison of the respective click probabilities. This is equivalent to discrimination between the two possible states incident on the detector. The theory illustrated below provides

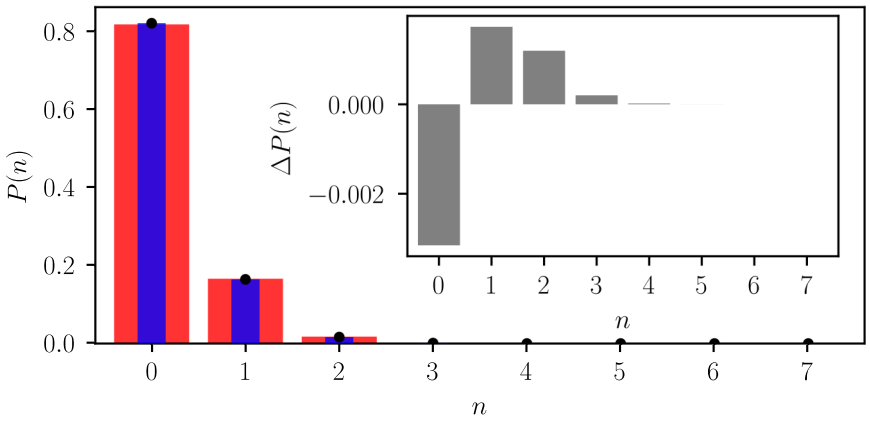

FIGURE 3.6 – Photon number distributions for a realistic system with Poissonian noise. The y-axis has the photon-number probability $P(n)$ and the x-axis has the photon-number n. Plotted is the unconditioned state (black dots), idler click conditioned state (red bars) and idler no-click conditioned state (thin blue bars). An inset is plotted with the photon-number distribution difference $\Delta P(n)$ on the y-axis and photon-number n on the x-axis. Mean photon number of the signal state $\bar{n} = 0.1$, signal attenuation factor $\xi = 8.84 \times 10^{-3}$, idler channel system loss $\eta_{\mathrm{I}} = 0.5$, signal channel system loss $\eta_{\mathrm{S}} = 0.5$, idler detector background noise mean photon number $\bar{n}_{\mathrm{B,I}} = 4.49 \times 10^{-4}$ and signal detector background noise mean photon number $\bar{n}_{\mathrm{B,S}} = 0.2$.

the optimal method for state discrimination; it is worthwhile to find out how state discrimination with click probabilities fares against the optimal strategy. The generic state incident upon the detector when an object is absent $\hat{\rho}_0$ and when an object is present $\hat{\rho}_1$. As both $\hat{\rho}_0$ and $\hat{\rho}_1$ are non-orthogonal $\langle\hat{\rho}_0|\hat{\rho}_1\rangle \neq 0$ there will be errors $\mathrm{P_{err}}$ in the discrimination between the two states. We define the error probability as

$$\mathrm{P_{err}} = p_0 \mathrm{Tr}(\hat{\rho}_0 \hat{\pi}_1) + p_1 \mathrm{Tr}(\hat{\rho}_1 \hat{\pi}_0), \tag{3.67}$$

for POVM elements $\hat{\pi}_{\{1,0\}}$ and a priori probabilities $p_{\{1,0\}}$ corresponding to its respective state $\hat{\rho}_{\{1,0\}}$.

The Helstrom bound provides the minimum error possible $P_{\mathrm{err}}^{\mathrm{min}}$ for state discrimination, or in other words the optimal discrimination. This bound does not reveal what experimental measurement scheme yields the optimal discrimination, therefore the POVM element required to physically realise this measurement is often either unknown or difficult to implement with current technology [25]. We focus on the situation of discrimination between two states and knowing that $\hat{\pi}_0 = \hat{1} - \hat{\pi}_1$ and $p_0 + p_1 = 1$. A POVM element that minimises the probability of error $\mathrm{P_{err}}$ will express the optimal measurement. Minimisation occurs when the POVM element $\hat{\pi}_1$ is a projector onto the negative-eigenvalue eigenstates of $(p_0\hat{\rho}_0 - p_1\hat{\rho}_1)$ as is apparent when

$\mathrm{P_{err}}$ is expressed as [53]

$$\mathrm{P_{err}} = p_0 + \mathrm{Tr}\big((p_0\hat{\rho}_0 - p_1\hat{\rho}_1)\hat{\pi}_1\big) \tag{3.68}$$

Therefore, the Helstrom bound (when there are only two states) is [142]

$$P_{\mathrm{err}}^{\mathrm{min}} = \frac{1}{2}\big(1 - ||p_0\hat{\rho}_0 - p_1\hat{\rho}_1||\big), \tag{3.69}$$

where $||\hat{A}|| = \mathrm{Tr}(\sqrt{\hat{A}^\dagger\hat{A}})$ is the trace norm for a matrix $\hat{A}$. Figure 3.7 compares the equal priors ($p_0 = p_1 = \frac{1}{2}$) Helstrom bound and the click error probability: which is probability that the detector clicks when an object is absent and that the detector does not click when an object is absent. We define this click error probability as

$$\mathrm{P_{err}^{click}} = \frac{1}{2}\mathrm{Tr}(\hat{\rho}_{\mathrm{H0}}\hat{\pi}_{\mathrm{S}}) + \frac{1}{2}\mathrm{Tr}(\hat{\rho}_{\mathrm{S|I},1}(\hat{1} - \hat{\pi}_{\mathrm{S}})). \tag{3.70}$$

The click probability of error $\mathrm{P_{err}^{click}}$ is the click POVM element applied to the object absent state and the no-click POVM element applied to the object present state, for the scenario with thermal noise. Figure 3.7 shows for a range of mean photon numbers for a light source of mean photon number $\bar{n}$ and signal detector background $\bar{n}_{\mathrm{B,S}}$ with the colour bar representing $P_{\mathrm{err}}^{\mathrm{min}} - \mathrm{P_{err}^{click}}$. Negative values show the lack of saturation and a zero value means saturation of the Helstrom bound. Fig 3.7 it is clear that the Helstrom bound is saturated when either $\bar{n} \to 0$ or $\bar{n}_{\mathrm{B,S}} \to 0$. As when $\bar{n} \to 0$ the object present and absent state are equal and hence the discrimination is impossible for both Helstrom bound and the click measurement approach. Similarly, when $\bar{n}_{\mathrm{B,S}} \to 0$ and $\bar{n} \neq 0$, discrimination between object present and absent is trivially easy, which means the click measurement approach saturates the Helstrom bound. Lastly, the Helstrom bound shows that, even in regimes with parameters which understate the difficulty of typical LIDAR detection regimes, it is impossible to discriminate accurately between object present or absent in just a single-shot. The Helstrom bound in such regimes is approximately $\mathrm{P_{err}^{min}} \approx \frac{1}{2}$.

State discrimination also applies to many copies of the two quantum states [143], [144]. Important notation to support this is as follows. Suppose we have an arbitrary state ρ which has m identical copies, the ensemble of these copies $\rho^{\otimes m}$ is the tensor product of the state with itself m times. Here, m identical copies corresponds to m trials of measurement. The discrimination between the object and no object present hypotheses in this situation now relates to m copies of both ρ_0 and ρ_1. A LIDAR system with click detectors requires multiple trials of measurement; consequently, it is of interest to calculate the minimum error in such a situation. The m-trials

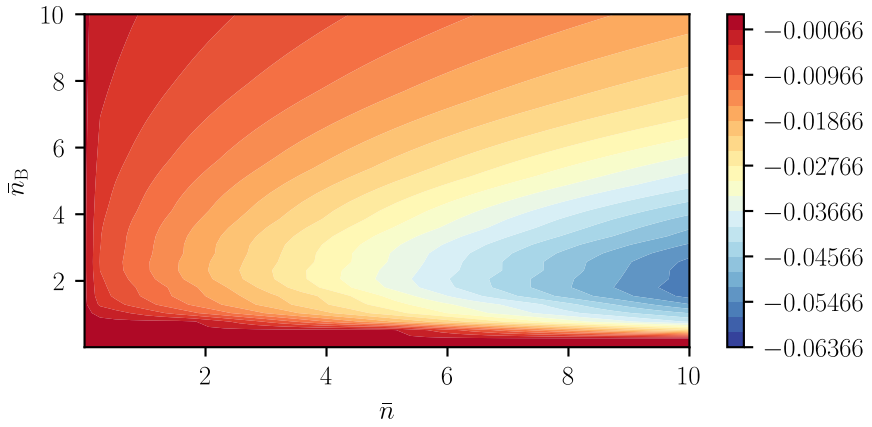

FIGURE 3.7 – Contour plot comparing the single-shot Helstrom bound $P_{\text{err}}^{\text{min}}$ and the click error probability $\text{P}_{\text{err}}^{\text{click}}$ for a range of mean photon number of signal $\bar{n}$ and signal detector background noise mean photon number $\bar{n}_{\text{B,S}}$ values. The colour bar represents $P_{\text{err}}^{\text{min}} - \text{P}_{\text{err}}^{\text{click}}$. The idler detector background noise mean photon number $\bar{n}_{\text{B,I}} = 0.01$, system loss of detectors $\eta_{\text{S/I}} = 0.5$ and signal attenuation factor $\xi = 0.5$.

Helstrom bound between two states is

$$P_{\text{err,m}}^{\text{min}} = \frac{1}{2}\left(1 - \|p_1\hat{\rho}_1^{\otimes m} - p_0\hat{\rho}_0^{\otimes m}\|\right). \tag{3.71}$$

After many trials, calculation of Eq. 3.71 is intractable. This is because the Hilbert space of Eq. 3.71 increases exponentially proportional to the number of trials. Moreover, in any case, the required measurements may be joint measurements of all trials, which is impractical. Therefore it is unknowable if a particular POVM element saturates the m-trials Helstrom bound. Fortunately, a calculable upper bound exists for the minimal error of discrimination. The calculable upper bound is known as the quantum Chernoff bound [145]. Following this, the upper bound of the minimum error is,

$$P_{\text{err,m}}^{\text{min}} \leq \frac{1}{2}e^{-m\xi_{\text{QCB}}}, \tag{3.72}$$

where $\xi_{\text{QCB}} = -\ln\left(\min_{0\leq s\leq 1} \text{Tr}\left(\hat{\rho}_0^s\hat{\rho}_1^{(1-s)}\right)\right)$. The Bhattacharyya bound is weaker than the quantum Chernoff bound [22] and is only a reasonable bound when there is a lot of background noise; however, it is easier to calculate,

$$P_{\text{err,m}}^{\text{min}} \leq \frac{1}{2}e^{-m\xi_{\text{BB}}}, \tag{3.73}$$

where $\xi_{\text{BB}} = -\ln\left(\text{Tr}\left(\hat{\rho}_0^{0.5}\hat{\rho}_1^{0.5}\right)\right)$. For both the quantum Chernoff and Bhattacharyya bounds it is shown that as m increases the minimum error upper bound exponentially decreases. The knowledge that state discrimination improves with the number of measurement trials is important

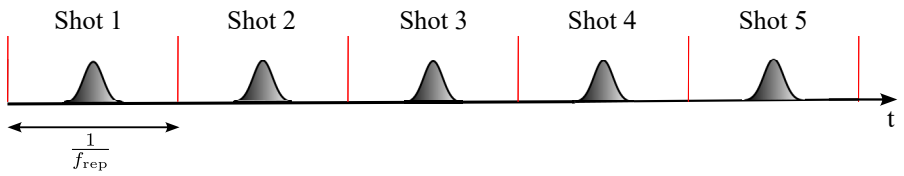

FIGURE 3.8 – A pulse train mapped onto (successive measurements) shots with time on the x-axis, for a pulsed source. Each shot has a temporal duration $\frac{1}{f_{\text{rep}}}$.

and chimes with what we expect. This tells us that accurate discrimination between object present and absent states with the use of click detectors (even with their sub-optimal POVM elements) is possible, after a sufficient number of measurements.

3.6 PROPERTIES OF A SINGLE MEASUREMENT

The LIDAR system is dependent upon a succession of measurements. Therefore, the make-up of a single measurement, or in other words a shot, is a topic that first needs properly covered. Our model assumes a perfect one-to-one mapping of pulses to shots (with a source repetition rate set by f_{rep}) as shown in Fig. 3.8. This mapping is perfectly fine in the low detector timing jitter regime and where count rates are slow enough that detector dead times are negligible. It is easy to set the temporal duration of a shot for a pulsed source according to the reciprocal of the source repetition rate. CW systems require an artificial determiner for the duration of a shot. For CW a possible determiner is the coincidence window duration τ_c. Furthermore, the second order coherence function $g^2(\tau)$ can instruct what temporal duration for a shot is sensible, for both CW and pulsed.

Within the duration of one shot multiple modes could exist, due to the spontaneous and stimulated aspects of our light source and background. In lieu of this, it suffices to model each shot to only have one mode of the source. This assumption is valid due to the click/no-click nature of the detectors and the low mean photon numbers considered. The theory is simplified with the aforementioned assumption, as the click probabilities are calculated with only one mode in each channel. Moreover, it is clear that the mean photon numbers for the source and background are dependent on the temporal window size of a shot. Henceforth this thesis focuses on a pulsed pump source, noting that we consider idler-detector-gated CW for the experimental results in Ch. 8 and that a pulse-source does not have the aspect of covertness that CW has, as discussed in Ch. 6.8.

3.7 Click-count distributions

Inference of the presence or absence of an object is facilitated by comparison of the single-shot click probabilities for either hypothesis [146]. However, as previously shown a single-shot measurement with simple click detectors can not effectively distinguish between the two hypotheses of object present and absent. This is because when background noise is present a click in a single-shot system can either originate from the reflected signal beam or from background noise, which for high noise and weak signal regimes the object present and absent click probabilities are near-equal. Therefore, multi-shot hypothesis testing is performed [31], [147]–[149]. Achieving accurate state discrimination with multi-shot hypothesis testing line is in line with the knowledge from the Chernoff bound that state discrimination improves with the number of measurements. The click-count distribution differs from the photon-number distributions introduced in Ch. 2 as the click-count distribution does not reveal the innate photon statistics that a particular state of light has, unlike the photon-number distribution. Click-count distributions are Poissonian, but in the scenario of a large number of shots and a low click probability it is well-approximated by the Binomial distribution. The use of the Binomial distribution means that each shot of the experiment at each detector corresponds to a Bernoulli trial. A click or no-click event occurs according to a click probability p_{generic} and generates a corresponding Binomial click-count distribution P_{generic} [150]

$$P_{\text{generic}}(x) = \binom{N}{x} p_{\text{generic}}^{x} (1 - p_{\text{generic}})^{N-x}, \tag{3.74}$$

for a click-count x and number of shots N. Furthermore, in the limit of many shots the Gaussian distribution approximates the Binomial click distribution, assuming satisfaction of the criterion detailed in Appendix C. This approximation is used henceforth as it greatly simplifies the analytical and computational demands.

For CI the click-count is the number of signal detector clicks and the number of shots N is the ratio of the integration time T and the shot temporal window size τ_{c}

$$N = \lfloor T/\tau_{\text{c}} \rfloor , \tag{3.75}$$

where $\lfloor x \rfloor$ is the floor function, which rounds to the greatest integer less or equal to x. Figure 3.9 shows the CI click-count probability distribution for both object present $P_{\text{CI:H1}}$ and absent $P_{\text{CI:H0}}$, in the scenario with thermal noise.

For QI, if the click-count in question are coincident clicks, the number of shots is the number

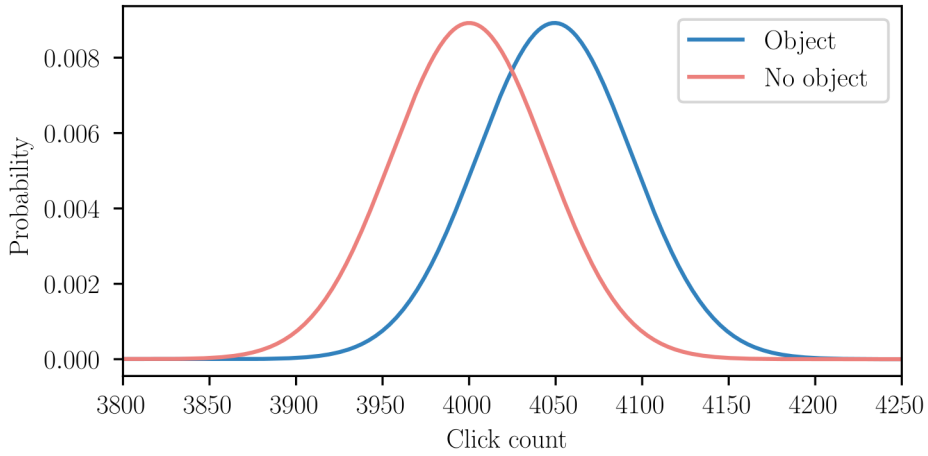

Figure 3.9 – CI probability distribution displaying click-counts for both object present (coloured blue) and absent (coloured red) hypotheses. Mean photon number of the signal state $\bar{n} = 0.1$, system loss of signal detector $\eta_{\mathrm{S}} = 0.5$, signal attenuation factor $\xi = 0.5$ and mean photon number of background and dark counts for signal detector $\bar{n}_{\mathrm{B,S}} = 1$. The number of shots is 8×10^3.

of idler clicks k. If the click-count in question are non-coincidence clicks, the number of shots is $N - k$ (total number of shots subtracted by number of idler clicks). Each set of system parameters gives rise to an idler click distribution P_{I} and each (number of idler clicks) value k in P_{I} has a corresponding object present $P_{\mathrm{H1:k}}$ and absent $P_{\mathrm{H0:k}}$ signal coincidence click distribution. Figure 3.10 shows the coincidence and non-coincidence click distributions for both object present and absent hypotheses, after a set number of idler click events $k = 1.98 \times 10^4$ and in the thermal noise scenario. Equation 4.14 quantifies the advantage of the inclusion of non-coincidence clicks and also discusses system parameter regimes where non-coincidence clicks are particularly useful.

Existing literature often overlooks non-coincidence signal clicks events as a source of useful information. In addition, the rangefinding protocol discussed later in this thesis requires the recording of all types of click. It is clear that bulk of the useful information for inference is from the number of coincidence clicks; however, there is a small amount of useful information gained from considering the non-coincidence clicks. The benefit of non-coincidence events stems from a sub-optimal idler system loss $\eta_{\mathrm{I}} < 1$, therefore would-be coincidence clicks are sometimes missed when the idler detector does not fire.

3.8 Log-likelihood value

A click-count value might infer the presence of an object in one parameter regime or the absence of an object in another. A framework that facilitates fair comparison of incoming click data

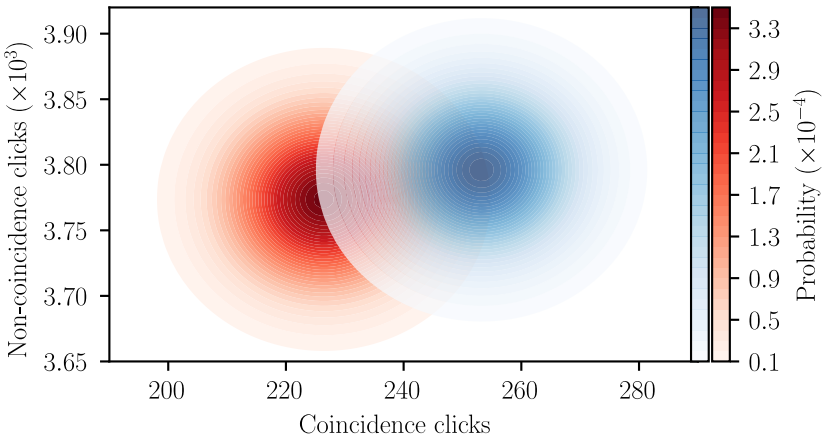

FIGURE 3.10 – QI probability distribution displaying coincidence click-counts and non-coincidence click-counts for both object present (coloured blue) and absent (coloured red) hypotheses. Mean photon number of the signal state $\bar{n} = 0.1$, system loss of all detectors $\eta_{\mathrm{S/I}} = 0.5$, signal attenuation factor $\xi = 0.5$, mean photon number of background and dark counts for signal detector $\bar{n}_{\mathrm{B,S}} = 1$ and mean photon number of background and dark counts for idler detector $\bar{n}_{\mathrm{B,I}} = 0.01$. The number of shots is 8×10^3 and the number of idler click events displayed is 452.

between different situations is desired. The log-likelihood value (LLV) forms the basis of this framework. The LLV is also appropriate for use in dealing with multi-channel detector data, as it reduces multiple channels of data pertaining to two simple hypotheses into a single value. This value also provides a simple test, in this context commonly known as the likelihood ratio test. The use of the LLV for hypothesis testing is justified by the Neyman-Pearson lemma, which states that it provides the most powerful test for a set statistical significance level [151].

For CI the object present $P_{\mathrm{CI:H1}}$ and absent $P_{\mathrm{CI:H0}}$ click distributions in their Binomial form after N shots defines the LLV which converts click data x into an LLV

$$\Lambda(x, N) = \ln\left(\frac{P_{\mathrm{CI:H1}}(x, N)}{P_{\mathrm{CI:H0}}(x, N)}\right). \tag{3.76}$$

It is clear from Eq. 3.76 that $\Lambda(x, N) > 0$ means that presence of an object is more likely as for a given number of clicks x the object present probability is higher than the object absent probability. It is also clear that $\Lambda(x, N) = 0$ means that both regimes are equally as likely and $\Lambda(x, N) < 0$ infers that absence of an object is more likely. An advantage of using the LLV as a test is that it is self-calibrating. This self-calibration occurs when the LLV detection threshold $d_{\mathrm{LLV}} = 0$, as the detection decision is automatically set according to the equal likelihood of the presence and absence of an object. We will consider later the effect of setting LLV decision levels on false alarm probabilities and their extension to receiver operator curves.

For QI the object present $P_{\mathrm{H1:k}}$ and absent $P_{\mathrm{H0:k}}$ click distributions in their Binomial form after N shots and k idler click events define the LLV conditioned by k idler clicks which converts click data $\underline{x}$ into an LLV

$$\Lambda(\underline{x}, k) = \ln\left(\frac{P_{\mathrm{H1}}(\underline{x}, k)}{P_{\mathrm{H0}}(\underline{x}, k)}\right), \tag{3.77}$$

where $\underline{x} = (x, y)$ with x the coincidence click-count and y the non-coincidence click-count. The LLV for QI functions as a test in an identical way to the CI protocol.

As the click probabilities, click data and number of shots are all real and positive Eq. 3.76 and Eq. 3.77 are recast as linear equations. The CI LLV in linear form is

$$\Lambda(x, N) = Mx + NC. \tag{3.78}$$

Appendix D defines the constants M and C. The QI LLV in linear form is

$$\Lambda(\underline{x}, k) = (M_1 x + kC_1) + (M_2 y + (N - k)C_2). \tag{3.79}$$

Appendix D also defines constants $M_1,\ M_2,\ C_1,$ and C_2. From Eq. 3.79 it is easy to disregard non-coincidence clicks in the LLV analysis by excluding the right-hand term.

3.9 Log-likelihood distributions

In the following analysis we focus on the statistical moments of the QI LLV distributions after a mean number of idler clicks $k = \mu_{\mathrm{I}} = N\mathrm{Pr}_{\mathrm{I}}$. Figure 3.11 shows the object present $P_{\mathrm{H1:\Lambda(x,\mu_I)}}$ and absent $P_{\mathrm{H0:\Lambda(x,\mu_I)}}$ LLV distributions for idler clicks $k = \mu_{\mathrm{I}}$. If the click distributions are well approximated by a Gaussian, all of the LLV distributions are Gaussian too, as linear transformations and combinations preserve normality [152]. The results below show the object present hypothesis, but the analysis is similar for object absent. The mean and standard deviation for the object present LLV distribution conditioned by mean idler clicks μ_{I} is derived in Appendix E. The mean is

$$\mu_{H1:\Lambda(x,\mu_{\mathrm{I}})} = N\big(\mathrm{Pr}_{\mathrm{I}}(M_1\mathrm{Pr}_{\mathrm{S|I,1}} + C_1 - M_2\mathrm{Pr}_{\mathrm{S|I,0}} - C_2) + M_2\mathrm{Pr}_{\mathrm{S|I,0}} + C_2\big), \tag{3.80}$$

and the standard deviation is

$$\sigma_{H1:\Lambda(x,\mu_{\mathrm{I}})} = \big(N(\mathrm{Pr}_{\mathrm{I}}(M_1^2\mathrm{Pr}_{\mathrm{S|I,1}}(1 - \mathrm{Pr}_{\mathrm{S|I,1}}) - \\ - M_2^2\mathrm{Pr}_{\mathrm{S|I,0}}(1 - \mathrm{Pr}_{\mathrm{S|I,0}})) + M_2^2\mathrm{Pr}_{\mathrm{S|I,0}}(1 - \mathrm{Pr}_{\mathrm{S|I,0}})\big)^{\frac{1}{2}}.$$

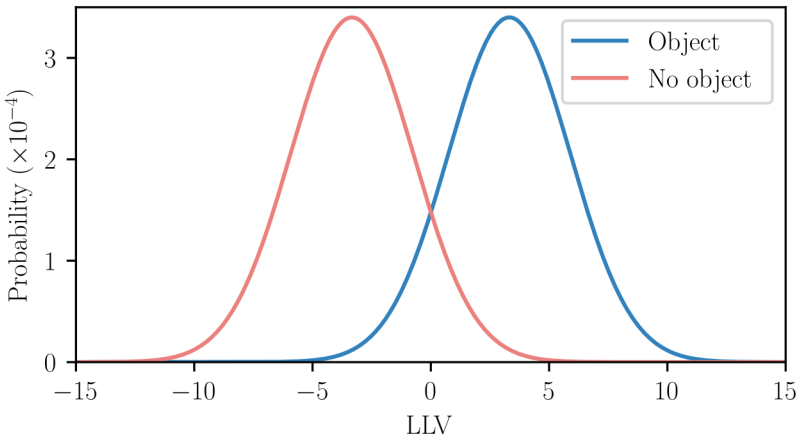

FIGURE 3.11 – QI LLV probability distribution for both object present (coloured blue) and absent (coloured red) hypotheses. $\bar{n} = 0.1$, $\eta_{\mathrm{S/I}} = 0.5$, $\xi = 0.5$, $\bar{n}_{\mathrm{B,S}} = 1$, $\bar{n}_{\mathrm{B,I}} = 0.01$. The number of shots is 8×10^3 and the number of idler click events displayed is 452.

When the detection threshold $d_{\mathrm{LLV}} = 0$ we calculate the probability of error by integrating over the partition of the LLV distributions that reside in their false decision LLV region. The LLV probability of error is

$$\mathrm{P}_{\mathrm{err}}^{\mathrm{LLV}} = \frac{1}{2}\left(\int_{z=0}^{\infty} P_{\mathrm{H0:\Lambda(x,\mu_I)}}(z) + \int_{z=-\infty}^{0} P_{\mathrm{H1:\Lambda(x,\mu_I)}}(z)\right), \tag{3.81}$$

where z is an LLV. Figure 3.12 is a schematic which shows the two types of error which comprises the LLV probability of error defined in Eq. 3.81, the probability of false alarm is the area of the object absent LLV distribution which has values that are greater than the detection threshold d_{LLV}. Whereas, the probability of false negative is the area of the object present LLV distribution which has values that are less than the detection threshold d_{LLV}. Figure 3.13 shows the comparison of P_{err} for the LLV framework and the quantum Chernoff bound as a function of the number of shots, for QI and CI. In Fig. 3.13 we calculate the quantum Chernoff bound for QI using the number of trials $\lfloor \mathrm{Pr_I} \times m \rfloor$, this approach means we can compare the quantum Chernoff bound for QI and CI fairly, as CI has m trials. The approach for calculating the quantum Chernoff bound is similar if we wish to include non-coincidence clicks. In Fig. 3.13 we use a Monte-Carlo simulation as described in Ch. 7 to generate the LLV probability of error for the number of shots that do not satisfy the Gaussian approximation criteria defined in Appendix C. For the parameter regime in Fig. 3.13 the click probability of error $\mathrm{P}_{\mathrm{err}}^{\mathrm{click}}$ defined in Eq. 3.70 does not saturate the Helstrom bound, for QI. This means that the LLV framework also does not saturate the Helstrom bound. However, the CI and QI LLV framework for most

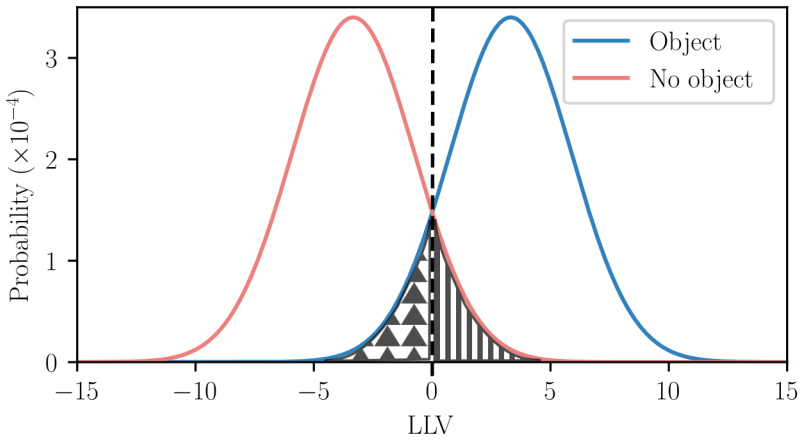

FIGURE 3.12 – Schematic depicting the two types of error which comprises the LLV probability of error defined in Eq. 3.81. The shaded regions depict these two types of error in a QI LLV probability distribution for both object present (coloured blue) and absent (coloured red) hypotheses. The shaded region of triangles represents the probability of false negative and shaded region of horizontal bars represent the probability of false alarm.

number of trials m lies below the quantum Chernoff bound.

The lack of explicit calculation of an optimal performance bound for our multi-shot system can be solved by first acknowledging that our system belongs to a generalised class of sensing problems: quantum sensing in ancilla-assisted phase-covariant optical channels [52]. The results from Nair and Gu in Ref. [52] has provided probe and measurement-independent ultimate performance bounds (expressed in the quantum fisher information) for this class of sensing problems, subject to energy and mode-number constraints [153]. These performance bounds differ from the Helstrom bound discussed earlier as it makes no assumption about the probe state used. In particular, for phase-covariant Gaussian channels, N independent and identically distributed TMSV probes tends towards being the optimal probe as the mean photon number $\bar{n} \to 0$. For QI we do not discriminate using the TMSV, as we instead discriminate using the idler-click (no-click) conditioned states which do not tend towards the optimal probe. The optimality of CI is also discussed in Ref. [52]. Furthermore, while not optimal, our CI system can be enhanced by the use of threshold detection with photon-number-resolving detectors as explored in Cohen et al. in Ref. [96]. However, this enhancement is negligible for the parameter regimes we are concerned with: weak signal strength $\bar{n} << 1$ and a low SNR $\bar{n} < \bar{n}_{\mathrm{B,S}}$. Later in this thesis, we revisit analysis with the LLV distributions in the context of detection confidence by defining a figure of merit (F.O.M) based off the LLV framework.

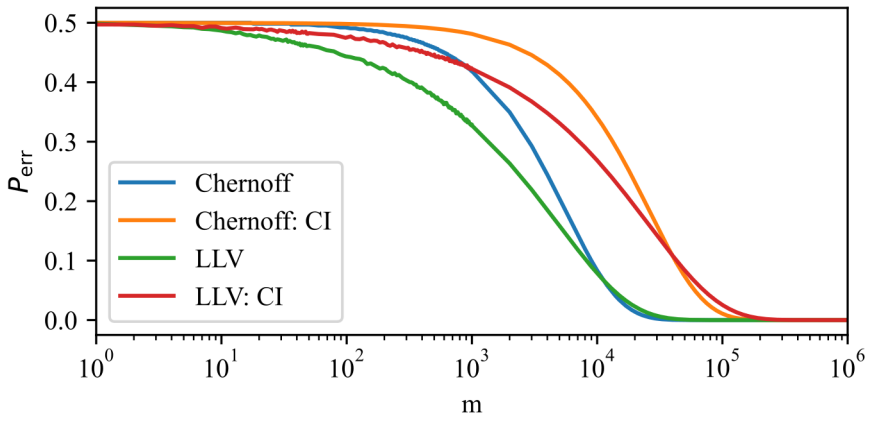

Figure 3.13 – Comparison of the quantum Chernoff bound and the probability of error of the LLV framework, for QI with signal channel thermal noise and excluding non-coincidence clicks. The CI LLV probability of error and quantum Chernoff bound is also plotted. Probability of error P_{err} on the y-axis and shots m on the x-axis. The object present and absent states are being discriminated between. Mean photon number of the signal state $\bar{n} = 0.1$, system loss of all detectors $\eta_{S/I} = 0.5$, signal attenuation factor $\xi = 0.5$, mean photon number of background and dark counts for signal detector $\bar{n}_{B,S} = 1$ and mean photon number of background and dark counts for idler detector $\bar{n}_{B,I} = 0.01$.

3.10 Deleterious effects

In reality our system is susceptible to deleterious effects such as timing jitter, sensor dead-time and after-pulsing. These effects serve to disrupt the idealistic system presented thus far. This section briefly describes each deleterious effect and the reasoning behind its exclusion from our model.

Timing jitter results from the uncertainty of the timing of a detection event. There are multiple possible sources of this uncertainty; for example, electronic timing jitter from the processing of incoming click data. Another example is timing jitter intrinsic to the detector, as photons may penetrate the detector at different depths and hence different times to initiate the registration of a photo-count. Timing jitter limits the accuracy of time correlation between idler and signal channels, undermining the maximum potency of coincidence counting. Additionally, timing jitter creates uncertainty of the return of the signal beam, which limits the accuracy of rangefinding. Our model neglects timing jitter as typical values are much smaller than the timing correlation and depth resolution aimed for in our system. The timing resolution aimed for in our system ensures the effect of timing jitter is negligible.

After registering a detection event, a detector is not immediately sensitive to another detection event: it takes time to return to single-photon sensitivity [154]. Sensor dead-time is the name

for this time required. The process of recharging a SPAD is known as quenching; this stops the avalanche process after a detection event and recharges the reverse bias voltage. Sensor dead-time means that some detection events are missed, thereby obscuring the true photo-count statistics. Detector saturation occurs when sensor dead-time is prevalent, causing a large error in our registering of the amount of incident light. Our model also neglects sensor dead-time due to the low mean photon numbers considered. Detection events are infrequent compared to typical sensor dead-times in low mean photon number regimes; hence, the effect of sensor dead-time is negligible. Moreover, detector multiplexing could be used to allow for sensor dead-time to become less of an issue, as it means a single detector within a multiplex is less likely to have another detection event within a sensor dead-time window [80].

After-pulsing occurs when a detection event triggers a subsequent detection event due to the initial excitation. This deleterious effect is neglected in our system, as it is easy to ignore click events suspected of having an after-pulse origin. These events occur very soon after the initial event and in low mean photon number regimes, it is valid to exclude events so soon after the initial event, as the ratio of an after-pulsed click to an independent click increases as the mean photon numbers reduce. The formalism for a click POVM which includes the deleterious effects of timing jitter and dead-time is given by Gouzien et. al [155]. Furthermore, we could include the contribution of after-pulsing by conditioning an appropriate increase of the (detector) background noise for the subsequent shots after a detection event.

This chapter begins with the formalism of measurement of a quantum state; this leads to the introduction of the POVM — the construct we use to calculate the probability of a measurement outcome for a particular quantum state. We place the POVM in the context of a click detector, which is the type of detector we use for our LIDAR protocol and consider various extensions to our POVM to improve the realism of our measurement model. We then calculate the click probabilities for our LIDAR system for different types of background noise and for both CI and QI. Even though our detectors are not photon-number resolving we discuss the photon-number distributions and what is known as heralding gain. Object detection requires discrimination between the object present and absent hypothesis. We then discuss quantum state discrimination. For example, the Helstrom bound provides the minimum error possible for state discrimination. Following this, we compare the Helstrom bound to the error for state discrimination using click probabilities. In realistic scenarios, we must use multiple trials of the experiment to discriminate between the two similar hypotheses (object present and absent); however, the Helstrom bound quickly becomes intractable. Instead, we calculate the bounds of the minimum error via the quantum Chernoff bound and Bhattacharyya bound when there are

many shots of the experiment. We lead to describing what a shot of the experiment means. For multi-shot hypothesis testing, we will have click-count probability distributions, this leads to a discussion about the log-likelihood value (LLV). We present this LLV framework as a method of processing detector data to add context to it, as it functions as a detection decision test. We also state how we can re-express our click-count distributions as LLV distributions. Finally, we discuss various effects which apply to a more realistic treatment of an object detection system.

Chapter 4: System performance

The ability to assess system performance is paramount for any functioning LIDAR protocol. This chapter introduces the figure of merit (FOM), which quantifies system performance regimes where QI performs better than CI, i.e. where there is a quantum advantage. The knowledge of which system parameters convey a quantum advantage is important for justifying the additional effort required for realising quantum-enhanced systems. The quantum fisher information (QFI) metric is a particular approach used to assess the performance of a QI protocol [54]; however, as we focus on the detector data (click-counts) to assess system performance we therefore do not consider the QFI metric further. Instead, we discuss in Ch. 4.2 the classical Fisher information when analysing system performance in terms of the statistics of the detector data. For brevity, this chapter focuses on QI with only coincidence clicks beset by thermal noise. It is easy to reconsider the FOMs with coherent noise instead and for many regimes the inclusion of non-coincidence events does not improve system performance considerably for the system parameter regimes we consider in this chapter.

4.1 Signal-to-noise ratio

One ubiquitous FOM is the signal-to-noise ratio (SNR) [73]. It characterises the amount of signal in comparison to the noise in the system. For CI this is the ratio of signal clicks when there is no noise and signal clicks when an object is absent and there is noise. In terms of click probabilities the CI SNR is

$$\mathrm{SNR}_{\mathrm{CI}} = \frac{\mathrm{Pr}_{\mathrm{CI:H1}} - \mathrm{Pr}_{\mathrm{CI:H0}}}{\mathrm{Pr}_{\mathrm{CI:H0}}}. \tag{4.1}$$

For QI the SNR is the ratio of coincidence clicks when there is no noise and coincidence clicks when an object is absent and there is noise. Similar to CI, the QI SNR in terms of click probabilities is

$$\mathrm{SNR}_{\mathrm{QI}} = \frac{\mathrm{Pr}_{\mathrm{S|I,1}} - \mathrm{Pr}_{\mathrm{H0}}}{\mathrm{Pr}_{\mathrm{H0}}}. \tag{4.2}$$

A problem with the SNR as a FOM is that a SNR value is not unique. It is possible for very different parameter regimes to produce the same SNR. Therefore, it is difficult to discern whether a certain parameter regime allows for confident object detection within a time-frame using the SNR metric. Nevertheless, we define the SNR quantum advantage

$$\text{Q.A.}_{\text{SNR}} = \frac{\text{SNR}_{\text{QI}}}{\text{SNR}_{\text{CI}}}, \tag{4.3}$$

this shows us the parameter regimes that have the best SNR improvement from use of a quantum-enhanced protocol. With a perfectly correlated source the quantum advantage for SNR is $\text{Q.A.}_{\text{SNR}} = g^{(2)}(\tau)$, for an appropriate time delay τ between signal and idler channels and when the mean photon number $\bar{n} < 1$ [73].

4.2 Cramér-Rao lower bound

This section introduces the Cramér-Rao lower bound (CRLB) as a FOM. Literature already exists that treats system performance for a QI-based object detection protocol via this method in [76]. In our protocol, the target object dictates the signal attenuation factor ξ. Therefore, a method for object detection is by estimation of the signal attenuation $\hat{\xi}$ parameter. The optimal estimator for $\hat{\xi}$ satisfies the CRLB $\Delta^2\hat{\xi}_{\text{min}}$. The CRLB is the lower bound for the variance of an unbiased estimator. In this section we consider only unbiased estimators, i.e. the expectation value of our signal attenuation estimator is the signal attenuation $\mathbb{E}(\hat{\xi}) = \xi$. However, in this section we do not need to know if our estimator $\hat{\xi}$ satisfies the CRLB.

The CRLB functions as a FOM as it shows the minimum uncertainty a particular protocol has when interpreting detector data for the presence of an object. The CRLB is the reciprocal of the Fisher information for that parameter [156]

$$\Delta^2\hat{\xi}_{\text{min}} = \frac{1}{I(\xi)}. \tag{4.4}$$

In the context of our protocol, when an object is present, Fisher information tells us the amount of information a click-count possesses about the true value of $\hat{\xi}$. For this FOM we consider the click-count distributions to be Poisson distributions. This is due to the ease granted by an analytic form of the Fisher information of ξ as the parameter within a Poisson distribution given in [76]. We can use this Poisson distribution model as the Poisson distribution is a good approximation of the Binomial distribution if the number of shots is large and the probability of success is small. The conventional click-count distributions used in this thesis also applies to

this theory (albeit with a different Fisher information). The Fisher information of ξ within a Poisson distribution is

$$I(\xi) = \frac{1}{\mu}\left(\frac{d\mu}{d\xi}\right)^2, \tag{4.5}$$

where μ is the mean of the click-count distribution. For CI the CRLB is

$$\Delta^2\hat{\xi}_{\mathrm{CI}} = \left[\frac{1}{N\mathrm{Pr}_{\mathrm{CI:H1}}}\left(\frac{N\eta_{\mathrm{S}}\bar{n}}{(\bar{n}_{\mathrm{B,S}}+\eta_{\mathrm{S}}\xi\bar{n}+1)^2}\right)^2\right]^{-1}. \tag{4.6}$$

For QI the CRLB is

$$\begin{aligned}\Delta^2\hat{\xi}_{\mathrm{QI}} = \Bigg[\frac{1}{N\mathrm{Pr}_{\mathrm{I}}\mathrm{Pr}_{\mathrm{S|I,1}}}\Bigg(&\frac{N\eta_{\mathrm{S}}\bar{n}}{(\bar{n}_{\mathrm{B,S}}+\eta_{\mathrm{S}}\xi\bar{n}+1)^2}- \\ &-(1-\mathrm{Pr}_{\mathrm{I}})\frac{N\eta_{\mathrm{S}}\bar{n}_{\times}}{(\bar{n}_{\mathrm{B,S}}+\eta_{\mathrm{S}}\xi\bar{n}_{\times}+1)^2}\Bigg)^2\Bigg]^{-1},\end{aligned} \tag{4.7a}$$

when $N_{\mathrm{idler}} = N\mathrm{Pr}_{\mathrm{I}}$. The lower the CRLB the better the system is for estimating the properties of a possible target object. Therefore, we define a quantum advantage in the CRLB framework as

$$\mathrm{Q.A.}_{\mathrm{CRLB}} = \frac{\Delta^2\hat{\xi}_{\mathrm{CI}}}{\Delta^2\hat{\xi}_{\mathrm{QI}}}. \tag{4.8}$$

An issue with the signal attenuation CRLB as a FOM is that it does not directly tell how easy a detection decision is.

4.3 Distinguishability measure

System performance comparison of QI and CI using click-counts directly is problematic as coincidence clicks in QI and signal clicks in CI are not the same type of object. This lack of equivalence between types of click makes it challenging to use click-counts as a performance metric. Our framework addresses this problem by recasting click-counts of any type into an LLV. The LLV framework is how we interpret detector data and make detection decisions [90]. Therefore it is wise to derive a FOM from the LLV framework. First, we define the Q-function for a Gaussian distribution with LLV detection threshold d_{LLV}, mean μ and standard deviation σ,

$$\mathrm{Q}(d_{\mathrm{LLV}},\mu,\sigma) = \frac{1}{\sqrt{2\pi}\sigma}\int_{d_{\mathrm{LLV}}}^{\infty} e^{-\left(\frac{z-\mu}{\sqrt{2}\sigma}\right)^2} dz. \tag{4.9}$$

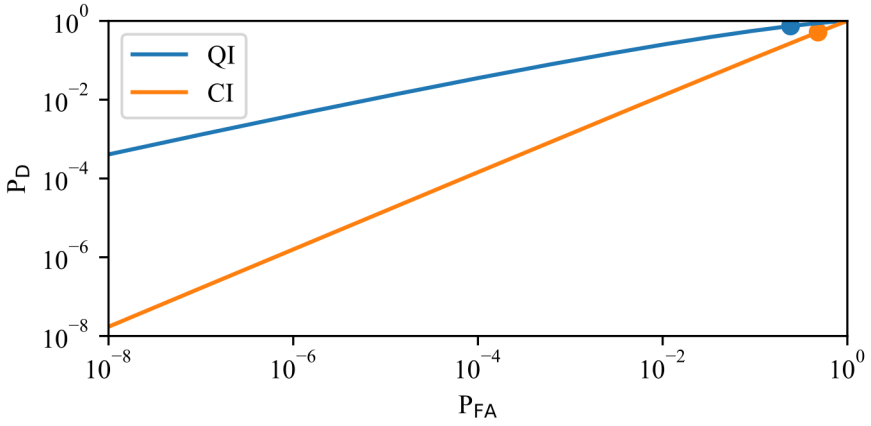

FIGURE 4.1 – ROC curve of QI and CI. Dots represent where $d_{\mathrm{LLV}} = 0$. $N = 8.75 \times 10^{5}$, $\bar{n} = 1 \times 10^{-3}$, $\eta_{\mathrm{S/I}} = 0.5$, $\xi = 1.99 \times 10^{-2}$, $\bar{n}_{\mathrm{B,S}} = 1 \times 10^{-2}$, $\bar{n}_{\mathrm{B,I}} = 4.49 \times 10^{-4}$.

We generate a receiver operator characteristic (ROC) curve by calculating the commonplace statistical measures of probability of detection

$$\mathrm{P_D}(d_{\mathrm{LLV}}) = \mathrm{Q}(d_{\mathrm{LLV}}, \mu_{\mathrm{H1:\Lambda(x,k)}}, \sigma_{\mathrm{H1:\Lambda(x,k)}}), \tag{4.10}$$

and probability of false alarm $\mathrm{P_{FA}}$

$$\mathrm{P_{FA}}(d_{\mathrm{LLV}}) = \mathrm{Q}(d_{\mathrm{LLV}}, \mu_{\mathrm{H0:\Lambda(x,k)}}, \sigma_{\mathrm{H0:\Lambda(x,k)}}), \tag{4.11}$$

over a range of LLV detection threshold values. Figure 4.1 shows the ROC curve for QI and CI, with the dots representing where $d_{\mathrm{LLV}} = 0$, it is clear that QI performs better than CI. For any LLV detection threshold value d_{LLV} we can relate the sum of Eq. 4.10 and Eq. 4.11 to the LLV error probability in Eq. 3.81 such that we can compare with the Chernoff bound.

The ROC is useful to analyse the trade-offs between different errors; however, an advantage of the LLV framework is that it is self-calibrating. That is, the equal likelihoods of object present and absent occurs at the LLV detection threshold $d_{\mathrm{LLV}} = 0$. To summarise, we have a self-calibrating method to assess system performance. If we relax the detection threshold d_{LLV} we have system performance in terms of a ROC curve. If we keep the LLV detection threshold constant $d_{\mathrm{LLV}} = 0$ this simplifies the following use of our framework. Confidence in our detection decision is interlinked with the overlap of the object present and absent LLV distributions. The overlap is encoded in the distinguishability measure we define as

$$\phi = 1 - \left[\mathrm{P_{FN}}(0) + \mathrm{P_{FA}}(0)\right], \tag{4.12}$$

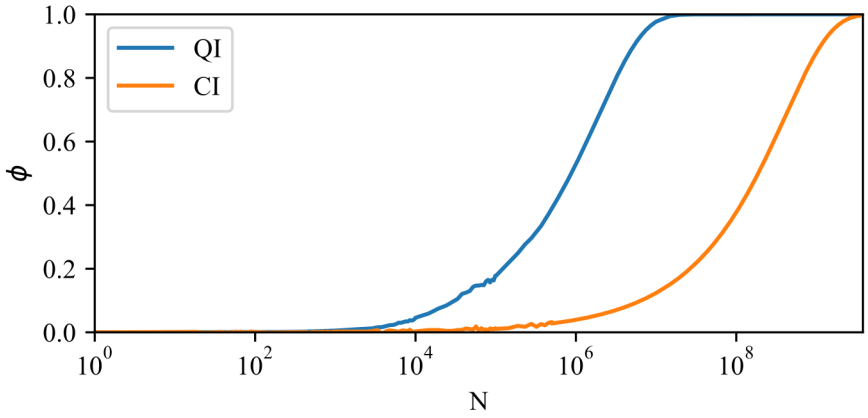

FIGURE 4.2 – Distinguishability as a function of shots for QI and CI. $\bar{n} = 1 \times 10^{-3}$, $\eta_{S/I} = 0.5$, $\xi = 1.99 \times 10^{-2}$, $\bar{n}_{B,S} = 1 \times 10^{-2}$, $\bar{n}_{B,I} = 4.49 \times 10^{-4}$.

where the probability of false negative $P_{FN}(0) = 1 - P_D(0)$. The distinguishability is defined by the two different types of error in statistical hypothesis testing. The interpretation of the distinguishability measure is that $\phi = 0$ means there is total overlap and $\phi = 1$ means both distributions are completely separate. The distinguishability measure is a figure of merit (FOM) which directly characterises system performance in the context of confident detection decision-making. An acceptable value for P_{FA} within the distinguishability measure ϕ sets what we mean by confident detection. We can increase the distinguishability ϕ by increasing the number of shots. Figure 4.2 shows how distinguishability ϕ increases as a function of shots for QI and CI. A Monte-Carlo simulation (detailed in Ch. 7) generates the distinguishability values for shots $N < 5.5 \times 10^5$. The use of distinguishability ϕ as a FOM contrasts with other FOM's such as SNR and CRLB, as these are not directly based on decision-making. We define the distinguishability quantum advantage

$$\text{Q.A.}_{\phi} = \frac{\phi_{QI}}{\phi_{CI}}. \tag{4.13}$$

However, there are deficiencies in the use of ϕ as a FOM. For example, when the distinguishability of a system $\phi \to 1$, it is known as saturation. A quantifiable comparison between systems becomes meaningless in such situations. For example, in the scenario with a parameter regime such that QI has a distinguishability $\phi_{QI} = 1$ and CI has a distinguishability $\phi_{CI} < 1$, we are unable to specify exactly how much better QI is compared to CI. Moreover, this lack of quantifiable comparison also occurs if $\phi = 0$. Due to the aforementioned deficiencies, there are only limited regimes with a well-defined distinguishability quantum advantage Q.A._{ϕ}.

If we compare the distinguishability for a QI system that does ($\phi_{\mathrm{I},0}$) and does not ($\phi_{\mathrm{I},1}$) include non-coincidence clicks we can quantify the benefit of considering non-coincidence clicks. We quantify this benefit by defining a relative difference of distinguishabilities

$$\Delta\phi_{\mathrm{I},0} = \frac{\phi_{\mathrm{I},0} - \phi_{\mathrm{I},1}}{\phi_{\mathrm{I},1}} \times 100\%. \tag{4.14}$$

For the system parameters in Fig. 3.10 in Ch. 3, the non-coincidence relative advantage is $\Delta\phi_{\mathrm{I},0} = 1.157\%$. This advantage is small, however there are regimes where the inclusion of non-coincidence clicks improves system performance significantly. For example, the benefit of non-coincident clicks increases as the idler channel system loss parameter η_{I} decreases. The reduction of idler channel system loss parameter η_{I} means that the upsurge of signal clicks when an object is present is no longer being registered as a coincidence click, due to the low efficiency of registering idler clicks. To demonstrate that non-coincidence clicks are more useful in such regimes, we alter two parameters in Fig. 3.10. The new number of shots $N = 1 \times 10^5$ and idler channel system loss parameter $\eta_{\mathrm{I}} = 0.05$. With these updated parameters the non-coincidence relative advantage is $\Delta\phi_{\mathrm{I},0} = 25.3\%$, which shows a significant benefit for considering non-coincidence clicks.

A threshold distinguishability ϕ_t is set to ensure that the effectiveness of the LLV test is consistent in different regimes. Threshold distinguishability ϕ_t facilitates direct comparison of different parameter regimes in the LLV framework. For analytic simplicity, we calculate the threshold distinguishability from the LLV distributions which have a mean number of idler clicks. The components (types of error) which underlie the distinguishability ϕ, probability of false negative $\mathrm{P_{FN}}$ and probability of false alarm $\mathrm{P_{FA}}$, both affect our interpretation of the LLV for inference of object presence or absence. Therefore, if we wish that the effectiveness of the LLV test is consistent when comparing different regimes in the threshold distinguishability framework, we assume that the influence these types of error have upon the threshold distinguishability is identical for all of the regimes we compare. Moreover, for a single regime each object present and absent LLV distribution distinguishability differs slightly with respect to the number of idler clicks k. This discrepancy means that the effectiveness of the LLV test differs depending on the number of idler clicks recorded. We ignore this discrepancy if it does not exceed the bound as detailed in Appendix F. The purpose of ignoring this discrepancy is that all idler click knowledge is discarded in post-processing and a particular parameter regime only has one type of LLV, i.e a single channel of data. Clearly, the higher ϕ_{t} is the more confident the detection decision. In this thesis, threshold distinguishability is set to be $\phi_{\mathrm{t}} = 0.8$ in line with convention [78]. One

reason for this convention is that such a high threshold distinguishability $\phi_{\mathrm{t}} = 0.8$ corresponds to a visually obvious lack of overlap between the object present and absent distributions, which is useful for pedagogical purposes. Another reason is that the probability of false alarm $\mathrm{P_{FA}} = 0.1$, for regimes when the two types of error ($\mathrm{P_{FN}}$ and $\mathrm{P_{FA}}$) are approximately symmetrical. The two types of error are often symmetrical in regimes when the Gaussian approximation is valid. As we base our notion of confident detection on an acceptably low value of the probability of false alarm $\mathrm{P_{FA}}$, it is clear that the value $\mathrm{P_{FA}} = 0.1$ is adheres to this.

We define the number of shots required to reach threshold distinguishability

$$N_{\mathrm{t}} = \left\lfloor \frac{\mathrm{F}^{-1}(\phi_{\mathrm{t}})}{\mathrm{Pr_I}} \right\rfloor, \tag{4.15}$$

where $\mathrm{F}^{-1}(\phi_{\mathrm{t}})$ is the inverse of the function ϕ_{t}, as derived in Appendix G. The calculation of shots required for threshold distinguishability N_{t} enables the direct comparison of LLVs from different parameter regimes. The ability to ensure that all system parameter regimes have the same LLV test effectiveness means that signal processing is entirely within the LLV framework. We define a quantum advantage

$$\mathrm{Q.A.} = \frac{N_{t:\mathrm{CI}}}{N_{t:\mathrm{QI}}}, \tag{4.16}$$

where $N_{t:\mathrm{QI}}$ is N_t shots required for threshold distinguisabitity for QI and similarly for CI. In other words, the quantum advantage Q.A. as the ratio of the number of shots required for CI and QI to reach threshold distinguishability. In a physical system, this quantity gives a reasonable approximation to the relative amount of time it would take to determine the presence or otherwise of a target object for each system under the same conditions. The use of the quantum advantage Q.A. in terms of shots required surpasses the deficiencies of the distinguishability FOM. For example, no longer is saturation $\phi \to 1$ or divergence $\phi \to 0$ an issue, as the distinguishability is preset to the threshold ϕ_t. This means that there is a more resilient FOM for the LLV framework, with a quantum advantage interpreted in the operator-friendly metric of a factor of the relative time required to reach confident detection. By operator-friendly we mean that a person using this protocol would find it straight-forward to interpret the FOM.

4.4 Rolling window and average distinguishability

In any realistic system the underlying statistics for the click-counts can change due to changes in the environment, our source light, or due to a target object appearing or disappearing. In order to analyse dynamically changing incoming data, we apply a rolling window to our statistics. We

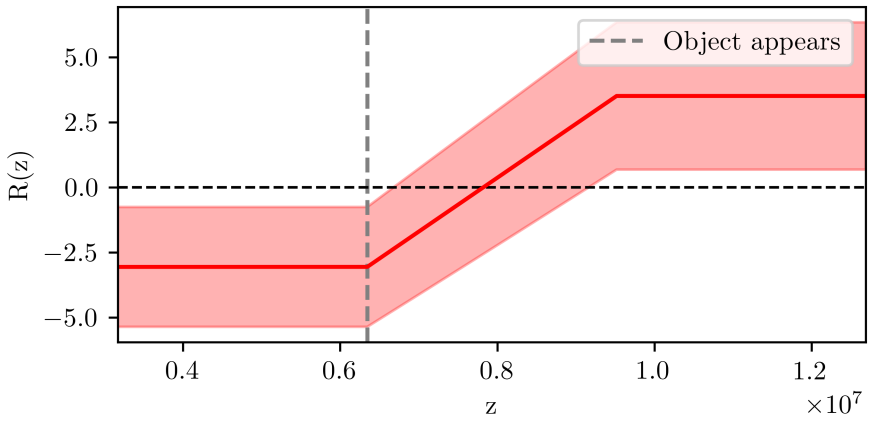

FIGURE 4.3 – Rolling window trajectory of QI mean LLV (solid line coloured red) with a red shaded region limited by a standard deviation of error plus and minus the mean. Regime changes from object absent to present suddenly at time-bin $z = 2N_{\mathrm{t}}$ marked by the vertical dashed line (coloured grey). $N_{\mathrm{t}} = 3.172 \times 10^{6}$, $\bar{n} = 1 \times 10^{-3}$, $\eta_{\mathrm{S/I}} = 0.5$, $\xi = 1.99 \times 10^{-2}$, $\bar{n}_{\mathrm{B,S}} = 1 \times 10^{-2}$, $\bar{n}_{\mathrm{B,I}} = 4.49 \times 10^{-4}$.

consider time-bins z via the total number of shots elapsed in our data collection. We define the cumulative number of coincidence clicks after z time-bins $T(z)$ and cumulative idler clicks $T_{\mathrm{I}}(z)$, where z time-bins is the total number of recorded shots. There is an initialisation stage while $z < N_{\mathrm{t}}$. We have an LLV $R(z)$ for each time-bin z defined as

$$R(z) = \Lambda\left(T(z) - T(z - N_t), T_{\mathrm{I}}(z) - T_{\mathrm{I}}(z - N_t)\right), \tag{4.17}$$

for every time-bin $z \geq N_{\mathrm{t}}$.

Figure 4.3 illustrates the change in LLV statistics between the object absent regime and the object present regime. The object suddenly appears at the time-bin denoted by the vertical dashed line. The system fully updates from object absent to present regime over $z = N_t$ time bins. Figure 4.3 illustrates what $\phi_t = 0.8$ (and ϕ in general) means for the distinctness of the object present and absent distributions. However, the duration of a shot is too short to practically process data in a rolling-window shot-by-shot.

As previously mentioned, it is often impractical to analyse the system on a shot-by-shot basis. This is due to the very short time-scale of a shot. Therefore, we consider analysis of system performance through the framework of LLV samples. In this framework, a sample of an LLV is taken every N_{t} shots and N_{t} is the discrete unit of time considered instead of a single-shot. We

define the mean LLV sample rolling window $R(\tilde{s})$ with refresh rate of S LLV samples as

$$R(\tilde{s}) = \frac{1}{S} \sum_{i=\tilde{s}-S+1}^{\tilde{s}} \Lambda_i, \tag{4.18}$$

where the sample number is $\tilde{s} \geq S$ and Λ_i is an LLV sample. It is clear that Eq. 4.18 has an initialisation stage when $\tilde{s} < S$, just like in the shot-by-shot rolling window introduced earlier. The sample rolling window is a realistic approach to processing LLV data, as the time-scale involved in N_{t} is reasonable. The analysis of the experimental data in Ch. 8 uses the LLV sample rolling window method, rather than assessing the statistics on a shot-by-shot approach. This is due to the very large number of shots for a given LLV sample, for example an integration time $T = 0.1$ s and a coincidence window size $\tau_{\mathrm{c}} = 2$ ns has $N = 5 \times 10^7$ shots.

The framework of considering data on an LLV sample basis rather than shot-by-shot basis extends to system performance. We define the average distinguishability, which is the LLV sample distributions after S samples. If we assume that the statistics are stable, the distributions that underpin the average distinguishability have the same mean values as the shot-by-shot distinguishability defined in Eq. 4.12 but with a smaller standard deviation as the number of samples increase. Therefore, the average distinguishability for S LLV samples is

$$\phi_{\mathrm{avg}}(S) = 1 - \left((1 - \mathrm{Q}(0, \mu_{\mathrm{H1:}\Lambda(\mathrm{x,k})}, \frac{\sigma_{\mathrm{H1:}\Lambda(\mathrm{x,k})}}{\sqrt{S}})) + \mathrm{Q}(0, \mu_{\mathrm{H0:}\Lambda(\mathrm{x,k})}, \frac{\sigma_{\mathrm{H0:}\Lambda(\mathrm{x,k})}}{\sqrt{S}}) \right). \tag{4.19}$$

The use of the average distinguishability allows for system performance analysis in the LLV framework with the constraints of realistic data processing in mind. If $S = 1$ the average distinguishability reduces to just the distinguishability.

4.5 FOM COMPARISON

This section provides a visual comparison of the different FOMs considered. We show the various types of quantum advantage metric introduced earlier on a contour plot, where the mean photon number of our source is varied on the x-axis and the mean photon number of the signal detector background noise is varied on the y-axis. Figure 4.4 shows SNR quantum advantage $\mathrm{Q.A.}_{\mathrm{SNR}}$. The lack of uniqueness for the SNR Q.A. as we vary the background noise is apparent in Fig. 4.4, but it does show that the quantum advantage improves as the signal strength $\bar{n}$ reduces. The reason for the lack of uniqueness in Fig. 4.4 as we vary the background noise is because the SNR Q.A. does not depend upon the background noise, this Q.A. is formulated such that the influence of noise is removed. Figure 4.5 shows CRLB quantum advantage $\mathrm{Q.A.}_{\mathrm{CRLB}}$.

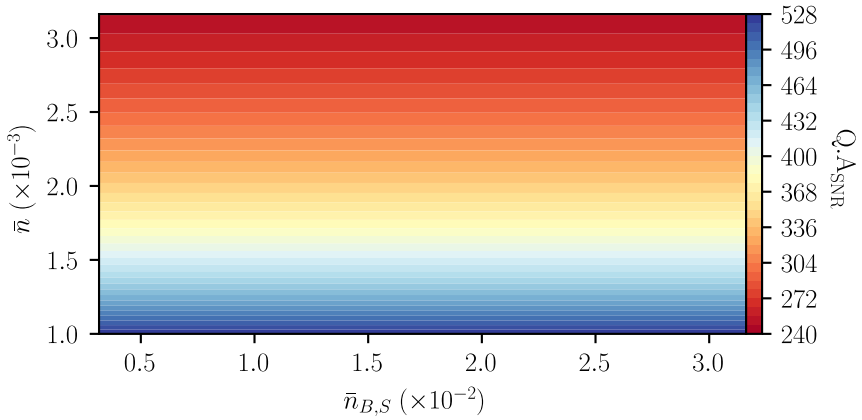

Figure 4.4 – Contour plot of SNR quantum advantage Q.A.$_{\mathrm{SNR}}$ for varied background noise and signal strength. $\eta_{\mathrm{S/I}} = 0.5$, $\xi = 1.99 \times 10^{-2}$ and $\bar{n}_{\mathrm{B,I}} = 4.49 \times 10^{-4}$.

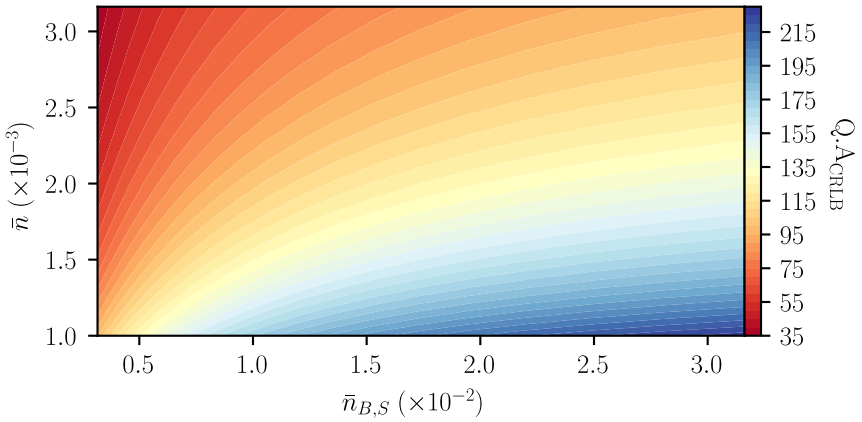

Figure 4.5 – Contour plot of CRLB quantum advantage Q.A.$_{\mathrm{CRLB}}$ for varied background noise and signal strength. $\eta_{\mathrm{S/I}} = 0.5$, $\xi = 1.99 \times 10^{-2}$ and $\bar{n}_{\mathrm{B,I}} = 4.49 \times 10^{-4}$.

For each data point in Fig. 4.5, we use the QI shots required for threshold distinguishability $N_{\mathrm{t:QI}}$, whereas Fig. 4.4 does not depend on the number of shots. Figure 4.6 shows the quantum advantage Q.A. in terms of shots required. Both the CRLB quantum advantage Q.A.$_{\mathrm{CRLB}}$ in Fig 4.5 and the shots required quantum advantage Q.A. in Fig. 4.6 show that the quantum advantage is most pronounced in the scenario of high signal channel background noise $\bar{n}_{\mathrm{B,S}}$ and low signal strength $\bar{n}$. Figure 4.6 has an advantage compared to the previous two figures as it directly shows an operator-friendly value of how much quicker QI is compared to CI as a factor, for an LLV sample which would give us a confident detection decision.

This chapter discusses the different types of figure of merit (FOM) for the detector data we can use to assess system performance and quantify the quantum advantage (Q.A.), which is the advantage QI has over CI for a particular FOM. We discuss the signal-to-noise ratio

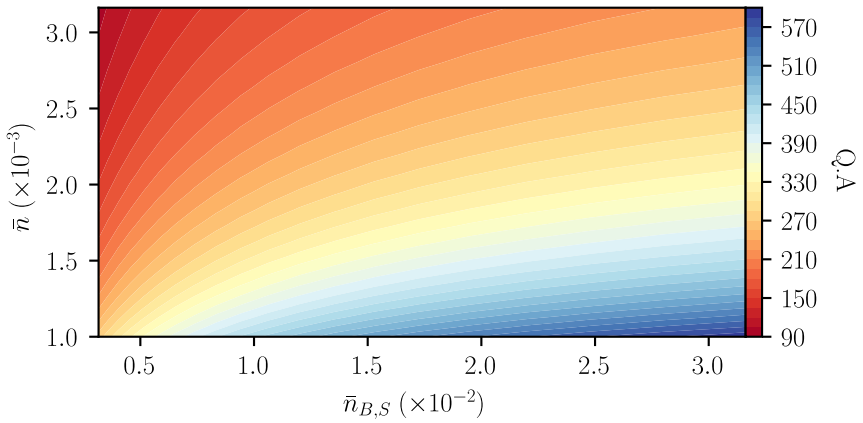

FIGURE 4.6 – Contour plot of quantum advantage Q.A. = $\frac{N_{\mathrm{t:CI}}}{N_{\mathrm{t:QI}}}$ for varied background noise and signal strength. $\eta_{\mathrm{S/I}} = 0.5$, $\xi = 1.99 \times 10^{-2}$ and $\bar{n}_{\mathrm{B,I}} = 4.49 \times 10^{-4}$.

(SNR). The use of this FOM is straightforward; however, its deficiency is that the same SNR could correspond to scenarios where accurate discrimination is possible or not. We lead onto a FOM rooted in estimation theory: the Cramér-Rao lower bound (CRLB). It gives the optimal minimum variance of the estimation of the parameter relevant to the presence of an object. However, it does not directly describe whether accurate discrimination is possible. We lead onto the FOMs borne by our LLV framework. We begin by discussing the distinguishability measure: our measure of the overlap between the object present and absent LLV distributions. There are deficiencies with the distinguishability measure as an FOM, as it can become saturated or null in some regimes. From this, we lead onto another FOM, the shots required to reach a threshold distinguishability. This FOM quantifies the time required for a measurement capable of accurate discrimination. We also discuss analysing detector data and performance analysis in dynamic situations via a rolling window approach. Lastly, we plot the quantum advantage (Q.A.) of the different FOMs. These plots reveal that the Q.A. is most pronounced in the low signal strength and high background noise regimes.

Chapter 5: Multi-mode distributed twin-beam state

5.1 Motivation

The TMSV introduced earlier is an idealisation of the output from SPDC. However, there are many modes available to us in each channel (signal and idler) of the twin-beam squeezed state. For example, to name a couple, there are the spectral and polarisation modes. If we consider M modes in each channel, we refer to the twin-beam squeezed state as the Multi-mode distributed twin-beam state (M:TBSS). It is clear that the 1:TBSS state is equivalent to the familiar TMSV. This chapter develops the theory to use these multiple modes in each arm. In particular, there is a non-trivial quantum advantage in spectrally resolving both the idler and signal channels of the twin-beam squeezed state. Each spectral mode has a set bandwidth to which a detector corresponding to that mode is sensitive. An advantage with the improved performance granted by (spectrally) resolving more modes in each arm is that we are able to detect confidently an object when using a lower mean photon number. Confident detection with a lower mean photon number enables improved covertness of a LIDAR system. Moreover, in a high background noise and low dark noise scenario, more detectors means less chance sensor dead-time will affect our system [80].

5.2 Mode-matching

This section develops the formalism for showing which signal modes correlate with which idler modes. Set notation is used, as the total number of combinations of different events increases drastically with the number of modes M. For a M:TBSS system there are $2M$ modes. We label the i^{th} idler state as mIi, of which the set of M idler states is $\mathbf{mI} = \{\text{mI}1, \ldots, \text{mI}i, \ldots, \text{mI}M\}$. There is a similar approach for the signal states, as the set of M signal states is $\mathbf{mS} = \{\text{mS}1, \ldots, \text{mS}k, \ldots, \text{mS}M\}$. There is also the set $\mathbf{B} = \{b_1, \ldots, b_i, \ldots, b_M\}$. The set $\mathbf{B}$ represents

the shared photon-number for an idler mode and its correspondingly correlated signal mode. We define |I| as the number of idler detectors that click and similarly |S| as the number of signal detectors that click. From this, we define the set of the particular idler detectors that click as $\mathbf{mI}_{|\mathrm{I}|:z} \subset \mathbf{mI}$, where $1 \leq z \leq \binom{M}{|\mathrm{I}|}$. Furthermore, we define the set of the particular signal detectors that click as $\mathbf{mS}_{|\mathrm{S}|:y} \subset \mathbf{mS}$, where $1 \leq y \leq \binom{M}{|\mathrm{S}|}$. We also define the complement of the idler and signal detector click set as $\mathbf{mI}^{\mathrm{c}}_{|\mathrm{I}|:z}$ and $\mathbf{mS}^{\mathrm{c}}_{|\mathrm{S}|:y}$, respectively. This formalism allows for consideration of all possible combinations of idler and signal detector click or no-click events. An example of the sets of the particular idler detectors that click when $M = 3$ and $|I| = 2$ is $\mathbf{mI}_{2:1} = \{\mathrm{mI1}, \mathrm{mI2}\}$, $\mathbf{mI}_{2:2} = \{\mathrm{mI2}, \mathrm{mI3}\}$ and $\mathbf{mI}_{2:3} = \{\mathrm{mI1}, \mathrm{mI3}\}$. From this it is obvious how the complement sets and the signal detector sets are expressed.

A mapping $f(\mathbf{mI}, \mathbf{mS})$ encodes how idler and signal modes are correlated. By defining the conditions of this mapping, we can express how idler and signal modes correlate in any way. This level of freedom for mode correlation means that M:TBSS theory is applicable to any of the degrees of freedom our light possesses. However, the remainder of this thesis shall focus on the case of idler and signal mode anti-correlations. This mirrors the anti-correlations of spectral modes from an SPDC output. If two modes have the same photon-number set element $b_i \in \mathbf{B}$ then they are photon-number correlated, we use this set to describe the mapping. The mapping (from a particular mode to photon-number set element) for spectral anti-correlations is thus

$$f(\mathbf{mI}, \mathbf{mS}) : \mathrm{mI}i \rightarrow b_i \text{ and } \mathrm{mS}k \rightarrow b_{M-k+1}, \ \forall i, k. \tag{5.1}$$

If we consider a 3:TBSS system, the idler mode mI1 correlates with the signal mode mS3. Figure 5.1 shows an idealised representation of a joint spectral amplitude (JSA) for a state with three frequency anti-correlated spectral modes. Figure 5.1 also shows how the idler and signal modes correlate with each other, with the respective index denoted b_i beside each mode. The utility of the index set $\mathbf{B}$ is apparent for succinctly representing mode correlation. This is a simplified scenario, as a realistic JSA does not have a perfect one-to-one correspondence between modes. Nevertheless, this idealised JSA is sufficient granted we acknowledge the loss of useful light when only considering signal and idler modes with one-to-one correspondence. Moreover, each spectral mode mIi or mSk represents a set bandwidth of frequencies with central frequency $\omega_{i/k}$. As the mode number i, k increases, this represents an increase of frequency of central frequency for this spectral mode. This thesis only considers arbitrary frequency values.

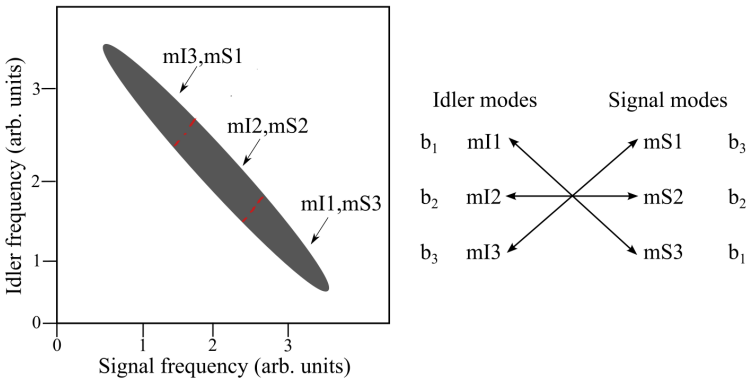

Figure 5.1 – Idealised representation of a joint spectral amplitude (JSA) with three spectral modes. Note the one-to-one anti-correlation between idler and signal frequencies.

5.3 Squeezing operator

We extend the theory of a two-mode squeezing operator introduced in Ch. 2 for M:TBSS. The M:TBSS unitary transformation operator is

$$\hat{U} = e^{-\chi \hat{a}_p \sum_{z=1}^{M} \hat{a}^{\dagger}_{Sz} \hat{a}^{\dagger}_{I(M+1-z)} + \chi \hat{a}^{\dagger}_p \sum_{z=1}^{M} \hat{a}_{Sz} \hat{a}_{I(M+1-z)}}. \tag{5.2}$$

We model SPDC when this unitary transformation operator is applied to the pump mode and the $2M$ mode vacuum [100],

$$\hat{U}|\alpha\rangle \otimes |\{0\}_{2M}\rangle, \tag{5.3}$$

where $|\{0\}_{2M}\rangle = |0\rangle \otimes \ldots 2M \cdots \otimes |0\rangle$. This is for the case of a evenly distributed JSA, that is each mode in M:TBSS has equal photon number distributions. Furthermore, there are perfect one-to-one frequency correlations for the state given by Eq. 5.3. Appendix J shows the case of an unevenly distributed JSA. The remainder of this thesis focuses on the case of an evenly distributed JSA for M:TBSS.

As previously done in Ch. 2, we apply the parametric approximation to the operators acting upon the pump mode as it is an intense coherent state. This transforms these operators into classical variables, which vastly simplifies the analysis [116] as the pump field is no longer represented by an operator. The unitary transformation operator is restated as a squeezing operator. Additionally, the pump mode is traced out of the system.

Similar to Ch. 2 we define $\zeta = \chi^{(2)}\alpha$, where α is the classical pump amplitude that was originally $\hat{a}_{\mathrm{p}}$. With the change of variables, we define the M:TBSS two-mode squeezing operator

as

$$\hat{S}_{2,M}(\zeta) = {}_{\mathrm{p}}\langle\alpha|\hat{U}|\alpha\rangle_{\mathrm{p}} \tag{5.4a}$$

$$= e^{-\zeta \sum_{z=1}^{M} \hat{a}^{\dagger}_{Sz}\hat{a}^{\dagger}_{I(M+1-z)} + \zeta^{*} \sum_{z=1}^{M} \hat{a}_{Sz}\hat{a}_{I(M+1-z)}} \tag{5.4b}$$

Equation 5.4b is an unfavourable form of the M:TBSS two-mode squeezing operator for calculation. Therefore, we use the disentangling theorem to recast $\hat{S}_{2,M}$ into a more favourable form [123], [157]. The following operators are set as

$$\hat{K}_{+} = \sum_{z=1}^{M} \hat{a}^{\dagger}_{Sz}\hat{a}^{\dagger}_{I(M+1-z)}, \tag{5.5a}$$

$$\hat{K}_{-} = \hat{K}^{\dagger}_{+}, \tag{5.5b}$$

$$\hat{K}_{3} = \frac{1}{2}\sum_{z=1}^{M} \hat{a}^{\dagger}_{Sz}\hat{a}_{Sz} + \hat{a}_{I(M+1-z)}\hat{a}^{\dagger}_{I(M+1-z)}. \tag{5.5c}$$

The disentangling theorem requires satisfaction of the following commutator relations $[\hat{K}_3, \hat{K}_{\pm}] = \pm\hat{K}_{\pm}$ and $[\hat{K}_{+}, \hat{K}_{-}] = -2\hat{K}_3$. Proof of this satisfaction is shown in Appendix H. Thanks to the disentangling theorem and setting $\zeta = re^{i\theta}$ into exponential form, the squeezing operator $\hat{S}_{2,M}(\zeta)$ is framed as

$$\hat{S}_{2,M}(\zeta) = e^{-e^{i\theta}\tanh(r)\hat{K}_{+}} e^{\ln(\cosh^{-2}(r))\hat{K}_3} e^{e^{-i\theta}\tanh(r)\hat{K}_{-}}. \tag{5.6}$$

With the squeezing operator in this form, it is applied to the $2M$ mode vacuum state.

5.4 M:TBSS STATE

In this section we express the M:TBSS state. The squeezing operator $\hat{S}_{2,M}$ applied to the $2M$ mode vacuum is

$$|\psi\rangle_{\text{M:TBSS}} = \hat{S}_{2,M}(\zeta)|\{0\}_{2M}\rangle = e^{-e^{i\theta}\tanh(r)\hat{K}_{+}} e^{ln(\cosh^{-2}(r))\hat{K}_3} e^{e^{-i\theta}\tanh(r)\hat{K}_{-}}|\{0\}_{2M}\rangle \tag{5.7}$$

The three exponential components of this favourable form act from right to left, hence the derivation is split into three parts. A similar form of our M:TBSS state is given by Kok and Braunstein in Ref. [158], where they focus on the polarisation correlations instead. Appendix I

details the derivation of $|\psi\rangle_{\text{M:TBSS}}$. Hence, the M:TBSS state is

$$|\psi\rangle_{\text{M:TBSS}} = (\text{sech}(r))^M \sum_{n=0}^{\infty} (-e^{i\theta}\tanh(r))^n \sum_{b_1,\ldots,b_M=0}^{n} \delta_{b_1+\cdots+b_M,n} |b_1,\ldots,b_M\rangle_{\mathbf{mI}} \otimes$$
$$\otimes |b_M,\ldots b_1\rangle_{\mathbf{mS}}, \tag{5.8a}$$
$$= \frac{1}{(\bar{n}+1)^{\frac{M}{2}}} \sum_{n=0}^{\infty} \left(-e^{i\theta}\sqrt{\frac{\bar{n}}{\bar{n}+1}}\right)^n \sum_{b_1,\ldots,b_M=0}^{n} \delta_{b_1+\cdots+b_M,n} |b_1,\ldots,b_M\rangle_{\mathbf{mI}} \otimes$$
$$\otimes |b_M,\ldots b_1\rangle_{\mathbf{mS}}, \tag{5.8b}$$

as $\sinh^2(r) = \bar{n}$. Our detectors are phase-insensitive and hence do not register the off-diagonals of a density matrix. Similar to the QI state $\hat{\rho}_{\text{SI}}$ introduced in Ch. 3 we can express the M:TBSS density matrix with diagonals only. The M:TBSS density matrix with off-diagonals disregarded is

$$\hat{\rho}_{\text{M:TBSS}} = \sum_{n=0}^{\infty} \text{P}(n,M) \sum_{b_1,\ldots,b_M=0}^{n} \delta_{b_1+\cdots+b_M,n} |b_1,\ldots,b_M\rangle\langle b_M,\ldots,b_1|_{\mathbf{mI}} \otimes$$
$$\otimes |b_M,\ldots,b_1\rangle\langle b_1,\ldots,b_M|_{\mathbf{mS}}, \tag{5.9a}$$

where $\text{P}(n,M) = \frac{\bar{n}^n}{(\bar{n}+1)^{n+M}}$.

5.5 M:TBSS MEASUREMENT OPERATORS

The generalised form of the idler detector POVM describes the single-shot measurement made by all idler detectors in a M:TBSS system. We define the idler detector POVM as

$$\hat{\pi}_{\text{I}}(M, \mathbf{mI}_{|\text{I}|:z}) = \bigotimes_{\substack{i=1 \\ \text{mI}i \in \mathbf{mI}_{|\text{I}|:z}}}^{M} \hat{\pi}_{\text{I},\checkmark}(i) \otimes \bigotimes_{\substack{i=1 \\ \text{mI}i \in \mathbf{mI}^{\text{c}}_{|\text{I}|:z}}}^{M} \hat{\pi}_{\text{I},\times}(i). \tag{5.10}$$

We define $A(i) = \frac{1}{1+\bar{n}_{\text{B,I}}(i)}$ and $B(i) = 1 - \frac{\eta_{\text{I}}(i)}{1+\bar{n}_{\text{B,I}}(i)}$. Where $\bar{n}_{\text{B,I}}(i)$ is the idler detector background noise and $\eta_{\text{I}}(i)$ is the idler detector system loss for mode mIi. The mode mIi click and no-click measurement operators, respectively

$$\hat{\pi}_{\text{I},\checkmark}(i) = \sum_{p=0}^{\infty} (1 - A(i)B(i)^p) |p\rangle\langle p|_{\text{mI}i}, \tag{5.11a}$$
$$\hat{\pi}_{\text{I},\times}(i) = \sum_{p=0}^{\infty} A(i)B(i)^p |p\rangle\langle p|_{\text{mI}i}. \tag{5.11b}$$

The generalised form of the signal detector POVM is

$$\hat{\pi}_{\mathrm{S}}(M, \mathbf{mS}_{|\mathrm{S}|:y}) = \bigotimes_{\substack{i=1 \\ \mathrm{mS}k \in \mathbf{mS}_{|\mathrm{S}|:y}}}^{M} \hat{\pi}_{\mathrm{S},\checkmark}(i) \otimes \bigotimes_{\substack{i=1 \\ \mathrm{mS}k \in \mathbf{mS}^{\mathrm{c}}_{|\mathrm{S}|:y}}}^{M} \hat{\pi}_{\mathrm{S},\times}(i). \tag{5.12}$$

We define $D(k) = \frac{1}{1+\bar{n}_{\mathrm{B,S}}(k)}$, $G(k) = 1 - \frac{\xi(k)\eta_{\mathrm{S}}(k)}{1+\bar{n}_{\mathrm{B,S}}(k)}$. Where $\bar{n}_{\mathrm{B,S}}(k)$ is the signal detector background noise, $\eta_{\mathrm{S}}(k)$ is the signal detector system loss and $\xi(k)$ is the signal attenuation factor for mode mSk. The mode mSk click and no-click measurement operators, respectively

$$\hat{\pi}_{S,\checkmark}(k) = \sum_{p=0}^{\infty}(1 - D(k)G(k)^p)|p\rangle\langle p|_{\mathrm{mS}k}, \tag{5.13a}$$

$$\hat{\pi}_{S,\times}(k) = \sum_{p=0}^{\infty} D(k)G(k)^p|p\rangle\langle p|_{\mathrm{mS}k}. \tag{5.13b}$$

5.6 Generalised click probability

In this section we define the M:TBSS generalised form of the click probabilities with the idler detector event combination $\mathbf{mI}_{|\mathrm{I}|:z}$ and with the signal detector event combination $\mathrm{F}_{|\mathrm{S}|:y}$. We first define the idler detector generalised click probability as

$$\Pr_{\mathrm{I}}(M, \mathbf{mI}_{|\mathrm{I}|:z}) = \mathrm{Tr}\left(\hat{\rho}_{\mathrm{M:TBSS}}\ \hat{\pi}_{\mathrm{I}}(M, \mathbf{mI}_{|\mathrm{I}|:z})\right) \tag{5.14a}$$

$$= \sum_{n=0}^{\infty} P(n, M) \sum_{b_1,\ldots,b_M=0}^{n} \delta_{b_1+\cdots+b_M,n} \times$$

$$\times \prod_{\substack{i=1 \\ \mathrm{mI}i \in \mathbf{mI}_{|\mathrm{I}|:z}}}^{M} (1 - A(i)B(i)^{b_i}) \prod_{\substack{i=1 \\ \mathrm{mI}i \in \mathbf{mI}^{\mathrm{c}}_{|\mathrm{I}|:z}}}^{M} A(i)B(i)^{b_i}. \tag{5.14b}$$

Therefore, when an object is present the generalised signal detector click probability after idler detector measurement conditioning is

$$\Pr_{\mathrm{S|I},1}(M,\mathbf{mI}_{|\mathrm{I}|:z},\mathbf{mS}_{|\mathrm{S}|:y}) = \mathrm{Tr}\Bigg(\frac{1}{\Pr_{\mathrm{I}}(M,\mathbf{mI}_{|\mathrm{I}|:z})}\mathrm{Tr}_{\mathbf{mI}}\big(\hat{\rho}_{\mathrm{M:TBSS}}\;\hat{\pi}_{\mathrm{I}}(M,\mathbf{mI}_{|\mathrm{I}|:z})\big)\times \\ \times\,\hat{\pi}_{S}(M,\mathbf{mS}_{|\mathrm{S}|:y})\Bigg), \tag{5.15a}$$

$$= \frac{1}{\Pr_{\mathrm{I}}(M,\mathbf{mI}_{|\mathrm{I}|:z})}\sum_{n=0}^{\infty}P(n,M)\sum_{b_1,\ldots,b_M=0}^{n}\delta_{b_1+\cdots+b_M,n}\times \\ \times\prod_{\substack{i=1\\ \mathrm{m}i\in\mathbf{mI}_{|\mathrm{I}|:z}}}^{M}(1-A(i)B(i)^{b_i})\prod_{\substack{i=1\\ \mathrm{m}i\in\mathbf{mI}^{\mathrm{c}}_{|\mathrm{I}|:z}}}^{M}A(i)B(i)^{b_i}\times \\ \times\prod_{\substack{k=1\\ \mathrm{m}S k\in\mathbf{mS}_{|\mathrm{S}|:y}}}^{M}(1-D(k)G(k)^{b_{M+1-k}})\prod_{\substack{k=1\\ \mathrm{m}S k\in\mathbf{mS}^{\mathrm{c}}_{|\mathrm{S}|:y}}}^{M}D(k)G(k)^{b_{M+1-k}}. \tag{5.15b}$$

When an object is absent this means that any idler event does not affect the click probability at the signal detector. The lack of effect from the idler measurement is because the signal state is lost to the environment. This loss to the environment is treated by replacing the signal state with a M-mode vacuum state $\hat{\rho}_{\mathrm{H0}} = |\{0\}_M\rangle$. Therefore, the M:TBSS general form of the no object present click probability is

$$\Pr(M,H_0,\mathbf{mS}_{|\mathrm{S}|:y}) = \mathrm{Tr}\Big(\hat{\rho}_{\mathrm{H}_0}\hat{\pi}_S(M,\mathbf{mS}_{|\mathrm{S}|:y})\Big), \tag{5.16a}$$

$$= \prod_{\substack{k=1\\ \mathrm{m}S k\in\mathbf{mS}_{|\mathrm{S}|:y}}}^{M}(1-D(k))\prod_{\substack{k=1\\ \mathrm{m}S k\in\mathbf{mS}^{\mathrm{c}}_{|\mathrm{S}|:y}}}^{M}D(k). \tag{5.16b}$$

5.7 Generalised click-count distribution and LLV

The generalised click probability theory for M:TBSS covers all possible types of events for our click detectors. We denote the number of click events for a particular combination of idler detector clicks and no-clicks as

$$x_{\mathrm{I}}(\mathbf{mI}_{|\mathrm{I}|:z}). \tag{5.17}$$

Therefore, the M:TBSS idler click-count binomial probability distribution is

$$\mathrm{P}_{\mathrm{I}}(M,\mathbf{mI}_{|\mathrm{I}|:z},x_{\mathrm{I}}) = \binom{N}{x_{\mathrm{I}}}\Pr_{\mathrm{I}}^{x_{\mathrm{I}}}(1-\Pr_{\mathrm{I}})^{N-x_{\mathrm{I}}}, \tag{5.18}$$

where we use short-hand for the corresponding click event $x_{\mathrm{I}} \equiv x_{\mathrm{I}}(\mathbf{mI}_{|\mathrm{I}|:z})$ and we also use shorthand for the relevant click probability $\mathrm{Pr}_{\mathrm{I}} \equiv \mathrm{Pr}_{\mathrm{I}}(M, \mathbf{mI}_{|\mathrm{I}|:z})$. After this, we define the number of click events for a particular combination of idler and signal detector clicks and no-clicks as

$$x(\mathbf{mI}_{|\mathrm{I}|:z}, \mathbf{mS}_{|\mathrm{S}|:y}). \tag{5.19}$$

We add a condition that we only care for events when there is at least one signal detector that clicks $|\mathrm{S}| \geq 1$, as any difference between the object present or absent scenario is manifest in the signal detector click-count statistics. Following from this, we define the M:TBSS object present binomial click-count probability distribution for an event combination $(\mathbf{mI}_{|\mathrm{I}|:z}, \mathbf{mS}_{|\mathrm{S}|:y})$ as

$$\mathrm{P}(M, \mathbf{mI}_{|\mathrm{I}|:z}, \mathbf{mS}_{|\mathrm{S}|:y}, x_{\mathrm{I}}, x) = \binom{x_{\mathrm{I}}}{x} \mathrm{Pr}^{x}(1 - \mathrm{Pr})^{x_{\mathrm{I}} - x}, \tag{5.20}$$

where we use short-hand for the corresponding click event $x \equiv x(\mathbf{mI}_{|\mathrm{I}|:z}, \mathbf{mS}_{|\mathrm{S}|:y})$ and for the relevant click probability $\mathrm{Pr} \equiv \mathrm{Pr}_{\mathrm{S|I},1}(M, \mathbf{mI}_{|\mathrm{I}|:z}, \mathbf{mS}_{|\mathrm{S}|:y})$. Furthermore, we define the M:TBSS object absent binomial click-count probability distribution

$$\mathrm{P}(M, \mathrm{H}_0, \mathbf{mS}_{|\mathrm{S}|:y}, x_{\mathrm{I}}, x) = \binom{x_{\mathrm{I}}}{x} \mathrm{Pr}_{\mathrm{H0}}^{x_{\mathrm{I}}}(1 - \mathrm{Pr}_{\mathrm{H0}})^{M - x_{\mathrm{I}}}, \tag{5.21}$$

where we use the shorthand $\mathrm{Pr}_{\mathrm{H0}} \equiv \mathrm{Pr}(M, \mathrm{H}_0, \mathbf{mS}_{|\mathrm{S}|:y})$. The M:TBSS LLV which considers all possible idler and signal click event combinations (with the condition that $|\mathrm{S}| \geq 1$) is

$$\Lambda(M, \mathbf{x}) = \ln\Bigg(\prod_{|\mathrm{I}|=0}^{M} \prod_{|\mathrm{S}|=1}^{M} \prod_{z=1}^{|z|} \prod_{y=1}^{|y|} \frac{\mathrm{P}(M, \mathbf{mI}_{|\mathrm{I}|:z}, \mathbf{mS}_{|\mathrm{S}|:y}, x_{\mathrm{I}}, x)}{\mathrm{P}(M, \mathrm{H}_0, \mathbf{mS}_{|\mathrm{S}|:y}, x_{\mathrm{I}}, x)} \Bigg), \tag{5.22}$$

where we use the shorthand $|z| \equiv \binom{M}{|\mathrm{I}|}$ and $|y| \equiv \binom{M}{|\mathrm{S}|}$. We also refer to $\mathbf{x}$ as the vector containing the click-count information of all considered events. It is clear that there are many channels of data arising from the myriad of possible click event. The benefit of the LLV framework is apparent as the LLV reduces all these data channels into one value. The full M:TBSS theory is useful as a comprehensive treatment of the multi-mode light we consider. For example, it facilitates the possibility of simulating M:TBSS range-finding scenarios or accounting for single-shot multi-clicks when probing targets in regimes without considerable loss. However, the simplified M:TBSS theory we present next suffices for further discussion of the use of multi-mode light.

5.8 Simplified M:TBSS for LIDAR

We do not need the entire suite of features granted by M:TBSS theory to apply it to a LIDAR system capable of multi-mode discrimination for each beam. In this section we present a simplified form of M:TBSS thanks to a few assumptions. We assume that the system parameters are identical for each mode. This simplifies the POVMs as $\forall i,k\ A(i)=A, B(i)=B, D(k)=D$ and $G(k)=G$. We also assume that the M:TBSS state has an evenly distributed JSA. Lastly, we only consider coincidence clicks limited to when the number of idler clicks $|\mathrm{I}|=1$. These assumptions vastly reduce the number of probabilities required to characterise a LIDAR system, thereby simplifying this particular application of the theory.

As we only consider coincidence clicks, the mapping from idler detectors that clicked to signal detectors that clicked is

$$\mathbf{mS}_{1:y} = f(\mathbf{mI}_{1:z}, \mathbf{mS}). \tag{5.23}$$

We do not consider no-click events and so we drop the mode no-click operators from the generalised measurement operators in Eq. 5.10 and Eq. 5.12. Therefore, the simplified M:TBSS idler click probability is

$$\mathrm{Pr}_{\mathrm{I}}(M, \mathbf{mI}_{1:z}) = \sum_{n=0}^{\infty} P(n,M) \sum_{b_1,\ldots,b_M=0}^{n} \delta_{b_1+\cdots+b_M,n}(1-AB^{b_1}). \tag{5.24}$$

The simplified M:TBSS coincidence click probability is

$$\mathrm{Pr}_{\mathrm{S|I},1}(M, \mathbf{mI}_{1:z}) = \frac{1}{\mathrm{Pr}_{\mathrm{I}}(M, \mathbf{mI}_{1:z})} \sum_{n=0}^{\infty} P(n,M) \sum_{b_1,\ldots,b_M=0}^{n} \delta_{b_1+\cdots+b_M,n}(1-AB^{b_1})(1-DG^{b_1}). \tag{5.25}$$

Furthermore, the simplified M:TBSS object absent coincidence click probability is

$$\mathrm{Pr}_{\mathrm{H0}}(M, \mathbf{mI}_{1:z}) = (1-D). \tag{5.26}$$

The total number of idler clicks, signal clicks and coincidence clicks is also dependent on the number of detectors M. The click probabilities for each mode are equivalent, therefore calculating the total number of clicks for the simplified M:TBSS system is an easy multiplicative task. After N shots, the mean total number of idler clicks $N_{\mathrm{I}} = N\mathrm{Pr}_{\mathrm{I}}(M, \mathbf{mI}_{1:z})M$ and the mean total number of signal detector noise clicks $N_{\mathrm{S:noise}} = N\mathrm{Pr}_{\mathrm{H0}}(M, \mathbf{mI}_{1:z})M$. The mean total number of coincidence clicks, for object present and absent respectively, $N_{\mathrm{S|I},1} = N\mathrm{Pr}_{\mathrm{I}}(M, \mathbf{mI}_{1:z})\mathrm{Pr}_{\mathrm{S|I},1}(M, \mathbf{mI}_{1:z})M$ and $N_{\mathrm{H0|I},1} = N\mathrm{Pr}_{\mathrm{I}}(M, \mathbf{mI}_{1:z})\mathrm{Pr}_{\mathrm{H0}}(M, \mathbf{mI}_{1:z})M$.

Due to the assumptions made for simplified M:TBSS the click-count probability distributions are parameterised only by number of modes M and the set of idler detectors that click once in total $\mathbf{mI}_{1:z}$. Therefore, we set the notation for the simplified M:TBSS idler click-count probability distribution as $\mathrm{P_I}(M, \mathbf{mI}_{1:z}, x_\mathrm{I})$. Similarly, we set the notation for the simplified M:TBSS coincidence click-count probability distribution for object present as $\mathrm{P}(M, \mathbf{mI}_{|1|:z}, x_\mathrm{I}, x)$ and object absent as $\mathrm{P}(M, \mathrm{H_0}, \mathbf{mI}_{|\mathrm{I}|:z}, x_\mathrm{I}, x)$. As the simplified M:TBSS LLV constitutes M independent click-count probability distributions, it is easy to state the LLV in its linear form

$$\Lambda(M, \mathbf{x}) = \sum_{z=1}^{|z|} \mathrm{M}_1 x(\mathbf{mI}_{1:z}) + x_\mathrm{I}(\mathbf{mI}_{1:z})\mathrm{C}_1, \tag{5.27}$$

where $\mathrm{M}_1 = \ln\left(\frac{\mathrm{Pr}_{\mathrm{S|I},1}(M,\mathbf{mI}_{1:z})(1-\mathrm{Pr}_{\mathrm{H0}}(M,\mathbf{mI}_{1:z}))}{\mathrm{Pr}_{\mathrm{H0}}(M,\mathbf{mI}_{1:z})(1-\mathrm{Pr}_{\mathrm{S|I},1}(M,\mathbf{mI}_{1:z}))}\right)$ and $C_1 = \ln\left(\frac{1-\mathrm{Pr}_{\mathrm{S|I},1}(M,\mathbf{mI}_{1:z})}{1-\mathrm{Pr}_{\mathrm{H0}}(M,\mathbf{mI}_{1:z})}\right)$.

5.8.1 Figures of Merit

All of the FOMs introduced in Ch. 4 applies to M:TBSS theory. The SNR for the simplified M:TBSS is

$$\mathrm{SNR}_{\mathrm{M:TBSS}} = \frac{\mathrm{Pr}_{\mathrm{S|I},1}(M, \mathbf{mI}_{1:z}) - \mathrm{Pr}_{\mathrm{H0}}(M, \mathbf{mI}_{1:z})}{\mathrm{Pr}_{\mathrm{H0}}(M, \mathbf{mI}_{1:z})}. \tag{5.28}$$

As for QI (1:TBSS), we set the simplified M:TBSS click-count distribution as Poissonian for the CRLB of signal attenuation factor estimation $\Delta^2\hat{\xi}_{\mathrm{min}}$. The simplified M:TBSS CRLB is

$$\Delta^2\hat{\xi}_{\mathrm{min}} = \left(\frac{d\xi}{d\mu}\right)^2 \mu, \tag{5.29}$$

where $\mu = N_{\mathrm{S|I},1}$. The distinguishability and shots required for threshold distinguishability follow suit based off the LLV defined in Eq. 5.27. It is also straight-forward to express a quantum advantage comparing CI with M:TBSS for any of our FOM.

5.8.2 Performance comparison

It is trivial to show that system performance improves by increasing M for a system with a mean photon number $\bar{n}$ for each mode, as the total mean photon number in the system increases with M modes. Instead, we want to show a non-trivial advantage of increasing the number of spectral modes M without increasing the total mean photon number. To show the non-trivial advantage we need to be sure that the comparison of M:TBSS with QI is fair. This condition for fairness requires that the total mean photon number of our light source and the background noise is equal for any M:TBSS state. We want to solve for the M:TBSS mean photon number

$\bar{n}_{\mathrm{M}}$ that gives us the same number of clicks as a 1:TBSS state with mean photon number $\bar{n}$ would. We exclude the influence of idler detector background noise to investigate solely how the mean photon number is distributed over the number of spectral modes M. Therefore, the M:TBSS mean photon number is found from

$$N_{\mathrm{I}|\bar{n}_{\mathrm{B,I}}=0} = N\mathrm{Pr}_{\mathrm{I}}(1, \mathbf{mI}_{1:z})\Big|_{\bar{n}_{\mathrm{B,I}}=0} = N\mathrm{Pr}_{\mathrm{I}}(M, \mathbf{mI}_{1:z})\Big|_{\bar{n}_{\mathrm{B,I}}=0} M, \tag{5.30}$$

where $\mathrm{Pr}_{\mathrm{I}}(1, \mathbf{mI}_{1:z})$ is a function of 1:TBSS mean photon number $\bar{n}$ and $\mathrm{Pr}_{\mathrm{I}}(M, \mathbf{mI}_{1:z})$ is a function of M:TBSS mean photon number $\bar{n}_M$. Calculation of the M:TBSS mean photon number $\bar{n}_M$ from Eq. 5.30 is greatly assisted by the knowledge that when only one mode of the M:TBSS is regarded the photon statistics are thermal, as derived in Appendix K. Hence, the M:TBSS mean photon number in terms of the 1:TBSS mean photon number is

$$\bar{n}_M = \frac{\bar{n}}{M - \eta_{\mathrm{I}}\bar{n} + \eta_{\mathrm{I}} M\bar{n}}. \tag{5.31}$$

There is a similar approach for calculation of the M:TBSS signal detector background noise $\bar{n}_{\mathrm{M:B,S}}$. Therefore, the M:TBSS signal detector background noise in terms of the 1:TBSS signal detector background noise is

$$\bar{n}_{\mathrm{M:B,S}} = \frac{\bar{n}_{\mathrm{B,S,E}}}{M - \bar{n}_{\mathrm{B,S,E}} + M\bar{n}_{\mathrm{B,S,E}}} + \bar{n}_{\mathrm{D}}, \tag{5.32}$$

where we define the 1:TBSS signal detector environmental background noise mean photon number $\bar{n}_{\mathrm{B,S,E}}$ and the detector dark count mean photon number $\bar{n}_{\mathrm{D}} = \bar{n}_{\mathrm{B,I}}$. We assume that the only noise for the idler detector is from detector dark counts, as we can shield the idler detector system from the environment. By separating the environmental noise and dark counts in our analysis this means that M:TBSS systems will have different noise counts, due to the added dark counts as the number of detectors increase. However, it is still fair to compare different M:TBSS systems as the signal light and the environmental noise is still distributed fairly. It is clear that the benefit from increasing the number of spectral modes M is limited by the dark counts having a dominant effect over the distributed environmental noise. This limitation from dark counts means there is an optimal number of spectral modes M. Figure 5.2 shows how the SNR varies with the number of spectral modes M. As shown by Frick in Ref. [159] the optimal number of spectral modes M_{opt} is when

$$\frac{\partial \mathrm{SNR}}{\partial \mathrm{M}}\bigg|_{M_{\mathrm{opt}}=M} = 0. \tag{5.33}$$

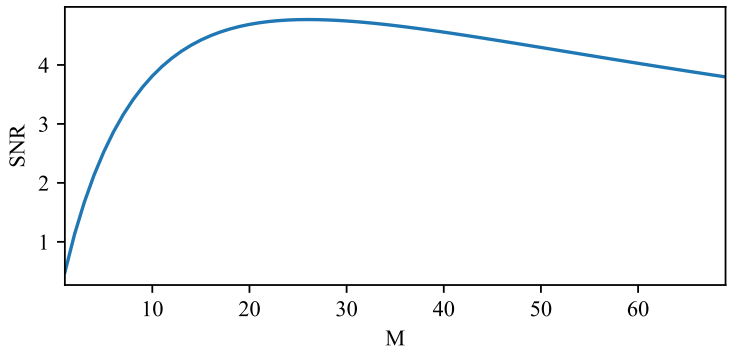

FIGURE 5.2 – SNR as a function of modes M. $\bar{n} = 0.5$, $\eta_{\mathrm{S/I}} = 0.5$, $\xi = 0.5$, $\bar{n}_{\mathrm{B,S}} = 0.51$, $\bar{n}_{\mathrm{B,I}} = 0.01$. The optimal number of spectral modes $M_{\mathrm{opt}} = 26$.

Moreover, the use of the LLV framework to quantify M:TBSS performance is shown in the object absent to present rolling window in Fig. 5.3. The distinguishability for 1:TBSS $\phi_1 = 0.552$, 2:TBSS $\phi_2 = 0.705$, 3:TBSS $\phi_3 = 0.761$ and 4:TBSS $\phi_4 = 0.787$. It is clear from both Fig. 5.3 and the distinguishabilities that the relative advantage reduces as $M < M_{\mathrm{opt}}$ increases. The different time-series plots for M:TBSS in Fig. 5.3 appears piece-wise. This is due to the sudden nature of the object absent to present regime change at $N = 200$, the rolling window which takes $N = 100$ shots to update fully to the other regime and that this is the average of 1×10^4 Monte-Carlo simulated LLV trajectories. At each shot number N there is a distribution of LLV values, which has accrued due to the many Monte-Carlo simulation runs. From this distribution we are able to plot the error bars shown in Fig. 5.3 as the standard deviation above and below the mean LLV. In Ch. 7 we discuss the methodology behind the Monte-Carlo simulation used to generate Fig. 5.3 and that while we can analytically generate this figure, the individual trajectories which constitute the distribution of LLV values are of interest for signal processing and testing our protocol.

To summarise, this chapter begins with a motivation of why we wish to extend the theory of the non-classical light we consider for QI, as there are multi-mode correlations between the two beams. Hence, it is advantageous to develop a generalised theory to exploit them. We lead onto the prerequisite theory about the notation for expressing mode correlations. After this, we derive the state vector and density matrix for the multi-mode twin-beam state of light: the multi-mode distributed twin-beam squeezed state (M:TBSS). We then lead onto the click detector POVMs pertaining to all the possible combinations of events and the corresponding click probabilities. We then define the LLV for the M:TBSS. To ease the application of this theory to our LIDAR protocol, we can make a few simplifications and refer to this as simplified M:TBSS. We mention that the previously defined FOMs also apply to the M:TBSS theory.

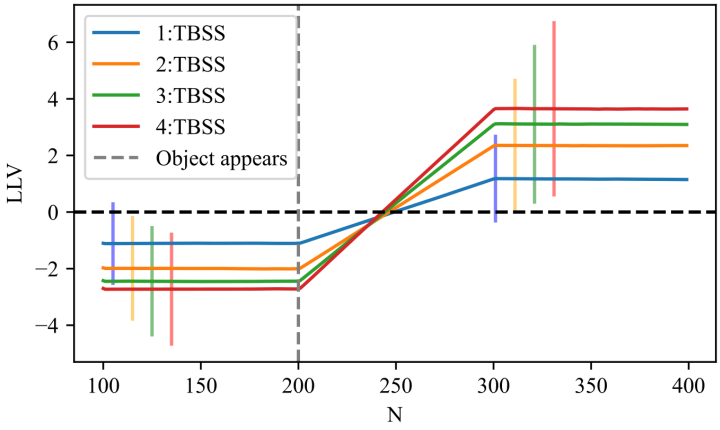

Figure 5.3 – Rolling window of the mean LLV from object absent to present for 1:TBSS, 2:TBSS, 3:TBSS and 4:TBSS, with an error bar of one standard deviation plotted too. Rolling window size of 100 shots, $\bar{n} = 0.5$, $\eta_{\mathrm{S/I}} = 0.5$, $\xi = 0.5$, $\bar{n}_{\mathrm{B,S}} = 0.51$, $\bar{n}_{\mathrm{B,I}} = 0.01$.

From this, we lead onto performance comparison for a different number of modes used for each beam. Our performance analysis reveals an optimal number of modes we can use in each beam to maximise distinguishability.

Chapter 6: Practical jamming-resilient LIDAR protocol

6.1 Foundation to protocol

A LIDAR model requires the ability to detect and range-find a possible target object. Earlier in this thesis we introduced the tools for detecting or ruling out a possible target object, for a known distance. In this chapter we provide our method for range-finding. We introduce essential aspects of range-finding such as spatial resolution, temporal resolution and target object scattering properties. Furthermore, in this chapter we reinforce the knowledge that improved covertness and jamming-resilience is granted by the use of quantum-enhanced LIDAR when detecting or range-finding a target object.

The previous chapters of this thesis present the precursor material before introduction of our LIDAR model. Chapter 2 discusses the light sources used and the type of noise in our system. Chapter 3 discusses the detectors used and how we make measurements. Moreover, in Ch. 3 we include effects such as system loss and signal attenuation from probing a possible target object. Chapter 4 introduces the methods for assessing system performance. The ability to assess system performance is paramount for any remote sensing protocol, as it instructs the practicality of object detection and ranging in certain scenarios. Chapter 5 extends our theory to include multi-mode information on both the idler and signal channels. The use of this multi-mode information improves system performance and covertness, it also grants additional resilience to jamming.

6.2 Range-finding

We perform range-finding by exploiting timing information and prior knowledge of the reflection properties of a possible target object. It takes more time for our signal light to reach the object and back-scatter towards our detector than it does for our idler light. We refer to this time

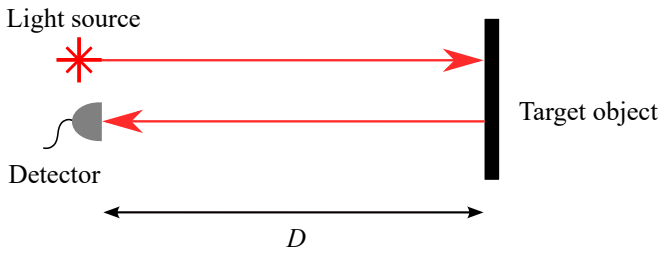

Figure 6.1 – Idealised diagram of the probing a target object and that light back-reflecting towards our detector.

taken as the time delay

$$t(D) = \frac{2D}{c}, \tag{6.1}$$

where c is the speed of light in the medium (approximated as the speed of light in a vacuum for simplicity). Figure 6.1 visualises the path for light to leave our source and reflect from the target object back towards our detector. The distance of this path is what sets the time delay $t(D)$.

A technology which facilitates range-finding for classical single-photon LIDAR is known as time-correlated single-photon counting (TCSPC). This involves time-tagged pulses which are then correlated with the return photon-count statistics [9], [160]. However, there are downsides to the use of pulsed light sources for remote sensing. For example, there is a reduction of covertness as pulses are easier to detect than a CW source with the equivalent power, due to the short duration the power of a pulse is concentrated within. Therefore, an alternative modality for remote sensing is classical CW LIDAR via amplitude or frequency modulation of the source light output [161]. A CW or pseudo-thermal source for classical ghost imaging-based LIDAR is also possible [162]–[164]. Nevertheless, accurate remote sensing is difficult at low signal strength and high noise regimes for any modality of classical single-photon LIDAR.

Our CI model is not the optimal modality for classical LIDAR. For example, this is because of the lack of modulation or use of classical correlations. For a pulsed source our CI model can perform range-finding akin to TCSPC. Whereas, the CI model with a CW light source cannot accurately range-find due to the lack of timing information available for the probe beam. The remainder of this thesis will focus on ranging for QI, ignoring CI. We can ignore CI for our treatment of range-finding as the system performance analysis of CI and QI in Ch. 4 shows that even if we perfectly know the distance of the target that QI performs better.

We use the strong non-classical temporal correlations between the idler and signal beams to range-find [81]. The idler beam is locally measured and therefore has no delay as its distance from source to detector is known, whereas the signal beam does have a delay due to the distance

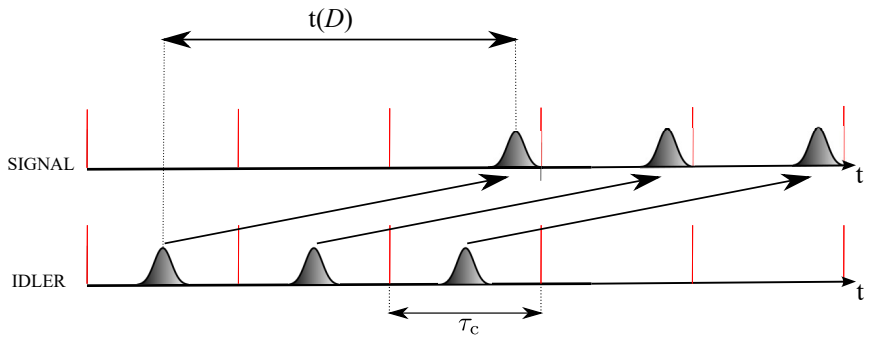

Figure 6.2 – Idealised depiction of detector click-event post-processing for the signal and idler channels as a function of time discretised into time-bins. Clicks events are represented by the coloured pulses. The signal beam is delayed by $M_{\text{delay}}(D) = 2$ time-bins.

of the object. This delay is often unknown as the distance of the object is often unknown. The quantum advantage from coincidence counting is recovered by correctly matching idler and signal channels with an appropriate delay. We segment time into time-bins, where each time-bin corresponds to a shot of the system (which has a temporal duration set by the coincidence window size τ_c). Therefore, the expected signal beam delay is also discretised into time-bins. Our pump source can be either in pulsed or CW operation, it does not matter as the idler and signal output from the SPDC process are pulses. The expected delay of the signal beam in shots for an object at distance D from the detector is

$$M_{\text{delay}}(D) = \lfloor t(D) f_{\text{rep}} \rfloor \,, \tag{6.2}$$

where the source repetition rate $f_{\text{rep}} = 1/\tau_c$, which is dependent on the coincidence window size τ_c. Therefore, the idler data stream is matched with the signal data stream shifted back $M_{\text{delay}}(D)$ shots, for an inspected distance D. Figure 6.2 shows how delay-matching in post-processing will correlate the signal and idler channel channels segmented into time-bins of temporal size τ_c. The desire for considering a system with a discretised delay is that separate data channels do not suffer from coincidence counting cross-talk, as the coincidence windows do not overlap. Chapter 8 demonstrates range-finding when the discretised delay approach is not possible (due to the small distances we attempt to discriminate between); therefore, the effect of cross-talk and the lack of our discretised delay approach is discussed there. We define the spatial resolution of the system D_r as

$$D_r = \frac{c}{2 f_{\text{rep}}}. \tag{6.3}$$

Timing jitter due to our detector (and to a lesser degree to our source and the object) can cause the misbinning of click events. The deleterious effect of misbinning could be that an object is falsely inferred at a wrong distance, thereby affecting the range-finding ability of our protocol. As the target object distance is never an integer value of the spatial resolution there is an increased chance of misbinning, as on average the return clicks can be closer to the edges of a particular time-bin. However, as mentioned earlier, timing jitter is neglected in our model as we set the coincidence window size τ_c such that the effect of timing jitter is negligible. Previous literature for simple-detection based QI range-finding describes timing jitter corresponding to ≈ 10 cm range uncertainty [159], which is smaller than the range resolution we specify henceforth at 30 cm. We define the (realistic) temporal resolution $t_r(D)$ which determines how quickly our system can make a confident LLV sample for a distance D. This depends on the source repetition rate f_{rep} and the threshold distinguishability ϕ_t, therefore the temporal resolution is

$$t_r(D) = \frac{N_t(D)}{f_{\text{rep}}}. \tag{6.4}$$

There is also a quantum LIDAR range formula (for Lambertian-type scatterers) [165]. This allows for calculation of the maximum range $D_{\max}$ our protocol can detect an object, for one LLV sample of N shots. The quantum LIDAR range formula is

$$D_{\max} = \sqrt{\frac{c_{\max:I} A n \xi_{\text{obj}}}{2\pi c_{\text{noise}}}}, \tag{6.5}$$

where $c_{\max:I}$ is the maximum idler count rate, A is detector area, n is the number of photons given an idler count, ξ_{obj} is the intrinsic reflectivity of an object and c_{noise} is the noise count rate. We can relate this directly to our model by setting $c_{\max:I} = \left(N \times \Pr_I + 4\sqrt{N \times \Pr_I(1-\Pr_I)}\right)\frac{1}{\tau_c \times N}$ and $c_{\text{noise}} = \left(N \times \Pr_{H0}\right)\frac{1}{\tau_c \times N}$. Of course, the estimation from Eq. 6.5 does not set a hard limit for how far we can range a target object. We can beat the maximum range $D_{\max}$ set by Eq. 6.5 by taking more LLV samples.

6.3 Scattering and absorption of our probe light

This section deals with the scattering and absorption our probe beam experiences during the process of interrogating a target object. This process includes the journey towards an object, the reflection or absorption upon the object and the journey back towards our detector. The medium between our detectors and the target object can absorb or scatter some of our light, which is known as the atmospheric extinction. A modality of remote sensing known as

differential absorption LIDAR utilises the atmospheric extinction to investigate the properties of the atmosphere [166]. However, we neglect the effects of atmospheric absorption and scattering. This is due to the relatively short stand-off distance we typically consider for quantum-enhanced LIDAR and the high atmospheric transmissivity for visible and near-IR wavelengths. Another property we neglect is beam divergence of our signal beam from source to object. We neglect this property because of the relatively short distances we typically consider and that beam divergence is partially prevented if the beam is sufficiently collimated.

The signal attenuation factor ξ encodes all loss from the process of probing a target object. Within this factor ξ we define the object reflectance factor ξ_{obj}. A object reflectance factor of $\xi_{\text{obj}} = 1$ is an object that completely reflects all light incident upon it back to the detector and $\xi_{\text{obj}} = 0$ is an object that completely absorbs or reflects all light incident upon it not to the detector. Typical values in a realistic scenario of the signal attenuation factor are $\xi \ll 1$, where often the bulk of the loss is due to the intermediate space between the object and target, rather than the reflective property of the object itself (ξ_{obj}). We make an idealisation that a target object either perfectly adheres to the reflective properties of a specular or a Lambertian reflector. A specular reflector reflects light at an angle equal to its incident angle. An example of a specular reflector is a perfect mirror. A target object with specular reflectance directed is relatively easy to detect compared to a Lambertian scatterer, granted that it is angled such that the reflected light is aimed towards our detector. We refer to a specular reflector angled in this way as a cooperative target and we assume this scenario is true for the remainder of our discourse on specular reflectors. Figure 6.3 visualises what a specular reflector is in terms of beam geometry. Due to the assumptions of no beam divergence or atmospheric extinction the signal attenuation factor for a specular reflector as a function of object distance is

$$\xi(D) = \xi_{\text{obj}} \tag{6.6}$$

We now consider the Lambertian reflector and its influence on our signal attenuation factor ξ [167]. To derive ξ in our Lambertian model we have our initial intensity of light I_0 and our detected intensity of light $\mathrm{I}_{\text{det}} = \xi \mathrm{I}_0$. Light incident upon a Lambertian reflector is equally diffused over all possible angles upon reflection. Figure 6.4 visualises a perfect Lambertian reflector with beam geometry. A more realistic approach for describing target reflectivity of a rough-surface is the Rayleigh-fading target statistical model. It considers the speckle that tends to occur when LIDAR wavelengths interrogate rough surfaces. Here, speckle refers to the Rayleigh-distributed amplitude and uniformly-distributed phase in the return light. Reference [34] applies

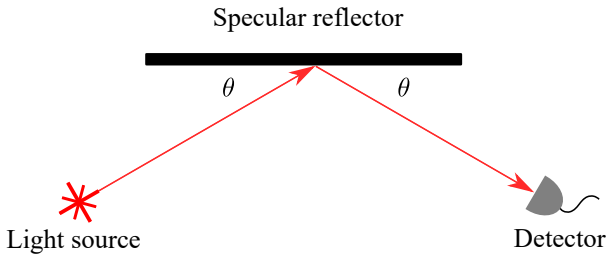

FIGURE 6.3 – A representation of a specular reflector. The angle of incidence θ for the light normal to the target object is the same as the angle of reflectance.

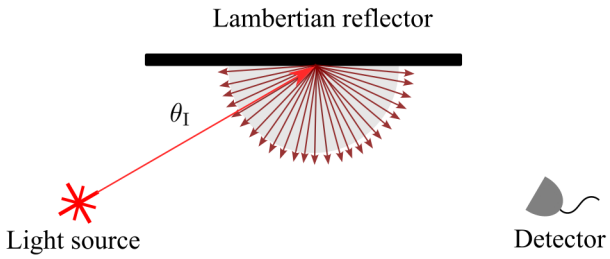

FIGURE 6.4 – A representation of a Lambertian reflector. A beam with angle of incidence θ_{I} strikes the Lambertian reflector and the reflected light is equally diffuse.

this model in the context of QI. However, we do not consider the Rayleigh-fading target model further as we restrict ourselves to the idealised scenarios of either a specular or Lambertian reflector. Lambert's cosine law applies to Lambertian reflectors. This law dictates that for a diffusely reflecting object, the initial intensity of light I_0 scales with the cosine of the incident angle θ_{I} with respect to the normal of the plane of the object. As the light reflects off the object with angle θ_{R}, we apply Lambert's cosine law a second time. Hence, we define the resulting intensity after scattering from the object $\mathrm{I_S} = \mathrm{I}_0\xi_{\mathrm{obj}}\cos(\theta_{\mathrm{I}})\cos(\theta_{\mathrm{R}})$. The double application of Lambert's cosine law is obvious in Fig. 6.5 as it shows our incident light I_0 striking the reflector at an angle θ_{I} and with the reflected beam leaving the object towards the detector at an angle θ_{R}. If our light source and detector is situated close together and the object is sufficiently far away from our detector then the angle of incidence and reflectance are approximately the same $\theta_{\mathrm{I}} \approx \theta_{\mathrm{R}} = \theta$. Realistic Lambertian objects are rough-surfaced and can move throughout the detection process, consequently the angle θ changes constantly. Therefore, we take the average of Lambert's law applied twice $\cos^2(\theta) = \frac{1}{2}$, which yields $\mathrm{I_S} = \frac{1}{2}\xi_{\mathrm{obj}}\mathrm{I}_0$ for the intensity after scattering off an object. No attenuation occurs upon the beam as it travelled towards the detector due to the lack of beam divergence, however it will attenuate as a function of distance

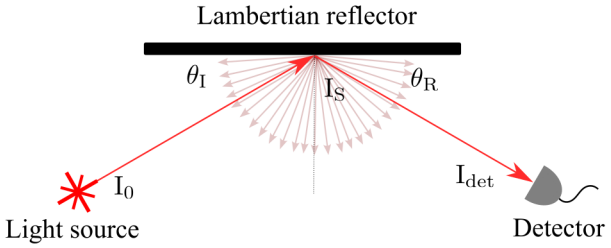

FIGURE 6.5 – A representation of why Lambert's cosine law is applied twice. A beam with angle of incidence θ_{I} strikes the Lambertian reflector and the reflected light returns to the detector with angle θ_{R}.

due to the diffuse nature of the post-reflected light. If the detector is at a distance D from the object, the light will spread out within a hemisphere with area $\mathrm{A}_D = 2\pi D^2$ due to the inverse square law. The factor of 2π in A_D is due to the light diffusing equally in all directions of a hemisphere. Furthermore, we define $\mathrm{A_{det}}$ as the area of our detector. The remainder of this thesis we set the area of the detector $\mathrm{A_{det}} = 1\ \mathrm{m}^2$ for the simulation results of range-finding. The ratio of $\mathrm{A_{det}}$ and A_D is the attenuation solely from distance. We restate the intensity of the light upon the detector as $\mathrm{I_{det}} = \mathrm{I_S}\frac{A_{\mathrm{det}}}{2\pi D^2} = \mathrm{I_0}\xi_{\mathrm{obj}}\frac{\mathrm{A_{det}}}{4\pi D^2}$. Therefore, for the Lambertian reflector model, the signal attenuation factor object distance is

$$\xi(D) = \frac{\mathrm{A_{det}}\xi_{\mathrm{obj}}}{4\pi D^2}. \tag{6.7}$$

6.4 LLV AND DISTANCE

It is intuitive to see that the signal attenuates as a function of travelled distance, which in turn affects the click probabilities and consequently the LLV. Of course, for the idealised model of a specular reflector there is no signal attenuation from distance, but a more realistic model of the specular reflector has signal attenuation mainly caused by beam divergence. Our model for the Lambertian reflector does however have signal attenuation affected by distance. Hence, the number of shots to reach threshold distinguishablity N_{t} increases with detector distance D. We require a specific LLV conditioned by k idler clicks for each each distance D

$$\Lambda_D(\underline{x}_D, k) = \ln\left(\frac{P_{\mathrm{H1},D}(\underline{x}_D, k)}{P_{\mathrm{H0},D}(\underline{x}_D, k)}\right), \tag{6.8}$$

with $P_{\mathrm{H1},D}$ ($P_{\mathrm{H1},D}$) defined as the click probability distribution for an object present (absent) at distance D after N_t shots, respectively. We also introduce $\underline{x}_D$ to refer to the click-count data from the idler detector data channel with no delay and the signal detector data channel with delay in time-bins $M_{\mathrm{delay}}(D)$. For a set of system parameters and for an inspected distance D, there is an expected mean coincidence click-count $\mu_{\mathrm{D:I},1}$ resulting from its corresponding number of shots $N_{\mathrm{t}}(D)$ required for threshold distinguishability. This expected mean coincidence click-count can differ for each inspected distance, whereas the expected mean LLV is approximately constant for all inspected distances. This is due to the adherence of the threshold distinguishability requirement which means the LLV test effectiveness is consistent for all inspected distances. Hence, the LLV is directly comparable for different distances. This ability to interpret different possible inspected distances simultaneously is a valuable feature for a range-finding protocol. The range-finding theory also applies to the multi-mode light (M:TBSS) we introduce in Ch. 5. Each idler channel and its respective correlated signal channel is encoded within $\underline{x}_{\mathrm{D}}$.

6.5 Range-finding statistics

The distance of a possible target object is unknown in a range-finding scenario, therefore the expected delay is also unknown. We systematically work through different possible distances (delays) from near to far, in search of the correct location. Analysis of the LLV distribution statistics for different inspected distances is essential for understanding how our LLV framework can discern the presence of a target object when range-finding. However, we are not able to generate analytically LLV distributions for inspected distances that are not at the correct object distance. This is because we are not able to predict how our signal light will cause accidental coincidence clicks with the idler data stream for incorrect signal beam delays. Instead, we computationally generate (via a Monte-Carlo simulation) the inspected distance LLV distributions by processing simulated data streams via the relevant LLV for that inspected distance $\Lambda_D(x_D, k)$. The methodology for this simulation is expanded upon in Ch. 7. We are able to discern that a certain delay is the correct one if it is sufficiently distinguished from the statistics of the LLV distributions corresponding to its neighbouring delays. This is because the correct delay LLV distribution is the only distribution underpinned by the strong temporal correlations for idler and signal beams. In the following section, we set a coincidence window size as $\tau_{\mathrm{c}} = \frac{1}{f_{\mathrm{rep}}} = 2 \times 10^{-9}$ s. This means that we have an spatial resolution of $D_{\mathrm{r}} = 0.3$ m.

Distance (m)	N_{t}	M_{delay}	ξ
2	6.64×10^3	6	1
2.7	6.64×10^3	9	1
3	6.64×10^3	10	1
3.3	6.64×10^3	11	1
6	6.64×10^3	20	1

Table 6.1 – Inspected distance properties for an object with specular reflectance and a spatial resolution of $D_{\mathrm{r}} = 0.3$ m. The columns are the distance (m), the shots required for threshold distinguishability $N_{\mathrm{t}}(D)$, signal stream delay in shots $M_{\mathrm{delay}}(D)$ for each object distance and ξ. System parameters are $\bar{n} = 0.01$, $\eta_{\mathrm{S/I}} = 0.5$, signal attenuation $\xi = 1$, $\bar{n}_{\mathrm{B,S}} = 0.5$ and $\bar{n}_{\mathrm{B,I}} = 4.49 \times 10^{-4}$.

6.5.1 Specular reflection

We first show the LLV statistics for a set of inspected distances for the specular reflector. For all inspected distances D, the LLV for k idler clicks is the same $\forall D,\ \Lambda_D(\underline{x}_D, k) = \Lambda(\underline{x}_D, k)$. The reason is that for our idealised model the signal attenuation parameter $\xi(D)$ does not vary with distance. Therefore, each inspected distance has the same shots required for threshold distinguishability $N_{\mathrm{t}}(D)$. Table 6.1 shows the properties for each inspected distance, when we have a specular reflector. Where we use the method in Appendix G to calculate N_{t}. Figure 6.6 shows the mean and one standard deviation error bar for a set of inspected distance LLV distributions. The target object is situated at a distance of $D_{\mathrm{correct}} = 3$ m. For the system parameters in Fig. 6.6 the expected object present mean LLV for all distances is $\mu_{\mathrm{E}} \approx 3.22$. In Fig. 6.6 it is clear that only the correct inspected distance LLV distribution has a mean identical to the expected object present mean LLV μ_{E}. It is therefore apparent that the target object is situated at 3 m, due to this strong signature. Figure 6.7 shows the inspected distance LLV distribution statistics when an object is absent. Whereas, for an object absent, all inspected distances statistics match their respective object absent statistical outcome.

6.5.2 Lambertian reflection

We now consider a target object with Lambertian scattering properties. Each inspected distance D has its own unique LLV conditioned by k idler clicks $\Lambda_D(\underline{x}_D, k)$. This is because for our Lambertian model the signal attenuation parameter $\xi(D)$ varies with distance. In consequence, each inspected distance has a unique value for shots required for threshold distinguishability $N_{\mathrm{t}}(D)$. Table 6.2 shows the properties for each inspected distance. Where we use the method in Appendix G to calculate N_{t}. The results for N_{t} from Appendix G are numerically consistent with the Monte-Carlo simulation approach as detailed in Ch. 7.2.1 to find the distinguishability ϕ — and hence find N_{t}. To put the shots required for confident detection for the 6 m distance

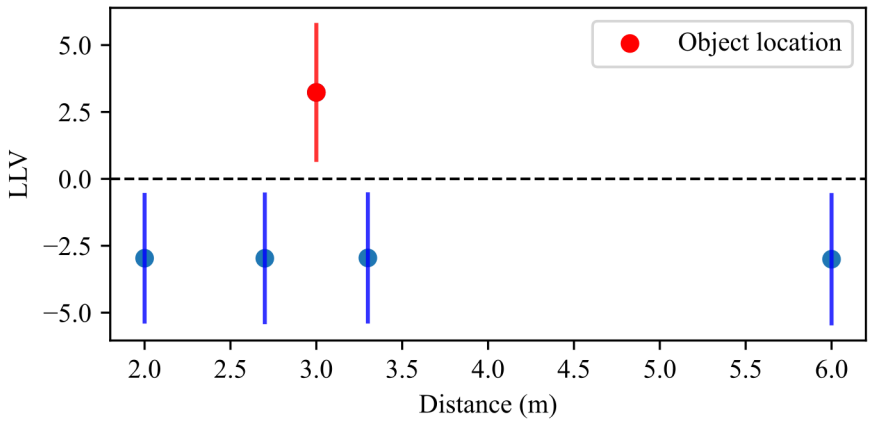

Figure 6.6 – Inspected distance LLV distributions when a specular reflecting object is situated at a distance 3 m. Mean and one standard deviation error bar plus and minus the mean plotted. The correct distance 3 m is shown as a blue dot and error bar. The shots required for threshold distinguishability N_{t}, signal stream delay in shots $M_{\mathrm{delay}}(D)$ for each object distance and ξ is given in Tab. 6.1. The horizontal (black) dashed line is the detection threshold $d_{\mathrm{LLV}} = 0$. $\bar{n} = 0.01$, $\eta_{\mathrm{S/I}} = 0.5$, $\bar{n}_{\mathrm{B,S}} = 0.5$ and $\bar{n}_{\mathrm{B,I}} = 4.49 \times 10^{-4}$. This figure is generated from 10^4 simulation runs.

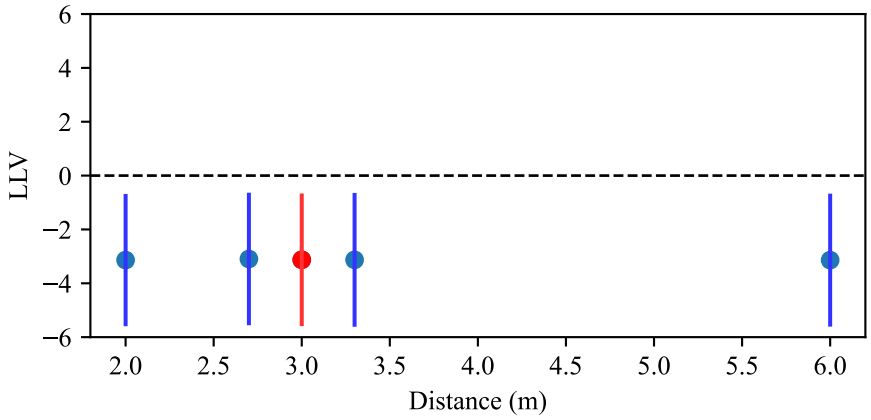

Figure 6.7 – Inspected distance LLV distributions when a specular reflecting object is absent. Mean and one standard deviation error bar plus and minus the mean plotted. The correct distance 3 m is shown as a blue dot and error bar. The shots required for threshold distinguishability $N_{\mathrm{t}}(D)$, signal stream delay in shots $M_{\mathrm{delay}}(D)$ for each object distance and ξ is given in Tab. 6.1. The horizontal (black) dashed line is the detection threshold $d_{\mathrm{LLV}} = 0$. $\bar{n} = 0.01$, $\eta_{\mathrm{S/I}} = 0.5$, $\bar{n}_{\mathrm{B,S}} = 0.5$ and $\bar{n}_{\mathrm{B,I}} = 4.49 \times 10^{-4}$. This figure is generated from 10^4 simulation runs.

Distance (m)	N_{t}	M_{delay}	ξ
2	1.35×10^{5}	6	1.98×10^{-2}
2.7	4.41×10^{5}	9	1.09×10^{-2}
3	6.69×10^{5}	10	8.84×10^{-3}
3.3	9.76×10^{5}	11	7.31×10^{-3}
6	1.05×10^{7}	20	2.21×10^{-3}

Table 6.2 – Inspected distance properties for a Lambertian reflecting object and a spatial resolution of $D_{\mathrm{r}} = 0.3$ m. The columns are the distance (m), the shots required for threshold distinguishability N_{t}, signal stream delay in shots $M_{\mathrm{delay}}(D)$ for each object distance and ξ. System parameters are $\bar{n} = 0.1$, $\eta_{\mathrm{S/I}} = 0.5$, signal attenuation $\xi = 1$, $\bar{n}_{\mathrm{B,S}} = 0.5$ and $\bar{n}_{\mathrm{B,I}} = 4.49 \times 10^{-4}$.

into perspective we use the coincidence window size $\tau_{\mathrm{c}} = 2$ ns used in the first experimental results in Ch. 8. Hence, the time required for a confident detection LLV sample at the distance of 6 m is $t \approx 0.02$ s. Meanwhile, Fig. 6.8 shows the mean and one standard deviation error bar for each inspected distance LLV distribution, for a set of distances. The target object is situated at a distance of $D_{\mathrm{correct}} = 3$ m. For the system parameters in Fig. 6.8 the expected object present mean LLV for all distances is $\mu_{\mathrm{E}} \approx 3.22$. Figure 6.8 does not show real-time statistics, as a single LLV sample for a far distance takes longer to acquire than a near distance in the Lambertian model. Therefore, we discard some simulation run results for the near distance in order to match the quantity of simulation results with the far distance. Figure 6.8 shows the object present statistics and the correctly inspected distance 3 m shows a strong signature, due to the correct coincidence matching. However, all of the falsely inspected distances display varying levels of a shifted LLV because the influence of accidental coincidence events are amplified by the mismatch of real incoming click-counts and what is expected from a certain inspected distance. Regardless, the two nearest inspected distances to the true distance (2.7 m and 3.3 m) are not shifted enough to obscure the LLV signature of the true distance. Whereas, for an object absent, all inspected distances statistics match their respective object absent statistical outcome and is identical to Fig. 6.7.

6.6 Real-time range-finding

An example of real-time range-finding for our protocol is now demonstrated. In this section we demonstrate real-time range-finding on an object with Lambertian scattering properties. For different inspected differences (i.e. different parameter regimes) to have their LLV's interpreted the same, we must ensure that each LLV sample is formed from its corresponding shots required for threshold distinguishability $N_t(D)$. Hence, for each inspected distance D an LLV sample is taken every $N_{\mathrm{t}}(D)$ shots. We define a set of K LLV samples as $\{\Lambda_1, \ldots, \Lambda_K\}$, with each LLV

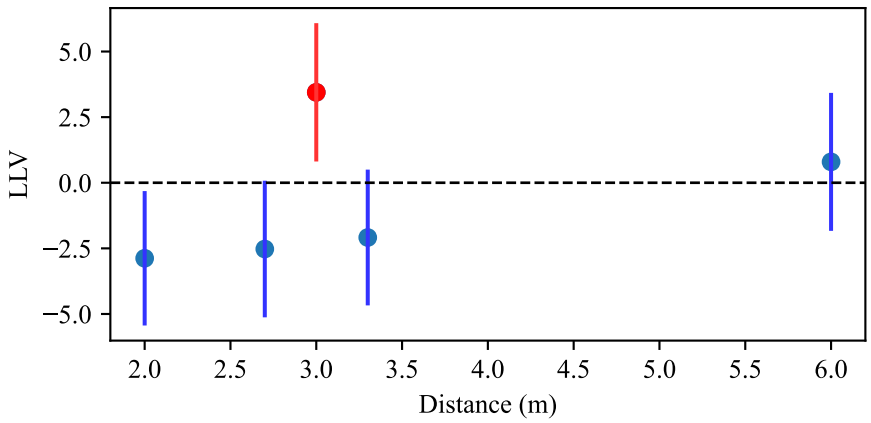

FIGURE 6.8 – LLV of simulated range-finding statistics when a Lambertian reflecting object is situated at a distance 3 m. The figure displays the mean and one standard deviation error bar, for each inspected distance. The correct distance 3 m is shown as a blue dot and error bar. The shots required for threshold distinguishability $N_{\mathrm{t}}(D)$, signal stream delay in shots $M_{\mathrm{delay}}(D)$ for each object distance and ξ is given in Tab. 6.2. The horizontal (black) dashed line is the detection threshold $d_{\mathrm{LLV}} = 0$. $\bar{n} = 0.1$, $\eta_{\mathrm{S/I}} = 0.5$, signal attenuation is modelled by the reflection of a perfect Lambertian scatterer at distance D, $\bar{n}_{\mathrm{B,S}} = 0.1$ and $\bar{n}_{\mathrm{B,I}} = 4.49 \times 10^{-4}$. This figure is generated from 10^4 simulation runs.

sample taken every $N_{\mathrm{t}}(D)$ shots. Chapter 4 defines the LLV sample rolling window $R(\tilde{s})$. Here, we specify a special case of this where the sample number $\tilde{s} = S$. Hence, it is no longer a rolling window and is instead the LLV sample mean $\mu_{\mathrm{S}} = \frac{\Sigma_{i=1}^{S} \Lambda_i}{S}$, for a total number of samples S, where $S \leq K$.

The LLV sample mean $\mu_{\mathrm{S}}(D)$ is plotted as a function of time-bin z in Fig. 6.9. This figure is generated from a Monte-Carlo simulation, as introduced in Ch. 7. The number of LLV samples $\lfloor z/N_{\mathrm{t}}(D) \rfloor$ that comprise $\mu_{\mathrm{S}}(D)$ increases with the elapsed time z in time-bins. The more LLV samples there are the sooner a confident detection decision is made, as for an unvarying system the statistics converge to the relevant inspected distance LLV distribution. The search for an object is executed by scanning from near to far, this is because near inspected distance have more LLV samples after an elapsed time and hence a confident detection decision is made sooner. Our range-finding protocol stops searching once there is a signature of an object at a distance D. Figure 6.9 shows how the different inspected distances (excluding 6 m) roughly converge by the last time-bin. The reason why the 6 m inspected distance only has a point in Fig. 6.9 is because the total elapsed time is equal to the number of shots for just one sample for the 6 m inspected distance. All inspected distances make the correct LLV test decision as well, with only the 3 m inspected distance displaying a strong signature for the object present LLV test decision. Our LIDAR protocol is able to extend to any distance. However, we limited the maximum distance

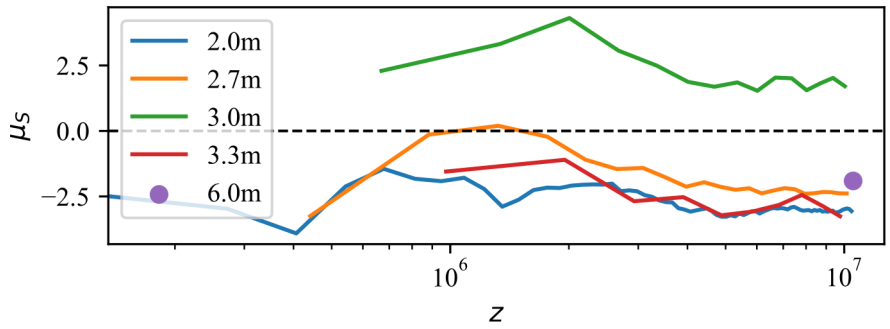

Figure 6.9 – Real-time signal trajectory of μ_{S} for the near (1.2 m), correct (3 m), one delay bin after correct (3.3 m) and far (6 m) inspected distances. Each inspected distance LLV sample has μ_{S} on the vertical axis and elapsed time in shots (i.e. time-bins) $z = M_{\mathrm{elapsed}}$ on the horizontal axis. The horizontal (black) dashed line is the detection threshold $d_{\mathrm{LLV}} = 0$. The total elapsed time in shots is $N_{\mathrm{t}}(6)$. The object situated at a distance 3 m. N_{t}, $M_{\mathrm{delay}}(D)$ and ξ given in Tab. 6.2. $f_{\mathrm{rep}} = 0.5$ GHz, $\bar{n} = 0.1$, $\eta_{\mathrm{S/I}} = 0.5$, signal attenuation is modelled by the reflection off a perfect Lambertian scatterer at distance D, $\bar{n}_{\mathrm{B,S}} = 0.1$ and $\bar{n}_{\mathrm{B,I}} = 4.49 \times 10^{-4}$.

considered in this chapter to a short-range 6 m, as the inverse square law for the Lambertian scatterer causes the shots required to drastically increase in value at a great computational cost for Monte-Carlo simulation.

Furthermore, the requirement that each LLV sample for an inspected distance must be made every $N_{\mathrm{t}}(D)$ shots is not necessary. However, if we wish to make an LLV sample for an inspected distance sooner, this at the expense of detection decision error and comparability of LLV between inspected distances. By recording an LLV sample sooner, this would mean that the shots is less than the shots required for threshold distinguishability $N < N_t(D)$. Therefore, this would cause P_{D} to decrease and P_{FA} to increase due to the larger overlap with a smaller integration time.

6.7 Velocity estimation

The ability to estimate the velocity of an object is invaluable for instructing the subsequent possible location of that object. There is classical LIDAR technology that uses the Doppler effect to estimate object velocity [168]. This can extend to quantum-enhanced LIDARs. The optimal performance for the precision of range and velocity estimation (via the Doppler effect) is limited by bounds set in [84]. However, we do not further consider velocity estimation via the Doppler shift as it is experimentally challenging to implement, as the Doppler shift for sensible velocities is near imperceptible. Instead, we present a cruder approach which depends on the upsurge of LLV at the inspected distance with the correct delay as an object moves through

space. For example, we present a simple demonstration of velocity estimation. An object is travelling directly towards our detector with an unknown velocity v_{obj}. We detect an object at a far distance D_{far} with the far distance LLV data stream at time-bin z_1. Following from this, we detect an object at a near distance D_{near} with the near distance LLV data stream at time-bin z_2. If we assume that the object is at a constant velocity, we can estimate its velocity with

$$v_{\text{obj}} = \frac{D_{\text{far}} - D_{\text{near}}}{\tau_{\text{c}}(z_2 - z_1)}. \tag{6.9}$$

Of course, some error arises due to the delay bin approach, which considers any distance D in a range $[D, D + D_{\text{r}})$ as the same distance.

6.8 Covertness

QI performs better than CI for object detection and ranging, particularly in low signal strength and high background noise regimes. A trivial point is that covertness is afforded by QI enabling confident detection at a lower signal strength than CI, because of the better performance of QI [86]. There are other aspects which mean that quantum-enhanced LIDAR enables covertness in a way that CI does not. For example, the theory for M:TBSS enables us to exploit that our source hops randomly around the spectrum within its JSA. This means that any particular spectral mode can have a lower signal strength for an M:TBSS enabled detector system than would be allowed for one-mode QI (which detects all of the spectral modes in one detector). The ability of M:TBSS to detect objects confidently using signal light weaker than one-mode QI (i.e. 1:TBSS) requires enables further covertness. Another point is that QI is able to detect and range-find using a CW-source pump, whereas for our experiment CI is completely unable to range-find. There is an inherent reduction of covertness with the use of a pulsed source, as with a pulsed source the signal power is highly concentrated temporally and therefore easier for a third party to detect. This is opposed to a CW-source which has the same signal strength but is temporally spread and is therefore relatively more difficult for a third party to detect. The ability of QI (and M:TBSS) to detect and range-find with a CW-source pump at considerably weaker signal strengths and with than CI highlights the improved covertness a quantum-enhanced LIDAR protocol provides.

6.9 Jamming-resilience

One of the major benefits of our quantum-enhanced LIDAR protocol is its resilience to jamming. Jamming can occur via a hostile party deliberately shining dynamic bright light towards our detector in order to obstruct our ability to accurately range-find or detect target objects. The coincidence counting approach for our quantum-enhanced LIDAR means that the influence of background light is reduced compared to the influence it has on CI.

Our LLV is based on prior estimation of the system parameters before jamming. Therefore, our LLV is out of tune to the real statistics during jamming. Fortunately, we can dynamically sample the real background noise when the strength of our signal is much weaker than the environmental background $\bar{n} << \bar{n}_{\mathrm{B,S}}$. Therefore, our LLV is dynamically updated and this can counter the effect of a varying background. Our method for dynamic background tracking is that we continually re-estimate the mean photon number of the signal detector $\bar{n}_{\mathrm{B,S}}$. This re-estimation is based off the average of the signal detector clicks from the rolling window size of previous samples, for each sample number. CI is not able to benefit from dynamic tracking as the signal is negligible compared to the varying background in the regimes we analyse.

The following section shows simulation of a jamming scenario for two different types of jamming. The first type is sinusoidal jamming, which is a slowly varying sine wave of background variation. This type of jamming is easy to track and hence mitigate its effect. The second type of jamming is pseudo-random fast jamming. An intermediate form of jamming (somewhere between sinusoidal slow jamming and pseudo-random fast jamming) is also possible. For this intermediate jamming scenario, we can take the (largest) Fourier components of the background light to partially mitigate the effect of this jamming. We can use the active background tracking techniques for sinusoidal slow jamming on the largest Fourier components. Whereas, for completely pseudo-random fast jamming, due to the unpredictable amplitude of noise this means that dynamic background tracking has less benefit than the (slow) sinusoidal jamming. In the following sections Ch. 6.9.1 and Ch. 6.9.2 we plot at the same time object present and object absent statistics under the influence of a varying background. The statistics that we plot are by LLV sample number, each of which is comprised of N shots. We are able to range-find under the presence of jamming, using the approach presented earlier by searching for the upsurge of LLV statistics at the correct delay with respect to neighbouring falsely guessed delays. However, to avoid over-complicating our exposition of jamming-resilience we assume that we know the distance of the object and hence its delay.

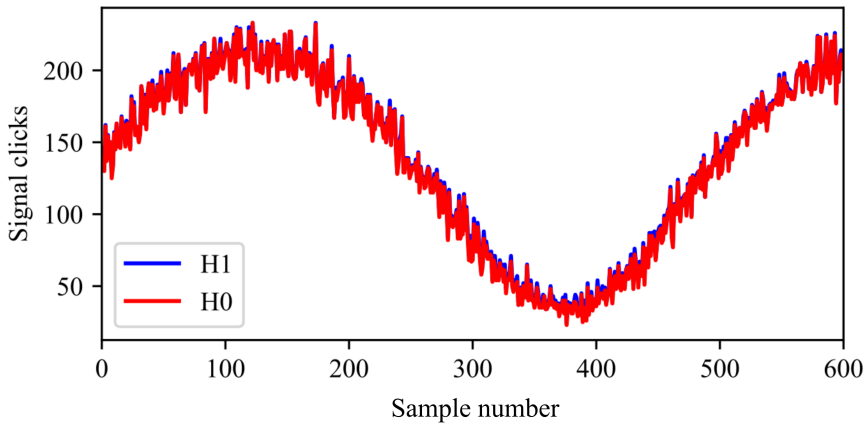

Figure 6.10 – Signal clicks as a function of sample number. Object present and absent statistics shown, undergoing sinusoidal slow jamming. The horizontal (black) dashed line is the detection threshold $d_{\mathrm{LLV}} = 0$. $\bar{n} = 0.02$, $\eta_{\mathrm{S/I}} = 0.5$, signal attenuation factor $\xi = 0.5$, $\bar{n}_{\mathrm{B,S}} = \bar{n}_{\mathrm{B,S,E}} + \bar{n}_{\mathrm{B,I}}$, $\bar{n}_{\mathrm{B,S,E}} = 0.3$ and $\bar{n}_{\mathrm{B,I}} = 0.0001$. Each sample is comprised of $N = 600$ shots. Amplitude of the sinusoidal jamming $\mathrm{a} = 0.8\bar{n}_{\mathrm{B,S,E}}$ and periodicity $\mathrm{b} = \pi/250$.

6.9.1 Slow jamming

As a function of sample number $\tilde{s}$ the mean photon number of the signal detector environmental noise in the presence of sinusoidal slow jamming is $\bar{n}_{\mathrm{B,S,E}}(\tilde{s}) = \mathrm{a}\sin(\mathrm{b} \times \tilde{s}) + \bar{n}_{\mathrm{B,S,E}}$, where a is the amplitude of the jamming and b is the periodicity. Figure 6.10 shows the signal clicks for both object present and absent as a function of sample number $\tilde{s}$. It is clear in Fig. 6.10 that the signal clicks for either situation of object present or absent are near identical.

In Fig. 6.11 we apply an LLV sample rolling window with refresh rate of $S = 90$ samples to the LLV statistics for object present and absent, for both CI and QI. The benefit of applying a rolling window is that it reduces the variance of our statistics, as per the theory of the average distinguishability introduced in Ch. 4, which improves our distinguishability and ability to visually discern between object present and absent scenarios. It is clear that the QI statistics for object present and absent are distinguished from each other, but are still negatively affected by the jamming. It is also clear that CI LLV statistics are not distinguished from each other. In Fig. 6.11 for CI (and infrequently QI) false LLV test decisions are made due to the jamming. With the dynamic background tracking shown in Fig. 6.12 for QI, we see that the effect of jamming is countered by the dynamic background tracking and the QI statistics no longer given false LLV test decisions. For example in Fig. 6.11 without the dynamic background tracking, the lower background noise (with respect to the initial background noise estimation) at around sample number 400 is misconstrued by our LLV statistics as a reduction of the likelihood of

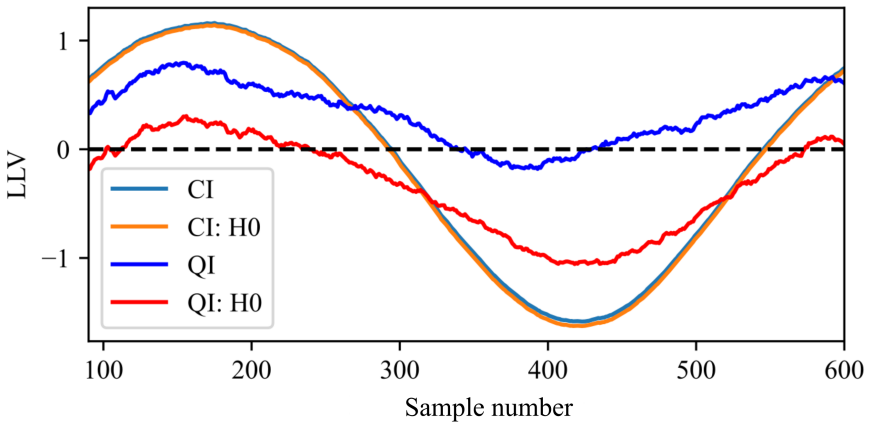

Figure 6.11 – LLV as a function of rolling window sample number. Object present and absent statistics shown for QI and CI, undergoing sinusoidal slow jamming. The horizontal (black) dashed line is the detection threshold $d_{\mathrm{LLV}} = 0$. $\bar{n} = 0.02$, $\eta_{\mathrm{S/I}} = 0.5$, signal attenuation factor $\xi = 0.5$, $\bar{n}_{\mathrm{B,S}} = \bar{n}_{\mathrm{B,S,E}} + \bar{n}_{\mathrm{B,I}}$, $\bar{n}_{\mathrm{B,S,E}} = 0.3$ and $\bar{n}_{\mathrm{B,I}} = 0.0001$. Each sample is comprised of $N = 600$ shots. Amplitude of the sinusoidal jamming a $= 0.8\bar{n}_{\mathrm{B,S,E}}$ and periodicity b $= \pi/250$.

object presence, because of the relative reduction of coincidence clicks. Whereas in Fig. 6.12 with dynamic background tracking, this lower background noise at sample number 400 is accounted for by a (dynamically) updated LLV test. Therefore, the LLV test correctly anticipates a relative reduction of coincidence clicks originating from noise, thereby increasing the object present LLV statistics.

6.9.2 Fast jamming

In the presence of pseudo-random fast jamming, for any sample number $\tilde{s}$, the mean photon number of signal detector environmental noise is subject to selection by a pseudo-random number in a range of values from $[\bar{n}_{\mathrm{B,S,E}} - a\bar{n}_{\mathrm{B,S,E}}, \bar{n}_{\mathrm{B,S,E}} + a\bar{n}_{\mathrm{B,S,E}}]$. Where we define a as the range amplitude for the fast jamming. Figure 6.13 shows the signal clicks for both object present and absent as a function of sample number $\tilde{s}$, undergoing pseudo-random fast jamming. It is clear in Fig. 6.13 that the signal clicks for either situation of object present or absent are near identical. In Figure 6.14 we apply an LLV sample rolling window with refresh rate of $S = 90$ to the LLV statistics for object present and absent, for both CI and QI. It is clear that the QI statistics for object present and absent are distinguished from each other. Moreover, the CI LLV statistics are not distinguished from each other, we can see that false LLV test decisions are made due to the pseudo-random fast jamming for CI. Figure 6.15 shows the dynamic background tracking for QI. We see that the dynamic background tracking for the pseudo-random fast jamming does not provide any notable advantage in this regime of jamming.

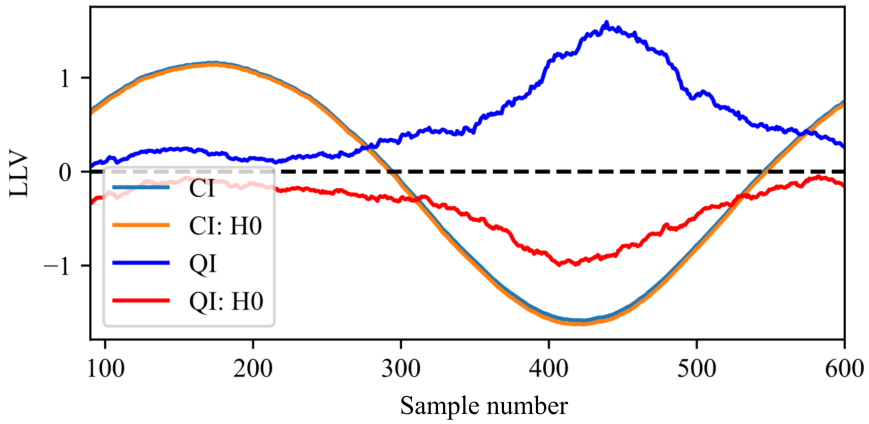

Figure 6.12 – LLV as a function of rolling window sample number. Dynamic background tracking is applied for QI. Object present and absent statistics shown for QI and CI, undergoing sinusoidal slow jamming. The horizontal (black) dashed line is the detection threshold $d_{\mathrm{LLV}} = 0$. $\bar{n} = 0.02$, $\eta_{\mathrm{S/I}} = 0.5$, signal attenuation factor $\xi = 0.5$, $\bar{n}_{\mathrm{B,S}} = \bar{n}_{\mathrm{B,S,E}} + \bar{n}_{\mathrm{B,I}}$, $\bar{n}_{\mathrm{B,S,E}} = 0.3$ and $\bar{n}_{\mathrm{B,I}} = 0.0001$. Each sample is comprised of $N = 600$ shots. Amplitude of the sinusoidal jamming $\mathrm{a} = 0.8\bar{n}_{\mathrm{B,S,E}}$ and periodicity $\mathrm{b} = \pi/250$.

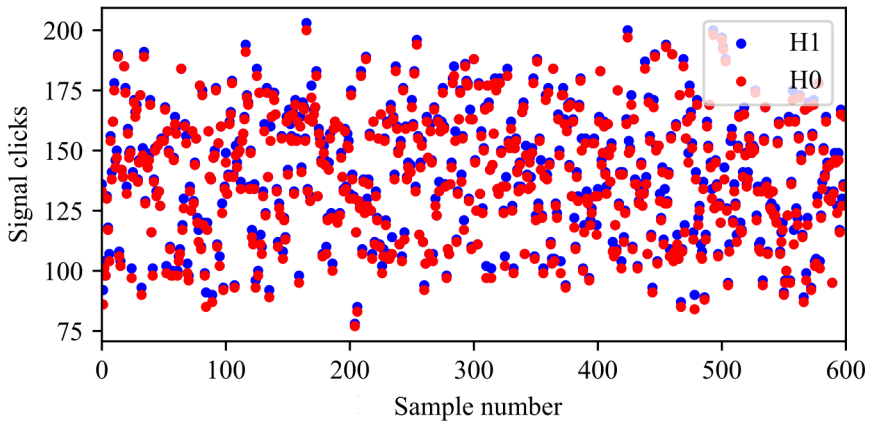

Figure 6.13 – Signal clicks as a function of sample number. Object present and absent statistics shown, undergoing pseudo-random fast jamming. The horizontal (black) dashed line is the detection threshold $d_{\mathrm{LLV}} = 0$. $\bar{n} = 0.02$, $\eta_{\mathrm{S/I}} = 0.5$, signal attenuation factor $\xi = 0.5$, $\bar{n}_{\mathrm{B,S}} = \bar{n}_{\mathrm{B,S,E}} + \bar{n}_{\mathrm{B,I}}$, $\bar{n}_{\mathrm{B,S,E}} = 0.3$ and $\bar{n}_{\mathrm{B,I}} = 0.0001$. Each sample is comprised of $N = 600$ shots. Amplitude of the range of the fast jamming $\mathrm{a} = 0.4$.

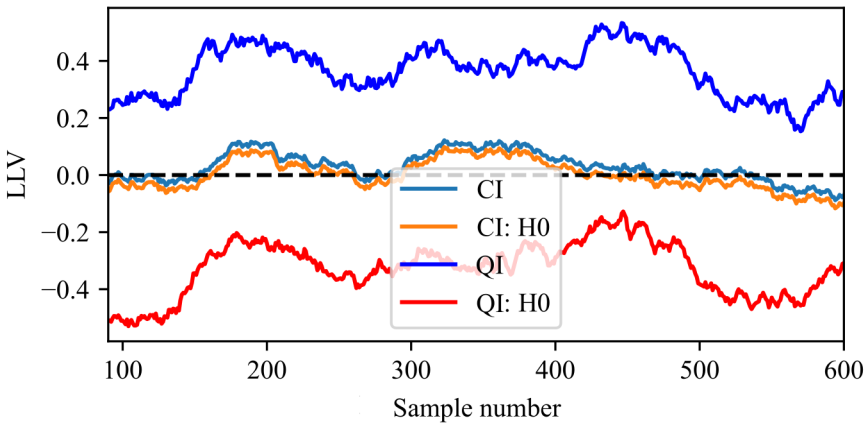

Figure 6.14 – LLV as a function of rolling window sample number. Object present and absent statistics shown for QI and CI, undergoing pseudo-random fast jamming. The horizontal (black) dashed line is the detection threshold $d_{\mathrm{LLV}} = 0$. $\bar{n} = 0.02$, $\eta_{\mathrm{S/I}} = 0.5$, signal attenuation factor $\xi = 0.5$, $\bar{n}_{\mathrm{B,S}} = \bar{n}_{\mathrm{B,S,E}} + \bar{n}_{\mathrm{B,I}}$, $\bar{n}_{\mathrm{B,S,E}} = 0.3$ and $\bar{n}_{\mathrm{B,I}} = 0.00001$. Each sample is comprised of $N = 600$ shots. Amplitude of the range of the fast jamming a = 0.4.

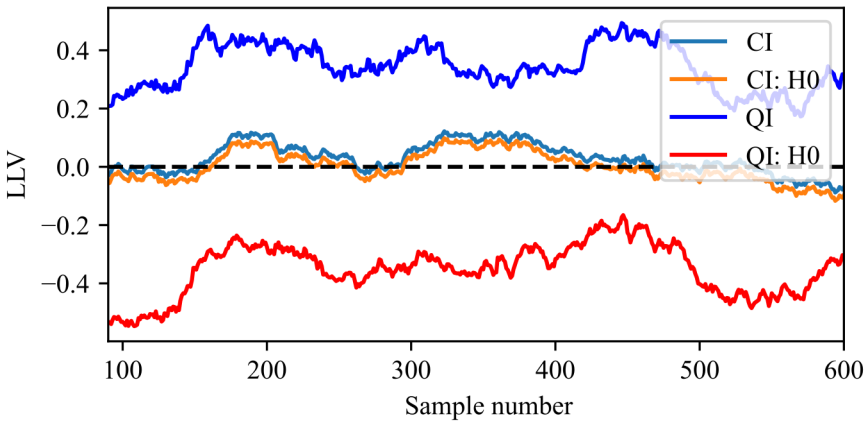

Figure 6.15 – LLV as a function of rolling window sample number. Dynamic background tracking is applied for QI. Object present and absent statistics shown for QI and CI, undergoing pseudo-random fast jamming. The horizontal (black) dashed line is the detection threshold $d_{\mathrm{LLV}} = 0$. $\bar{n} = 0.02$, $\eta_{\mathrm{S/I}} = 0.5$, signal attenuation factor $\xi = 0.5$, $\bar{n}_{\mathrm{B,S}} = \bar{n}_{\mathrm{B,S,E}} + \bar{n}_{\mathrm{B,I}}$, $\bar{n}_{\mathrm{B,S,E}} = 0.3$ and $\bar{n}_{\mathrm{B,I}} = 0.00001$. Each sample is comprised of $N = 600$ shots. Amplitude of the range of the fast jamming a = 0.4.

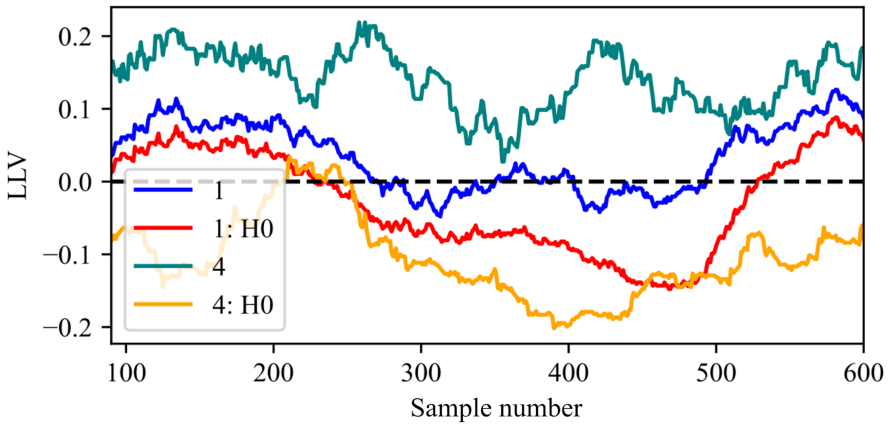

Figure 6.16 – LLV as a function of rolling window sample number. Object present and absent statistics shown for 4:TBSS (denoted as 4) and 1:TBSS (denoted as 1), undergoing sinusoidal slow jamming. The horizontal (black) dashed line is the detection threshold $d_{\mathrm{LLV}} = 0$. $\bar{n} = 0.0005$, $\eta_{\mathrm{S/I}} = 0.5$, signal attenuation factor $\xi = 0.5$, $\bar{n}_{\mathrm{B,S}} = \bar{n}_{\mathrm{B,S,E}} + \bar{n}_{\mathrm{B,I}}$, $\bar{n}_{\mathrm{B,S,E}} = 0.3$ and $\bar{n}_{\mathrm{B,I}} = 0.00001$. Each sample is comprised of $N = 2800$ shots. Amplitude of the sinusoidal jamming $\mathrm{a} = 0.8\bar{n}_{\mathrm{B,S,E}}$ and periodicity $\mathrm{b} = \pi/250$.

6.9.3 M:TBSS

There are situations such that the jamming is so intense or the return signal is so weak that even QI (1:TBSS) is unable to accurately discriminate between object present or absent, even with dynamic background tracking. Therefore, this section presents how the increase of spectral modes for an M:TBSS system can improve the resilience to jamming. The jamming-resilience is afforded by an M:TBSS system because as the number of M spectral modes increases, the background noise incident on each of the M signal detectors is reduced. This reduction occurs as we assume that the bandwidth of each detector for an M:TBSS system is a segment of the bandwidth for a detector in a 1:TBSS system, therefore a higher M means that each detector bandwidth (and hence the incoming background noise) is smaller. With a reduction of the background noise, this reduces the ability for jamming to negatively influence our system due to this spectral filtering. Another reason why jamming-resilience is improved by an M:TBSS system is that an increase of M decreases our M:TBSS mean photon number $\bar{n}_{\mathrm{M}}$, thereby the HG is more pronounced. Moreover, as we have access to the idler detectors and a 3rd party does not, we know which of the M signal detectors is conditioned after an idler click. Figure 6.16 shows object present and absent LLV for 1:TBSS and 4:TBSS as a function of LLV sample number, in the presence of sinusoidal slow jamming. 1:TBSS is greatly affected by the jamming and 4:TBSS is not as affected, but it still causes false LLV test decisions. Figure 6.17 shows the same as Fig. 6.16 but with dynamic background tracking applied. 1:TBSS still makes false LLV test

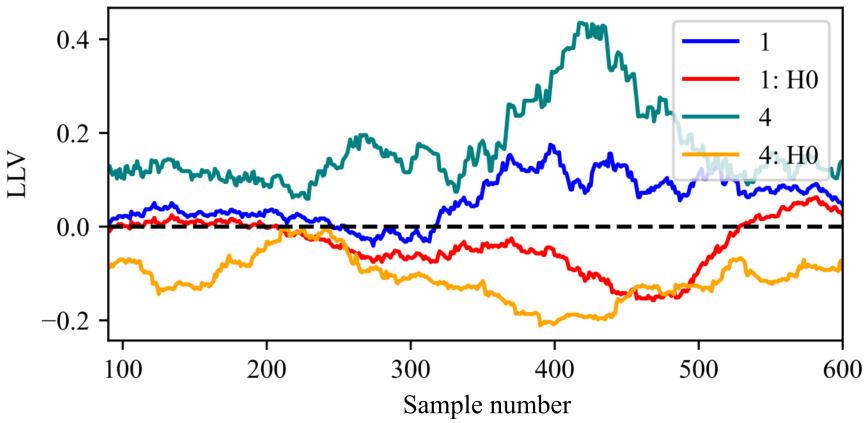

Figure 6.17 – LLV as a function of rolling window sample number. Dynamic background tracking is applied for both 1:TBSS and 4:TBSS. Object present and absent statistics shown for 4:TBSS (denoted as 4) and 1:TBSS (denoted as 1), undergoing sinusoidal slow jamming. The horizontal (black) dashed line is the detection threshold $d_{\mathrm{LLV}} = 0$. $\bar{n} = 0.0005$, $\eta_{\mathrm{S/I}} = 0.5$, signal attenuation factor $\xi = 0.5$, $\bar{n}_{\mathrm{B,S}} = \bar{n}_{\mathrm{B,S,E}} + \bar{n}_{\mathrm{B,I}}$, $\bar{n}_{\mathrm{B,S,E}} = 0.3$ and $\bar{n}_{\mathrm{B,I}} = 0.00001$. Each sample is comprised of $N = 2800$ shots. Amplitude of the sinusoidal jamming $\mathrm{a} = 0.8\bar{n}_{\mathrm{B,S,E}}$ and periodicity $\mathrm{b} = \pi/250$.

decisions, but 4:TBSS now makes consistent correct LLV test decisions. This shows a scenario where 4:TBSS is resilient to intense jamming, when 1:TBSS is not. Figure 6.18 shows object present and absent LLV for 1:TBSS and 4:TBSS as a function of rolling window sample number, in the presence of pseudo-random fast jamming. 1:TBSS is greatly affected by the jamming and 4:TBSS is not as affected, but it still causes false LLV test decisions. Figure 6.19 shows the same as Fig. 6.18 but with dynamic background tracking applied. 1:TBSS still makes false LLV test decisions, but 4:TBSS now makes consistent correct LLV test decisions. This again shows a scenario where 4:TBSS is resilient to intense jamming, when 1:TBSS is not. Contrary to the previous application of dynamic background tracking, Fig. 6.19 shows an improvement in the LLV test decisions compared to Fig. 6.18. This is because the amplitude of the jamming is greater in Fig. 6.18 than in Fig. 6.14.

We begin this chapter by relating the previous chapters to the necessary background for presenting a LIDAR protocol with jamming-resilience. We discuss the basics behind range-finding and how it relates to our discretised time framework for coincidence matching. We then discuss different models for expected signal attenuation, which correspond to various types of scattering off a possible target object. We discuss how to incorporate delay information into our LLV framework. After this, there are plots of the range-finding statistics for specular and Lambertian reflectors at different distances. However, these are not real-time range-finding statistics. We demonstrate how the LLV is affected nonlinearly when we consider delays for

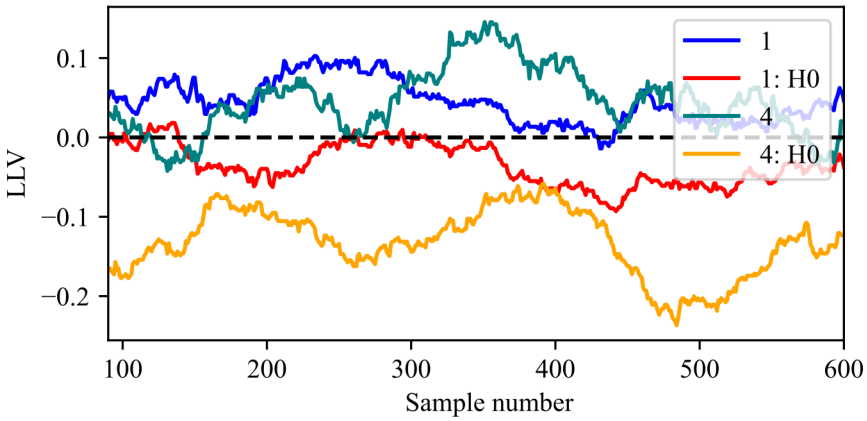

Figure 6.18 – LLV as a function of rolling window sample number. Object present and absent statistics shown for 4:TBSS (denoted as 4) and 1:TBSS (denoted as 1), undergoing pseudo-random fast jamming. The horizontal (black) dashed line is the detection threshold $d_{\mathrm{LLV}} = 0$. $\bar{n} = 0.0005$, $\eta_{\mathrm{S/I}} = 0.5$, signal attenuation factor $\xi = 0.5$, $\bar{n}_{\mathrm{B,S}} = \bar{n}_{\mathrm{B,S,E}} + \bar{n}_{\mathrm{B,I}}$, $\bar{n}_{\mathrm{B,S,E}} = 0.3$ and $\bar{n}_{\mathrm{B,I}} = 0.00001$. Each sample is comprised of $N = 2800$ shots. Amplitude of the range of the fast jamming a $= 0.8$.

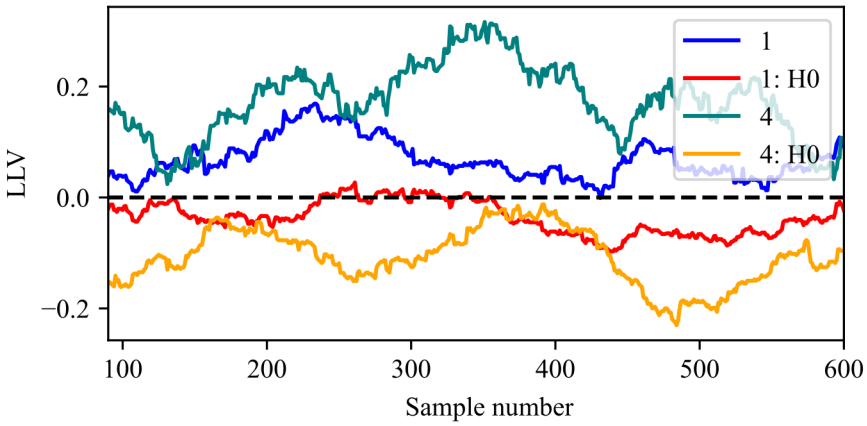

Figure 6.19 – LLV as a function of rolling window sample number. Dynamic background tracking is applied for both 1:TBSS and 4:TBSS. Object present and absent statistics shown for 4:TBSS (denoted as 4) and 1:TBSS (denoted as 1), undergoing pseudo-random fast jamming. The horizontal (black) dashed line is the detection threshold $d_{\mathrm{LLV}} = 0$. $\bar{n} = 0.0005$, $\eta_{\mathrm{S/I}} = 0.5$, signal attenuation factor $\xi = 0.5$, $\bar{n}_{\mathrm{B,S}} = \bar{n}_{\mathrm{B,S,E}} + \bar{n}_{\mathrm{B,I}}$, $\bar{n}_{\mathrm{B,S,E}} = 0.3$ and $\bar{n}_{\mathrm{B,I}} = 0.00001$. Each sample is comprised of $N = 2800$ shots. Amplitude of the range of the fast jamming a $= 0.8$.

coincidence matching that do not correspond to the real delay (location) of the object. We then show a set of LLV trajectories for a real-time scenario. For Lambertian scatterers, there are more LLV samples for the nearer object location guesses. Therefore, it is obvious it is easier to rule out or confirm the location of an object at closer distances. We have a short discussion about velocity estimation and how our system provides a level of covertness unobtainable in conventional LIDAR systems. We discuss how our system functions in the presence of dynamic noise (jamming) and show that the LLV framework allows us to counter this jamming, along with the innate resilience granted by coincidence counting for QI. We show simulated signal click and LLV trajectories for different types of jamming for CI and QI, which shows the inability of CI to function under such jamming. Finally, we extend our jamming-resilience capabilities by incorporating the M:TBSS theory to show that the more modes in each beam, the more resilient the system is to jamming.

Chapter 7: Simulation methodology

7.1 Motivation and foundations

Throughout this thesis, we strive to characterise our LIDAR system with analytic instead of numerical techniques. The reason for this is that it is often simpler and computationally less expensive. However, there are multiple situations when an analytic approach is either unavailable or not desired. In these situations we simulate what we require. Moreover, simulation allows us to emulate experimental data sets to test our LIDAR protocol. This chapter details the methodology of our simulations.

Monte Carlo simulation is a commonly used tool to estimate probabilistic outcomes which are difficult or impossible to calculate through analytic methods. This type of simulation entails repeated random sampling to generate an outcome (which is a random variable). In the context of our LIDAR system, a click-count is an outcome of a simulation run. Each simulation run $\tilde{s}$ comprises of N iterations, where an iteration is synonymous with a single experimental shot of our system. After multiple simulation runs, we generate a probability distribution of the random variable (i.e. the click-count). The simulated probability distribution allows us to estimate the true probability distribution of the random variable. We can improve this estimation by increasing the number of simulation runs. Moreover, for the next iteration of a simulation run, the outcome of that iteration does not depend on the outcomes from the previous iterations. The outcome only depends upon its current situation (whether an object is present or not, for example) and the probability of such an outcome. This is known as a Markovian process. Therefore, the type of simulation we consider is called Markov-chain Monte Carlo [169].

We wish to generate a discrete random variable X which corresponds to an outcome of a single shot of our experiment. This random variable has a probability mass function defined as

$$\Pr(X = x_j) = p_j, \text{ where } j = 0, 1, \ldots, J \text{ and } \sum_{j}^{J} p_j = 1. \tag{7.1}$$

Where p_j the probability of an outcome x_j of a single shot of our experiment. We use the

discrete inverse transform method to sample the discrete random variable X from a uniformly distributed random number U [170]. Where we set

$$X = \begin{cases} x_0 & \text{if } U < p_0 \\ x_1 & \text{if } p_0 \leq U \leq p_0 + p_1 \\ & \dots \\ x_j & \text{if } \sum_{i=0}^{j-1} p_i \leq U < \sum_{i=0}^{j} p_i \\ & \dots \\ x_J & \text{if } \sum_{i=0}^{J-1} p_i \leq U < \sum_{i=0}^{J} p_i \end{cases} \tag{7.2}$$

For a single experimental shot if the only outcome is either a click event or a no-click event then Eq. 7.2 reduces to simulation of a Bernoulli trial, where p_0 is the probability of a no-click and p_1 is the probability of a click. However, we require the formalism of Eq. 7.2 when simulating an M:TBSS system, due to the multiple different types of outcome for a single experimental shot. As this is a discrete example of the inverse transform method we search (through the index j) until we find the outcome x_j which satisfies the condition for our uniformly distributed random variable U set by Eq. 7.2. Once the outcome x_j is found for a given U, we now have our desired random variable $X = x_j$.

When simulating a single experimental shot for QI, there are two discrete random variables corresponding to X_I the idler detector outcomes and X_S the signal detector outcomes. Therefore, for each iteration, there are two uniformly distributed random numbers U_I and U_S, corresponding to the idler and signal detector random variables respectively. Figure 7.1 shows diagrammatically the process for simulating a QI system. From this diagram it is apparent that our model is a Markov chain, as it does not matter how many clicks or no-clicks precede an iteration of the simulation. This fact is reflected by the lack of change of probabilities p_1, p_2, p_3 and p_4 from iteration 1 to iteration 2. Following on from this, there are multiple approaches to simulating M:TBSS when $M > 1$, this is expanded upon in Ch. 7.3.1.

7.2 QI and CI click-count simulation

7.2.1 Method

This section details the methodology for simulating a click-count (for QI and CI), which is then processed into an LLV. For each simulation run $\tilde{s}$ there are N iterations. Each iteration i has

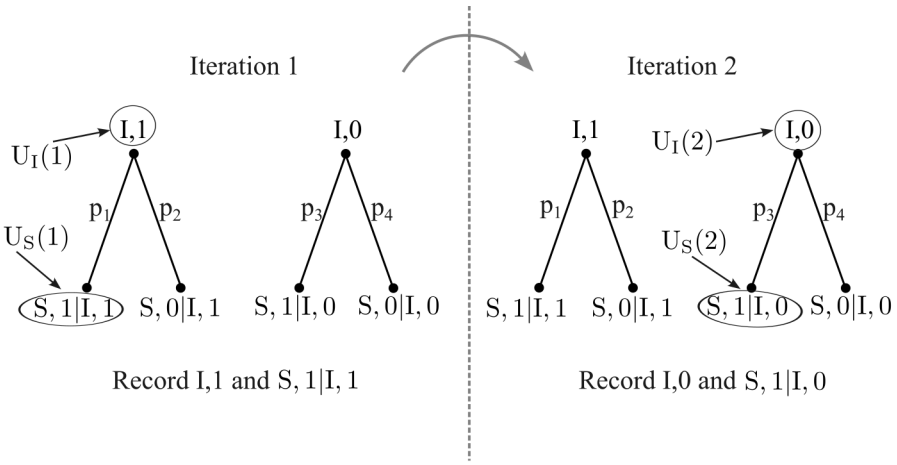

Figure 7.1 – Diagram of two iterations of a Markov Chain Monte-Carlo simulation of a QI system. The Markovian nature of our simulation is obvious as the recorded outcome of an iteration does not affect the probabilities p_1, p_2, p_3, p_4 for signal click or no-click after idler click or no-click for the subsequent iteration. We define $\mathrm{U_{I/S}}(i)$ as the random number generated for the idler or signal detector outcome for iteration i.

two uniformly distributed random numbers $\mathrm{U_I}(i)$ and $\mathrm{U_S}(i)$. As discussed earlier, the outcome of an iteration is found by a search involving $\mathrm{U_I}(i)$ and $\mathrm{U_S}(i)$, therefore we have the detector outcome random variable $X_\mathrm{I}(i)$ and $X_\mathrm{S}(i)$, for the idler and signal detectors respectively. If we want a fair comparison of QI and CI from one simulation run, the random numbers $\mathrm{U_S}$ which selects the outcomes for the signal detector for QI should be the same for CI. Moreover, if we want a fair comparison of object present and absent scenarios for one simulation run, we reuse random numbers for the object absent simulation after it has selected the outcomes for the object present simulation.

From each simulation run, the number of each type of idler detector and signal detector outcome is recorded. The data that is recorded for a simulation run is then processed into the relevant LLV. Following this, we define the number of simulation runs $\tilde{N}$. The set of LLVs after a number of simulation runs $\tilde{N}$ is our simulated LLV distribution. If the Gaussian approximation is valid for the system parameters, the convergence of the simulated LLV distribution to the expected analytic LLV distribution is discussed in Ch. 7.2.2. We define the mean of our simulated LLV distribution as

$$\tilde{\mu} = \frac{1}{\tilde{N}} \sum_{\tilde{s}=1}^{\tilde{N}} \Lambda(\tilde{s}), \tag{7.3}$$

where $\Lambda(\tilde{s})$ is the LLV from simulation run $\tilde{s}$. The standard deviation of our simulated LLV distribution is

$$\tilde{\sigma} = \sqrt{\frac{1}{\tilde{N}} \sum_{\tilde{s}=1}^{\tilde{N}} \big(\Lambda(\tilde{s}) - \tilde{\mu}\big)^2}. \tag{7.4}$$

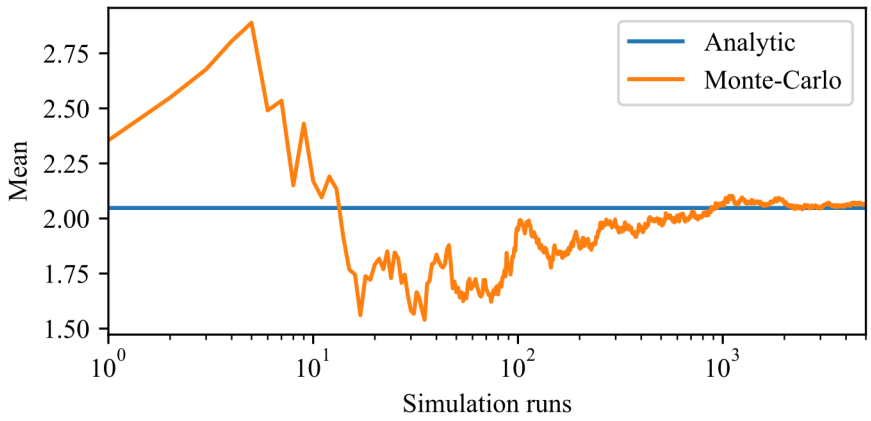

Figure 7.2 – The convergence of Monte-Carlo generated LLV distribution mean towards the analytically calculated mean LLV. With mean on the y-axis and number of simulation runs on the x-axis. $\bar{n} = 0.001$, $\bar{n}_{\mathrm{B,S}} = 0.1$, $\bar{n}_{\mathrm{B,I}} = 0.00001$, $\xi = 0.5$, $\eta_{\mathrm{S}} = 0.3$, $\eta_{\mathrm{I}} = 0.3$ and $N = 1 \times 10^5$.

However, in situations when the simulated LLV distribution is not Gaussian, complete characterisation of the distribution by the first two moments ($\tilde{\mu}$ and $\tilde{\sigma}$) is not possible. Therefore, if we want to calculate the distinguishability measure from the simulated object present and absent LLV distributions, this requires a manual search for the elements that have positive or negative LLVs.

7.2.2 Convergence

This section shows how a simulated LLV distribution converges to what is expected analytically. This is for a set of system parameters where the Gaussian approximation is valid, therefore the LLV distribution is fully characterised by its mean and standard deviation. Figure 7.2 shows the analytic mean and the mean of the Monte-Carlo generated LLV distribution as the number of simulation runs $\tilde{N}$ accumulates. Whereas, Fig. 7.3 shows the analytic standard deviation and the standard deviation of the Monte-Carlo generated LLV distribution as the number of simulation runs $\tilde{N}$ accumulates. Convergence is guaranteed by the strong law of large numbers which states that for the mean of a set of independent and identically distributed random variables, it converges to the expected mean as $\tilde{N}$ tends to infinity [171].

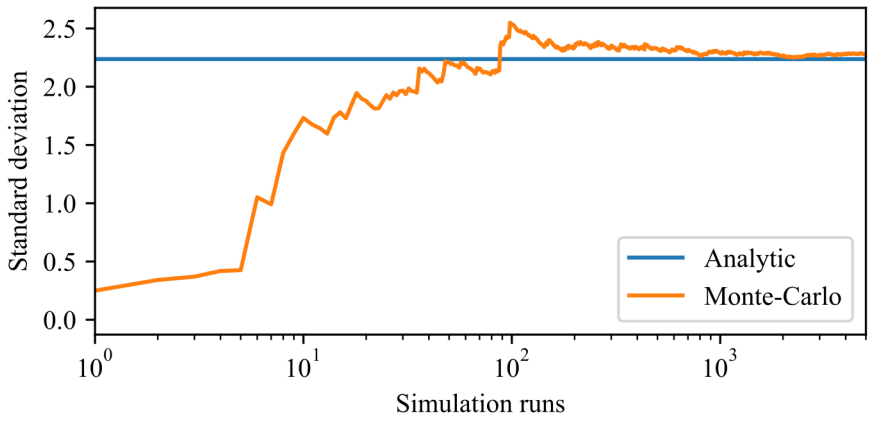

Figure 7.3 – The convergence of Monte-Carlo generated LLV distribution standard deviation towards the analytically calculated standard deviation LLV. With mean on the y-axis and number of simulation runs on the x-axis. $\bar{n} = 0.001$, $\bar{n}_{\mathrm{B,S}} = 0.1$, $\bar{n}_{\mathrm{B,I}} = 0.00001$, $\xi = 0.5$, $\eta_{\mathrm{S}} = 0.3$, $\eta_{\mathrm{I}} = 0.3$ and $N = 1 \times 10^5$.

7.3 M:TBSS LLV simulation

7.3.1 Method

There are two different methods we use to simulate a single shot of the experiment for M:TBSS. The first method uses the simplified M:TBSS theory. For an iteration i, there are M uniformly distributed random numbers $\mathrm{U_I}(M, i)$ for the set of M idler detectors and there are M uniformly distributed random numbers $\mathrm{U_S}(M, i)$ for the set of M signal detectors. For each iteration only the idler detector click and signal detector click which is correlated to the idler detector is recorded.

It is difficult to simulate the full theory of M:TBSS with the first method. This is because for the full theory of M:TBSS the click probabilities are framed to consider all detectors and their outcomes together, rather than as M separate Bernoulli trials. Instead, we require an alternative approach for simulation. For an iteration i, only one random number generates the outcome for M idler detectors and only one random number generates the outcome for M signal detectors. Unlike simplified M:TBSS, QI and CI, full M:TBSS does not have a Bernoulli trial for each shot. Instead, there are many possible outcomes (when $M > 1$) which are sampled according to the general form given in Ch. 7.2.

7.4 Simulation case examples

Throughout this thesis, we have set system parameters such that we can use the analytic approach as much as possible. Monte-Carlo simulation can also generate many of these figures. For example, we analytically calculate the LLV distributions in Fig. 3.11; however, we can also generate them following the simulation technique described in Ch. 7.2.1. In this section we shall focus on the situations where an analytic approach is not optional and simulation is required.

Figure 3.13 shows how the Bhattacharyya bound compares to the probability of error for the LLV framework as a function of shots N. We use the Gaussian approximation for the click-count distributions (and therefore the LLV distributions) to save computation time. However, when shots $N < 2000$ the Gaussian approximation fails and we must generate the LLV distributions by simulation. Therefore, we calculate the probability of error for the LLV framework for shots $N < 2000$ via simulation. Figure 4.2 shows the distinguishability ϕ as a function of shots N. Similar to Fig. 3.13, there are data points for when the Gaussian approximation fails as there are too few shots, therefore we simulate the LLV distributions for each N which is too small for Gaussian approximation validity. Figure 5.3 is a rolling window of the mean LLV with an error bar of one standard deviation for M:TBSS from an object absent to object present situation. The Gaussian approximation is more prone to failure for $M > 1$ as there are more types of event for the same number of shots, meaning there is a smaller mean number of click-counts for each distribution.

The figures in Ch. 6 for range-finding all require Monte-Carlo simulation as we can not analytically predict how different delays will affect coincidence click matching to a simulated stream of click events. Moreover, if we want to simulate a realistic incoming stream of click events the full formalism which includes non-coincidence clicks is required, because we need to simulate every possible type of click that will occur. This is because non-coincidence clicks may be coincident with clicks at another delay. The need for Monte-Carlo simulation is particularly obvious for Fig. 6.9 as it displays an LLV-processed random variable on a time-series. The figures pertaining to jamming, Fig. 6.10 to Fig. 6.19, need Monte-Carlo simulation because it is also an LLV-processed random variable on a time-series.

Chapter 8: Application to experiment

This chapter showcases the simple-detection quantum LIDAR experiment performed at the University of Strathclyde. Mateusz Mrozowski and Jonathan Pritchard devised the experiment. Mateusz Mrozowski conducted the experiment. John Jeffers and myself developed the underpinning theoretical framework. Jonathan Pritchard, myself and Mateusz Mrozowski performed analysis of the data. Ch. 1 details the premise of our experiment. If we exclude the idler detector measurements, the experimental setup reduces to a CI system.

8.1 Experimental setup

Figure 8.1 is a schematic of the setup used to conduct the experiment for object detection and Fig. 8.16 is a schematic of the setup used to conduct the range-finding experiment. Here, a photon pair is generated at 810 nm from a 405 nm CW pump via Type-II spontaneous parametric down conversion (SPDC). The nonlinear medium which facilitates SPDC here is a periodically-poled Potassium titanyl phosphate (ppKTP) crystal stabilised at the temperature 62°C. The reason for a stabilised crystal temperature is that it is required for phase-matching and hence effective generation of the down converted light. The poling period of the ppKTP crystal is temperature-dependent — we require a particular poling period which matches (and cancels out) the phase-mismatch of our light as it travels through the crystal. Furthermore, each beam has a temperature-dependent refractive index, which affects the wave-vectors and hence the phase-matching of the system [172]. Appendix L provides further details of our source characterisation. The use of type-II SPDC facilitates easy separation of the idler and signal beams as their polarisations are orthogonal. Moreover, as we use a quasi-phase matched and periodically-poled crystal for SPDC generation the output light is collinear. This in turns allows for a simpler experimental setup than SPDC generation from a birefringent crystal. To avoid residual pump light interfering with our system, we include a LP (long-pass) filter after the crystal, this LP filter blocks out light with a wavelength smaller than $\omega = 750$ nm. We then separate the resulting photon pair on a polarising beam-splitter (PBS). The idler photon is

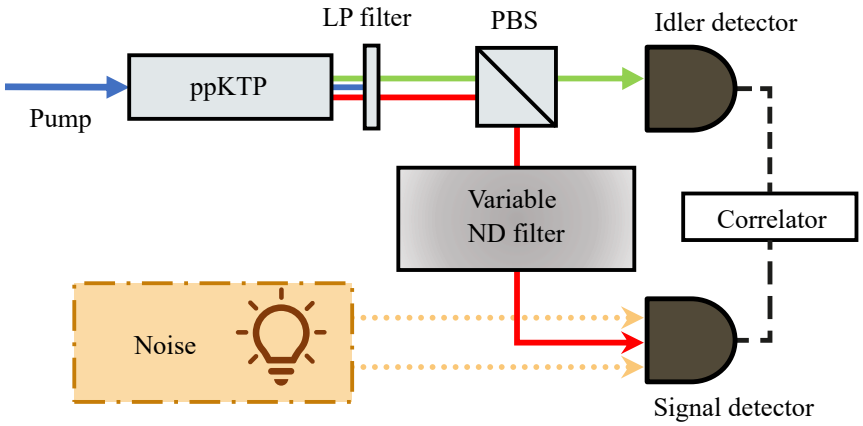

Figure 8.1 – Schematic of the quantum LIDAR experiment.

detected directly in a shielded environment. Noise is injected to the system using an 810 nm LED driven by a low-noise current driver to provide a constant noise independent from the target. This noise is combined with the attenuated signal and coupled into a single photon detector. We can change the noise levels to demonstrate operation at a variety of SNRs. Furthermore, to emulate controllably the loss associated with finite target reflectivity in the object present (H1) hypothesis, the signal photons pass through a calibrated ND (neutral density) filter. For the target absent hypothesis (H0), a beam block is placed in the signal path, allowing coupling of only the noise into the signal detector.

8.2 System parameter estimation

We process the click-count data from the experiment into an LLV. This processing requires calculation of the underlying click probabilities for the system, which depends upon estimation of system parameters. In this section we demonstrate how we estimate the system parameters from experimentally acquired data. From a data-set we have multiple samples, with each sample consisting of click-count data accumulated during integration time T. We use the binomial distribution to approximate the Poisson photo-count statistics of a sample of this time T. As the Binomial distribution constitutes N Bernoulli trials, this means that we consider the make-up of the integration time T as a succession of discrete experimental shots N. A shot is defined to have the temporal duration of τ_c, where τ_c is the coincidence window size set by the time-tagging equipment. Therefore, each sample has $N = \left\lfloor \frac{T}{\tau_c} \right\rfloor$ shots.

8.2.1 Detector dark count characterisation

We begin estimation of the system parameters by characterising the detector dark count for idler $\bar{n}_{\mathrm{D,I}}$ and signal detector $\bar{n}_{\mathrm{D,S}}$. The system is isolated as much as possible from the background environmental noise such that the only noise source arises from detector dark counts. Furthermore, we switch off the pump, meaning there is no source light.

The click probability for the idler and signal detectors under the conditions required for detector dark count characterisation is estimated via the estimators $\hat{\mathrm{Pr}}_{\mathrm{I}}$, $\hat{\mathrm{Pr}}_{\mathrm{S}}$, respectively. The idler and signal detector click probability estimators are, respectively,

$$\hat{\mathrm{Pr}}_{\mathrm{I}} = \frac{N_{\mathrm{idler}}}{N} \tag{8.1}$$

and

$$\hat{\mathrm{Pr}}_{\mathrm{S}} = \frac{N_{\mathrm{signal}}}{N}, \tag{8.2}$$

Where we define N_{idler} and N_{signal} as the average of many click-count samples for idler and signal data channels, respectively, for the relevant data-set (the pump switched off data-set for this situation). These values converge to the mean of its respective click-count distribution as the number of samples increases, if we assume that the underlying statistics are stable. Both estimators satisfy the CRLB for $\mathrm{Pr}_{\mathrm{I/S}}$.

As the dark noise is assumed thermal, the idler detector click probability is

$$\mathrm{Pr}_{\mathrm{I:off}} = 1 - \frac{1}{1 + \bar{n}_{\mathrm{D,I}}}. \tag{8.3}$$

Following from this, we substitute the estimator Eq. 8.1 for $\mathrm{Pr}_{\mathrm{I:off}}$ and solve for $\bar{n}_{\mathrm{D,I}}$. Therefore, the idler detector dark count mean photon number is

$$\bar{n}_{\mathrm{D,I}} = \frac{1}{1 - \hat{\mathrm{Pr}}_{\mathrm{I}}} - 1. \tag{8.4}$$

Following a similar approach, the signal detector dark count mean photon number $\bar{n}_{\mathrm{D,S}}$ is defined as

$$\bar{n}_{\mathrm{D,S}} = \frac{1}{1 - \hat{\mathrm{Pr}}_{\mathrm{S}}} - 1. \tag{8.5}$$

For example, when the coincidence window size is set as $\tau_{\mathrm{c}} = 2$ ns and the integration time for each sample is $T = 0.1$ s we can proceed with characterising the dark count mean photon numbers of our experiment. The dark count mean photon number for the idler detector is

$\bar{n}_{\mathrm{D,I}} = 2.38 \times 10^{-6}$ and for the signal detector it is $\bar{n}_{\mathrm{D,S}} = 4.18 \times 10^{-6}$.

8.2.2 System loss and signal mean photon number estimation

Now that estimation of the dark count mean photon numbers is complete, the pump is switched on. With the pump switched on, we can estimate the idler channel system loss η_{I}, signal channel system loss η_{S} and the mean photon number of the light source $\bar{n}$. The system is still isolated from the environmental background noise and there is no attenuation in the signal beam.

A common value encountered in analysis of photon-pair experiments is the heralding efficiency. We define the idler detector heralding efficiency as

$$\mathrm{HE_I} = \frac{N_{\mathrm{coinc.}}}{N_{\mathrm{idler}}}. \tag{8.6}$$

We define $N_{\mathrm{coinc.}}$ as the average of many click-count samples for the coincidence click data channel. Furthermore, the signal detector heralding efficiency is

$$\mathrm{HE_S} = \frac{N_{\mathrm{coinc.}}}{N_{\mathrm{signal}}}. \tag{8.7}$$

Estimation of the system loss parameters are neatly approximated by the heralding efficiency. Therefore, the idler and signal system loss estimators are

$$\hat{\eta}_{\mathrm{I}} = \mathrm{HE_S}, \tag{8.8}$$

and

$$\hat{\eta}_{\mathrm{S}} = \mathrm{HE_I}. \tag{8.9}$$

This approximation for estimating the system loss for the idler and signal detectors is valid in the parameter-space where the system loss parameters are $0.15 \leq \eta_{\mathrm{S}}, \eta_{\mathrm{I}} \leq 0.99$, the dark count mean photon numbers are $5 \times 10^{-9} \leq \bar{n}_{\mathrm{D,S}}, \bar{n}_{\mathrm{D,I}} \leq 5 \times 10^{-6}$ and the mean photon number is $3.3 \times 10^{-3} \leq \bar{n} \leq 8.3 \times 10^{-3}$. Appendix N describes the details for the system loss estimation approximation. For estimation of the light source mean photon number we use the idler click probability estimator $\hat{\mathrm{Pr}}_{\mathrm{I}} = \frac{N_{\mathrm{idler}}}{N}$ for when the pump is switched on. Hence, our estimation of the light source mean photon number is

$$\bar{n} = \frac{(1 - \hat{\mathrm{Pr}}_{\mathrm{I}})^{-1} - 1 - \bar{n}_{\mathrm{D,I}}}{\hat{\eta}_{\mathrm{I}}}. \tag{8.10}$$

8.2.3 Background noise and signal attenuation

Now that we have estimated the system parameters that are (relatively) unvarying, we now proceed to estimate system parameters that are susceptible to change throughout the object detection and ranging process. These parameters include the environmental background noise and the signal attenuation factor. As the idler detector is optically-shielded from the environment, its total background noise mean photon number equals the dark count mean photon number $\bar{n}_{\mathrm{B,I}} = \bar{n}_{\mathrm{D,I}}$. However, the signal detector is exposed to the environment when probing for a possible target object. Therefore, we must estimate the (measured) signal detector background noise mean photon number $\bar{n}_{\mathrm{B,S}}$. The signal detector background noise mean photon number is estimated by blocking the signal beam and collecting the click-count statistics. Our experiment injects Poissonian noise into the signal detector channel; consequently, the signal detector and coincidence click probabilities differ from the prior dark count estimation. Moreover, for simplicity, we assume that the Poissonian noise dwarfs the signal detector thermal dark noise, such that we approximate the signal channel noise as solely Poissonian in nature. Therefore, we use the object absent click probability in the presence of Poissonian noise, as defined in Eq. 3.62. This click probability has an estimator $\hat{\mathrm{P}}\mathrm{r}_{\mathrm{H0}} = \frac{N_{\mathrm{signal}}}{N}$. Thus, the estimation of the measured mean photon number of the signal detector background noise is

$$\bar{n}_{\mathrm{B,S}} = -\ln\left(1 - \hat{\mathrm{P}}\mathrm{r}_{\mathrm{H0}}\right) \tag{8.11}$$

For our experiment the signal attenuation factor ξ has a preset value for each ND filter used to emulate the loss from probing a possible target object. Appendix M describes the method for calculating the signal attenuation factor ξ for a particular ND filter. Otherwise, for a realistic system with an unknown signal attenuation factor ξ, it is the last system parameter we estimate. Appendix O details the method for estimating an unknown signal attenuation factor and compares this to the CRLB.

8.3 Experimental results

In this section we show a selection of experimental results. We demonstrate capabilities such as object detection, system performance metrics and object detection in the presence of different types of jamming. We also demonstrate range-finding with and without jamming. We show both the unprocessed raw data (signal clicks) and the (CI and QI) LLVs from a rolling window of a sample refresh rate S. The rolling window allows for both easier visual interpretation of

the statistics and improved distinguishability. The system parameters for the experimental results are framed in terms such as click-count rate in Hz and dB for signifying loss or SNR. In this section we will relate the experimental results terminology to the terms primarily used throughout this thesis, such as mean photon number and attenuation factors. Of course, it is more general to state the experimental results in terms of Hz and dB, as the mean photon number and attenuation factor depends upon the type of click probability and the coincidence window used. For a particular experiment, we calibrate our model off an initial data set (for the noise only situation and object present) to estimate the system parameters. Following the estimation of the system parameters, we are able to process click-count data into an LLV for inference of object presence. Throughout our showcase of the experimental results, we superimpose two data-sets for a particular set of system parameters: the object present (H1) and absent (H0) data-sets. Even though we record these data-sets separately, they adhere to the same system parameter regimes. For the experimental data we present we calculate that the signal system loss $\eta_{\mathrm{S}} = 0.233$ and the idler system loss $\eta_{\mathrm{I}} = 0.1958$. We also calculate the SNR from measured data rather than via the click probabilities as in Ch. 4.

8.3.1 Object detection

The data we show in Fig. 8.2 is when there is ≈ 1 MHz of signal noise, 50μW of pump power giving a pair production rate of 377 ± 5 kHz, a ND40 filter to cause 33.5 dB of signal attenuation and an integration time for each sample $T = 0.1$ s. The coincidence window size $\tau_{\mathrm{c}} = 2$ ns. From an initial set of 100 samples we estimate the system parameters to calibrate the system. The ND40 filter corresponds to a signal attenuation factor of $\xi = 1.79 \times 10^{-3}$. The mean photon number of the source is $\bar{n} = 9.83 \times 10^{-4}$, the idler detector background noise mean photon number is negligible and the signal detector background noise mean photon number $\bar{n}_{\mathrm{B,S}} = 2.07 \times 10^{-3}$. For the object present hypothesis, the signal return rate of 167 ± 1 Hz yields a CI SNR of $\mathrm{SNR}_{\mathrm{CI}} = -37.9 \pm 0.1$ dB. The object present (no noise) coincidence click rate is 39.1 ± 0.4 Hz and the object absent (noise-engaged) coincidence click rate is 200.2 ± 0.5 Hz. These values give the QI SNR $\mathrm{SNR}_{\mathrm{QI}} = -7.1 \pm 0.1$ dB. It is clear from Fig. 8.2 that the click-count statistics are very similar for object present and absent data-sets. Figure 8.3 shows a rolling window of CI LLV as a function of sample number $\tilde{s}$. Equation 4.18 defines the LLV sample rolling window, for a refresh rate of $S = 50$ samples. Figure 8.4 shows a rolling window of QI LLV as a function of sample number $\tilde{s}$, for a refresh rate also of $S = 50$ samples. In Fig. 8.4 we have set the refresh rate high enough such that the object present and absent QI rolling average LLV statistics are clearly distinguishable. For the same refresh rate the CI rolling average LLV

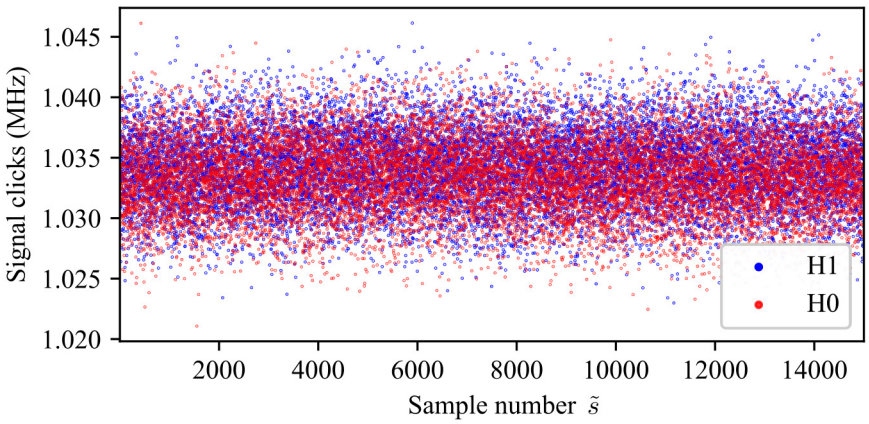

FIGURE 8.2 – Signal clicks as a function of sample number $\tilde{s}$. Both object present (H1) and object absent (H0) data-sets superimposed. This example has ≈ 1 MHz of signal noise, 50μW of pump power, a ND40 filter to cause 33.5 dB of signal attenuation and an integration time for each sample $T = 0.1$ s. The coincidence window size $\tau_c = 2$ ns.

statistics are not clearly distinguishable. However, with a suitable increase of sample refresh rate S, we could clearly distinguish between object present and absent CI rolling average LLV statistics, at the cost of an increased time required to reach confident detection for an LLV sample.

The data we show in Fig. 8.5 is when there is ≈ 1 MHz of signal noise, 150μW of pump power giving a pair production rate of 1.13 ± 0.02 MHz, a ND80 filter to cause 52 dB of signal attenuation and an integration time for each sample $T = 1$ s. This increase of integration time compared to the ND40 data-set is to counter the extremely low return rate of signal photons for ND80. From an initial set of 100 samples we estimate the system parameters to calibrate the system. The ND80 filter corresponds to a signal attenuation factor of $\xi = 3.09 \times 10^{-5}$, this degree of attenuation approaches values typically encountered outside the laboratory [86]. The mean photon number of the source is $\bar{n} = 2.97 \times 10^{-3}$, the idler detector background noise mean photon number is negligible and the signal detector background noise mean photon number $\bar{n}_{B,S} = 2.01 \times 10^{-3}$. For the object present hypothesis, the signal return rate of 7.1 ± 0.9 Hz therefore corresponds to a CI SNR of $\text{SNR}_{\text{CI}} = -51.5 \pm 0.6$ dB. The object present (no noise) coincidence click rate is 1.8 ± 0.1 Hz and the object absent (noise-engaged) coincidence click rate is 577 ± 1 Hz. These values give the QI SNR $\text{SNR}_{\text{QI}} = -25.1 \pm 0.2$ dB.

It is clear from Fig. 8.5 that the click-count statistics are very similar for object present and absent data-sets. Figure 8.6 and Fig. 8.7 shows a rolling window of CI/QI LLV as a function of sample number $\tilde{s}$, for a refresh rate of $S = 150$ samples. The QI rolling average LLV statistics

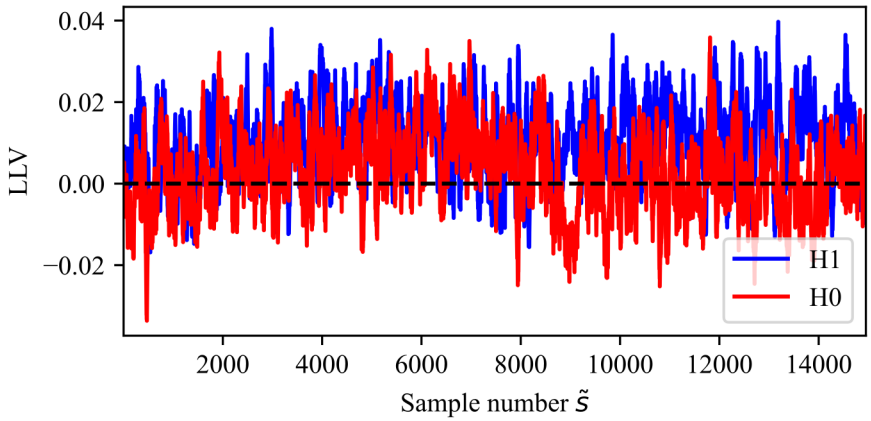

Figure 8.3 – CI rolling window LLV as a function of sample number $\tilde{s}$, for a refresh rate of $S = 50$ samples. Both object present (H1) and object absent (H0) data-sets superimposed. This example has ≈ 1 MHz of signal noise, 50μW of pump power, a ND40 filter to cause 33.5 dB of signal attenuation and an integration time for each sample $T = 0.1$ s. The coincidence window size $\tau_c = 2$ ns.

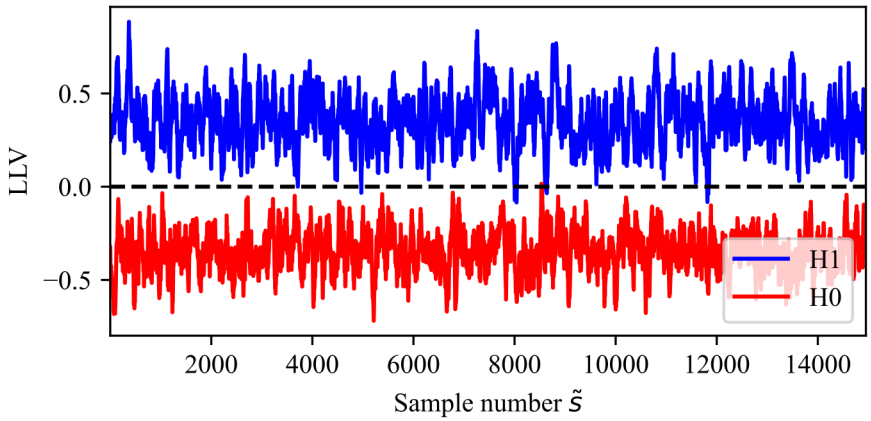

Figure 8.4 – QI rolling window LLV as a function of sample number $\tilde{s}$, for a refresh rate of $S = 50$ samples. Both object present (H1) and object absent (H0) data-sets superimposed. This example has ≈ 1 MHz of signal noise, 50μW of pump power, a ND40 filter to cause 33.5 dB of signal attenuation and an integration time for each sample $T = 0.1$ s. The coincidence window size $\tau_c = 2$ ns.

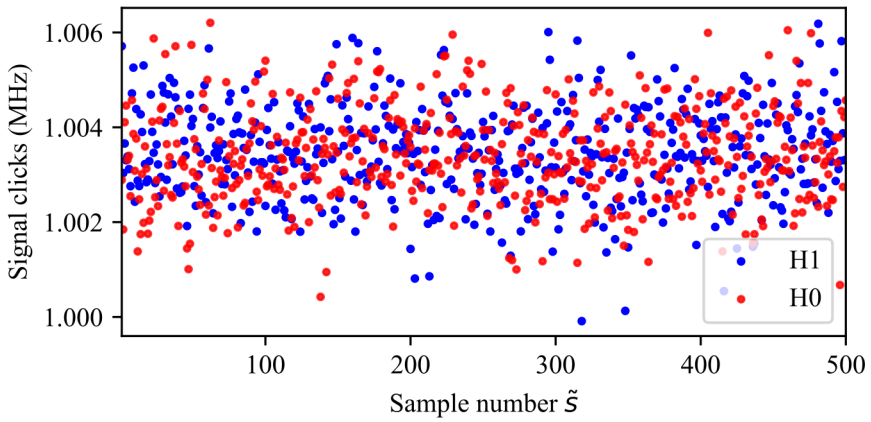

Figure 8.5 – Signal clicks as a function of sample number $\tilde{s}$. Both object present (H1) and object absent (H0) data-sets superimposed. This example has ≈ 1 MHz of signal noise, 150μW of pump power, a ND80 filter to cause 52 dB of signal attenuation and an integration time for each sample $T = 1$ s. The coincidence window size $\tau_c = 2$ ns.

are clearly disjoint for object present and absent. The CI rolling average LLV statistics have the wrong detection decisions for object present and absent, even with an increase of sample refresh rate S. Thus showing that CI does not function in this parameter regime.

8.3.2 System performance

The previous section visually demonstrated the advantage of QI compared to CI for object detection with LLV data. This section utilises some aspects of the system performance analysis introduced in Ch. 4. We focus on the experiment when there is ≈ 1 MHz of signal noise, 50μW of pump power giving a pair production rate of 377 ± 5 kHz, a ND40 filter to cause 33.5 dB of signal attenuation and an integration time for each sample $T = 0.1$ s. We use the entire data-set as to estimate the system parameters. Equation 4.19 defines the average distinguishability as a function of sample rolling window size. Figure 8.8 plots how average distinguishability ϕ_{avg} increases with number of samples S for both theory-predicted and experimentally-measured CI and QI. From Fig. 8.8 we see good agreement between experiment and theory. QI reaches the peak distinguishability with $S = 50$ samples, this corresponds to an integration time of 5 s to reach peak distinguishability. A common approach to assessing system performance for LIDAR protocols is by a ROC. Chapter 4 describes how a ROC is calculated from object present and absent LLV distributions. Figure 8.9 shows the ROC based off the object present and absent distributions averaged from $S = 50$ samples. Plotted are both the theoretically predicted and experimentally measured ROCs for CI, QI and CI averaged by $17 * S$ samples to match the QI

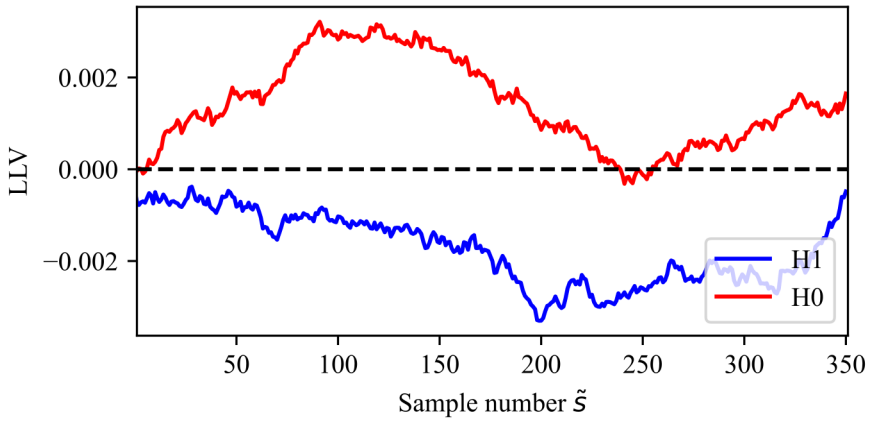

Figure 8.6 – CI rolling window LLV as a function of sample number $\tilde{s}$, for a refresh rate of $S = 150$ samples. Both object present (H1) and object absent (H0) data-sets superimposed. This example has ≈ 1 MHz of signal noise, 150µW of pump power, a ND80 filter to cause 52 dB of signal attenuation and an integration time for each sample $T = 1$ s. The coincidence window size $\tau_c = 2$ ns.

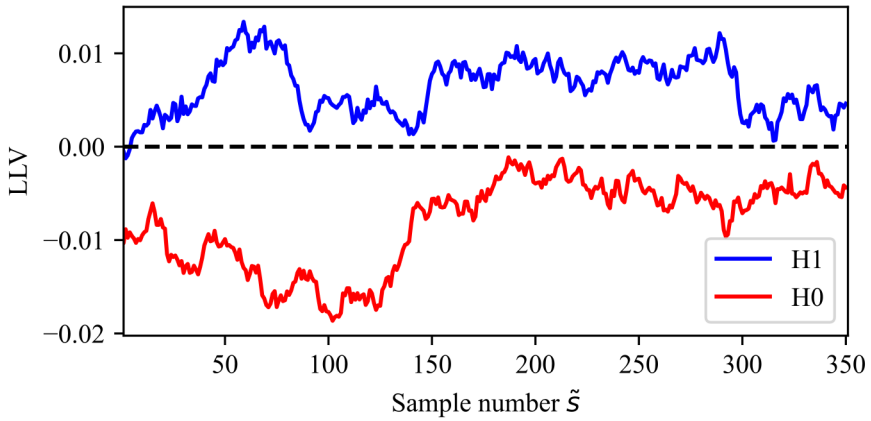

Figure 8.7 – QI rolling window LLV as a function of sample number $\tilde{s}$, for a refresh rate of $S = 150$ samples. Both object present (H1) and object absent (H0) data-sets superimposed. This example has ≈ 1 MHz of signal noise, 150µW of pump power, a ND80 filter to cause 52 dB of signal attenuation and an integration time for each sample $T = 1$ s. The coincidence window size $\tau_c = 2$ ns.

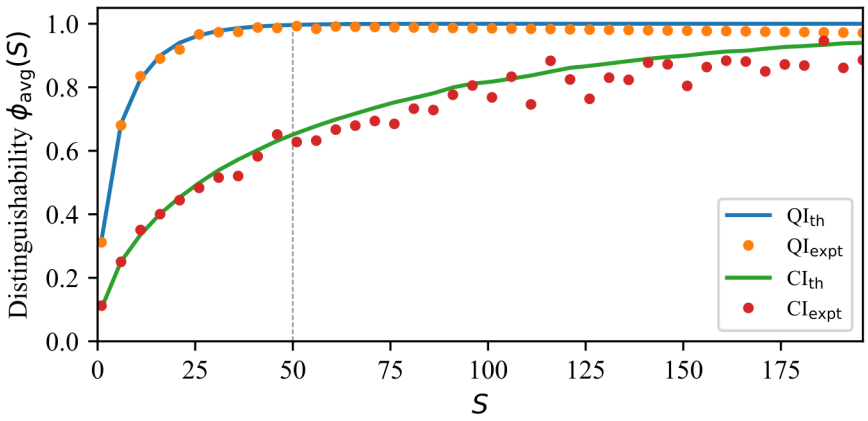

Figure 8.8 – Average distinguishability ϕ_{avg} as a function of sample refresh rate S. This example has ≈ 1 MHz of signal noise, 50μW of pump power, a ND40 filter to cause 33.5 dB of signal attenuation and an integration time for each sample $T = 0.1$ s. The coincidence window size $\tau_c = 2$ ns. QI_{th} is the theory-predicted QI average distinguishability and QI_{expt} is the experimental data QI average distinguishablity. CI_{th} is the theory-predicted CI average distinguishability and CI_{expt} is the experimental data CI average distinguishablity. The vertical dashed grey line signifies the number of samples $S = 50$ used in the ROC curve in Fig. 8.9.

ROC. Once again, there is good agreement between theory and experiment for the ROC. It is clear that the refresh rate S affects system performance. Another parameter that we can adjust that affects system performance is the coincidence window size (duration of a shot) τ_c. However, even though the probability of a click increases with respect to an increased coincidence window size, the noise-filtering benefit of QI due to inter-beam temporal correlations is reduced and the heralding gain benefit is also reduced as the mean photon numbers are increased.

8.3.3 Object detection in a jamming situation

So far our exposition of experimental data for object detection assumes that the system parameters do not change with time and that the LLV trained from an initial calibration data-set applies to the remainder of the data-set. However, in reality LIDAR systems operate in highly dynamic situations, where the background noise or our return signal varies over time. This section presents experimental results which demonstrate the jamming-resilience theory introduced in Ch. 6.9 for object detection when there is the deliberate temporal variation of background noise, known as classical jamming. Intentional jamming techniques involve emitting strong modulated light or laser signals (for our experiment we use an LED to inject jamming noise), or deploying countermeasures to confuse or blind the LIDAR sensor. The purpose of intentional jamming of LIDAR systems is to hinder accurate data gathering, thereby compromising situational awareness. The results shown below experimentally demonstrate

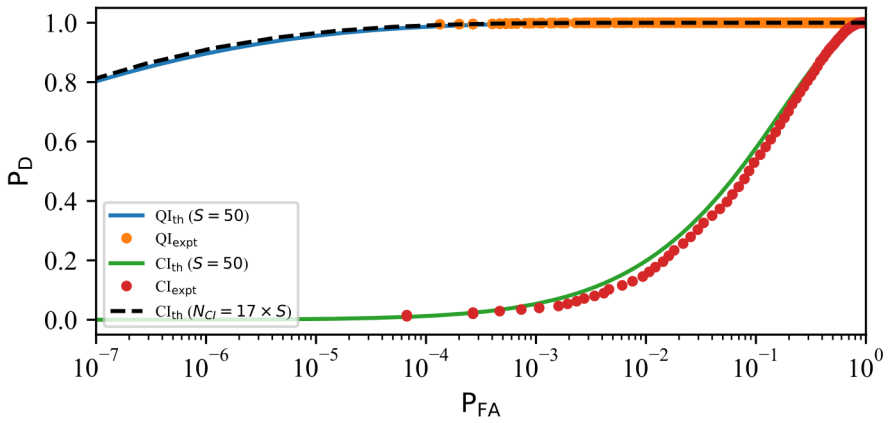

FIGURE 8.9 – ROC for CI and QI. The x-axis shows probability of false alarm P_{FA} and the y-axis shows probability of detection P_D. This example has ≈ 1 MHz of signal noise, 50μW of pump power, a ND40 filter to cause 33.5 dB of signal attenuation and an integration time for each sample $T = 0.1$ s. The coincidence window size $\tau_c = 2$ ns. QI_{th} is the theory-predicted QI average distinguishability and QI_{expt} is the experimental data QI average distinguishablity. CI_{th} is the theory-predicted CI average distinguishability and CI_{expt} is the experimental data CI average distinguishablity. All ROCs are generated from object present and absent distributions averaged from $S = 50$ samples, apart from the black dashed line which is CI averaged from $17 * S$ samples.

that QI is resilient to classical jamming. Moreover, as mentioned in Ch. 6.9 active background tracking is possible when $\bar{n} \ll \bar{n}_{B,S}$. The ability to track the background actively means we are able to update the LLV proactively to attempt to further counter the effects of jamming. For our experiment, we consult a look-up table (LUT) for background tracking instead of proactively re-calculating the LLV.

Figure 8.10 shows signal clicks as a function of sample number $\tilde{s}$ when there is sinusoidal jamming. This form of jamming is first described in Ch. 6.9.1. We calibrate our system with the first 200 samples, when there is no jamming. The object present and absent click-counts in Fig. 8.10 are indistinguishable from each other, this indistinguishabilty is reflected in Fig. 8.11 which shows the CI rolling window LLV for object present and absent data-sets. Figure 8.12 shows the QI rolling window LLV for object present and absent data-sets for a) without active background tracking b) active background tracking. We can see that for Fig. 8.12a) the object present and absent LLVs are distinguishable, however the effect of jamming results in the occurrence of false LLV test decisions. Whereas, Fig. 8.12b) the active background counters the effect of jamming and only correct LLV test decisions are made. Figure 8.12 experimentally confirms the jamming-resilience provided by QI as theoretically predicted in Ch. 6.9.

We now show the experimental results where the form of jamming is a pseudo-random noise,

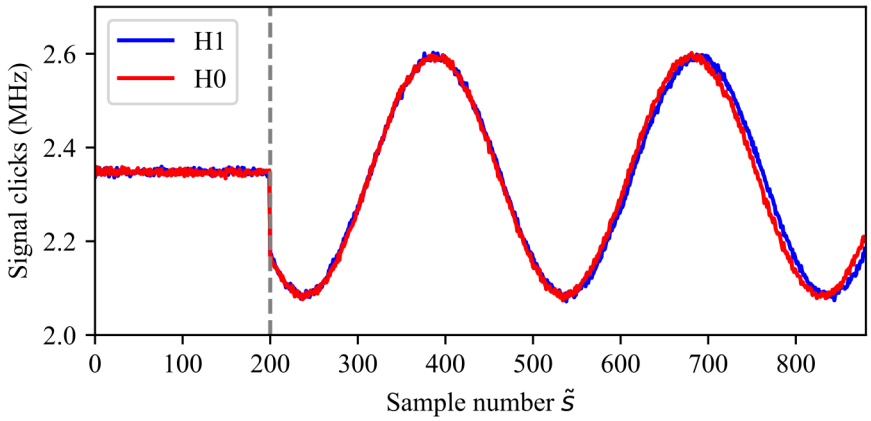

Figure 8.10 – Signal clicks (MHz) as a function of sample number $\tilde{s}$ when there is sinusoidal jamming. Both object present (H1) and object absent (H0) data-sets superimposed. This example has ≈ 2.4 MHz of signal noise which corresponds to a mean photon number $\bar{n}_{\mathrm{B,S}} = 4.65 \times 10^{-3}$. This figure has jamming with a modulation amplitude of 0.3 MHz which corresponds to a mean photon number of 4.76×10^{-4}. 50μW of pump power, a ND40 filter to cause 33.5 dB of signal attenuation and an integration time for each sample $T = 0.1$ s. The coincidence window size $\tau_{\mathrm{c}} = 2$ ns. The vertical dashed grey line at $\tilde{s} = 200$ represents the end of the calibration data-set.

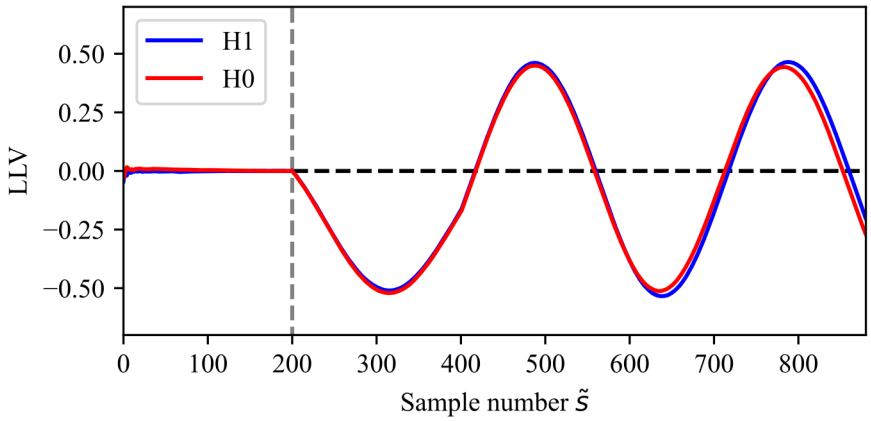

Figure 8.11 – CI rolling window LLV as a function of sample number $\tilde{s}$ when there is sinusoidal jamming, for a refresh rate of $S = 200$ samples. Both object present (H1) and object absent (H0) data-sets superimposed. This example has ≈ 2.4 MHz of signal noise which corresponds to a mean photon number $\bar{n}_{\mathrm{B,S}} = 4.65 \times 10^{-3}$. This figure has jamming with a modulation amplitude of 0.3 MHz which corresponds to a mean photon number of 4.76×10^{-4}. 50μW of pump power, a ND40 filter to cause 33.5 dB of signal attenuation and an integration time for each sample $T = 0.1$ s. The coincidence window size $\tau_{\mathrm{c}} = 2$ ns. The vertical dashed grey line at $\tilde{s} = 200$ represents the end of the calibration data-set.

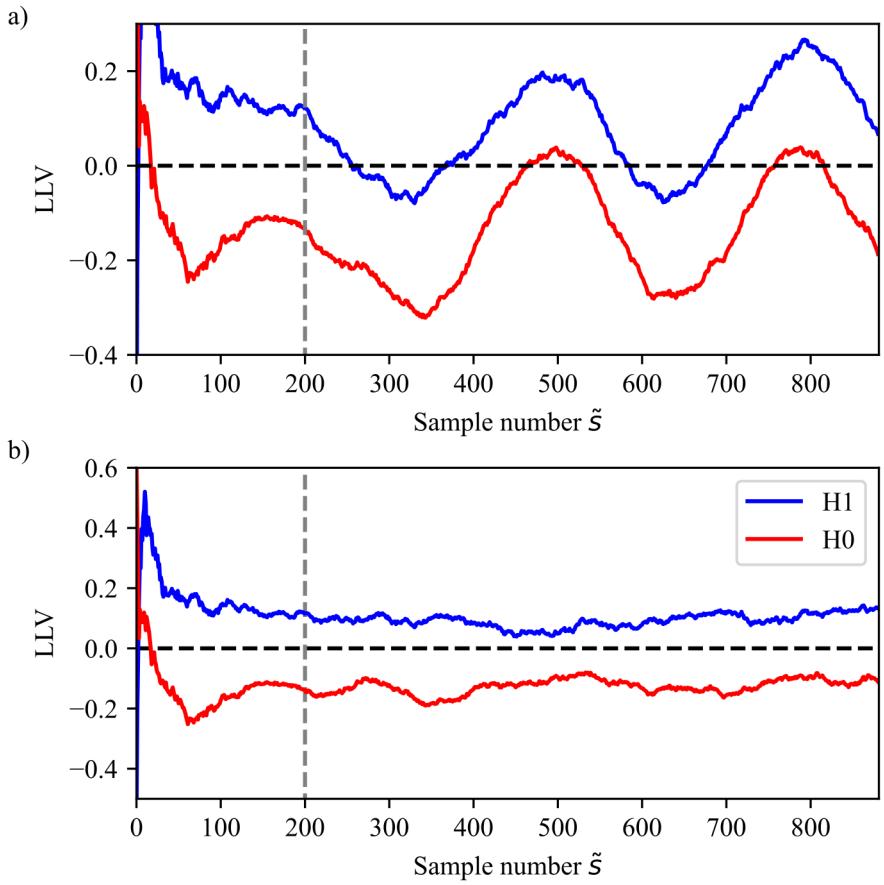

Figure 8.12 – QI rolling window LLV as a function of sample number $\tilde{s}$ when there is sinusoidal jamming a) without active background tracking b) with active background tracking. These plots have a refresh rate of $S = 200$ samples. Both object present (H1) and object absent (H0) data-sets superimposed. This example has ≈ 2.4 MHz of signal noise which corresponds to a mean photon number $\bar{n}_{\mathrm{B,S}} = 4.65 \times 10^{-3}$. This figure has jamming with a modulation amplitude of 0.3 MHz which corresponds to a mean photon number of 4.76×10^{-4}. 50μW of pump power, a ND40 filter to cause 33.5 dB of signal attenuation and an integration time for each sample $T = 0.1$ s. The coincidence window size $\tau_{\mathrm{c}} = 2$ ns. The vertical dashed grey line at $\tilde{s} = 200$ represents the end of the calibration data-set.

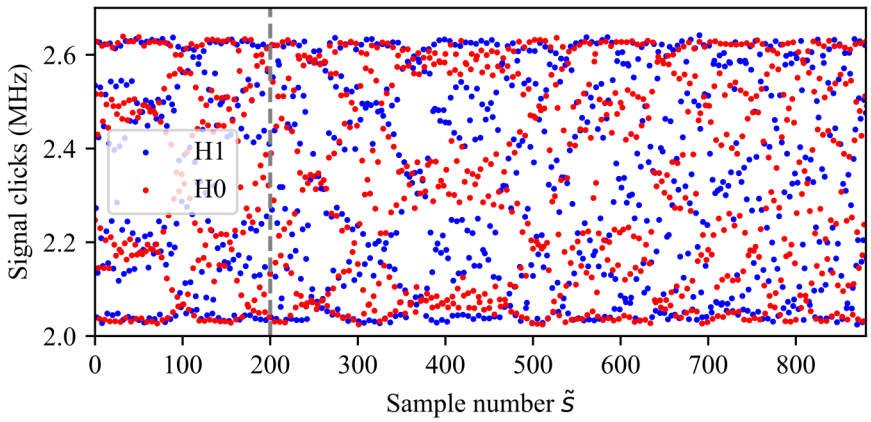

FIGURE 8.13 – Signal clicks (MHz) as a function of sample number $\tilde{s}$ when there is pseudo-random fast jamming. Both object present (H1) and object absent (H0) data-sets superimposed. This example has ≈ 2.4 MHz of signal noise which corresponds to a mean photon number $\bar{n}_{\mathrm{B,S}} = 4.65 \times 10^{-3}$. This figure has jamming with a modulation amplitude of 0.3 MHz which corresponds to a mean photon number of 4.76×10^{-4}. 50μW of pump power, a ND40 filter to cause 33.5 dB of signal attenuation and an integration time for each sample $T = 0.1$ s. The coincidence window size $\tau_{\mathrm{c}} = 2$ ns.

as first introduced in Ch. 6.9.2. Once again, we calibrate our system with the first 200 samples, when there is no jamming. Figure 8.13 shows signal clicks (MHz) as a function of sample number $\tilde{s}$. Figure 8.14 and Fig. 8.15 shows the CI and QI rolling window LLV as a function of sample number $\tilde{s}$, respectively. The reason that Fig. 8.15 does not show active background tracking is that for the rolling window size set, the change of noise is averaged out and so there is no need to track. Active background tracking is of use for smaller rolling windows sizes, due to the greater effect of the noise fluctuations.

8.3.4 RANGE-FINDING

The time-tagging software creates a virtual data channel for the coincidence counting. As it is virtual, it is easy to have multiple coincidence channels corresponding to different delays for matching the two real data channels: signal and idler. Chapter 6 demonstrates that a different delay corresponds to a possible target object situated at a distance set by that delay. For our experiment, we implement variations in target position with a mirror serving as the target positioned on a motorized translation stage. This setup enables movement of the target at a total range variation of 22 cm. Figure 8.16 shows how our experimental setup is modified to enable the extension to range-finding. We define three locations separated by 11 cm intervals, denoted as x_A, x_B and x_C. Following this, we assign three parallel coincidence detection channels with delays of $\tau_{x_A} = 1.77$ ns, $\tau_{x_B} = 2.52$ ns and $\tau_{x_C} = 3.27$ ns corresponding to the round-trip time

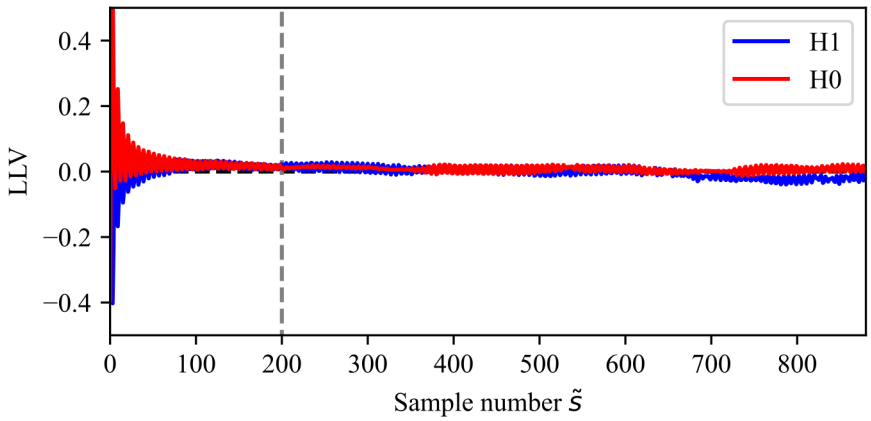

Figure 8.14 – CI rolling window LLV as a function of sample number $\tilde{s}$ when there is pseudo-random fast jamming, for a refresh rate of $S = 200$ samples. Both object present (H1) and object absent (H0) data-sets superimposed. This example has ≈ 2.4 MHz of signal noise which corresponds to a mean photon number $\bar{n}_{\mathrm{B,S}} = 4.65 \times 10^{-3}$. This figure has jamming with a modulation amplitude of 0.3 MHz which corresponds to a mean photon number of 4.76×10^{-4}. 50µW of pump power, a ND40 filter to cause 33.5 dB of signal attenuation and an integration time for each sample $T = 0.1$ s. The coincidence window size $\tau_{\mathrm{c}} = 2$ ns.

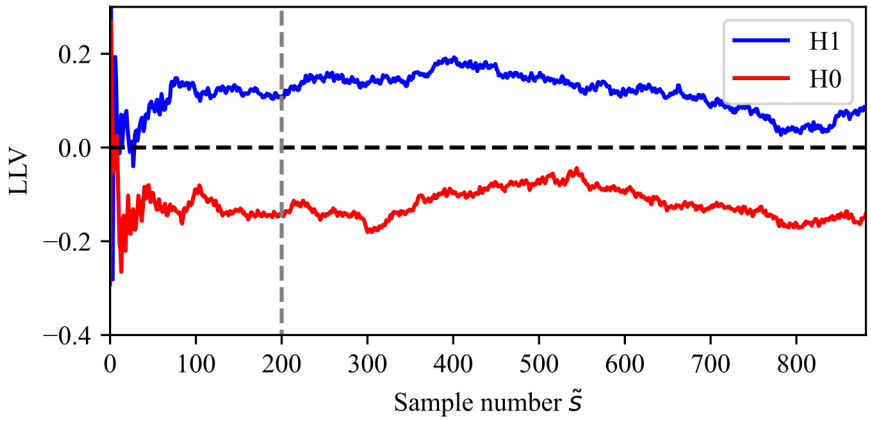

Figure 8.15 – QI LLV as a function of sample number $\tilde{s}$ when there is pseudo-random fast jamming, for a refresh rate of $S = 200$ samples. Both object present (H1) and object absent (H0) data-sets superimposed. This example has ≈ 2.4 MHz of signal noise which corresponds to a mean photon number $\bar{n}_{\mathrm{B,S}} = 4.65 \times 10^{-3}$. This figure has jamming with a modulation amplitude of 0.3 MHz which corresponds to a mean photon number of 4.76×10^{-4}. 50µW of pump power, a ND40 filter to cause 33.5 dB of signal attenuation and an integration time for each sample $T = 0.1$ s. The coincidence window size $\tau_{\mathrm{c}} = 2$ ns.

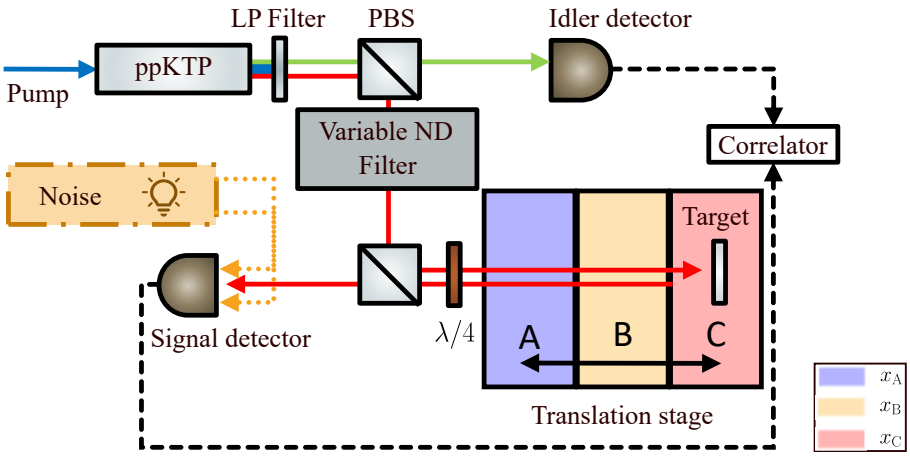

Figure 8.16 – Schematic of the quantum LIDAR experiment with an extension to range-finding capabilities.

to each location. For a coincidence channel for a set delay τ_x, we record a coincidence click if there is a signal click $[\tau_x - \frac{\tau_c}{2}, \tau_x + \frac{\tau_c}{2}]$ after the idler click. For the following results, we set the coincidence window size $\tau_c = 1$ ns. This value is mindful of the limitation to temporal resolution set by the ≈ 250 ps timing jitter of our system. However, as $\tau_c > |\tau_{x_B} - \tau_{x_A}|$ and $\tau_c > |\tau_{x_C} - \tau_{x_B}|$ we can not discretise the different delays into a shot-by-shot basis akin to the approach in Ch. 6 with Eq. 6.2. The inability to discretise the different delays according to shots necessarily leads to a degree of cross-talk between the coincidence counting channels. This cross-talk occurs in regimes where $\tau_c > |\tau_{x_B} - \tau_{x_A}|$, for any of the target delays τ_{x_B} and τ_{x_A}. The relative amount (as a fraction) of cross-talk for two different delay channels is $\frac{|\tau_{x_B} - \tau_{x_A} - \tau_c|}{\tau_c}$. For the following results, the relative cross-talk between the A,B channels (and the B,C channels) is 0.25. Therefore, cross-talk is not severely limiting for the example shown henceforth.

We now consider how to process the different coincidence delay channels into an LLV. The relatively short distances involved and the specular nature of the reflection ensures that there is a negligible difference in signal attenuation between the considered object locations. This means that the system parameters for each delay channel are identical: consequently, for each channel, the parameters that define the LLV only differ in delay. Therefore, range-finding in this scenario depends only upon our ability to match signal and idler data channels with the correct delay. We only train the LLV from an initial batch of data once. In the subsequent figures we omit plotting the calibration stage. We now present the experimental data for a range-finding scenario of a target object in three separate locations. The target begins at location x_A, then after 200 samples we stop recording and move the target with the translation stage to location x_B. Once the target has moved we resume recording, the same process follows for moving to

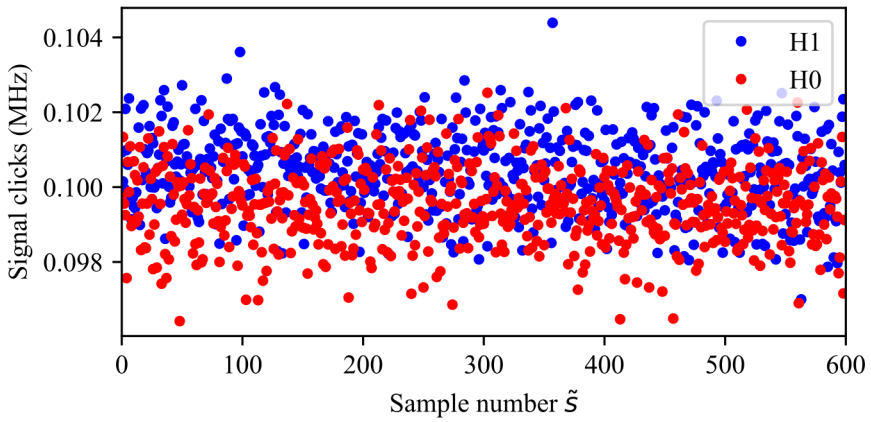

Figure 8.17 – Signal detector click-counts in MHz as a function of sample number $\tilde{s}$. Both object present (H1) and object absent (H0) data-sets superimposed. For the object present data set the object is three different locations, demarcated by the coloured regions. This example has ≈ 0.1 MHz of signal noise, 300µW of pump power, a ND40 filter to cause 33.5 dB of signal attenuation and an integration time for each sample $T = 0.1$ s. The coincidence window size $\tau_c = 1$ ns.

location x_C. Figure 8.17 shows the signal clicks in MHz as a function of sample number $\tilde{s}$, for both object present and absent scenarios. Figure 8.18 and Fig. 8.19 show the rolling window CI and QI LLVs as a function of sample number $\tilde{s}$, respectively. Where Fig. 8.19 shows three subplots corresponding to the three different delay channels for that LLV.

For Fig. 8.18 the object present and absent data-sets are distinguishable and would give a confident result with a higher sample refresh rate. However, it is unable to range the location of the object as it moves between the three different locations due to the lack of timing information available for CI. Figure 8.19 demonstrates that QI is able to range-find the location of a target object, as there is a clear upsurge in LLV for a delay channel when the target delay/location corresponds to that delay channel. Even though we are able to correctly range-find, the effect of cross-talk is noticeable for samples when the focused LLV delay channel has a delay adjacent to the correct delay for that sample number. We can negate the effect of cross-talk in our detection decision-making by increasing the LLV detection threshold d_{LLV} to a higher value than the conventional $d_{\text{LLV}} = 0$.

8.3.5 Range-finding in a jamming situation

This section describes how our protocol can range-find even when there is dynamic time-varying jamming. It combines the theory from Ch. 6.2 and Ch. 6.9. The results from this section demonstrate a major advantage of a QI-based LIDAR protocol: that we are able to range-find

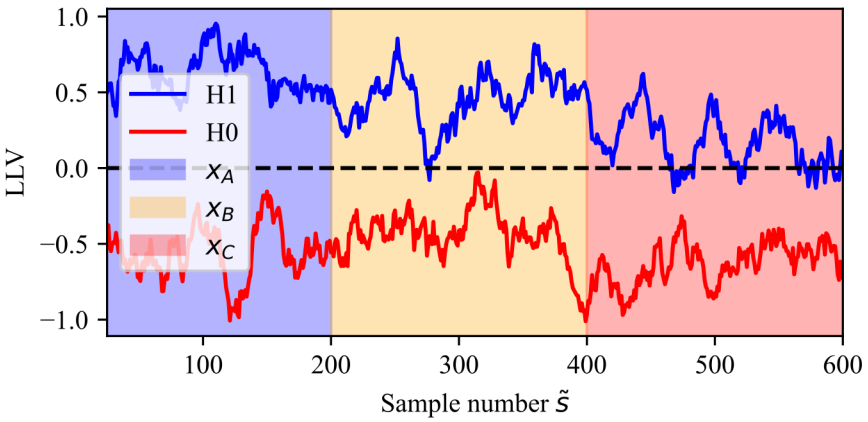

FIGURE 8.18 – CI rolling window LLV as a function of sample number $\tilde{s}$, for a refresh rate of $S = 25$ samples. Both object present (H1) and object absent (H0) data-sets superimposed. For the object present data set the object is three different locations, demarcated by the coloured regions. This example has ≈ 0.1 MHz of signal noise, 300μW of pump power, a ND40 filter to cause 33.5 dB of signal attenuation and an integration time for each sample $T = 0.1$ s. The coincidence window size $\tau_c = 1$ ns.

covertly in the presence of time-varying noise which could confuse conventional LIDAR systems. Figure 8.20 shows the signal clicks as a function of sample number $\tilde{s}$. The target begins at location x_A, then after 500 samples we stop recording and move the target with the translation stage to location x_B. Once the target has moved we resume recording, the same process follows for moving to location x_C. The object present and absent data-sets become out of sync due to imperfect splicing of the different data-sets corresponding to a change in target object location. The CI LLV object present and absent data-set is not plotted as it is unable to even detect the presence of an object due to the jamming (additionally, CI range-finding is impossible due to the lack of timing information as shown in Ch. 8.3.4. Figure 8.21 shows the QI rolling window LLV as a function of sample number $\tilde{s}$ with three subplots corresponding to the three different delay channels for that LLV.

We begin this chapter with a description of the experimental setup. We discuss how we can map our theoretical protocol onto this experiment via the estimation of the system parameters. We then present the experimental results. First, we demonstrate the ability to detect an object (at a known distance) for various parameter regimes. After, we discuss the system performance of QI compared to CI for object detection. Following this, we consider object detection in a jamming situation, which proves the inability of CI to object detect in this situation. We show how the experiment extends to facilitate range-finding capabilities. We then present the experimental results for QI (CI with a CW source can not perform range-finding). We

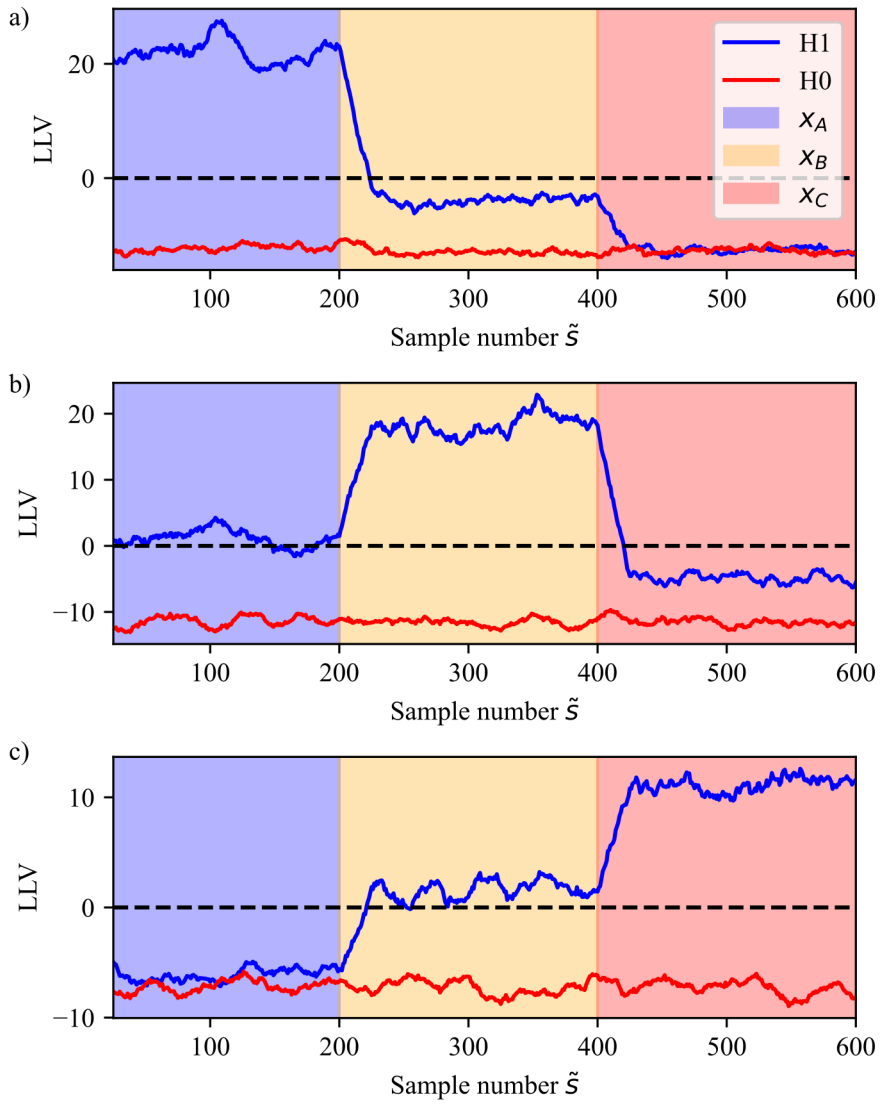

Figure 8.19 – QI rolling window LLV as a function of sample number $\tilde{s}$, for a refresh rate of $S = 25$ samples. Both object present (H1) and object absent (H0) data-sets superimposed. For the object present data set the object is three different locations, demarcated by the coloured regions. a) the LLV is for delay τ_{x_A}, b) the LLV is for delay τ_{x_B} and c) the LLV is for delay τ_{x_C}. This example has ≈ 0.1 MHz of signal noise, 300μW of pump power, a ND40 filter to cause 33.5 dB of signal attenuation and an integration time for each sample $T = 0.1$ s. The coincidence window size $\tau_c = 1$ ns.

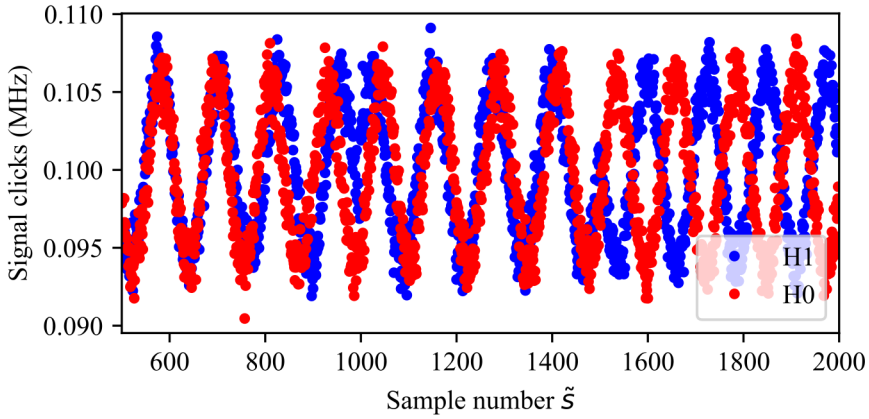

FIGURE 8.20 – Signal detector click-counts in MHz as a function of sample number $\tilde{s}$, in the presence of sinusoidal jamming. Both object present (H1) and object absent (H0) data-sets superimposed. The object present and absent data-sets become out of sync with the sinusoidal jamming due to imperfect splicing of the different object location data-sets. This example has ≈ 0.1 MHz of signal noise which corresponds to a mean photon number $\bar{n}_{\mathrm{B,S}} = 1.99 \times 10^{-5}$. This figure has jamming with a modulation amplitude of 10 kHz which corresponds to a mean photon number of 1.5×10^{-6}. 50μW of pump power, a ND40 filter to cause 33.5 dB of signal attenuation and an integration time for each sample $T = 0.1$ s. The coincidence window size $\tau_{\mathrm{c}} = 0.2$ ns.

conclude our experimental results by demonstrating the ability of QI to perform range-finding in a jamming situation.

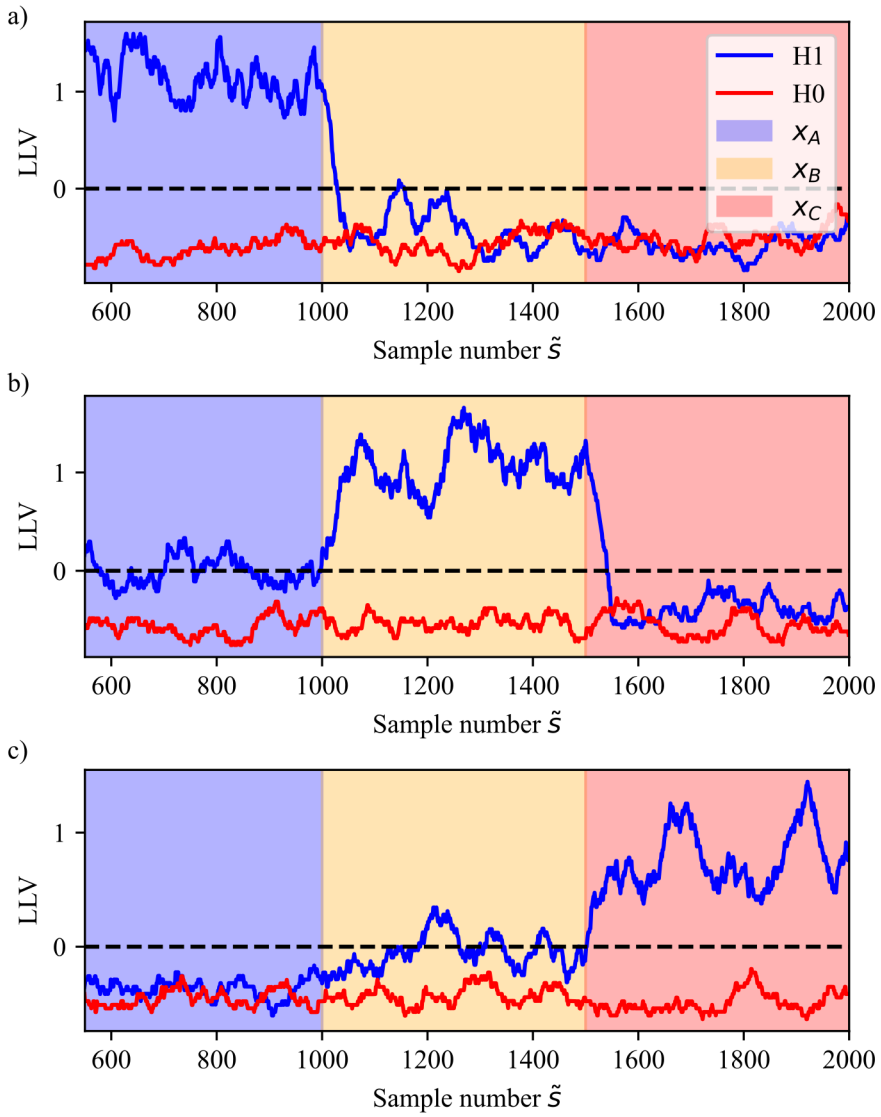

Figure 8.21 – QI rolling window LLV as a function of sample number $\tilde{s}$, for a refresh rate of $S = 50$ samples. This is in the situation of sinusoidal jamming. Both object present (H1) and object absent (H0) data-sets superimposed. For the object present data set the object is three different locations, demarcated by the coloured regions. a) the LLV is for delay τ_{x_A}, b) the LLV is for delay τ_{x_B} and c) the LLV is for delay τ_{x_C}. This example has ≈ 0.1 MHz of signal noise which corresponds to a mean photon number $\bar{n}_{\mathrm{B,S}} = 1.99 \times 10^{-5}$. This figure has jamming with a modulation amplitude of 10 kHz which corresponds to a mean photon number of 1.5×10^{-6}. 50μW of pump power, a ND40 filter to cause 33.5 dB of signal attenuation and an integration time for each sample $T = 0.1$ s. The coincidence window size $\tau_{\mathrm{c}} = 0.2$ ns.

Chapter 9: Conclusion

9.1 Aim of thesis

The aim of this thesis has been to provide a quantum-enhanced LIDAR protocol which is both operator-friendly and applicable for deployment outside of a laboratory environment. Previous literature does not demonstrate quantum-enhanced LIDAR with self-calibrated decision-making abilities and operator-friendly terminology. Moreover, this thesis aims to demonstrate that realisation of quantum-enhanced technologies for sensing applications are in the near-term.

9.2 Discussion of protocol abilities and experimental results

We have provided a quantum-enhanced LIDAR protocol that can detect objects and range-find. The theoretical and experimental results from our protocol reinforce the knowledge that simple-detection QI performs better than CI in high noise, lossy and low signal strength regimes. Our range-finding is covert when we use a CW pump in a low signal strength and high background noise regime. We introduce a new and operator-friendly performance analysis method, alongside more common-place approaches. A further operator-friendly feature of our protocol is that detection decision-making is inbuilt into the data processing framework. Furthermore, the framework is designed such that it is possible for the decision-making interpretation of the LLV to be identical for QI or CI, or different parameter regimes. This facilitates a direct comparison of the aforementioned modalities or assumed parameter regimes in our LLV framework.

There is a large amount of freedom to tailor the model, which underpins our protocol, to a certain scenario: it is not restricted to a certain platform. For example, it is not restricted to a certain wavelength, type of pump (pulsed or CW), or coincidence window size. Nor does the photon statistics of the background light or source light restrict it, a change of type of light only requires an updated set of relevant click probabilities. We can also modify the assumed target object scattering properties.

Our framework demonstrates a small advantage from using the often-overlooked non-

coincidence clicks as demonstrated by Eq. 4.14. This advantage stems from the missed idler clicks not registering a signal click as a true coincidence-click. Moreover, the LLV framework for analysing detector data easily extends to considering multi-mode correlations present in the non-classical light, as introduced in Ch. 5. As such, our framework allows for multiple data channels to reduce to a single metric. We theoretically demonstrate an advantage in using multi-mode light for state discrimination.

A problem in binary hypothesis testing is the inability to dynamically update the estimations of the two hypotheses, simultaneously. The relevant parameter regime for QI is well-suited to remedy this, as the signal strength is low compared to the background noise. Therefore, the signal detector statistics can estimate the background noise for the H0 hypothesis, even when H1 is true. This allows for dynamic updating of object present (H1) and object absent (H0) hypotheses, facilitating a level of self-calibration of the LLV. This feature reinforces the operator-friendly aspect of our protocol. It also shows the suitability of our likelihoodist statistical approach for a QI-based system.

Our results demonstrate accurate object detection in scenarios with a SNR of -51.5 dB and 52 dB of signal attenuation, this corresponds to object detection in realistic scenarios [86]. Our best improvement of SNR for QI compared to CI is 30 dB, which translates to accurate target discrimination 17x faster for QI than CI. Moreover, our QI object detection results have a 13 dB improvement compared to the QI findings from England et al. in Ref. [73] and they are comparable to the findings in from Liu et al. in Ref. [85]. Furthermore, our spatial resolution for range-finding is 11 cm, limited by the timing jitter of our room temperature detectors. However, what distinguishes our work from Ref. [85] is that we have a detection-decision orientated framework for processing detector data, we demonstrate range-finding, our framework shows its suitability for countering the effect of dynamic time-varying jamming and we have developed generalised theory to improve system performance by using multi-mode correlations between the two beams in QI. As such we have presented a jamming-resilient quantum-enhanced LIDAR protocol which is practical for real-life use and is operator-friendly.

9.3 Applications and possible future developments

One of the key limitations of QI for applications is that the signal strength is limited to $\bar{n} < 1$ for a quantum advantage. This makes detection of uncooperative targets at distance challenging due to the weak signal strength and the subsequent low return rate. For example, the demonstrated -52 dB loss is comparable to that expected from a Lambertian scatterer at

15 m using a 10 cm diameter telescope [91]. Cooperative specular reflectors, however, could allow for accurate target discrimination at more typical LIDAR distances within reasonable integration times. Our protocol could also provide accurate target discrimination of cooperative specular reflectors which are partially obscured, when CI is unable to (albeit at shorter distances than the unobscured situation). Lastly, high levels of incident probe light can damage or alter certain targets. Therefore, QI would allow accurate target discrimination of such fragile samples, due to its enhanced performance in weak signal strength regimes.

The other key limitation of QI is that it only outperforms classical coherent detection methods in the presence of high noise $\bar{n}_{\mathrm{B,S}} > 1$. Frequency-filtered natural daylight does not exceed this mean photon number for optical wavelengths [173]. Whereas active strong jamming would cause such a high noise mean photon number at optical wavelengths. This further demonstrates the applicability of QI for sensing in jamming situations. Furthermore, frequency-filtered natural background noise at microwave wavelengths does exceed this value, which gives credence to the desire for the development of QI protocols at the microwave wavelengths [174].

By considering the two key limitations of QI, it is clear that the main application of QI-based LIDAR is in scenarios when CI-based LIDAR fails or when coherence-based (optimal) classical LIDAR methods are inappropriate for use. CI-based LIDAR could fail in active jamming situations and/or when covertness is desired. Furthermore, coherence-based classical LIDARs are not covert. QI-based LIDAR is able to function in such regimes. In particular, the jamming-resilience from the coincidence-click noise filtering grants robustness. Additionally, the range-finding capabilities with a CW pump and functionality at low signal strength regimes grants a level of covertness.

Before considering experimental or theoretical extensions to our protocol we must consider how certain parameters in our system influence the performance of our system. Some parameters we have almost no control over, for example the signal attenuation factor ξ. We can only partially adjust the signal attenuation factor ξ by changing the area of our detectors to increase the size of the collection optics. Whereas, we can increase the system loss parameters $\eta_{\mathrm{I/S}}$ by improving the fibre-coupling, collection optics, or the detector quantum efficiency. However, detector quantum efficiency is inversely related to the timing jitter, hence we must compromise between an improved coincidence-count rate or spatial resolution. If we reduce the idler detector background noise $\bar{n}_{\mathrm{B,I}}$ this would improve the quality of our heralding measurements as less coincidence-clicks stem from detector dark noise. A better environmental-shielding method could reduce the detector background noise, as would cooling our detectors to reduce thermally-induced detector dark counts. For example, cooling our detectors from 30°C to −10°C would reduce

the dark count mean photon number by a factor of 100, for a particular reverse bias voltage of the SPAD [175]. Lastly, we could optimise our mean photon number $\bar{n}$ according to the requirements of a particular application. For example, a smaller mean photon number would improve the heralding gain and would improve covertness, albeit at the cost of an increased integration time for accurate target discrimination.

There are extensions to our experimental setup which could improve the system performance. For example, engineering to facilitate non-local dispersion cancellation shown by Blakey et al. in Ref. [71] would filter out more noise, thereby improving the SNR. We can enhance our spatial resolution for range-finding with the reduction of timing uncertainty via the use of superconducting nanowire detectors, albeit this requires the use of cryogenics to cool the detectors to their operating temperatures [176]–[178]. Future experiments could implement the multiplexed detector set-up by Yang et al. in Ref. [80]. This could extend to a multiplexed set-up for each detector in a set of spectrally resolving detectors, in line with M:TBSS theory in Ch. 5. This approach would achieve enhanced system performance, with the reduction of the deleterious effect of sensor dead-time and increased noise filtering. We could also improve our detection and estimation theoretical framework. Instead of a rolling window approach to mitigate the effects of a dynamic system, a more advanced approach would use a Kalman filter to ensure accuracy of the LLV test by not only continually re-estimating the underlying system parameters, but it would proactively predict the possible future parameters in a dynamic system.

This research has security and covertness at the forefront of its potential applications. We could obtain imaging security with a QKD-like protocol running adjacent to our LLV framework. Such a protocol would guarantee spoofing-resilience on-top of the jamming-resilience already provided. This QKD-like protocol would benefit from the lack of classical channel required, as the sender (Alice) and receiver (Bob) are the same person. Moreover, as Alice and Bob are the same person there would be no false basis measurements, thereby helping the resultant key-rate. However, the question remains as to which photonic degree of freedom would work best as a basis for this QKD-like framework, given the requirements of preservation during free-space propagation, reflection upon target object and practicality of the experiment.

To conclude, the outlook for deployment of QI-based LIDAR depends upon acknowledgement of its advantageous use in niche use-cases. Such as covert sensing, fragile-target probing and secure-imaging scenarios. The aforementioned future (possible) developments would improve the capabilities of QI-based LIDAR in these application-spaces.

Appendices

Chapter A: Fock basis method for click probability

This appendix demonstrates an alternative method for calculation of Eq. 3.31d. It also illustrates how usage of the coherent state basis for beamsplitter calculations is desired instead of the Fock basis approach shown here, due to the relative difficulty of this method. We consider the CI protocol with thermal noise $\hat{\rho}_{\mathrm{B}} = \hat{\rho}_{\mathrm{th}}(\bar{n}_{\mathrm{B}})$ and a coherent signal $\hat{\rho}_{\mathrm{source}} = |\alpha\rangle\langle\alpha|$. The output state from the beamsplitter is thus

$$\begin{aligned}
\hat{U}\hat{\rho}_{\mathrm{source}} \otimes \hat{\rho}_{\mathrm{B}}\hat{U}^{\dagger} &= \sum_{n=0}^{\infty} \frac{\bar{n}_{\mathrm{B}}^{n}}{(\bar{n}_{\mathrm{B}}+1)^{n+1}} \frac{1}{n!} (r\hat{a}_2^{\dagger} + t\hat{a}_3^{\dagger})^{n} \hat{D}_2(t\alpha)\hat{D}_3(r\alpha) \\
&\quad \times |0\rangle_2\langle 0| \otimes |0\rangle_3\langle 0| (r^{*}\hat{a}_2 + t^{*}\hat{a}_3)^{n} \hat{D}_2^{\dagger}(t\alpha)\hat{D}_3^{\dagger}(r\alpha), \qquad \text{(A.1a)} \\
&= \sum_{n=0}^{\infty} \frac{\bar{n}_{\mathrm{B}}^{n}}{(\bar{n}_{\mathrm{B}}+1)^{n+1}} \frac{1}{n!} \sum_{k,k'=0}^{n} \binom{n}{k}\binom{n}{k'} (r\hat{a}_2^{\dagger})^{n-k} (t\hat{a}_3^{\dagger})^{k} \\
&\quad \times |t\alpha\rangle_2\langle t\alpha| \otimes |r\alpha\rangle_3\langle r\alpha| (r^{*}\hat{a}_2)^{n-k'} (t^{*}\hat{a}_3)^{k'}, \qquad \text{(A.1b)} \\
&= \sum_{n=0}^{\infty} \frac{\bar{n}_{\mathrm{B}}^{n}}{(\bar{n}_{\mathrm{B}}+1)^{n+1}} \sum_{k=0}^{n} \binom{n}{k} |r|^{2(n-k)} |t|^{2k} \\
&\quad \times |t\alpha, n-k\rangle_2\langle t\alpha, n-k| \otimes |r\alpha, k\rangle_3\langle r\alpha, k|, \qquad \text{(A.1c)}
\end{aligned}$$

where we introduce the displaced number state $\hat{D}(\alpha)|n\rangle = |\alpha, n\rangle$ [179]. We also simplify the expression by setting $k = k'$, as the detectors only enact upon the diagonals of the density matrix. After this, we apply the method shown in Appendix. A.1. Hence, the state incident upon the detector is

$$\begin{aligned}
\hat{\rho}_{\mathrm{S}} &= \mathrm{Tr}_3\left(\hat{U}\hat{\rho}_{\mathrm{source}} \otimes \hat{\rho}_{\mathrm{B}}\hat{U}^{\dagger}\right), \qquad \text{(A.2a)} \\
&= \sum_{n=0}^{\infty} \frac{\bar{n}_{\mathrm{B}}^{n}}{(\bar{n}_{\mathrm{B}}+1)^{n+1}} \sum_{k=0}^{n} \binom{n}{k} |r|^{2(n-k)} |t|^{2k} |t\alpha, n-k\rangle\langle t\alpha, n-k|, \qquad \text{(A.2b)} \\
&= \sum_{u=0}^{\infty} \frac{(\bar{n}_{\mathrm{B}}|r|^2)^{u}}{(\bar{n}_{\mathrm{B}}|r|^2+1)^{u+1}} |t\alpha, u\rangle\langle t\alpha, u|. \qquad \text{(A.2c)}
\end{aligned}$$

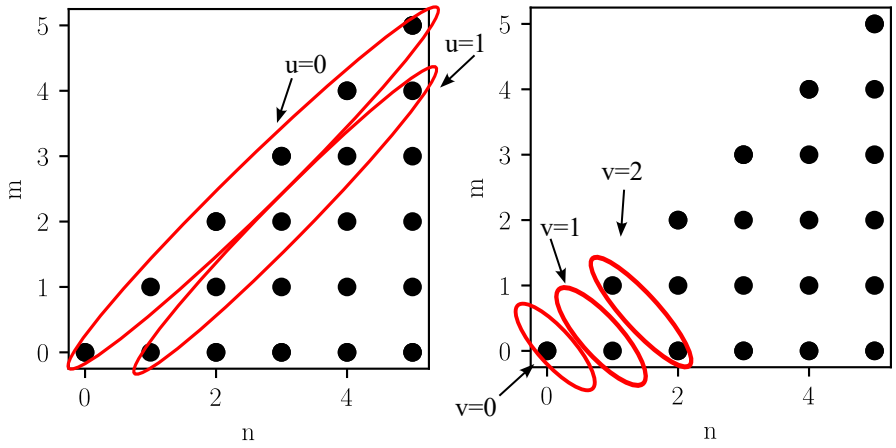

Figure A.1 – Plot showing how a change of variables into u and v spans the entire space summed originally by n and m.

Calculation of the click probability draws upon the results from Appendix A.2 for the overlap, hence the click probability is

$$\begin{aligned}
\Pr &= 1 - \langle 0|\hat{\rho}_{\mathrm{S}}|0\rangle, && \text{(A.3a)}\\
&= 1 - \sum_{u=0}^{\infty} \frac{(\bar{n}_{\mathrm{B}}|r|^2)^u}{(\bar{n}_{\mathrm{B}}|r|^2+1)^{u+1}} |\langle 0|t\alpha, u\rangle|^2, && \text{(A.3b)}\\
&= 1 - \frac{e^{\frac{-|t\alpha|^2}{\bar{n}_{\mathrm{B}}|r|^2+1}}}{\bar{n}_{\mathrm{B}}|r|^2+1}. && \text{(A.3c)}
\end{aligned}$$

A.1 Simplifying a double summation

The method of simplifying a double summation is used in the Fock basis method for beamsplitter calculations. Suppose there is a density matrix of form

$$\hat{\rho} = A \sum_{n=0}^{\infty} X^n \sum_{m=0}^{n} \binom{n}{m} Y^m Z^{n-m} |n-m\rangle\langle n-m|. \tag{A.4}$$

To tackle this problem, a discrete plot is made, resembling a right-angled triangle, with n and m on the axes as pictured in Fig. A.1. The subsequent change of variables is $u = n - m$ and $v = n + m$. Following this, it is easy to see the new form of the double summation will be

$$\hat{\rho} = A \sum_{u=0}^{\infty} (XZ)^u |u\rangle\langle u| \sum_{\substack{v=u \\ v\in S}}^{\infty} \binom{\frac{u+v}{2}}{\frac{v-u}{2}} (XY)^{\frac{v-u}{2}} \tag{A.5}$$

Where $S = \{u, \ldots, u+2k\},\ k \in \mathcal{N}$. Additionally, setting $y = \frac{v-u}{2}$ and expanding for the first few number states, we see a pattern emerge, that allows the second summation to be rewritten as,

$$\hat{\rho} = A \sum_{u=0}^{\infty} (XZ)^u |u\rangle\langle u| \sum_{y=0}^{\infty} \binom{u+y}{y} (XY)^y. \tag{A.6}$$

Knowing that

$$\sum_{y=0}^{\infty} \binom{u+y-1}{y} (XY)^y = \frac{1}{(1-XY)^u}. \tag{A.7}$$

The second summation can be rewritten again as,

$$\sum_{y=0}^{\infty} \binom{u+y}{y} (XY)^y = \sum_{y=0}^{\infty} \frac{(u+y-1)!}{y!(u-1)!} \frac{(u+y)}{u} (XY)^y, \tag{A.8a}$$

$$= \frac{1}{(1-XY)^u} + \frac{XY}{u} \frac{\partial}{\partial(XY)} \left(\frac{1}{(1-XY)^u} \right), \tag{A.8b}$$

$$= \frac{1}{(1-XY)^u} \left(1 + \frac{XY}{1-XY} \right). \tag{A.8c}$$

Supplanting this result into the density matrix receives,

$$\hat{\rho} = \frac{A}{1-XY} \sum_{u=0}^{\infty} \left(\frac{XZ}{1-XY} \right)^u |u\rangle\langle u|. \tag{A.9}$$

A.2 Calculating the displaced number state overlap

We want to calculate the displaced number state overlap $|\langle 0|t\alpha, u\rangle|^2$. This derivation beings with calculation of the non-conjugated term in the overlap

$$\langle 0|t\alpha, u\rangle = \langle 0| \hat{D}(t\alpha) |u\rangle, \tag{A.10a}$$

$$= \frac{1}{\sqrt{u!}} \langle 0| \hat{D}(t\alpha) \hat{a}^{\dagger u} |0\rangle. \tag{A.10b}$$

We use the relation [180], $\hat{D}(\alpha)\hat{a}^{\dagger m}\hat{D}^{\dagger}(\alpha) = (\hat{a}^{\dagger} - \alpha^{*})^{m}$ and Eq. A.10b is rearranged into the form

$$\langle 0|t\alpha, u\rangle = \frac{1}{\sqrt{u!}} \langle 0| \left(\hat{a}^{\dagger} - (t\alpha)^{*}\right)^{u} \hat{D}(t\alpha) |0\rangle , \tag{A.11a}$$

$$= \frac{1}{\sqrt{u!}} \sum_{p=0}^{u} \binom{u}{p} (-(t\alpha)^{*})^{u-p} \langle 0| \hat{a}^{\dagger p} \hat{D}(t\alpha) |0\rangle , \tag{A.11b}$$

$$= \frac{1}{\sqrt{u!}} (-(t\alpha)^{*})^{u} \langle 0|t\alpha\rangle, \tag{A.11c}$$

$$= \frac{e^{\frac{-|t\alpha|^{2}}{2}}}{\sqrt{u!}} (-(t\alpha)^{*})^{u}. \tag{A.11d}$$

Above in Eq. A.11b the only non-zero term is when $p = 0$. Following on from the above, the overlap is

$$|\langle 0|t\alpha, u\rangle|^{2} = \frac{e^{-|t\alpha|^{2}}}{u!} |t\alpha|^{2u}. \tag{A.12}$$

Chapter B: Photon-number distribution definitions

In this appendix we define the photon-number distributions for the unconditioned ρ_{S}, idler no-click conditioned $\hat{\rho}_{\mathrm{S|I},0}$ and idler click conditioned $\hat{\rho}_{\mathrm{S|I},1}$ states. We provide the distributions for both noise types we consider in this thesis: thermal (Fig. 3.5) and Poissonian (Fig. 3.6). The photon-number distribution of the unconditioned state with thermal noise (Eq. 3.47) is

$$P(n)_{\mathrm{S}} = \frac{(\xi\eta_{\mathrm{S}}\bar{n} + \bar{n}_{\mathrm{B,S}})^n}{(\xi\eta_{\mathrm{S}}\bar{n} + \bar{n}_{\mathrm{B,S}} + 1)^{(n+1)}}. \tag{B.1}$$

Following this the photon-number distribution of the idler no-click conditioned state (Eq. 3.52) is

$$P(n)_{\mathrm{I},0} = \frac{(\xi\eta_{\mathrm{S}}\bar{n}_{\mathrm{X}} + \bar{n}_{\mathrm{B,S}})^n}{(\xi\eta_{\mathrm{S}}\bar{n}_{\mathrm{X}} + \bar{n}_{\mathrm{B,S}} + 1)^{(n+1)}}, \tag{B.2}$$

where $\bar{n}_{\mathrm{X}} = \bar{n}\frac{(1+\bar{n}_{\mathrm{B,I}}-\eta_{\mathrm{I}})}{(1+\bar{n}_{\mathrm{B,I}}+\bar{n}\eta_{\mathrm{I}})}$. The photon-number distribution of the idler click conditioned state with thermal noise (Eq. 3.54b) is

$$\begin{aligned} P(n)_{\mathrm{I},1} = \frac{1}{\mathrm{Pr}_{\mathrm{I}}}\Bigg(&\frac{(\xi\eta_{\mathrm{S}}\bar{n} + \bar{n}_{\mathrm{B,S}})^n}{(\xi\eta_{\mathrm{S}}\bar{n} + \bar{n}_{\mathrm{B,S}} + 1)^{(n+1)}} - \\ &- (1 - \mathrm{Pr}_{\mathrm{I}})\frac{(\xi\eta_{\mathrm{S}}\bar{n}_{\mathrm{X}} + \bar{n}_{\mathrm{B,S}})^n}{(\xi\eta_{\mathrm{S}}\bar{n}_{\mathrm{X}} + \bar{n}_{\mathrm{B,S}} + 1)^{(n+1)}}\Bigg). \end{aligned} \tag{B.3a}$$

For the photon-number distributions with Poissonian noise, the derivation followed a similar method as given in Appendix A.2, instead with the source with thermal statistics and the noise with Poissonian statistics from the coherent state with amplitude $\beta = \frac{\sqrt{\bar{n}_{\mathrm{B,S}}}}{t}$. The photon-number distribution of the unconditioned state with Poissonian noise (Eq. 3.56) is

$$P(n)_{\mathrm{S}} = \sum_{u=0}^{\infty} \frac{(\xi\eta_{\mathrm{S}}\bar{n})^u}{(\xi\eta_{\mathrm{S}}\bar{n} + 1)^{u+1}} |\langle n|t\beta, u\rangle|^2, \tag{B.4}$$

where the overlap between the n-photon Fock state and the displaced number state $|t\beta, u\rangle$ is

$$\langle n|t\beta, u\rangle = \frac{1}{\sqrt{u!}} \sum_{\substack{p=0 \\ p\leq n}}^{u} \binom{u}{p} (-(t\beta)^*)^{u-p} \frac{\sqrt{n!}}{(n-p)!} (t\beta)^{n-p} e^{-|t\beta|^2/2}. \tag{B.5}$$

The photon-number distribution of the idler no-click conditioned state with Poissonian noise (Eq. 3.58) is

$$P(n)_{\mathrm{I},0} = \sum_{q=0}^{\infty} \frac{(\xi\eta_{\mathrm{S}}\bar{n}_{\times})^q}{(\xi\eta_{\mathrm{S}}\bar{n}_{\times}+1)^{q+1}} |\langle n|t\beta, q\rangle|^2, \tag{B.6}$$

where Eq. B.5 defines $\langle n|t\beta, q\rangle$. The photon-number distribution of the idler click conditioned state with Poissonian noise (Eq. 3.60) is

$$P(n)_{\mathrm{I},1} = \frac{1}{\mathrm{Pr}_{\mathrm{I}}} \Big(P(n)_{\mathrm{S}} - (1-\mathrm{Pr}_{\mathrm{I}}) P(n)_{\mathrm{I},0} \Big), \tag{B.7}$$

where $P(n)_{\mathrm{S}}$ and $P(n)_{\mathrm{I},0}$ are the relevant photon-number distributions for states with Poissonian noise.

Chapter C: Gaussian approximation requirements

The Gaussian regime affords analytic simplicity and computational speed. This regime refers to the system parameters that permits the approximation of the Binomial click-count distributions as Gaussian distributions, with negligible error produced. The following criteria is applied to ensure the Gaussian approximation is valid for the system parameters set. The criteria is that all distributions for the system parameters in question must not be too skewed and that the mean is not too skewed towards the limits of the range of possible values [181]. We can apply two rough rules of thumb which is that both

$$\frac{|1-2p|}{\sqrt{Np(1-p)}} < 0.3, \tag{C.1}$$

and

$$Np > 5, \tag{C.2}$$

are satisfied. Where p is the success probability which underlies the distribution and N is the number of shots. In practice, not all Binomial distributions require a Gaussian validity check; instead, a validity check only applies to the Binomial distribution most prone to failing the Gaussian approximation. In the scenario of low signal strength with signal loss in a noisy environment, the weakest distribution is the object absent signal coincidence click-count distribution after a thresholded minimum of idler clicks. The mean and standard deviation of the idler click distribution is μ_{I} and σ_{I} respectively. The thresholded minimum of idler clicks is $\mathrm{I}_{\min} = \lfloor \mu_{\mathrm{I}} - 4\sigma_{\mathrm{I}} \rfloor$. Hence, the form of the weakest distribution is

$$P_{\min}(x) = \binom{\mathrm{I}_{\min}}{x} p_{\min}^{x} (1-p_{\min})^{\mathrm{I}_{\min}-x}, \tag{C.3}$$

where $p_{\min}$ is the least likely type of signal click event in the analysed system when the object is absent. The least likely type of signal click event for the system is the coincidence click. If

this distribution satisfies Eq. C.1 then the Gaussian approximation is valid for the given system parameters. If the Gaussian regime applies to even the weakest distribution, an approximation to Gaussian is possible for all Binomial distributions for the system parameters set. This approximation from Binomial to Gaussian is

$$P(x, N, p) = \binom{N}{x} p^x (1-p)^{N-x}. \tag{C.4}$$

to

$$P(x, \mu, \sigma) \approx \frac{1}{\sigma\sqrt{2\pi}} e^{-0.5(\frac{x-\mu}{\sigma})^2}, \tag{C.5}$$

where $\mu = Np$ and $\sigma = \sqrt{Np(1-p)}$.

Chapter D: Deriving the linear form of the LLV

The generic LLV in its ratio of click probability distributions form

$$\Lambda(\underline{x}, k) = \ln\left(\frac{P_{\mathrm{H1}}(\underline{x}, k)}{P_{\mathrm{H0}}(\underline{x}, k)}\right), \tag{D.1}$$

$\underline{x}$ is the vector of the click-counts by type of click event, k is the relevant number of shots (CI total shots and QI number of idler clicks) and $P_{\mathrm{H}\{1,0\}}(\underline{x}, k)$ is the probability for object present or absent respectively. The probability distribution for click events is originally Binomial, due to the Bernoulli trials undertaken. For the remainder of the appendices I use shorthand notation for the click probabilities $\mathrm{Pr}_{\mathrm{H1:CI}} \equiv p_{\mathrm{H1}}$, $\mathrm{Pr}_{\mathrm{H0:CI}} \equiv p_{\mathrm{H0}}$, $\mathrm{Pr}_{\mathrm{I}} \equiv p_{\mathrm{I}}$, $\mathrm{Pr}_{\mathrm{S|I},1} \equiv p_{\mathrm{S|I},1}$, $\mathrm{Pr}_{\mathrm{S|I},0} \equiv p_{\mathrm{S|I},0}$ and $\mathrm{Pr}_{\mathrm{H0}} \equiv p_{\mathrm{H0}}$. The CI protocol is focused on first, as there is only one element in $\underline{x} \equiv x$. The object present and absent probability density functions in its Binomial form, respectively

$$P_{\mathrm{H1}}(x, N) = \binom{N}{x} p_{\mathrm{H1}}^{x} (1 - p_{\mathrm{H1}})^{N-x}, \tag{D.2}$$

$$P_{\mathrm{H0}}(x, N) = \binom{N}{x} p_{\mathrm{H0}}^{x} (1 - p_{\mathrm{H0}})^{N-x}. \tag{D.3}$$

As N, x and all the click probabilities are all real and positive Eq. D.1 can be expressed as a linear equation. Hence, for CI Eq. D.1 is

$$\Lambda(x, N) = Mx + NC, \tag{D.4}$$

where $M = \ln\left(\frac{p_{\mathrm{H1}}(1-p_{\mathrm{H0}})}{p_{\mathrm{H0}}(1-p_{\mathrm{H1}})}\right)$ and $C = \ln\left(\frac{1-p_{\mathrm{H1}}}{1-p_{\mathrm{H0}}}\right)$. The LLV for QI easily extends to include idler not firing events in the linear equation. The signal click-count x conditioned by k idler click events and signal click-count y after $N - k$ idler no-firing events in the QI protocol is

transformed by the LLV defined as

$$\Lambda(\underline{x}, k) = \underline{M}^{\mathrm{T}}\underline{x} + \underline{NC}^{\mathrm{T}}, \tag{D.5}$$

where $\underline{M}^{\mathrm{T}} = (M_1\ M_2)$, $\underline{x} = (x\ y)$, $\underline{C}^{\mathrm{T}} = (C_1\ C_2)$ and $\underline{N} = \binom{k}{N-k}$. Where

$$M_1 = \ln\left(\frac{p_{\mathrm{S|I},1}(1-p_{\mathrm{H0:I1}})}{p_{\mathrm{H0:I1}}(1-p_{\mathrm{S|I},1})}\right), \tag{D.6}$$

$$M_2 = \ln\left(\frac{p_{\mathrm{S|I},0}(1-p_{\mathrm{H0:I0}})}{p_{\mathrm{H0:I0}}(1-p_{\mathrm{S|I},0})}\right), \tag{D.7}$$

$$C_1 = \ln\left(\frac{1-p_{\mathrm{S|I},1}}{1-p_{\mathrm{H0:I1}}}\right), \tag{D.8}$$

$$C_2 = \ln\left(\frac{1-p_{\mathrm{S|I},0}}{1-p_{\mathrm{H0:I0}}}\right). \tag{D.9}$$

.

Chapter E: Click to LLV distribution

All click-count distributions are easily transformed into LLV forms, assuming that the Gaussian approximation is valid. The LLV for CI Eq. D.4 and QI Eq. D.5 are linear; this property faciltates easy transformation from click-count to LLV distribution. The first two statistical moments fully specify a Gaussian distribution and as linear transformations preserve normality it is easy to transform click-count to LLV distribution. We focus upon the object present scenario for the following analysis (the object absent scenario requires a simple replacement of the relevant click probabilities). Shown below is the transformation into LLV moments for the mean $\mu_{\mathrm{H1:CI}} = Np_{\mathrm{H1}}$ and standard deviation $\sigma_{\mathrm{H1:CI}} = \sqrt{Np_{\mathrm{H1}}(1-p_{\mathrm{H1}})}$ for CI

$$\begin{aligned} \mu_{\mathrm{H1:CI:\Lambda}} &= \Lambda(\mu_{\mathrm{H1:CI}}, N), && \text{(E.1)} \\ &= M\mu_{\mathrm{H1:CI}} + NC. && \text{(E.2)} \end{aligned}$$

and

$$\sigma_{\mathrm{H1:CI:\Lambda}} = M\sigma_{\mathrm{H1:CI}}. \quad \text{(E.3)}$$

However, it is not as simple for QI. Equation D.5 encodes both coincidence clicks and non-coincidence click-count distributions into the one LLV distribution. Equation D.5 amounts to a linear combination and linear combinations preserve normality. Therefore, the resulting LLV distribution is still normal. When there are k idler click events, a click-count distribution's statistical moments $(\mu_{\mathrm{H1}:k}, \sigma_{\mathrm{H1}:k})$ are transformed into its respective LLV statistical moments as

$$\begin{aligned} \mu_{\mathrm{H1:\Lambda}(x,k)} &= M_1 k p_{\mathrm{S|I},1} + C_1 k + M_2 \left((N-k)p_{\mathrm{S|I},0}\right) + \\ &+ (N-k)C_2. && \text{(E.4)} \end{aligned}$$

for the mean and

$$\begin{aligned}\sigma_{\mathrm{H1}:\Lambda(x,k)} &= \big(M_1^2 k p_{\mathrm{S|I},1}(1-p_{\mathrm{S|I},1}) + \\ &+ M_2^2(N-k)p_{\mathrm{S|I},0}(1-p_{\mathrm{S|I},0})\big)^{0.5} \end{aligned} \tag{E.5}$$

for the standard deviation. Much of the characterisation of system performance is oriented around the LLV distributions conditioned by mean idler clicks $\mu_{\mathrm{I}} = Np_{\mathrm{I}}$, rather than for k idler clicks. Therefore, the mean of the object present LLV distribution conditioned by mean idler clicks is defined as

$$\begin{aligned}\mu_{\mathrm{H1}:\Lambda(x,\mu_{\mathrm{I}})} &= N\big(p_{\mathrm{I}}(M_1 p_{\mathrm{S|I},1} + C_1 - M_2 p_{\mathrm{S|I},0} - C_2) + \\ &+ M_2 p_{\mathrm{S|I},0} + C_2\big), \end{aligned} \tag{E.6}$$

and the standard deviation of the object present LLV distribution conditioned by mean idler clicks is

$$\begin{aligned}\sigma_{\mathrm{H1}:\Lambda(x,\mu_{\mathrm{I}})} &= \Big(N\big(p_{\mathrm{I}}(M_1^2 p_{\mathrm{S|I},1}(1-p_{\mathrm{S|I},1}) + \\ &- M_2^2 p_{\mathrm{S|I},0}(1-p_{\mathrm{S|I},0})) + \\ &+ M_2^2 p_{\mathrm{S|I},0}(1-p_{\mathrm{S|I},0})\big)\Big)^{0.5}. \end{aligned} \tag{E.7}$$

Chapter F: Distinguishability discrepancy

The LLV conditioned by k idler clicks processes coincidence (and possibly non-coincidence) click data which has had k idler clicks, once this processing has occurred the knowledge of the underlying click data is obscured and only an LLV is known. Neglecting our knowledge of how many idler clicks there has been simplifies the post-processing of LLV data. Therefore, for any LLV conditioned by k idler clicks this LLV can be processed with any other LLV with $\tilde{k} \neq k$ idler clicks. In other words, each LLV conditioned by any number of idler clicks are equivalent to each other in post-processing. Hence, it is important that the discrepancy in the effectiveness of each LLV test conditioned by k idler clicks is limited. Otherwise this equivalence is erroneous.

For a set of system parameters, QI has object present and absent LLV distributions for each k idler clicks. This corresponds to a distinguishability for each LLV conditioned by k idler clicks, which is denoted as ϕ_k. The system performance is characterised in terms of the threshold distinguishability ϕ_{t}, which is calculated from the LLV distributions conditioned on the mean number of idler clicks. Consequently, there must be only a limited discrepancy between any ϕ_k and ϕ_{t}, for LLV equivalence to be valid.

Bounds are placed on what is considered to be extremal numbers of k idler clicks. We define the minimum and maximum k idler clicks as $I_{\min} = \lfloor \mu_{\mathrm{I}} - 4\sigma_{\mathrm{I}} \rfloor$ and $I_{\max} = \lfloor \mu_{\mathrm{I}} + 4\sigma_{\mathrm{I}} \rfloor$, respectively, where μ_{I} is the mean and σ_{I} is the standard deviation of the idler clicks distribution.

The upper bound for distinguishability discrepancy is arbitrarily set as $\mathrm{T}_\phi = 0.05$. Therefore, a regime has an acceptable amount of distinguishability discrepancy if both criterion

$$\frac{|\phi_{\mathrm{t}} - \phi_{\mathrm{I}_{\min}}|}{\phi_{\mathrm{t}}} \leq \mathrm{T}_\phi \text{ and } \frac{|\phi_{\mathrm{t}} - \phi_{\mathrm{I}_{\max}}|}{\phi_{\mathrm{t}}} \leq \mathrm{T}_\phi \tag{F.1}$$

are satisfied.

Chapter G: Solving distinguishability equation

The distinguishability measure for the LLV distributions conditioned on the mean number of idler clicks is defined as

$$\begin{aligned}\phi &= 1-\big((1-\mathrm{Q}(0,\mu_{\mathrm{H1:}\Lambda(x,\mu_\mathrm{I})},\sigma_{\mathrm{H1:}\Lambda(x,\mu_\mathrm{I})}))+\\ &+ \mathrm{Q}(0,\mu_{\mathrm{H0:}\Lambda(x,\mu_\mathrm{I})},\sigma_{\mathrm{H0:}\Lambda(x,\mu_\mathrm{I})})\big).\end{aligned} \tag{G.1}$$

where $\mathrm{Q}(d_\mathrm{LLV},\mu,\sigma)$ is the Gaussian Q-function. We use the object present/absent LLV distribution mean $\mu_{\Lambda(x,\mu_\mathrm{I})}$ and standard deviation $\sigma_{\Lambda(x,\mu_\mathrm{I})}$ in the following derivation. The Gaussian Q-function can be approximated by the error function $\mathrm{erf}(d_\mathrm{LLV})$ as

$$\mathrm{Q}(d_\mathrm{LLV},\mu,\sigma)=0.5\left(1-\mathrm{erf}(\frac{d_\mathrm{LLV}-\mu}{\sigma\sqrt{2}})\right). \tag{G.2}$$

Hence, the definition of ϕ is restated as

$$\phi=0.5\left(\mathrm{erf}(\frac{-\mu_{\mathrm{H0:}\Lambda}}{\sigma_{\mathrm{H0:}\Lambda}\sqrt{2}})+\mathrm{erf}(\frac{\mu_{\mathrm{H1:}\Lambda}}{\sigma_{\mathrm{H1:}\Lambda}\sqrt{2}})\right). \tag{G.3}$$

The signs for above are dictated by the need for a positive argument in the error function. Solving Eq. G.3 to find the parameters required for $\phi=\phi_\mathrm{t}$ needs the shots required for threshold distinguishability N_t to be found. Firstly, for QI the shots required is decomposed into $N_\mathrm{t}=N_\mathrm{I1}+N_\mathrm{I0}$ and $N_\mathrm{t}=\frac{N_\mathrm{I1}}{p_\mathrm{I}}$, where N_I1 and N_I0 are shots when the idler does and does not fire, respectively. If we combine the previous two expressions it is clear that $N_\mathrm{I0}=N_\mathrm{I1}(\frac{1}{p_\mathrm{I}}-1)$. Equation G.3, framed in terms of the variable N_I1 when $\phi=\phi_\mathrm{t}$ is expressed as

$$\phi_\mathrm{t}=0.5\left(\mathrm{erf}(-G_0\sqrt{N_\mathrm{I1}})+\mathrm{erf}(G_1\sqrt{N_\mathrm{I1}})\right), \tag{G.4}$$

where

$$G = \frac{M_1 p_{\mathrm{I}1} + C_1 + (\frac{1}{p_{\mathrm{I}}} - 1)(M_2 p_{\mathrm{I}0} + C_2)}{\sqrt{2}\left(M_1^2 p_{\mathrm{I}1}(1 - p_{\mathrm{I}1}) + M_2^2(\frac{1}{p_{\mathrm{I}}} - 1)p_{\mathrm{I}0}(1 - p_{\mathrm{I}0})\right)^{0.5}}. \tag{G.5}$$

From Eq. G.5, we substitute the relevant click probabilities to yield the object present coefficient G_1 and object absent coefficient G_0, respectively. Therefore, $N_{\mathrm{I}1}$ is numerically solved with the inverse function of ϕ_{t}

$$N_{\mathrm{I}1} = \mathrm{F}^{-1}(\phi_{\mathrm{t}}). \tag{G.6}$$

Following this, the shots required to reach threshold distinguishability is

$$N_{\mathrm{t}} = \left\lfloor \frac{N_{\mathrm{I}1}}{p_{\mathrm{I}}} \right\rfloor. \tag{G.7}$$

The shots required to reach threshold distinguishability is used throughout this thesis. It is how we can ensure a particular system parameter regime will reach threshold distinguishability, as we have the ability to increase the integration time (increase the number of shots) when acquiring an LLV sample. This analytic approach we have demonstrated here to calculate the shots required to reach threshold distinguishability saves us from a computationally expensive numerical approach to estimate this value.

Chapter H: Commutator relations

We restate the operators shown in Eq. 5.5b, Eq. 5.5a and Eq. 5.5c. We demonstrate in this appendix that these operators satisfy the commutator relations which the disentangling theorem requires. We have that

$$\hat{K}_+ = \sum_{z=1}^{M} \hat{a}^\dagger_{Sz} \hat{a}^\dagger_{I(M+1-z)}, \tag{H.1a}$$

$$\hat{K}_- = \sum_{z=1}^{M} \hat{a}_{Sz} \hat{a}_{I(M+1-z)}, \tag{H.1b}$$

$$\hat{K}_3 = \frac{1}{2} \sum_{z=1}^{M} \hat{a}^\dagger_{Sz} \hat{a}_{Sz} + \hat{a}_{I(M+1-z)} \hat{a}^\dagger_{I(M+1-z)}. \tag{H.1c}$$

We begin with the commutator relation

$$[\hat{K}_+, \hat{K}_-] = -2\hat{K}_3 \tag{H.2}$$

If we expand the commutator and rearrange we get

$$[\hat{K}_+, \hat{K}_-] = \sum_{z,t=1}^{M} \hat{a}^\dagger_{Sz} \hat{a}_{St} \hat{a}^\dagger_{I(M+1-z)} \hat{a}_{I(M+1-t)} - \hat{a}_{Sz} \hat{a}^\dagger_{St} \hat{a}_{I(M+1-z)} \hat{a}^\dagger_{I(M+1-t)}. \tag{H.3}$$

We then separate the summation into terms where $z = t$ and rename the index as ν. We also isolate terms where $z \neq t$.

$$\begin{aligned}[\hat{K}_+, \hat{K}_-] = &\sum_{\nu=1}^{M} \hat{a}^\dagger_{S\nu} \hat{a}_{S\nu} \hat{a}^\dagger_{I(M+1-\nu)} \hat{a}_{I(M+1-\nu)} - \hat{a}_{S\nu} \hat{a}^\dagger_{S\nu} \hat{a}_{I(M+1-\nu)} \hat{a}^\dagger_{I(M+1-\nu)} + \\ &+ \sum_{\substack{z,t=1 \\ z\neq t}}^{M} \hat{a}^\dagger_{Sz} \hat{a}_{St} \hat{a}^\dagger_{I(M+1-z)} \hat{a}_{I(M+1-t)} - \hat{a}_{Sz} \hat{a}^\dagger_{St} \hat{a}_{I(M+1-z)} \hat{a}^\dagger_{I(M+1-t)}.\end{aligned} \tag{H.4a}$$

The expression is simplified thanks to the $z \neq t$ summation equalling to 0, since every term in it commutes. Therefore,

$$[\hat{K}_+, \hat{K}_-] = \sum_{\nu=1}^{M} \hat{a}^\dagger_{S\nu}\hat{a}_{S\nu}\hat{a}^\dagger_{I(M+1-\nu)}\hat{a}_{I(M+1-\nu)} - \hat{a}_{S\nu}\hat{a}^\dagger_{S\nu}\hat{a}_{I(M+1-\nu)}\hat{a}^\dagger_{I(M+1-\nu)}, \tag{H.5a}$$

$$= \sum_{\nu=1}^{M} \hat{a}^\dagger_{S\nu}\hat{a}_{S\nu}\hat{a}^\dagger_{I(M+1-\nu)}\hat{a}_{I(M+1-\nu)} - (1 + \hat{a}^\dagger_{S\nu}\hat{a}_{S\nu})\hat{a}_{I(M+1-\nu)}\hat{a}^\dagger_{I(M+1-\nu)}, \tag{H.5b}$$

$$= \sum_{\nu=1}^{M} \hat{a}^\dagger_{S\nu}\hat{a}_{S\nu}\left(\hat{a}^\dagger_{I(M+1-\nu)}\hat{a}_{I(M+1-\nu)} - \hat{a}_{I(M+1-\nu)}\hat{a}^\dagger_{I(M+1-\nu)}\right) -$$

$$- \hat{a}_{I(M+1-\nu)}\hat{a}^\dagger_{I(M+1-\nu)}, \tag{H.5c}$$

$$= -\sum_{\nu=1}^{M} \hat{a}^\dagger_{S\nu}\hat{a}_{S\nu} + \hat{a}_{I(M+1-\nu)}\hat{a}^\dagger_{I(M+1-\nu)} = -2\hat{K}_3. \tag{H.5d}$$

Thus, relation 1 is satisfied. Following from this, the next commutator relation is

$$[\hat{K}_3, \hat{K}_\pm] = \pm\hat{K}_\pm. \tag{H.6}$$

As the analysis is very similar for the + case as the − case, I shall only derive the + case here. Expansion of the commutator receives

$$\begin{aligned}[\hat{K}_3, \hat{K}_+] = \frac{1}{2}\sum_{z,t=1}^{M} (\hat{a}^\dagger_{Sz}\hat{a}_{Sz} + \hat{a}_{I(M+1-z)}\hat{a}^\dagger_{I(M+1-z)})\hat{a}^\dagger_{St}\hat{a}^\dagger_{I(M+1-t)} - \\ - \hat{a}^\dagger_{St}\hat{a}^\dagger_{I(M+1-t)}(\hat{a}^\dagger_{Sz}\hat{a}_{Sz} + \hat{a}_{I(M+1-z)}\hat{a}^\dagger_{I(M+1-z)})\end{aligned} \tag{H.7}$$

By separating the summation into two components: one where $z = t$, and the index renamed as ν, and one where $z \neq t$. The summation when $z \neq t$ equals to zero, hence the commutator reduces to

$$[\hat{K}_3, \hat{K}_+] = \frac{1}{2}\sum_{\nu=1}^{M} \left(\hat{a}^\dagger_{S\nu}\hat{a}_{S\nu} + \hat{a}_{I(M+1-\nu)}\hat{a}^\dagger_{I(M+1-\nu)}\right)\hat{a}^\dagger_{S\nu}\hat{a}^\dagger_{I(M+1-\nu)} -$$

$$- \hat{a}^\dagger_{S\nu}\hat{a}^\dagger_{I(M+1-\nu)}(\hat{a}^\dagger_{S\nu}\hat{a}_{S\nu} + \hat{a}_{I(M+1-\nu)}\hat{a}^\dagger_{I(M+1-\nu)}), \tag{H.8a}$$

$$= \frac{1}{2}\sum_{\nu=1}^{M}\Bigg(\hat{a}^\dagger_{S\nu}(\hat{a}_{S\nu}\hat{a}^\dagger_{S\nu} - \hat{a}^\dagger_{S\nu}\hat{a}_{S\nu}) + \hat{a}^\dagger_{S\nu}(\hat{a}_{I(M+1-\nu)}\hat{a}^\dagger_{I(M+1-\nu)} -$$

$$-\hat{a}^\dagger_{I(M+1-\nu)}\hat{a}_{I(M+1-\nu)})\Bigg)\hat{a}^\dagger_{I(M+1-\nu)}, \tag{H.8b}$$

$$= \frac{1}{2}\sum_{\nu=1}^{M} 2\hat{a}^\dagger_{S\nu}\hat{a}^\dagger_{I(M+1-\nu)} = \hat{K}_+. \tag{H.8c}$$

Relation 2 has been verified.

Chapter I: State vector derivation

In this appendix we apply the individual operators in Eq. 5.7 to the M mode vacuum. The combination of these three results yields the M:TBSS state vector in Eq. 5.8a. The first term in the derivation is

$$e^{e^{-i\theta}\tanh(r)\hat{K}_-}|\{0\}_{2M}\rangle = |\{0\}_{2M}\rangle. \tag{I.1}$$

This reduces to the vacuum state because the only non-zero terms are when the index of the exponent power expansion is zero. We now derive the second term

$$e^{ln(\cosh^{-2}(r))\hat{K}_3}|\{0\}_{2M}\rangle = \sum_{n=0}^{\infty}\frac{1}{n!}\big(\frac{1}{2}\ln(\cosh^{-2}r)\big)^n(\hat{K}_3)^n|\{0\}_{2M}\rangle. \tag{I.2}$$

We use the multi-nomial expansion and focus on [182]

$$\begin{aligned}(\hat{K}^3)^n|\{0\}_{2M}\rangle = &\sum_{b_1,c_1,\ldots,b_M,c_M=0}^{n}\delta_{b_1+c_1+\cdots+b_M+c_M,n}\frac{n!}{b_1!c_1!\ldots b_M!c_M!}(\hat{a}^\dagger_{\mathrm{S}1}\hat{a}_{\mathrm{S}1})^{b_1}\times\\ &\times\ldots(\hat{a}^\dagger_{\mathrm{S}M}\hat{a}_{\mathrm{S}M})^{b_M}(\hat{a}_{\mathrm{I}1}\hat{a}^\dagger_{\mathrm{I}1})^{c_1}\ldots(\hat{a}_{\mathrm{I}M}\hat{a}^\dagger_{\mathrm{I}M})^{c_M}|\{0\}_{2M}\rangle, &\text{(I.3a)}\\ = &\sum_{c_1,\ldots,c_M=0}^{n}\delta_{c_1+\cdots+c_M,n}\frac{n!}{c_1!\ldots c_M!}|\{0\}_{2M}\rangle &\text{(I.3b)}\\ = &\,M^n|\{0\}_{2M}\rangle. &\text{(I.3c)}\end{aligned}$$

In the above we use that for all i where $1\leq i\leq M$ the only non-zero terms are when $b_i=0$. Moreover, for all i, $(\hat{a}_{\mathrm{I}1}\hat{a}^\dagger_{\mathrm{I}1})^{c_i}|\{0\}_{2M}\rangle = |\{0\}_{2M}\rangle$. Therefore, the remainder of the derivation is

$$\begin{aligned}e^{ln(\cosh^{-2}(r))\hat{K}_3}|\{0\}_{2M}\rangle &= \sum_{n=0}^{\infty}\frac{1}{n!}\big(\frac{M}{2}\ln(\cosh^{-2}r)\big)^n, &\text{(I.4a)}\\ &= \big(\mathrm{sech}(r)\big)^M|\{0\}_{2M}\rangle. &\text{(I.4b)}\end{aligned}$$

The last derivation applies the multi-nomial expansion again,

$$\big(\mathrm{sech}(r)\big)^M e^{-e^{i\theta}\tanh(r)\hat{K}_+}|\{0\}_{2M}\rangle = \big(\mathrm{sech}(r)\big)^M \sum_{n=0}^{\infty}(-e^{i\theta}\tanh(r))^n \times \\ \times \sum_{b_1,\ldots,b_M=0}^{n} \delta_{b_1+\cdots+b_M,n}|b_1,\ldots,b_M\rangle_{\mathbf{mI}} \otimes |b_M,\ldots b_1\rangle_{\mathbf{mS}}. \tag{I.5a}$$

This state is the M:TBSS state vector in Eq. 5.8a.

Chapter J: Unevenly distributed joint spectral amplitude

This appendix details the case of a JSA that is not evenly distributed between the M spectral modes. Each correlated idler i and signal k mode has a weight Ω_i attributed to it, where $0 < \Omega_i < 1$ and $\sum_{i=1}^{M} \Omega_i = 1$. Hence, the unequal JSA M:TBSS squeezing operator is

$$\hat{S}_{2,M\neq}(\zeta) = \exp\left(-\zeta M \sum_{z=1}^{M} \Omega_z \hat{a}_{Sz}^{\dagger} \hat{a}_{I(M+1-z)}^{\dagger} + \zeta^{*} M \sum_{z=1}^{M} \Omega_z \hat{a}_{Sz} \hat{a}_{I(M+1-z)}\right). \tag{J.1}$$

By applying the disentangling theorem as before, the three operators that satisfy the required commutator relations are

$$\hat{K}_{+} = M \sum_{z=1}^{M} \Omega_z \hat{a}_{Sz}^{\dagger} \hat{a}_{I(M+1-z)}^{\dagger}, \tag{J.2a}$$

$$\hat{K}_{-} = \hat{K}_{+}^{\dagger}, \tag{J.2b}$$

$$\hat{K}_{3} = \frac{M^2}{2} \sum_{z=1}^{M} \Omega_z^2 (\hat{a}_{Sz}^{\dagger} \hat{a}_{Sz} + \hat{a}_{Iz} \hat{a}_{Iz}^{\dagger}). \tag{J.2c}$$

Furthermore, by applying the squeezing operator to the $2M$ mode vacuum this yields

$$\begin{aligned} |\psi\rangle_{\mathrm{M}\neq:\mathrm{TBSS}} =& \hat{S}_{2,M\neq}(\zeta)|\{0\}_{2M}\rangle = (\mathrm{sech}(r))^{M^2 \sum_{z=1}^{M} \Omega_z^2} \sum_{n=0}^{\infty} (-e^{i\theta}\tanh(r))^n \dots \\ & \dots \sum_{b_1,\dots,b_M=0}^{n} \delta_{b_1+\dots+b_M,n} M^n \prod_{i=1}^{M} \Omega_i^{b_i} |b_1 \dots, b_M\rangle_{\mathbf{mI}} \otimes |b_M, \dots, b_1\rangle_{\mathbf{mS}}, \end{aligned} \tag{J.3a}$$

$$\begin{aligned} =& \frac{1}{(\bar{n}+1)^{\frac{M^2}{2} \sum_{z=1}^{M} \Omega_z^2}} \sum_{n=0}^{\infty} \left(-e^{i\theta}\sqrt{\frac{\bar{n}}{\bar{n}+1}}\right)^n \dots \\ & \dots \sum_{b_1,\dots,b_M=0}^{n} \delta_{b_1+\dots+b_M,n} M^n \prod_{i=1}^{M} \Omega_i^{b_i} |b_1 \dots, b_M\rangle_{\mathbf{mI}} \otimes |b_M, \dots, b_1\rangle_{\mathbf{mS}}. \end{aligned} \tag{J.3b}$$

When all modes have the same weight $\Omega_i = \frac{1}{M}$, this state vector $|\psi\rangle_{\mathrm{M}\neq:\mathrm{TBSS}}$ reduces to the equally distributed JSA form presented earlier $|\psi\rangle_{\mathrm{M:TBSS}}$.

Chapter K: M:TBSS reduced state

The density matrix of the M:TBSS reduced state is $\hat{\rho}_{\text{M:TBSS(1)}} = \text{Tr}_{\forall \text{mS,mI}-\{\text{mI1}\}}\left(\hat{\rho}_{\text{M:TBSS}}\right)$, which is when all but one mode is traced out. Calculation of the M:TBSS mean photon number $\bar{n}_M$ from Eq. 5.30 is greatly assisted when we are aware that the photon statistics of the M:TBSS reduced state is thermal. From the photon-number distribution of this reduced state we can easily calculate the click probability when only one idler detector clicks — relevant to Eq. 5.30. Hence, the photon-number distribution of the reduced state for a photon-number q is

$$P(q) = \text{Tr}\left(\hat{\rho}_{\text{MTBSS(1)}}|q\rangle\langle q|\right), \tag{K.1a}$$

$$= \sum_{n=0}^{\infty} P(n,M) \sum_{b_2,\ldots,b_M=0}^{n} \delta_{b_2+\cdots+b_M,n-q}, \tag{K.1b}$$

$$= \sum_{l=0}^{\infty} P(l+q,M) \binom{l+M-2}{M-2}, \tag{K.1c}$$

$$= \frac{\bar{n}^q}{(\bar{n}+1)^{q+M}}\ {}_1F_0(M-1;\ ;\frac{\bar{n}}{\bar{n}+1}), \tag{K.1d}$$

$$= \frac{\bar{n}^q}{(\bar{n}+1)^{q+1}}. \tag{K.1e}$$

We can see clearly that Eq. K.1e is thermal, where in the derivation we have introduced the generalised hypergeometric function ${}_pF_q$ [183].

Chapter L: SPDC Photon Source

The QI source used in these experiments is a type-II collinear SPDC photon pair source based on a ppKTP crystal [184], with a polling period of 10 μm and stabilised at the temperature 62°C. A CW 405 nm pump laser focused to a $1/e^2$ radius of 11 μm is driven through the crystal to generate photon pairs at 810 nm. We use a Hanbury-Brown-Twiss configuration to characterise our source quality [185]. At a pump power $P = 0.3$ mW, the typical count rates were $N_{\text{idler}} = 0.562$ MHz and $N_{\text{signal}} = 0.507$ MHz signal photons. We used fiber-coupled single-photon counting modules (Excelitas SPCM-AQRH-14-FC) with a quantum efficiency of 60 % at 810 nm operating at room temperature as our detectors. Using a $\tau_c = 2$ ns coincidence window, we measured the typical rate of coincidences as $N_c = 0.138$ MHz. We measured the second-order coherence of the signal path conditioned on idler detection as $g^{(2)}(0) = 0.006$. The value for source brightness was $7.55 \pm 0.01 \times 10^6$ pairs/s/mW. The pump power for our experiments varied between 50 and 300 μW.

Chapter M: Target Reflectivity and Noise Source

Neutral density (ND) filters realises a replicable and finite target reflectivity for our experiment. To calibrate the filter loss and thus target reflectivity ξ, we take the ratio of the total signal count-rate with (without) the filter after subtracting the detector background measured with the SPDC source blocked. To ensure accuracy of our estimation of target reflectivity ξ at the highest attenuation levels, we use integration times of up to 1 second.

A low-noise current driver (Koheron DRV300-A-10) drives an LED, which provides our system with (artificial) background noise. The low-noise current driver facilitates a controllable and constant background count to the signal detector. Our LED light is not coherent like how laser light is, but it does have Poissonian photon statistics. Moreover, our noise source is independent of target reflectivity or position. Use of a low-noise current driver is necessary to make a comparison between CI and QI detection protocols, as CI is extremely susceptible to any drift in noise level. For the sections Ch. 8.3.3 and Ch. 8.3.5 that involve temporally modulated active jamming, we use a function generator to add modulation on top of a DC offset at the current driver.

Chapter N: System loss estimation approximation

As stated earlier, system loss calculated by Eq. 8.8 and Eq. 8.9 is an approximation. We estimate the heralding efficiency when there is limited noise in the system and there is no attenuation of our signal beam. The heralding efficiency of the signal and idler detectors, respectively, in terms of click probabilities and as an explicit function of system loss

$$\mathrm{HE_S} = \frac{N_{\mathrm{coinc.}}}{N_{\mathrm{signal}}} = \frac{\mathrm{Pr_{I1}Pr_I}}{\mathrm{Pr_S}} = A_\mathrm{I}\eta_\mathrm{I} \tag{N.1}$$

and

$$\mathrm{HE_I} = \frac{N_{\mathrm{coinc.}}}{N_{\mathrm{idler}}} = \mathrm{Pr_{I1}} = A_\mathrm{S}\eta_\mathrm{S}, \tag{N.2}$$

where A_I and A_S are constants. The signal attenuation factor $\xi = 1$ as there is no attenuation of the signal beam when we are estimating the system loss. The noise source is thermal as there are only dark counts during the system loss estimation, this determines which click probabilities we use. Equation 8.8 is valid when $A_\mathrm{I} \approx 1$ for all possible values of idler and signal system loss, where it is defined as

$$A_\mathrm{I} = \frac{1}{\mathrm{Pr_S}}\left(\frac{\bar{n} + \frac{\bar{n}_{\mathrm{D,I}}}{\eta_\mathrm{I}}}{\bar{n}_{\mathrm{D,I}} + \eta_\mathrm{I}\bar{n} + 1} - \frac{1}{\eta_\mathrm{I}}\left(\frac{1}{\eta_\mathrm{S}\bar{n} + \bar{n}_{\mathrm{D,S}} + 1} - (1 - \mathrm{Pr_I})\frac{1}{\eta_\mathrm{S}\bar{n}_\times + \bar{n}_{\mathrm{D,S}} + 1}\right)\right). \tag{N.3}$$

Equation 8.9 is valid when $A_\mathrm{S} \approx 1$ for all possible values of idler and signal system loss, where it is defined as

$$A_\mathrm{S} = \frac{1}{\mathrm{Pr_I}}\left(\frac{\mathrm{Pr_I}(\bar{n} + \frac{\bar{n}_{\mathrm{D,S}}+1}{\eta_\mathrm{S}})(\eta_\mathrm{S}\bar{n}_\times + \bar{n}_{\mathrm{D,S}} + 1) - F}{(\eta_\mathrm{S}\bar{n} + \bar{n}_{\mathrm{D,S}} + 1)(\eta_\mathrm{S}\bar{n}_\times + \bar{n}_{\mathrm{D,S}} + 1)}\right), \tag{N.4}$$

with $F = \big(\bar{n}_\times - (1 - \mathrm{Pr_I})\bar{n}\big) + \frac{1}{\eta_\mathrm{S}}\big(\bar{n}_{\mathrm{D,S}} + 1 - (1 - \mathrm{Pr_I})(\bar{n}_{\mathrm{D,S}} + 1)\big)$. If the approximation does not hold then calculation of the system loss $\eta_{\mathrm{I/S}}$ requires a numerical approach. Our maximum tolerance of the HE approximation error is $|1 - A_\mathrm{S}| = 0.01$ and $|1 - A_\mathrm{I}| = 0.01$, any set of parameters that exceeds this tolerance is not included in the parameter space mentioned in

Ch. 8.2.2 when our HE approximation is valid.

Chapter O: Signal attenuation factor estimation

In a realistic system, the signal attenuation factor is completely unknown from the onset. This appendix details how we would estimate this parameter in a system that does not use preset ND filters to emulate the signal attenuation. Chapter 4 introduces a FOM which uses the CRLB for estimation of the signal attenuation factor ξ. This section compares the variance of our method for estimating the signal attenuation factor $\Delta^2\hat{\xi}$ with the variance of the optimal estimator, as given by the CRLB $\Delta^2\hat{\xi}_{\text{min}}$. The CRLB in this section differs from Ch. 4 as we have Poissonian noise for the signal channel and we consider the click-count distributions to be binomial. The CRLB for CI is

$$\Delta^2\hat{\xi}_{\text{CI:min}} = \left(-\sum_{x=0}^{N} f_{\text{CI}}(x)\frac{\partial^2 \ln\big(f_{\text{CI}}(x)\big)}{\partial \xi^2}\right)^{-1}, \tag{O.1}$$

where $f_{\text{CI}}(x) = \binom{N}{x}(\text{Pr}_{\text{S}}(\xi))^x(1-\text{Pr}_{\text{S}}(\xi))^{N-x}$ and Eq. 3.57 defines $\text{Pr}_{\text{S}}(\xi)$. The CRLB for QI is

$$\Delta^2\hat{\xi}_{\text{QI:min}} = \left(-\sum_{x=0}^{N_{\text{idler}}} f_{\text{QI}}(x)\frac{\partial^2 \ln\big(f_{\text{QI}}(x)\big)}{\partial \xi^2}\right)^{-1}, \tag{O.2}$$

where $f_{\text{QI}}(x) = \binom{N_{\text{idler}}}{x}(\text{Pr}_{\text{S|I,1}}(\xi))^x(1-\text{Pr}_{\text{S|I,1}}(\xi))^{N_{\text{idler}}-x}$ and Eq. 3.61 defines $\text{Pr}_{\text{S|I,1}}(\xi)$. The CRLB estimator theory is shown for only one click-count sample, therefore to remain consistent with the theory developed in Ch. 4, our signal attenuation factor estimators $\hat{\xi}$ are also only from one click-count sample. Of course, if we were to increase the number of samples for our estimations this will consequently reduce the CRLB and the variance of our method of estimation. Moreover, to keep consistent with the CRLB theory introduced in Ch. 4 and for simplicity we only consider that ξ is a parameter that we estimate. Whereas, a more thorough treatment acknowledges that the other system parameters are also estimates and this in turn results in a multi-parameter CRLB and a vector of our estimators. We use the theory developed by Liu et al. in Ref. [76] for our CI and QI signal attenuation factor estimators. For a CI system the

signal attenuation factor estimator is

$$\hat{\xi}_{\mathrm{CI}} = \mathrm{argmax}_{\xi}\big(f_{\mathrm{CI}}(x)\big) \tag{O.3}$$

The QI system the signal attenuation factor estimator is

$$\hat{\xi}_{\mathrm{QI}} = \mathrm{argmax}_{\xi}\big(f_{\mathrm{QI}}(x)\big) \tag{O.4}$$

We can calculate the variance of our estimator $\hat{\xi}$ with the relation

$$\Delta^2\hat{\xi} = \mathbb{E}(\hat{\xi}^2) - \mathbb{E}(\hat{\xi})^2. \tag{O.5}$$

The expected value of $\hat{\xi}$ is given by

$$\mathbb{E}(\hat{\xi}) = \sum_{x=0}^{x_{\max}} w(x)\hat{\xi}(x), \tag{O.6}$$

where x is number of signal clicks for CI and number of coincidence clicks for QI, $x_{\max}$ is N for CI and N_{idler} for QI, and $w(x)$ is the probability for the estimator $\hat{\xi}$ to estimate the value $\xi(x)$. We calculate the probability $w(x)$ for CI/QI as

$$w(x) = f_{\mathrm{CI/QI}}(x), \tag{O.7}$$

this distribution has the actual signal attenuation factor ξ as its parameter. Figure O.1 compares the CI CRLB and the variance of our method for CI signal attenuation estimation, as a function of signal detector background noise. Whereas, Fig. O.2 compares the QI CRLB and the variance of our method for QI signal attenuation estimation, as a function of signal detector background noise. Our estimator essentially satisfies the CRLB for both CI and QI, this is expected as our estimation of the click probability for a binomial distribution satisfies the CRLB. It is also clear that the QI estimator is better than the CI estimator when comparing Fig. O.1 and Fig. O.2.

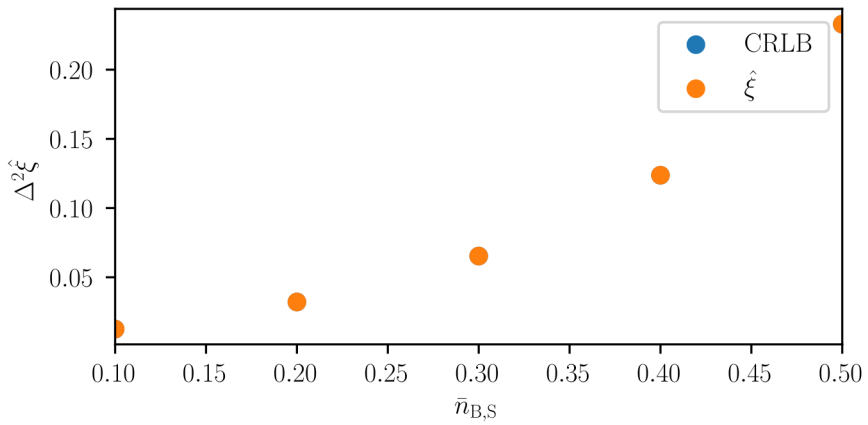

Figure O.1 – Comparison of the CRLB and our estimator $\hat{\xi}$ for CI. The variance of the estimation is on the y-axis $\Delta^2\hat{\xi}$ and signal detector background noise mean photon number on the x-axis. $\eta_S = 0.3$, $\xi = 0.5$, $\bar{n} = 0.05$ and $N = 50000$.

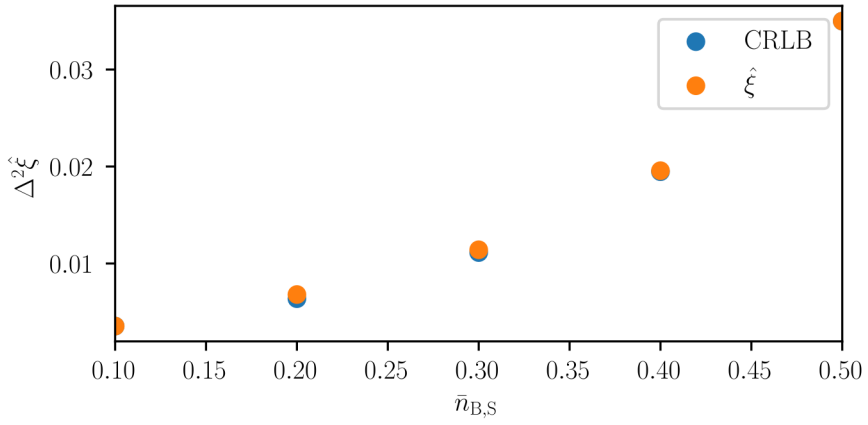

Figure O.2 – Comparison of the CRLB and our estimator $\hat{\xi}$ for QI. The variance of the estimation is on the y-axis $\Delta^2\hat{\xi}$ and signal detector background noise mean photon number on the x-axis. $N_{\text{idler}} = N \Pr_I$, $\eta_S = 0.3$, $\eta_I = 0.3$, $\xi = 0.5$, $\bar{n} = 0.05$, $\bar{n}_{B,I} = 0.0001$ and $N = 50000$.

Bibliography

[1] M. I. Skolnik, *Introduction to radar systems /2nd edition/*. McGraw-Hill, 1980.

[2] M. A. Richards, J. A. Scheer, and W. A. Holm, *Principles of Modern Radar: Basic principles*. SciTech Publishing Inc., 2010. DOI: 10.1049/SBRA021E.

[3] L. Guosui, G. Hong, and S. Weimin, "Development of random signal radars," *IEEE Trans Aerosp Electron Syst.*, vol. 35, p. 770, 1999, ISSN: 1557-9603. DOI: 10.1109/7.784050.

[4] P. McManamon, "Review of ladar: A historic, yet emerging, sensor technology with rich phenomenology," *Opt. Eng.*, vol. 51, p. 060 901, 2012. DOI: 10.1117/1.OE.51.6.060901.

[5] N. Li, C. P. Ho, J. Xue, *et al.*, "A progress review on solid-state lidar and nanophotonics-based lidar sensors," *Laser Photonics Rev.*, vol. 16, p. 2 100 511, 2022, ISSN: 1863-8880. DOI: https://doi.org/10.1002/lpor.202100511.

[6] M.-C. Amann, T. M. Bosch, M. Lescure, R. A. Myllylae, and M. Rioux, "Laser ranging: A critical review of unusual techniques for distance measurement," *Opt. Eng.*, vol. 40, p. 10, 2001. DOI: 10.1117/1.1330700.

[7] A Hooijer and R Vernimmen, "Global lidar land elevation data reveal greatest sea-level rise vulnerability in the tropics," *Nat. Comms.*, vol. 12, p. 3592, 2021, ISSN: 2041-1723. DOI: 10.1038/s41467-021-23810-9.

[8] S. Royo and M. Ballesta-Garcia, "An overview of lidar imaging systems for autonomous vehicles," *Appl. Sci.*, vol. 9, p. 4093, 2019, ISSN: 2076-3417. DOI: 10.3390/app9194093.

[9] J. S. Massa, G. S. Buller, A. C. Walker, S. Cova, M. Umasuthan, and A. M. Wallace, "Time-of-flight optical ranging system based on time-correlated single-photon counting," *Appl. Opt.*, vol. 37, p. 7298, 1998. DOI: 10.1364/AO.37.007298.

[10] M.-J. Sun, M. P. Edgar, G. M. Gibson, *et al.*, "Single-pixel three-dimensional imaging with time-based depth resolution," *Nat. Comms.*, vol. 7, p. 12 010, 2016, ISSN: 2041-1723. DOI: 10.1038/ncomms12010.

[11] J. Tachella, Y. Altmann, N. Mellado, *et al.*, "Real-time 3d reconstruction from single-photon lidar data using plug-and-play point cloud denoisers," *Nat. Comms.*, vol. 10, p. 4984, 2019, ISSN: 2041-1723. DOI: 10.1038/s41467-019-12943-7.

[12] R. H. Hadfield, J. Leach, F. Fleming, *et al.*, "Single-photon detection for long-range imaging and sensing," *Optica*, vol. 10, p. 1124, 2023. DOI: 10.1364/OPTICA.488853.

[13] A. M. Wallace, A. Halimi, and G. S. Buller, "Full waveform lidar for adverse weather conditions," *IEEE Trans. Veh. Technol.*, vol. 69, p. 7064, 2020. DOI: 10.1109/TVT.2020.2989148.

[14] R. Tobin, A. Halimi, A. McCarthy, P. J. Soan, and G. S. Buller, "Robust real-time 3d imaging of moving scenes through atmospheric obscurant using single-photon lidar," *Sci. Rep.*, vol. 11, p. 11 236, 2021, ISSN: 2045-2322. DOI: 10.1038/s41598-021-90587-8.

[15] A Einstein, B Podolsky, and N Rosen, "Can quantum-mechanical description of physical reality be considered complete?" *Phys. Rev.*, vol. 47, p. 777, 1935. DOI: 10.1103/PhysRev.47.777.

[16] J. H. Shapiro, "The quantum illumination story," *IEEE Aerosp. Electron. Syst. Mag.*, vol. 35, p. 8, 2020, ISSN: 1557-959X. DOI: 10.1109/MAES.2019.2957870.

[17] M. F. Sacchi, "Optimal discrimination of quantum operations," *Phys. Rev. A*, vol. 71, p. 62 340, 2005. DOI: 10.1103/PhysRevA.71.062340.

[18] M. F. Sacchi, "Entanglement can enhance the distinguishability of entanglement-breaking channels," *Phys. Rev. A*, vol. 72, p. 014 305, 2005. DOI: 10.1103/PhysRevA.72.014305.

[19] S. Lloyd, "Enhanced sensitivity of photodetection via quantum illumination," *Science*, vol. 321, p. 1463, 2008, ISSN: 00368075. DOI: 10.1126/science.1160627.

[20] C. Weedbrook, S. Pirandola, J. Thompson, V. Vedral, and M. Gu, "How discord underlies the noise resilience of quantum illumination," *New J. Phys.*, vol. 18, p. 43 027, 2016. DOI: 10.1088/1367-2630/18/4/043027.

[21] J. H. Shapiro and S. Lloyd, "Quantum illumination versus coherent-state target detection," *New J. Phys.*, vol. 11, p. 63 045, 2009. DOI: 10.1088/1367-2630/11/6/063045.

[22] S. H. Tan, B. I. Erkmen, V. Giovannetti, *et al.*, "Quantum illumination with gaussian states," *Phys. Rev. Lett.*, vol. 101, p. 253 601, 2008, ISSN: 00319007. DOI: 10.1103/PhysRevLett.101.253601.

[23] S. Pirandola and S. Lloyd, "Computable bounds for the discrimination of gaussian states," *Phys. Rev. A*, vol. 78, p. 12 331, 2008. DOI: 10.1103/PhysRevA.78.012331.

[24] G. D. Palma and J. Borregaard, "Minimum error probability of quantum illumination," *Phys. Rev. A*, vol. 98, p. 12 101, 2018. DOI: 10.1103/PhysRevA.98.012101.

[25] C. W. Helstrom, "Quantum detection and estimation theory," *J. Stat. Phys.*, vol. 1, p. 231, 1969. DOI: 10.1007/BF01007479.

[26] S. Guha and B. I. Erkmen, "Gaussian-state quantum-illumination receivers for target detection," *Phys. Rev. A*, vol. 80, p. 052 310, 2009, ISSN: 2469-9926. DOI: 10.1103/PhysRevA.80.052310.

[27] E. D. Lopaeva, I. R. Berchera, I. P. Degiovanni, S Olivares, G Brida, and M Genovese, "Experimental realization of quantum illumination," *Phys. Rev. Lett.*, vol. 110, p. 153 603, Apr. 2013. DOI: 10.1103/PhysRevLett.110.153603.

[28] S. Zhang, J. Guo, W. Bao, *et al.*, "Quantum illumination with photon-subtracted continuous-variable entanglement," *Phys. Rev. A*, vol. 89, p. 62 309, 2014. DOI: 10.1103/PhysRevA.89.062309.

[29] S. Zhang, X. Zou, J. Shi, J. Guo, and G. Guo, "Quantum illumination in the presence of photon loss," *Phys. Rev. A*, vol. 90, p. 052 308, 2014. DOI: 10.1103/PhysRevA.90.052308.

[30] B. S, G. S, W. C, V. D, S. J. H, and P. S, "Microwave quantum illumination," *Phys. Rev. Lett.*, vol. 114, p. 080 503, 2015. DOI: 10.1103/PhysRevLett.114.080503.

[31] M. M. Wilde, M. Tomamichel, S. Lloyd, and M. Berta, "Gaussian hypothesis testing and quantum illumination," *Phys. Rev. Lett.*, vol. 119, p. 120 501, 2017. DOI: 10.1103/PhysRevLett.119.120501.

[32] Q. Zhuang, Z. Zhang, and J. H. Shapiro, "Entanglement-enhanced neyman-pearson target detection using quantum illumination," *J. Opt. Soc. Am. B*, vol. 34, p. 1567, 2017. DOI: 10.1364/JOSAB.34.001567.

[33] Q. Zhuang, Z. Zhang, and J. H. Shapiro, "Optimum mixed-state discrimination for noisy entanglement-enhanced sensing," *Phys. Rev. Lett.*, vol. 118, p. 040 801, 2017. DOI: 10.1103/PhysRevLett.118.040801.

[34] Q. Zhuang, Z. Zhang, and J. H. Shapiro, "Quantum illumination for enhanced detection of rayleigh-fading targets," *Phys. Rev. A*, vol. 96, p. 20 302, 2017. DOI: 10.1103/PhysRevA.96.020302.

[35] B. Xiong, X. Li, X.-Y. Wang, and L. Zhou, "Improve microwave quantum illumination via optical parametric amplifier," *Ann. Phys-New York*, vol. 385, p. 757, Oct. 2017. DOI: 10.1016/j.aop.2017.08.024.

[36] S Pirandola, B. R. Bardhan, T Gehring, C Weedbrook, and S Lloyd, "Advances in photonic quantum sensing," *Nat. Photonics*, vol. 12, p. 724, Nov. 2018. DOI: 10.1038/s41566-018-0301-6.

[37] L. Fan and M. S. Zubairy, "Quantum illumination using non-gaussian states generated by photon subtraction and photon addition," *Phys. Rev. A*, vol. 98, p. 12 319, 2018. DOI: 10.1103/PhysRevA.98.012319.

[38] R. Nair and M. Gu, "Fundamental limits of quantum illumination," *Optica*, vol. 7, pp. 771–774, 2020. DOI: 10.1364/OPTICA.391335.

[39] A. Karsa and S. Pirandola, "Noisy receivers for quantum illumination," *IEEE Aerosp. Electron. Syst. Mag.*, vol. 35, p. 22, 2020. DOI: 10.1109/MAES.2020.3004019.

[40] A. Karsa, G. Spedalieri, Q. Zhuang, and S. Pirandola, "Quantum illumination with a generic gaussian source," *Phys. Rev. Res.*, vol. 2, p. 023 414, 2020. DOI: 10.1103/PhysRevResearch.2.023414.

[41] M.-H. Yung, F. Meng, X.-M. Zhang, and M.-J. Zhao, "One-shot detection limits of quantum illumination with discrete signals," *Npj quantum Inf.*, vol. 6, p. 75, 2020, ISSN: 2056-6387. DOI: 10.1038/s41534-020-00303-z.

[42] Y. Jo, S. Lee, Y. S. Ihn, Z. Kim, and S.-Y. Lee, "Quantum illumination receiver using double homodyne detection," *Phys. Rev. Res.*, vol. 3, p. 013 006, 2021. DOI: 10.1103/PhysRevResearch.3.013006.

[43] X. Chen and Q. Zhuang, "Entanglement-assisted detection of fading targets via correlation-to-displacement conversion," *Phys. Rev. A*, vol. 107, p. 62 405, 2023. DOI: 10.1103/PhysRevA.107.062405.

[44] R. Wei, J. Li, W. Wang, S. Meng, B. Zhang, and Q. Guo, "Comparison of snr gain between quantum illumination radar and classical radar," *Opt. Express*, vol. 30, p. 36 167, 2022. DOI: 10.1364/OE.468158.

[45] G. Sorelli, N. Treps, F. Grosshans, and F. Boust, "Detecting a target with quantum entanglement," *IEEE Aerosp. Electron. Syst. Mag.*, vol. 37, p. 68, 2022. DOI: 10.1109/MAES.2021.3116323.

[46] S. Borderieux, A. Coatanhay, and A. Khenchaf, "Estimation of the influence of a noisy environment on the binary decision strategy in a quantum illumination radar," *Sensors*, vol. 22, p. 4821, 2022, ISSN: 1424-8220. DOI: 10.3390/s22134821.

[47] A. R. U. Devi and A. K. Rajagopal, "Quantum target detection using entangled photons," *Phys. Rev. A*, vol. 79, p. 062 320, 2009. DOI: 10.1103/PhysRevA.79.062320.

[48] Z. Zhang, M. Tengner, T. Zhong, F. N. C. Wong, and J. H. Shapiro, "Entanglement's benefit survives an entanglement-breaking channel," *Phys. Rev. Lett.*, vol. 111, p. 010 501, 2013. DOI: 10.1103/PhysRevLett.111.010501.

[49] Z. Zhang, S. Mouradian, F. N. C. Wong, and J. H. Shapiro, "Entanglement-enhanced sensing in a lossy and noisy environment," *Phys. Rev. Lett.*, vol. 114, p. 110 506, 2015. DOI: 10.1103/PhysRevLett.114.110506.

[50] P Livreri, E Enrico, L Fasolo, *et al.*, "Microwave quantum radar using a josephson traveling wave parametric amplifier," 2022, pp. 1–5. DOI: 10.1109/RadarConf2248738.2022.9764353.

[51] R Assouly, R Dassonneville, T Peronnin, A Bienfait, and B Huard, "Quantum advantage in microwave quantum radar," *Nat. Phys.*, vol. 19, p. 1418, 2023, ISSN: 1745-2481. DOI: 10.1038/s41567-023-02113-4.

[52] R. Nair and M. Gu, "Quantum sensing of phase-covariant optical channels," *arXiv:quant-ph/2306.15256*, 2023. DOI: 10.48550/arXiv.2306.15256.

[53] S. M. Barnett and S. Croke, "Quantum state discrimination," *Adv. Opt. Photonics*, vol. 1, p. 238, 2009. DOI: 10.1364/AOP.1.000238.

[54] M Sanz, U. L. Heras, J. García-Ripoll, E Solano, and R. D. Candia, "Quantum estimation methods for quantum illumination," *Phys. Rev. Lett.*, vol. 118, p. 70 803, 2017. DOI: 10.1103/PhysRevLett.118.070803.

[55] S.-Y. Lee, Y. S. Ihn, and Z. Kim, "Quantum illumination via quantum-enhanced sensing," *Phys. Rev. A*, vol. 103, p. 12 411, 2021. DOI: 10.1103/PhysRevA.103.012411.

[56] R. Jonsson and R. D. Candia, "Gaussian quantum estimation of the loss parameter in a thermal environment," *J. Phys. A: Math. Theor.*, vol. 55, p. 385 301, 2022, ISSN: 1751-8121. DOI: 10.1088/1751-8121/ac83fa.

[57] L Davidovich and R. L. de Matos Filho, "Quantum illumination strategy for parameter estimation," *Phys. Rev. A*, vol. 108, p. 42 612, 2023. DOI: 10.1103/PhysRevA.108.042612.

[58] C. W. S. Chang, A. M. Vadiraj, J Bourassa, B Balaji, and C. M. Wilson, "Quantum-enhanced noise radar," *Appl. Phys. Lett.*, vol. 114, p. 112 601, 2019. DOI: 10.1063/1.5085002.

[59] S Barzanjeh, S Pirandola, D Vitali, and J. M. Fink, "Microwave quantum illumination using a digital receiver," *Sci. Adv.*, vol. 6, eabb0451, 2020. DOI: 10.1126/sciadv.abb0451.

[60] D. Luong, C. W. S. Chang, A. M. Vadiraj, A. Damini, C. M. Wilson, and B. Balaji, "Receiver operating characteristics for a prototype quantum two-mode squeezing radar," *IEEE T. Aero. Elec. Sys.*, vol. 56, p. 2041, 2020. DOI: 10.1109/taes.2019.2951213.

[61] M. Reichert, Q. Zhuang, J. H. Shapiro, and R. D. Candia, "Quantum illumination with a hetero-homodyne receiver and sequential detection," *Phys. Rev. Appl.*, vol. 20, p. 14 030, 2023. DOI: 10.1103/PhysRevApplied.20.014030.

[62] H. Shi, B. Zhang, and Q. Zhuang, "Fulfilling entanglement's optimal advantage via converting correlation to coherence," *arXiv:quant-ph/2207.06609*, 2023. DOI: 10.48550/arXiv.2207.06609.

[63] H. Shi, B. Zhang, J. H. Shapiro, Z. Zhang, and Q. Zhuang, "Optimal entanglement-assisted electromagnetic sensing and communication in the presence of noise," *arXiv:quant-ph/2309.12629*, 2023. DOI: 10.48550/arXiv.2309.12629.

[64] E. D. Lopaeva, I. R. Berchera, S Olivares, G Brida, I. P. Degiovanni, and M Genovese, "A detailed description of the experimental realization of a quantum illumination protocol," *Phys. Scr.*, vol. 2014, p. 014 026, 2014, ISSN: 1402-4896. DOI: 10.1088/0031-8949/2014/T160/014026.

[65] S. Ragy, I. R. Berchera, I. P. Degiovanni, *et al.*, "Quantifying the source of enhancement in experimental continuous variable quantum illumination," *J. Opt. Soc. Am. B*, vol. 31, p. 2045, Sep. 2014. DOI: 10.1364/JOSAB.31.002045.

[66] A Meda, E Losero, N Samantaray, *et al.*, "Photon-number correlation for quantum enhanced imaging and sensing," *J. Opt. (U. K.)*, vol. 19, p. 94 002, Sep. 2017. DOI: 10.1088/2040-8986/aa7b27.

[67] T Gregory, P.-A. Moreau, E Toninelli, and M. J. Padgett, "Imaging through noise with quantum illumination," *Sci. Adv.*, vol. 6, eaay2652, 2020. DOI: 10.1126/sciadv.aay2652.

[68] T Gregory, P.-A. Moreau, S Mekhail, O Wolley, and M. J. Padgett, "Noise rejection through an improved quantum illumination protocol," *Sci. Rep.*, vol. 11, p. 21 841, 2021, ISSN: 2045-2322. DOI: 10.1038/s41598-021-01122-8.

[69] G. Ortolano, E. Losero, S. Pirandola, M. Genovese, and I. Ruo-Berchera, "Experimental quantum reading with photon counting," *Sci. Adv.*, vol. 7, eabc7796, 2023, doi: 10.1126/sciadv.abc7796. DOI: 10.1126/sciadv.abc7796.

[70] J. Zhao, A. Lyons, A. C. Ulku, H. Defienne, D. Faccio, and E. Charbon, "Light detection and ranging with entangled photons," *Opt. Express*, vol. 30, p. 3675, 2022. DOI: 10.1364/OE.435898.

[71] P. S. Blakey, H. Liu, G. Papangelakis, *et al.*, "Quantum and non-local effects offer over 40 db noise resilience advantage towards quantum lidar," *Nat. Commun.*, vol. 13, p. 5633, 2022, ISSN: 2041-1723. DOI: 10.1038/s41467-022-33376-9.

[72] J. D. Franson, "Nonlocal cancellation of dispersion," *Phys. Rev. A*, vol. 45, p. 3126, 1992. DOI: 10.1103/PhysRevA.45.3126.

[73] D. G. England, B. Balaji, and B. J. Sussman, "Quantum-enhanced standoff detection using correlated photon pairs," *Phys. Rev. A*, vol. 99, p. 023 828, 2019, ISSN: 24699934. DOI: 10.1103/PhysRevA.99.023828.

[74] H. Yang, W. Roga, J. Pritchard, and J. Jeffers, "Quantum illumination with simple detection," *Proc. SPIE*, vol. 11347, E. Diamanti, S. Ducci, N. Treps, and S. Whitlock, Eds., p. 113470I, 2020. DOI: 10.1117/12.2555390.

[75] H. He, D. Giovannini, H. Liu, E. Chen, Z. Yan, and A. S. Helmy, "Non-classical semiconductor photon sources enhancing the performance of classical target detection systems," *J. Light. Technol.*, vol. 38, p. 4540, 2020. DOI: 10.1364/JLT.38.004540.

[76] H Liu, B Balaji, and A. S. Helmy, "Target detection aided by quantum temporal correlations: Theoretical analysis and experimental validation," *IEEE T. Aero. Elec. Sys.*, vol. 56, p. 3529, 2020, ISSN: 1557-9603. DOI: 10.1109/TAES.2020.2974054.

[77] H. Yang, W. Roga, J. D. Pritchard, and J. Jeffers, "Gaussian state-based quantum illumination with simple photodetection," *Opt. Express*, vol. 29, p. 8199, 2021. DOI: 10.1364/OE.416151.

[78] R. J. Murchie, J. D. Pritchard, and J. Jeffers, "Theoretical comparison of quantum and classical illumination for simple detection-based lidar," *Proc. SPIE*, vol. 11835, K. S. Deacon and R. E. Meyers, Eds., 118350G, 2021. DOI: 10.1117/12.2597042.

[79] S.-Y. Lee, D. H. Kim, Y. Jo, T. Jeong, Z. Kim, and D. Y. Kim, "Bound for gaussian-state quantum illumination using a direct photon measurement," *Opt. Express*, vol. 31, p. 38 977, 2023. DOI: 10.1364/OE.505405.

[80] H. Yang, N. Samantaray, and J. Jeffers, "Quantum illumination with multiplexed photodetection," *Phys. Rev. Appl.*, vol. 18, p. 034 021, Sep. 2022. DOI: 10.1103/PhysRevApplied.18.034021.

[81] J. G. Rarity, P. R. Tapster, J. G. Walker, and S Seward, "Experimental demonstration of single photon rangefinding using parametric downconversion," *Appl. Opt.*, vol. 29, p. 2939, 1990. DOI: 10.1364/AO.29.002939.

[82] Q. Zhuang, Z. Zhang, and J. H. Shapiro, "Entanglement-enhanced lidars for simultaneous range and velocity measurements," *Phys. Rev. A*, vol. 96, p. 40 304, 2017. DOI: 10.1103/PhysRevA.96.040304.

[83] M. Reichert, R. D. Candia, M. Z. Win, and M. Sanz, "Quantum-enhanced doppler lidar," *Npj quantum Inf.*, vol. 8, p. 147, 2022, ISSN: 2056-6387. DOI: 10.1038/s41534-022-00662-9.

[84] Z. Huang, C. Lupo, and P. Kok, "Quantum-limited estimation of range and velocity," *PRX Quantum*, vol. 2, p. 30 303, Jul. 2021. DOI: 10.1103/PRXQuantum.2.030303.

[85] H. Liu, D. Giovannini, H. He, *et al.*, "Enhancing lidar performance metrics using continuous-wave photon-pair sources," *Optica*, vol. 6, p. 1349, 2019. DOI: 10.1364/OPTICA.6.001349.

[86] S. Frick, A. McMillan, and J. Rarity, "Quantum rangefinding," *Opt. Express*, vol. 28, p. 37 118, 2020. DOI: 10.1364/OE.399902.

[87] Q. Zhuang, "Quantum ranging with gaussian entanglement," *Phys. Rev. Lett.*, vol. 126, p. 240 501, 2021. DOI: 10.1103/PhysRevLett.126.240501.

[88] Q. Zhuang and J. H. Shapiro, "Ultimate accuracy limit of quantum pulse-compression ranging," *Phys. Rev. Lett.*, vol. 128, p. 10 501, 2022. DOI: 10.1103/PhysRevLett.128.010501.

[89] H. Kuniyil, H. Ozel, H. Yilmaz, and K. Durak, "Noise-tolerant object detection and ranging using quantum correlations," *J. Opt. (U. K.)*, vol. 24, p. 105 201, Aug. 2022. DOI: 10.1088/2040-8986/ac899c.

[90] R. J. Murchie, J. D. Pritchard, and J. Jeffers, *Object detection and rangefinding with quantum states using simple detection*, 2023. DOI: 10.48550/arXiv.2307.10785.

[91] M. P. Mrozowski, R. J. Murchie, J. Jeffers, and J. D. Pritchard, "Demonstration of quantum-enhanced rangefinding robust against classical jamming," *Opt. Express*, vol. 32, p. 2916, 2024. DOI: 10.1364/OE.503619.

[92] H. Liu, C. Qin, G. Papangelakis, M. L. Iu, and A. S. Helmy, "Compact all-fiber quantum-inspired lidar with over 100 db noise rejection and single photon sensitivity," *Nat. Comms.*, vol. 14, p. 5344, 2023, ISSN: 2041-1723. DOI: 10.1038/s41467-023-40914-6.

[93] T. Brougham, N. Samantaray, and J. Jeffers, "Using random coherent states to mimic quantum illumination," *Phys. Rev. A*, vol. 108, p. 52 404, Nov. 2023. DOI: 10.1103/PhysRevA.108.052404.

[94] R. G. Torromé, "Quantum illumination with multiple entangled photons," *Adv. Quantum Technol.*, vol. 4, p. 2 100 101, 2020. DOI: 10.1002/qute.202100101.

[95] R. G. Torromé, *Quantum illumination with non-gaussian three photons states*, 2023. DOI: 10.48550/arXiv.2305.10458.

[96] L. Cohen, E. S. Matekole, Y. Sher, D. Istrati, H. S. Eisenberg, and J. P. Dowling, "Thresholded quantum lidar: Exploiting photon-number-resolving detection," *Phys. Rev. Lett.*, vol. 123, p. 203 601, 2019. DOI: 10.1103/PhysRevLett.123.203601.

[97] J. F. I. Smith, "Quantum interferometer and radar theory based on n00n, m and m or linear combinations of entangled states," vol. 7702, 2010, p. 77020I. DOI: 10.1117/12.849810.

[98] L. Maccone and C. Ren, "Quantum radar," *Phys. Rev. Lett.*, vol. 124, p. 200 503, 2020. DOI: 10.1103/PhysRevLett.124.200503.

[99] C. M. Caves and B. L. Schumaker, "New formalism for two-photon quantum optics. i. quadrature phases and squeezed states," *Phys. Rev. A*, vol. 31, p. 3068, May 1985. DOI: 10.1103/PhysRevA.31.3068.

[100] S. M. Barnett and P. L. Knight, "Squeezing in correlated quantum systems," *J. Mod. Optics*, vol. 34, p. 841, Jun. 1987, ISSN: 0950-0340. DOI: 10.1080/09500348714550781.

[101] D Renker, "Geiger-mode avalanche photodiodes, history, properties and problems," *Nucl. Instrum.*, vol. 567, p. 48, 2006, ISSN: 0168-9002. DOI: https://doi.org/10.1016/j.nima.2006.05.060.

[102] C Fabre and N Treps, "Modes and states in quantum optics," *Rev. Mod. Phys.*, vol. 92, p. 35 005, 2020. DOI: 10.1103/RevModPhys.92.035005.

[103] R Loudon, *The Quantum Theory of Light*. Oxford University Press, 2003.

[104] M. O. Scully and M. S. Zubairy, *Quantum Optics*. Cambridge University Press, 1997, ISBN: 9780521435956. DOI: DOI:10.1017/CBO9780511813993.

[105] K. J. Blow, R. Loudon, S. J. D. Phoenix, and T. J. Shepherd, "Continuum fields in quantum optics," *Phys. Rev. A*, vol. 42, p. 4102, Oct. 1990. DOI: 10.1103/PhysRevA.42.4102.

[106] E. H. Kennard, "Zur quantenmechanik einfacher bewegungstypen," *Z. Phys.*, vol. 44, p. 326, 1927, ISSN: 0044-3328. DOI: 10.1007/BF01391200.

[107] W Heisenberg, "Über den anschaulichen inhalt der quantentheoretischen kinematik und mechanik," *Z. Phys.*, vol. 43, pp. 172–198, 1927, ISSN: 0044-3328. DOI: 10.1007/BF01397280.

[108] R. J. Glauber, "Coherent and incoherent states of the radiation field," *Phys. Rev.*, vol. 131, 1963, ISSN: 0031899X. DOI: 10.1103/PhysRev.131.2766.

[109] E. C. G. Sudarshan, "Equivalence of semiclassical and quantum mechanical descriptions of statistical light beams," *Phys. Rev. Lett.*, vol. 10, p. 277, Apr. 1963. DOI: 10.1103/PhysRevLett.10.277.

[110] R. J. Glauber, "Photon correlations," *Phys. Rev. Lett.*, vol. 10, p. 84, Feb. 1963. DOI: 10.1103/PhysRevLett.10.84.

[111] Y. Kano, "A new phase-space distribution function in the statistical theory of the electromagnetic field," *J. Math. Phys.*, vol. 6, p. 1913, 2004, ISSN: 0022-2488. DOI: 10.1063/1.1704739.

[112] E Wigner, "On the quantum correction for thermodynamic equilibrium," *Phys. Rev.*, vol. 40, p. 749, Jun. 1932. DOI: 10.1103/PhysRev.40.749.

[113] C. M. Caves, K. S. Thorne, R. W. P. Drever, V. D. Sandberg, and M. Zimmermann, "On the measurement of a weak classical force coupled to a quantum-mechanical oscillator. i. issues of principle," *Rev. Mod. Phys.*, vol. 52, p. 341, 1980. DOI: 10.1103/RevModPhys.52.341.

[114] L. P. Grishchuk and M. V. Sazhin, "Squeezed quantum states of a harmonic oscillator in the problem of gravitational-wave detection," *Sov. Phys. JETP*, vol. 57, p. 1128, 1983, ISSN: 0038-5646.

[115] G Milburn and D. F. Walls, "Production of squeezed states in a degenerate parametric amplifier," *Opt. Commun.*, vol. 39, p. 401, 1981, ISSN: 0030-4018. DOI: 10.1016/0030-4018(81)90232-7.

[116] B. R. Mollow and R. J. Glauber, "Quantum theory of parametric amplification," *Phys. Rev.*, vol. 160, p. 1076, 1967. DOI: 10.1103/PhysRev.160.1076.

[117] R. W. Boyd, *Nonlinear optics*, R. W. Boyd, Ed. Academic Press, 2008, ISBN: 978-0-12-369470-6. DOI: https://doi.org/10.1016/B978-0-12-369470-6.00002-2.

[118] M. H. Rubin, D. N. Klyshko, Y. H. Shih, and A. V. Sergienko, "Theory of two-photon entanglement in type-ii optical parametric down-conversion," *Phys. Rev. A*, vol. 50, p. 05 122, 1994. DOI: 10.1103/PhysRevA.50.5122.

[119] W. P. Grice and I. A. Walmsley, "Spectral information and distinguishability in type-ii down-conversion with a broadband pump," *Phys. Rev. A*, vol. 56, p. 1627, 1997. DOI: 10.1103/PhysRevA.56.1627.

[120] D. S. Hum and M. M. Fejer, "Quasi-phasematching," *C. R. Phys.*, vol. 8, p. 180, 2007, ISSN: 1631-0705. DOI: 10.1016/j.crhy.2006.10.022.

[121] A. K. Ekert and P. L. Knight, "Correlations and squeezing of two-mode oscillations," *Am. J. Phys.*, vol. 57, p. 692, Aug. 1989, ISSN: 0002-9505. DOI: 10.1119/1.15922.

[122] F. Hong-yi and J. R. Klauder, "Eigenvectors of two particles' relative position and total momentum," *Phys. Rev. A*, vol. 49, p. 704, Feb. 1994. DOI: 10.1103/PhysRevA.49.704.

[123] S. Barnett and P. M. Radmore, *Methods in theoretical quantum optics*. Oxford Academic, 2002, ISBN: 0198563612. DOI: 10.1093/acprof:oso/9780198563617.001.0001.

[124] R. J. Glauber, "The quantum theory of optical coherence," *Phys. Rev.*, vol. 130, p. 2529, 1963. DOI: 10.1103/PhysRev.130.2529.

[125] R.-B. Jin and R. Shimizu, "Extended wiener-khinchin theorem for quantum spectral analysis," *Optica*, vol. 5, p. 93, 2018. DOI: 10.1364/OPTICA.5.000093.

[126] R. H. Brown and R. Q. Twiss, "Correlation between photons in two coherent beams of light," *Curr. Sci.*, vol. 66, p. 945, 1994, ISSN: 00113891.

[127] L. Mandel and E. Wolf, *Optical Coherence and Quantum Optics*. Cambridge University Press, 1995. DOI: 10.1017/cbo9781139644105.

[128] M. V. Fedorov and N. I. Miklin, "Schmidt modes and entanglement," *Contemp. Phys.*, vol. 55, p. 94, 2014, doi: 10.1080/00107514.2013.878554. DOI: 10.1080/00107514.2013.878554.

[129] I. R. Berchera and I. P. Degiovanni, "Quantum imaging with sub-poissonian light: Challenges and perspectives in optical metrology," *Metrologia*, vol. 56, p. 024 001, 2019, ISSN: 0026-1394. DOI: 10.1088/1681-7575/aaf7b2.

[130] R Loudon, "Non-classical effects in the statistical properties of light," *Rep. Prog. Phys.*, vol. 43, p. 913, 1980, ISSN: 0034-4885. DOI: 10.1088/0034-4885/43/7/002.

[131] M. D. Reid and D. F. Walls, "Violations of classical inequalities in quantum optics," *Phys. Rev. A*, vol. 34, p. 1260, Aug. 1986. DOI: 10.1103/PhysRevA.34.1260.

[132] R Loudon, "Non-classical effects in the statistical properties of light," *Rep. Prog. Phys.*, vol. 43, p. 913, 1980, ISSN: 0034-4885. DOI: 10.1088/0034-4885/43/7/002.

[133] S. M. Barnett and P. L. Knight, "Thermofield analysis of squeezing and statistical mixtures in quantum optics," *J. Opt. Soc. Am. B*, vol. 2, p. 467, 1985. DOI: 10.1364/JOSAB.2.000467.

[134] G. C. Ghirardi, A Rimini, and T Weber, "A general argument against superluminal transmission through the quantum mechanical measurement process," *Lett. Nuovo Cimento (1971-1985)*, vol. 27, p. 293, 1980, ISSN: 1827-613X. DOI: 10.1007/BF02817189.

[135] K. Kraus, A Böhm, J. D. Dollard, and W. H. Wootters, *States, Effects, and Operations: Fundamental Notions of Quantum Theory*. Springer Berlin, 1983. DOI: 10.1007/3-540-12732-1.

[136] S. M. Barnett, *Quantum Information*. Oxford University Press, 2009. DOI: 10.1093/oso/9780198527626.001.0001.

[137] I. Cusini, D. Berretta, E. Conca, *et al.*, "Historical perspectives, state of art and research trends of single photon avalanche diodes and their applications (part 1: Single pixels)," *Front. Phys.*, vol. 10, 2022, ISSN: 2296-424X.

[138] P. L. Kelley and W. H. Kleiner, "Theory of electromagnetic field measurement and photoelectron counting," *Phys. Rev.*, vol. 136, A316, Oct. 1964. DOI: 10.1103/PhysRev.136.A316.

[139] S. M. Barnett, L. S. Phillips, and D. T. Pegg, "Imperfect photodetection as projection onto mixed states," *Opt. Commun.*, vol. 158, p. 45, 1998, ISSN: 0030-4018. DOI: 10.1016/S0030-4018(98)00511-2.

[140] H Yuen and J Shapiro, "Optical communication with two-photon coherent states–part iii: Quantum measurements realizable with photoemissive detectors," *IEEE Trans. Inf. Theory*, vol. 26, p. 78, 1980, ISSN: 1557-9654. DOI: 10.1109/TIT.1980.1056132.

[141] D. B. Horoshko, S. D. Bièvre, G Patera, and M. I. Kolobov, "Thermal-difference states of light: Quantum states of heralded photons," *Phys. Rev. A*, vol. 100, p. 053 831, Nov. 2019. DOI: 10.1103/PhysRevA.100.053831.

[142] J. A. Bergou, "Discrimination of quantum states," *J. Mod. Opt.*, vol. 57, p. 160, Feb. 2010, doi: 10.1080/09500340903477756, ISSN: 0950-0340. DOI: 10.1080/09500340903477756.

[143] A. Chefles, "Quantum state discrimination," *Contemp. Phys.*, vol. 41, p. 0401, 2000, doi: 10.1080/00107510010002599. DOI: 10.1080/00107510010002599.

[144] W. Zhang, L. Yu, M. Yang, and Z. Cao, "Multicopy quantum state discrimination," *Sci. China: Phys. Mech. Astron.*, vol. 55, p. 60, 2012, ISSN: 1869-1927. DOI: 10.1007/s11433-011-4502-y.

[145] K. M. R. Audenaert, J Calsamiglia, R Muñoz-Tapia, *et al.*, "Discriminating states: The quantum chernoff bound," *Phys. Rev. Lett.*, vol. 98, p. 160 501, 2007. DOI: 10.1103/PhysRevLett.98.160501.

[146] P. H. Garthwaite, I. T. Jolliffe, and B. Jones, *Statistical inference*. Oxford University Press, 2002. DOI: 10.1093/oso/9780198572268.001.0001.

[147] M. Wilde, *Quantum information theory*. Cambridge University Press, 2013. DOI: 10.1017/CBO9781139525343.

[148] G. Spedalieri and S. L. Braunstein, "Asymmetric quantum hypothesis testing with gaussian states," *Phys. Rev. A*, vol. 90, p. 052 307, 2014, ISSN: 10941622. DOI: 10.1103/PhysRevA.90.052307.

[149] Q. Zhuang and S. Pirandola, "Entanglement-enhanced testing of multiple quantum hypotheses," *Commun. Phys.*, vol. 3, p. 103, 2020, ISSN: 2399-3650. DOI: 10.1038/s42005-020-0369-4.

[150] A Papoulis and S. Pillai, *Probability, Random Variables, and Stochastic Processes*. McGraw-Hill, 1984, pp. 57–63.

[151] J. Neyman and E. S. Pearson, "On the problem of the most efficient tests of statistical hypotheses," *Phil. Trans. Roy. Soc. Lond. A*, vol. 231, p. 0289, 1933. DOI: 10.1098/rsta.1933.0009.

[152] J. K. Ghosh, "Only linear transformations preserve normality," *Sankhyā: Indian J. Stat.*, vol. 31, p. 309, 1969, ISSN: 0581572X.

[153] D Petz and C Ghinea, "Introduction to quantum fisher information," 2011. DOI: 10.1142/9789814338745_0015.

[154] P. P. Rohde and T. C. Ralph, "Modelling photo-detectors in quantum optics," *J. Mod. Optics*, vol. 53, p. 1589, 2006, ISSN: 09500340. DOI: 10.1080/09500340600578369.

[155] Élie Gouzien, B. Fedrici, A. Zavatta, S. Tanzilli, and V. D'Auria, "Quantum description of timing jitter for single-photon on-off detectors," *Phys. Rev. A*, vol. 98, p. 13 833, Jul. 2018. DOI: 10.1103/PhysRevA.98.013833.

[156] A. Ly, M. Marsman, J. Verhagen, R. P. P. P. Grasman, and E.-J. Wagenmakers, "A tutorial on fisher information," *J. Math. Psychol.*, vol. 80, p. 040, 2017, ISSN: 0022-2496. DOI: 10.1016/j.jmp.2017.05.006.

[157] R. A. Fisher, M. M. Nieto, and V. D. Sandberg, "Impossibility of naively generalizing squeezed coherent states," *Phys. Rev. D*, vol. 29, p. 1107, Mar. 1984. DOI: 10.1103/PhysRevD.29.1107.

[158] P. Kok and S. L. Braunstein, "Postselected versus nonpostselected quantum teleportation using parametric down-conversion," *Phys. Rev. A*, vol. 61, p. 42 304, Mar. 2000. DOI: 10.1103/PhysRevA.61.042304.

[159] S. Frick, "Quantum rangefinding," *Ph.D. thesis, University of Bristol*, 2019.

[160] A. McCarthy, R. J. Collins, N. J. Krichel, V. Fernández, A. M. Wallace, and G. S. Buller, "Long-range time-of-flight scanning sensor based on high-speed time-correlated single-photon counting," *Appl. Opt.*, vol. 48, p. 6241, 2009. DOI: 10.1364/AO.48.006241.

[161] B Behroozpour, P. A. M. Sandborn, M. C. Wu, and B. E. Boser, "Lidar system architectures and circuits," *IEEE Commun. Mag.*, vol. 55, p. 135, 2017, ISSN: 1558-1896. DOI: 10.1109/MCOM.2017.1700030.

[162] B. I. Erkmen and J. H. Shapiro, "Unified theory of ghost imaging with gaussian-state light," *Phys. Rev. A*, vol. 77, p. 43 809, 2008. DOI: 10.1103/PhysRevA.77.043809.

[163] B. I. Erkmen and J. H. Shapiro, "Ghost imaging: From quantum to classical to computational," *Adv. Opt. Photonics*, vol. 2, p. 405, 2010. DOI: 10.1364/AOP.2.000405.

[164] T. Jiang, Y. Bai, W. Tan, *et al.*, "Ghost imaging lidar system for remote imaging," *Opt. Express*, vol. 31, p. 15 107, 2023. DOI: 10.1364/OE.485831.

[165] J. Jeffers, *Private communication*, 2021.

[166] N. C. Ahlquist and R. J. Charlson, "Measurement of the wavelength dependence of atmospheric extinction due to scatter," *Atmos. Environ. (1967)*, vol. 3, p. 551, 1969, ISSN: 0004-6981. DOI: https://doi.org/10.1016/0004-6981(69)90045-6.

[167] S. J. Koppal, *Computer Vision: A Reference Guide*. Springer, 2014, ISBN: 978-0-387-31439-6. DOI: 10.1007/978-0-387-31439-6_534.

[168] Y. Ma, J. Anderson, S. Crouch, and J. Shan, "Moving object detection and tracking with doppler lidar," *Remote Sens.*, vol. 11, 2019, ISSN: 2072-4292. DOI: 10.3390/rs11101154.

[169] M. Hanada and S. Matsuura, *MCMC from Scratch: A Practical Introduction to Markov Chain Monte Carlo*. Singapore: Springer, 2022. DOI: 10.1007/978-981-19-2715-7.

[170] S. Ross, "Chapter 4 - generating discrete random variables," in S. Ross, Ed. Academic Press, 2013, pp. 47–68, ISBN: 978-0-12-415825-2. DOI: https://doi.org/10.1016/B978-0-12-415825-2.00004-8.

[171] M. Gilli, D. Maringer, and E. Schumann, "Chapter 6 - generating random numbers," in M. Gilli, D. Maringer, and E. Schumann, Eds. Academic Press, 2019, pp. 103–132, ISBN: 978-0-12-815065-8. DOI: 10.1016/B978-0-12-815065-8.00017-0.

[172] S. Emanueli and A. Arie, "Temperature-dependent dispersion equations for ktiopo4 and ktioaso4," *Appl. Opt.*, vol. 42, p. 6661, 2003. DOI: 10.1364/AO.42.006661.

[173] R. G. Torrome and S. Barzanjeh, *Advances in quantum radar and quantum lidar*, 2023. DOI: 10.48550/arXiv.2310.07198.

[174] R. G. Torromé, N. B. Bekhti-Winkel, and P. Knott, *Introduction to quantum radar*, 2021. DOI: 10.48550/arXiv.2006.14238.

[175] J. A. Richardson, L. A. Grant, and R. K. Henderson, "Low dark count single-photon avalanche diode structure compatible with standard nanometer scale cmos technology," *IEEE Photonics Technol. Lett.*, vol. 21, p. 1020, 2009, ISSN: 1941-0174. DOI: 10.1109/LPT.2009.2022059.

[176] G. S. Buller, N. J. Krichel, A. McCarthy, *et al.*, "Kilometer range depth imaging using time-correlated single-photon counting," vol. 8155, Sep. 2011, p. 81551I. DOI: 10.1117/12.899377.

[177] A. McCarthy, N. J. Krichel, N. R. Gemmell, *et al.*, "Kilometer-range, high resolution depth imaging via 1560 nm wavelength single-photon detection," *Opt. Express*, vol. 21, p. 8904, 2013. DOI: 10.1364/OE.21.008904.

[178] G. G. Taylor, A. McCarthy, B. Korzh, *et al.*, "Long-range depth imaging with 13ps temporal resolution using a superconducting nanowire singlephoton detector," Optica Publishing Group, 2020, SM2M.6. DOI: 10.1364/CLEO_SI.2020.SM2M.6.

[179] H. Moya-Cessa, "Generation and properties of superpositions of displaced fock states," *J. Mod. Opt.*, vol. 42, p. 1741, 1995, ISSN: 13623044. DOI: 10.1080/09500349514551521.

[180] P. Král, "Displaced and squeezed fock states," *J. Mod. Opt.*, vol. 37, p. 889, 1990, ISSN: 13623044. DOI: 10.1080/09500349014550941.

[181] G. E. P. Box, *Statistics for experimenters: an introduction to design, data analysis, and model building*. Wiley, 1978.

[182] M. Abramowitz and I. A. Stegun, *Handbook of Mathematical Functions with Formulas, Graphs and Mathematical Tables*. Dover, 1965.

[183] L. J. Slater, *Generalized Hypergeometric Functions*. Cambridge University Press, 1966, ISBN: 9780521090612.

[184] S. M. Lee, H. Kim, M. Cha, and H. S. Moon, "Polarization-entangled photon-pair source obtained via type-ii non-collinear spdc process with ppktp crystal," *Opt. Express*, vol. 24, p. 2941, 2016. DOI: 10.1364/OE.24.002941.

[185] M Beck, "Comparing measurements of g(2)(0) performed with different coincidence detection techniques," *J. Opt. Soc. Am. B*, vol. 24, p. 2972, 2007. DOI: 10.1364/JOSAB.24.002972.